NASA Contractor Report 172599

The Investigation of Advanced Remote Sensing, Radiative Transfer and Inversion Techniques for the Measurement of Atmospheric Constituents

Adarsh Deepak and Pi-Huan Wang

Science and Technology Corporation
Hampton, Virginia

Contract NAS1-15198
March 1985

National Aeronautics and
Space Administration

Langley Research Center
Hampton, Virginia 23665

NASA Contractor Report 172599

The Investigation of Advanced Remote Sensing, Radiative Transfer and Inversion Techniques for the Measurement of Atmospheric Constituents

Adarsh Deepak and Pi-Huan Wang

Science and Technology Corporation
Hampton, Virginia

Contract NAS1-15198
March 1985

National Aeronautics and
Space Administration

Langley Research Center
Hampton, Virginia 23665

FOREWORD

This document, "The Investigation of Advanced Remote Sensing, Radiative Transfer and Inversion Techniques for the Measurement of Atmospheric Constituents," is the final report on investigations performed for the National Aeronautics and Space Administration (NASA) by the Institute for Atmospheric Optics and Remote Sensing (IFAORS), under Contract NAS1-15198. The period of performance was from December 15, 1977 to March 15, 1985.

We gratefully acknowledge M. P. McCormick, L. R. McMaster, G. K. Yue, W. P. Chu, and R. R. Adams for stimulating discussions and encouragement during the course of this work.

TABLE OF CONTENTS

TABLE OF CONTENTS (cont'd)

SUMMARY

Since atmospheric particulates and gaseous species (such as ozone) play a vital role in the modification and retention of the solar radiation in the atmosphere due to scattering and absorption, there has been an enhanced interest in recent years in the study of variability and background levels of atmospheric aerosols and gaseous species.

In order to fully understand how aerosols and gaseous species, such as ozone, affect the atmospheric quality, atmospheric chemistry, radiation balance, climate and transport processes, it is necessary to obtain accurate data of their optical, physical, spatial and temporal properties. In order to achieve these goals, IFAORS was awarded Contract NAS1-15198 by NASA-Langley Research Center, with the objective of developing advanced space and ground-based techniques for determining the characteristics of aerosol and gaseous species and their variability.

Work was performed on the development of the solar aureole technique, which is a simple, accurate and practical technique for the measurement of columnar aerosol size distributions. The experimental and theoretical details of the technique and its experimental validation are discussed in this report.

In addition, a multispectral solar extinction technique for the measurement of aerosol characteristics is also discussed. The various aspects and results of three satellite techniques, based on the multispectral measurement of horizon limb radiance, solar occultation, as in SAM II and SAGE, and upwelling radiance, as in LANDSAT and GOES satellites, are discussed.

The corrections to the aerosol extinction measurements due to the forward single and multiple scattered radiation entering the detector's

field of view along with the direct radiation are also discussed for both laser transmissometry and solar radiometry. Also discussed are the simulation of limb solar aureole radiance, and the variability of ozone at high altitudes during satellite sunrise/sunset events, using models based on earth's curvature. Analytical models used for representing typical aerosol size distributions are described along with examples of the parameterized graphical catalog plots.

SECTION 1

INTRODUCTION

Atmospheric particulates and gaseous species (such as ozone) have been of interest to atmospheric scientists and climatologists for their contribution to environmental quality, visibility, global radiation budget, global circulation and climate change. They play a vital role in the modification and possible retention of the Sun's radiation in the atmosphere due to scattering and absorption. Their effect on the atmosphere visibility and sky brightness is well known.

In order to fully understand how aerosols affect atmospheric quality, atmospheric chemistry, radiation balance, climate and transport processes, it is necessary to obtain accurate data of the physical, spatial, and temporal properties of aerosols in the atmosphere.

The overall objectives of this research program are to develop space and ground-based remote sensing techniques, involving the application of sophisticated radiative transfer codes and inversion techniques, for the determination of aerosols and gaseous characteristics and their variability.

In this connection, science support was provided to the NASA Langley Research Center under NASA Contract NAS1-15198 on the different tasks listed as follows:

1. Continue development of the ground-based solar aureole technique for monitoring aerosol size distributions.

2. Analysis of SAGE[1]/AEM-B and SAM II[2]/NIMBUS-7 experiment data using the modified SLIC and other computer programs to retrieve aerosol characteristics and optical properties.

3. Investigate the diurnal variations, if any, in the retrieved aerosol and gaseous characteristics for studying radiative interactions with the atmosphere.

4. Develop the theory and design of new instrument techniques and optimize them for extracting maximum information content about aerosols and gaseous species.

5. Determine the corrections due to multiple scattering, polarization, absorption and spherical atmospheres.

1.1 ORGANIZATION OF THE REPORT

In order to facilitate the readers' understanding the contents of the work performed under Contract NAS1-15198, this report has been organized into the following sections.

Section 2 contains the details of the work performed on the solar aureole technique for the measurement of aerosol size distributions. A multispectral solar extinction technique for the measurement of aerosol characteristics is discussed in Section 3. Section 4 contains the discussions on forward scattering corrections to aerosol extinction measurements by both laser transmissometry and solar radiometry. Section 5 discusses the analytical modeling of aerosol size distributions. Section 6 gives the details of satellite techniques based on the measurements of limb radiance, solar occultation and upwelling radiance - for the global measurement of aerosol characteristics.

---

[1] Stratospheric Aerosol and Gas Experiment

[2] Stratospheric Aerosol Measurement

The simulation of limb solar aureole radiance is presented in Section 7. In Section 8 the variability of ozone at high altitudes during satellite sunrise/sunset events, with the models utilizing the earth's curvature effects is discussed. Section 9 contains the acknowledgments, and Section 10, the references.

SECTION 2

SOLAR AUREOLE AEROSOL MEASUREMENT TECHNIQUE

2.1 INTRODUCTION

The solar aureole is a region of enhanced sky brightness extending for about 20° around the sun's disk. It is attributed to the predominant forward scattering of sunlight by atmospheric aerosols. The gradient of angular distribution of radiance in the solar aureole region is highly sensitive to the aerosol size distribution. Measurement of solar aureole radiance can, therefore, be effectively used to determine atmospheric aerosol properties. For this purpose, a simple photographic solar aureole measurement (PSAM) technique, developed in 1970 (Ref. 1), has since been successfully used to make radiance measurements along the almucantar, a scan for which the observation zenith angle equals the solar zenith angle, with local zenith as the axis of rotation. Almucantar radiance data in the solar aureole region has been successfully used to retrieve aerosol size distributions (Refs. 2-4). Such retrieval methods will be referred to as the solar aureole almucantar radiance (SAAR) methods. Subsequently, in 1974, the photographic solar aureole isophote (PSAI) method (Refs. 5-7) for determining aerosol characteristics was developed. The techniques for making solar aureole radiance measurements for the two methods are the same; the difference lies in the selection of scattered radiance data for determination of the aerosol size distributions. In one case, it is the almucantar radiance data; in the second, the isophote locii and their shapes. In the following sections we describe the various aspects of: 1) the experimental procedure (Section 2.2) which includes the photography and photographic-photometry aspects of making accurate measurements of the sky radiance distribution that are essential to the two

methods; 2) the radiative transfer and multiple scattering problems (Section 2.3); and, 3) the inversion of radiance data to retrieve the aerosol characteristics (Section 2.4).

It is hoped that this description will assist others in setting up their own photographic solar aureole measurement systems. Since a camera (single lens reflex) is likely to be a part of any laboratory, relatively inexpensive, portable photographic systems for making aureole measurements can readily be set up and thus employed to form a global network of stations for making measurements of atmospheric aerosol characteristics.

2.2 THE EXPERIMENTAL PROCEDURE

Descriptions of the photometry, sensitometry and densitometry techniques employed for extracting accurate sky radiance data from the photographs are given in the subsequent sections.

2.2.1 Historical Background

For many years, Volz (Ref. 8) has taken excellent color photographs of the solar aureole by occulting the sun with various kinds of objects, such as, a hand, pillar, or wall edge, for the purpose of visual and qualitative analysis of the sky scene in connection with his turbidity measurements. In 1970, on the suggestion of Professor A.E.S. Green, the author (A.D.) started making solar aureole radiance measurements with a Polaroid Land Camera, using the commercially available Black and White Polaroid-46L

transparency film (Ref. 1). Since then, such photographic measurements have been successfully performed for the purpose of retrieving aerosol size distributions (Refs. 2-7). Photoelectric measurements of the solar aureole radiance have been made by many researchers (Refs. 1, 9-15). Subsequently, a 35-mm SLR Minolta camera, with a 50-mm focal length lens, and Kodak Tri-X film were used (Ref. 2). The occultation of the sun was done by a 4.0D neutral density filter disk located coaxially on a support about 1.2 m from the lens. Later, solar aureole measurements were made with a Nikon camera with a 55-mm focal length lens, and a Hasselblad camera with an 80-mm lens, and using Kodak Plus-X film (Refs. 5-6). Excellent results have been obtained with the latter equipment.

2.2.2 Advantages of Photographic Measurements

Photographic film offers the following advantages over the photoelectric detectors. Photographic film is still the most compact recording device for storing large amounts of information (e.g., a 35-mm film frame typically contains about 10^6 individual picture elements, known as pixels). The film also has the capability of integrating over exposure times, thereby extending its range of detectability. Moreover, photography is relatively easy to use, and the stored records of the scene are permanent. Perhaps the greatest advantage of the film lies in the fact that the complete solar aureole scene can be recorded instantaneously. A scanning radiometer approach could take several minutes and introduce significant measurement errors, under time-varying conditions (clouds, smoke plumes, aircraft contrails, etc.)

or from moving platforms, such as balloons, aircrafts or satellites. It enables one to easily relate the radiance along a particular line-of-sight to some specific sky detail that may not be apparent otherwise. In addition, the use of photogrammetry enables one to make measurements not only of the radiance of, say, a cloud, but also of its dimensions.

A small format (35-mm or 70-mm) camera is a portable system which needs no external power supply, and its operating costs are relatively low. These attributes fulfill one of the aims of this research effort; namely, the development of inexpensive systems for making sky radiance and atmospheric extinction measurements, which may be inverted to retrieve the characteristics of atmospheric species.

The problems generally attributed to the use of photographic film as a photometric measure include such things as nonlinear response, limited dynamic range, reciprocity failure (the reduction in sensitivity as exposure time is increased), adjacency effects (nonindependence of adjacent pixels), and relatively high granularity. Camera shutter speed variations are also a source of error. Procedures will be described that overcome, minimize or take account of these effects.

2.2.3 Comparison with Photoelectric Measurements

Comparison of the results of simultaneous measurements of the solar aureole radiance by photographic and photoelectric methods, performed in 1970 at Gainesville, Florida (Ref. 1) and in 1977 at Tucson, Arizona (Ref. 16), in each case show extremely good agreement (within 2 percent) between the two sets of data. In the case of the experiment at Tucson, Arizona, in May 1977,

the data were obtained with our system and the University of Wisconsin Solar Aureole Photometer (Ref. 14). The agreement between the data is shown in Fig. 2.1.

2.2.4 Description of Experimental Equipment

Essentially, one needs the following equipment: camera, lens, film, spectral filters, adapters for mounting them on the lens and on the camera body, a neutral density (ND) occulting disk, a tripod with azimuth and elevation controls, a flat sturdy camera platform, an inclinometer (e.g., a plumb line and a protractor) for elevation measurements, and an accurate spirit level for adjusting the platform to attain horizontal level. Following is a brief description of the exposure equipment, which is schematically shown in Fig. 2.2 a), b).

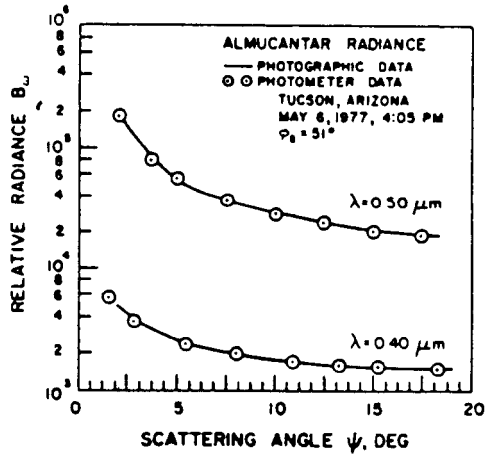

FIG. 2.1 Plots of relative almucantar radiance, obtained by photographic and radiometric systems, as a function of scattering angle for for λ = 0.4 μm *and* 0.5 μm.

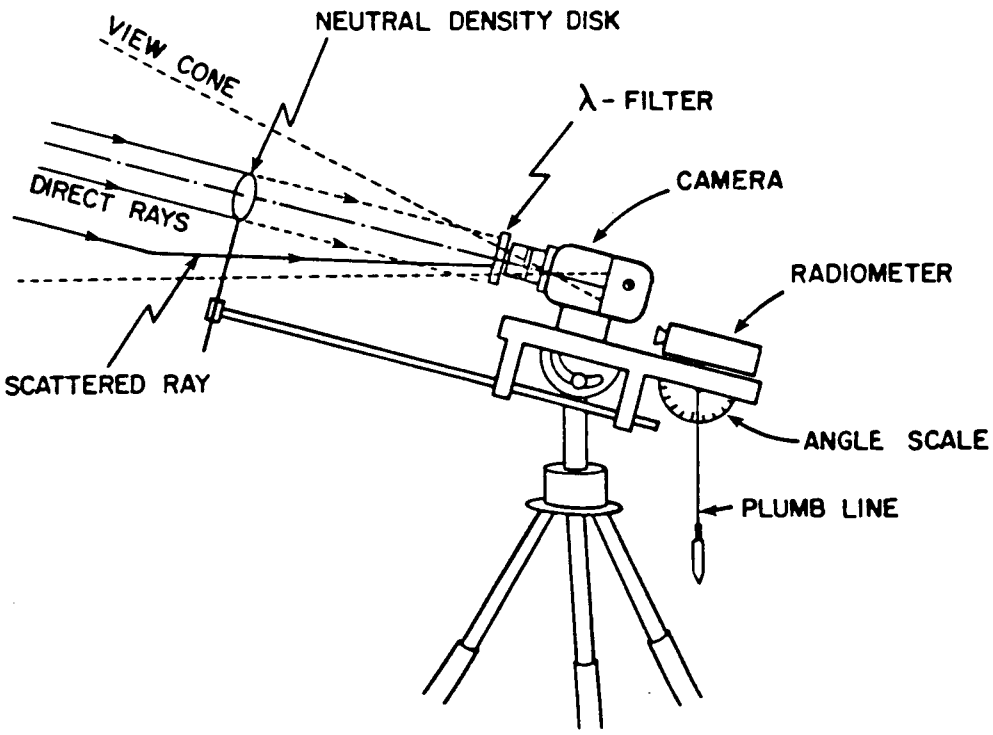

FIG. 2.2 a): Schematic Diagram of the Solar Aureole Photography Equipment and the Geometry of the Experimental Technique.

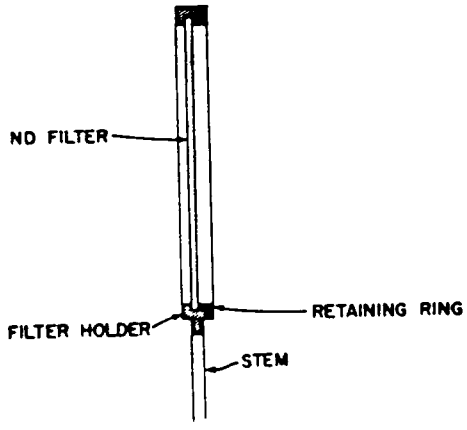

FIG. 2.2 b): Schematic Diagram of a Section of the Neutral Density Filter Disk Assembly, Showing the Filter Held in a Circular Snap-Type Frame

(i) Cameras and Lenses

Photography, in our case, was performed using a Nikon FTN 35-mm camera with a 55-mm lens, as well as a Hasselblad 70-mm camera with an 80-mm lens. The choice of lens is governed by two competing requirements: (1) we want to photograph as wide an angular field as possible around the sun, which implies a short focal length lens; while (2) we want the sun image size to be large enough (long focal length) to permit accurate microdensitometer measurements to be made of the image optical density. A 55-mm lens gives a FOV of about 36^{o} on a 36-mm film frame, and the 80-mm lens, a FOV of 38^{o} on a 56-mm frame, with diameters of the respective images of the half-degree sun of 0.48-mm and 0.70-mm. These choices have been found suitable for our purposes.

(ii) Photographic Film

For solar aureole photography, the requirements for the film are: good resolution, reasonably high speed, and a spectral response curve $S(\lambda)$ which is fairly uniform in the visible region. Kodak Tri-X and Plus-X films, both meet these criteria, and have, therefore, been used extensively in our work. Plus-X (ASA-125) has higher resolution but lower speed than Tri-X (ASA-400), and so in most of our work, we used the former. For photography at $\lambda = 0.7$ μm, Kodak Plus-X Aerial film 3401 with extended red sensitivity, was used. When using the Hasselblad camera, it was found very convenient to load the film in several detachable film magazines and take them along for field use.

(iii) Spectral Filters

Narrow band ($\Delta\lambda \sim 0.01$ μm) interference filters, which peak at $\lambda_o = 0.40$, 0.50, 0.55, 0.60, and 0.70 μm, were used to simplify the inversion and could easily be mounted in front of the camera lens. The use of narrow bandwidth simplifies the computations in that it permits the integration over the spectral transmission curve $T(\lambda)$ of the filter to be replaced by a factor $T(\lambda_o)\ \Delta\lambda$. If broadband Wratten filters are used, then integration must be formed over $T(\lambda)$ (Ref. 3). Since, in general, interference filters are designed for normal incidence, then as the incidence angle ϕ increases, the peak wavelength λ_ϕ of the filter is reduced and is given by the relation (Ref. 17):

$$\frac{(\lambda_N - \lambda\phi)}{\lambda_N} = \frac{d\lambda_N}{\lambda_n} = \frac{-\phi\ d\phi}{m'^2} \tag{1}$$

where λ_N is the peak wavelength at normal incidence and m' is the effective refractive index of the filter. For small ϕ, the shape of the bandpass does not change appreciably except for a small decrease in overall transmission. In a converging beam, because of the varying angles, the effective bandwidth is broadened and, in general, the peak wavelength is shifted to shorter wavelengths. The narrower the bandwidth, the more noticeable are the effects of the angle change.

On the other hand, an increase in temperature causes interference filters to shift in peak wavelength to larger wavelengths due to the expansion of the layers. For example, some typical filters at room temperature show a

shift of approximately 0.004 percent of the peak wavelength per ^{o}C. The shape $T(\lambda)$ of the bandpass curve and the transmission outside the bandpass are important, as they can greatly effect the unwanted "noise" background.

Thus, there is some advantage in choosing slightly broader bandpass filters. Inversion of aureole scattering data seems to be relatively more sensitive to the filter peak wavelength than to the filter bandwidth.

(iv) The Neutral Density Disk Assembly

The neutral density (ND) disk, made up of a 4.0D Kodak Wratten filter having a diameter slightly larger than that of the camera lens, is mounted in a narrow circular snap type frame with a thin stem attached to it. This complete unit will be referred to as the "neutral density or ND lollipop." Of the several designs of the ND lollipop tested, the one that minimized the amount of edge reflections and diffraction effects is shown schematically in Fig. 2.2 b).

The lollipop stem is mounted upright, on a support rod, about 1.2 m in front of the lens, so that the ND disk is coaxial with the lens. Its position along the support rod can be adjusted. All metal parts are painted black to minimize reflections and glint, which are nearly impossible to eliminate at grazing angles of incidence. The Wratten ND filter does not usually have a flat spectral response $D_{ND}(\lambda)$ but typically varies with λ in the spectral range 0.4 μm and 0.8 μm, as shown in Fig. 2.3.

The use of 4.0D filter, instead of an opaque occulting disk, permits the sun's disk, which is 10^4 to 10^6 times brighter than the sky (Fig. 1 in Ref. 1), to be photographed by suppressing the glare and flare

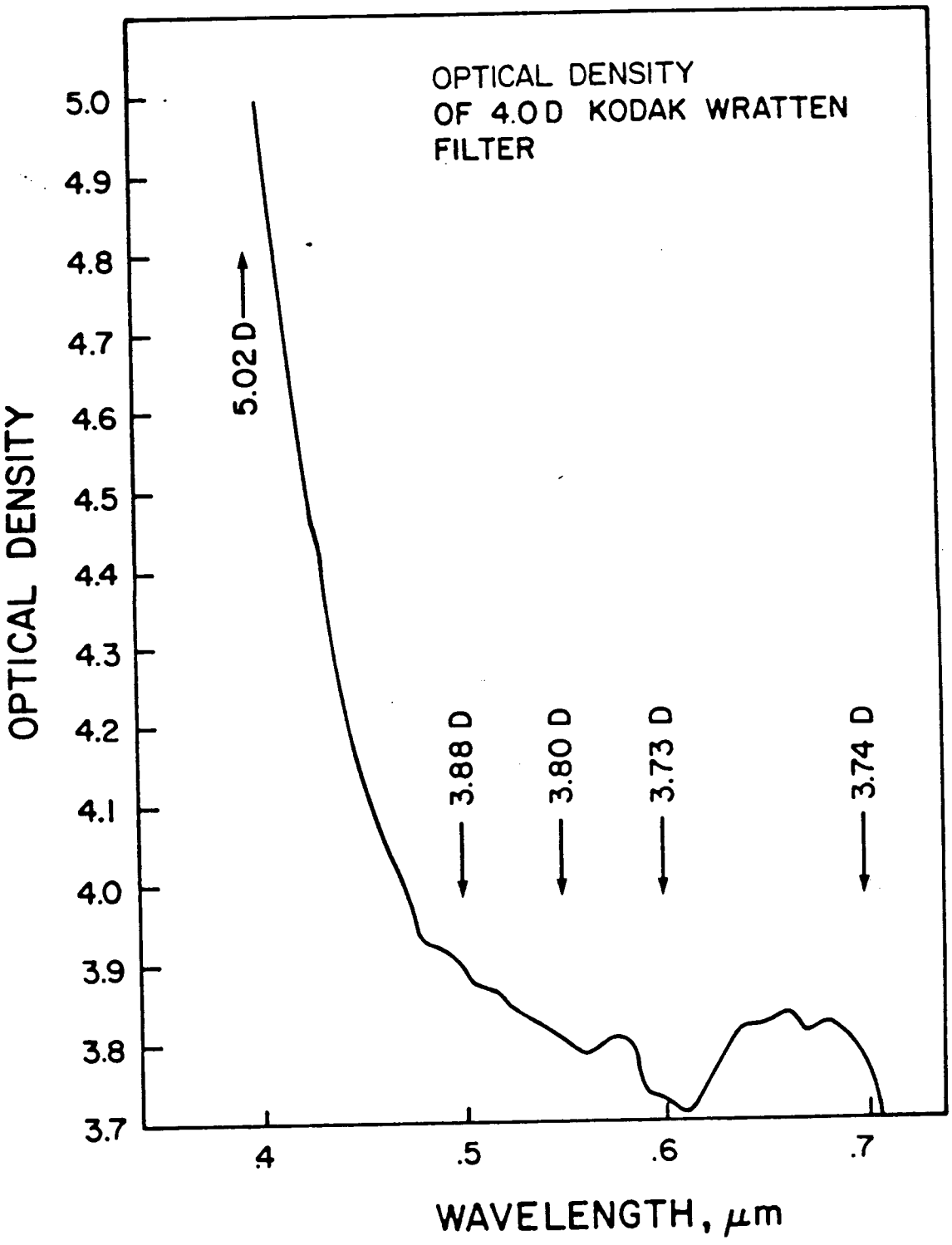

FIG. 2.3: Measured Spectral Response of a 4.0D Kodak Wratten Neutral Density Filter

effects. The "noise" due to these effects is reduced to within the fog level of the film. The sun's image not only provides the exact location of the sun's disk for measuring angular distances accurately, but, in addition, provides a reference optical density level relative to which the entire photograph can be calibrated.

Glass ND filters were also tried, but because of their much heavier weight and greater inertia, it was often difficult to dampen their small oscillatory motions in the breeze outside, thereby reducing the changes of taking of good solar aureole photographs.

2.2.5 Photography of Sun and Its Aureole

Described in the following is a step-by-step procedure for taking quality solar aureole photographs with an SLR camera (Hasselblad):

1. The camera platform is mounted on a sturdy tripod, and the tripod adjusted until the camera mounting plate is completely horizontal, as determined by an accurate spirit level.

2. The camera is mounted on the mounting plate, such that the lens axis is parallel to the plane of the inclinometer and the camera mounting plate (Fig. 2.2 a).

3. The inclinometer, consisting of a protractor behind a plumb line, is adjusted so that the elevation angle reads 90°.

4. The long support rod is then mounted on the platform and the alignment of the ND-disk adjusted, by watching through the viewfinder, such that the disk is coaxial with the camera lens, with its plane parallel to the lens. The disk is held at about 1.2 m (4 feet) from the lens; but its position can be adjusted.

5. A 2.0D ND filter is installed on the lens and the lens is manually stopped down to f/22. The reason for using the smallest possible f-stop is to obtain the largest possible depth-of-field, so that everything from the ND disk to infinity is focused as sharply as possible on the film plane.

6. Adjust the tripod elevation and azimuth such that the ND disk shadows the lens completely and concentrically. Then, by looking through the viewfinder, fine adjustments of the tripod azimuth and elevation controls are made until the solar disk appears centered in the ND disk. This centering is important to assure good quality pictures (Fig. 2.4), since in such a position, glint and other reflection effects are minimized. A photograph with the sun off-center within the ND-disk may sometimes give pictures which show this edge reflection.

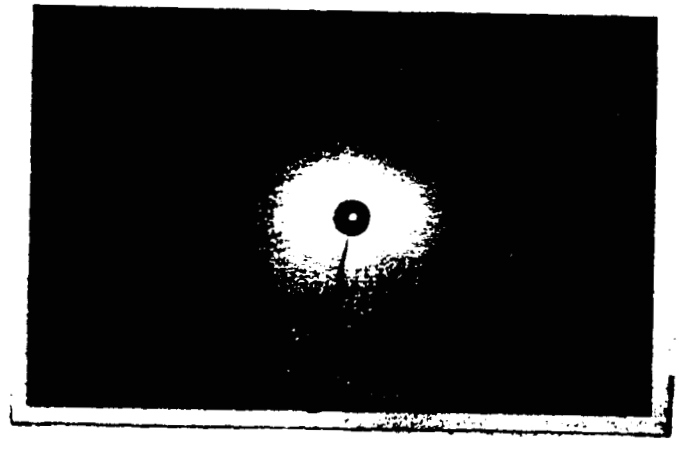

FIG. 2.4: Example of Good Quality Photograph of the Sun and its Aureole

7. Focus the lens to twice the distance between the lens and the occulting disk and stop the lens down to its smallest opening. This will have the effect of placing the occulting disk at the near limit of the "depth of field," as defined by the circle of confusion (Ref. 18) whose diameter is given by

$$c = \frac{F^2}{f(u - F)}$$

where F is the lens focal length, u is the focus distance and f is the lens f/stop. When the resulting negatives are scanned on the microdensitometer, the scanning aperture, as projected onto the specimen, should be adjusted to be equal to or greater than c as defined above.

8. Remove the 2.0D ND-filter, cycle the camera and attach the film magazine. A remote shutter cord is useful to minimize disturbance of the ND occulting disk.

9. Mount the wavelength filter on the lens and take a series of photographs at shutter speeds, bracketing those that are predetermined as optimum for each wavelength filter. The optimum exposure times used for solar aureole photography through wavelength filters primarily depend on the filter bandwidth and peak transmittance, speed, spectral response, and processing of the film, lens f/stop, atmospheric haze and the sun's elevation. Repeat exposures for each wavelength filter in succession. For example, for wavelength filters (λ 400 nm - λ 650 nm) with bandwidth $\Delta\lambda \sim$ 8 nm - 10 nm, Kodak Plus-X (ASA-125) Panchromatic film, lens aperture f/22, relatively clear skies, solar zenith angles between 15° to 60°, the optimum exposure time was found to be 1/15 to 1/30 second. The film was processed for photographic gamma close to unity. These exposure times should be considered as a starting point, from which one can determine the appropriate exposure times for one's own set of conditions.

We found that taking photographs at four exposure times from 1/8 to 1/60 second almost always provided at least one analyzable negative under the aforementioned conditions. The criterion for a good analyzable solar aureole exposure is that the optical density at the edge of the negative be only slightly greater than the density of the unexposed part of the film, with the processing gamma adjusted to place the highest density reading, including the occulted sun, well below the shoulder of the characteristic curve and within the range of the densitometer employed.

10. The time of day at which photographs are taken are noted, and at each of these times the solar zenith angle is read by the plumb-line.

The entire photography sequence should be completed as quickly as possible (less than a minute) so that the solar zenith angle and sky conditions can be assumed to remain practically constant for that set of photographs. About 25 cm of each film roll should be left unused for performing film sensitometry in the laboratory prior to processing of the film.

2.2.6 Laboratory Photgraphic Calibration Techniques

(A) Sensitometry

(i) Exposure

The photographic effect or the developed image optical density D increases up to a certain limit with increasing exposure E, which is defined by (Ref. 19-20)

$$E = It \tag{2}$$

where I is the intensity of incident light and t the exposure time. The relation between the density D and the amount of exposure is usually expressed by plotting D vs $\log_{10}E$ on linear graph paper. The plot is

referred to as the characteristic curve or the H-D curve (after Hurter and Driffield). In the linear portion of the curve, the density D is given by the relationship

$$D_{NET} = D - D_F = \gamma \, (\log_{10}E - \log_{10}E_F) \qquad (3)$$

where γ, the slope of the straight portion of the plot is called the photographic gamma, D is the gross visual density, D_F is the base-plus-fog density, and E_F is the extrapolated exposure corresponding to zero density above base plus fog (Fig. 2.5). Typical values of γ range between 0.9 and 1.2 for Kodak Plus-X film when processed in the way described below.

In our case, the H-D curve was obtained by performing film sensitometry (Ref. 21) on the unexposed portion of the film for each roll before it was processed. An EG&G Xenon Flash Senitometer, which provides uniform illumination over the entire length of a Kodak No. 2 Step Tablet was used for this purpose. The step tablet has 21 calibrated density steps, ranging from 0.04D to 3.04D. A Wratten 1.0D filter was installed inside the sensitometer, along with an EG&G three-line filter, to control the exposure intensity. A sufficient length of unexposed film was pulled from the film magazine (in total darkness) to cover the sensitometer exposure plate and the step tablet, making sure that the film emulsion side faced the plate. The sensitometer cover was closed and the film was exposed for 1/100 second.

(ii) Processing

Once sensitometric exposure has been completed, the film is ready for processing. Uniform processing is required for photographic photometry. Ideally, use of a sensitometric processing machine is recommended. However, such equipment is not generally available to the researcher. While commercial

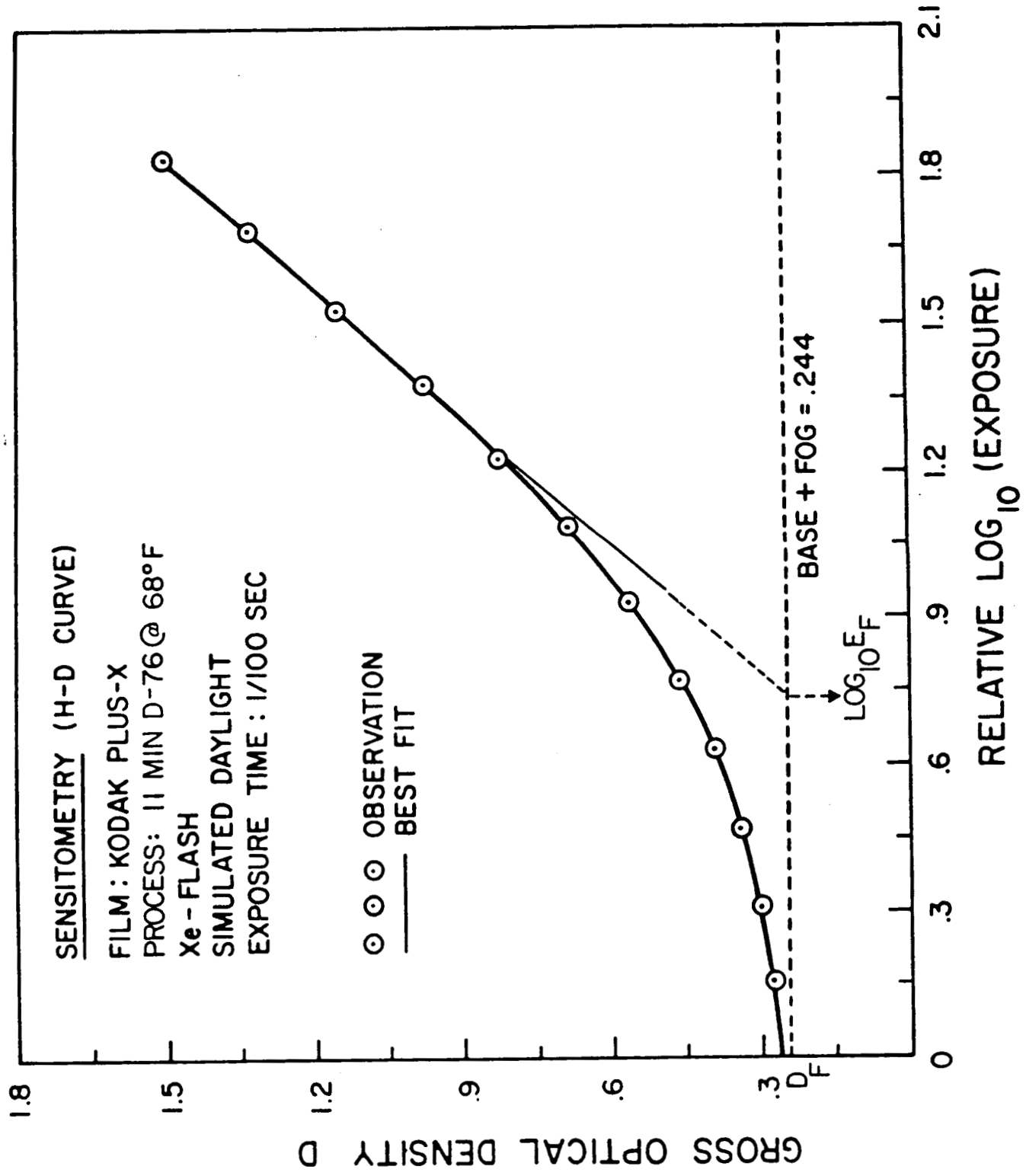

FIG. 2.5: H-D Curve of the Kodak Plus-X Film

roller transport processors are quite adequate for pictorial photography, forced processing using relatively high temperatures often results in longitudinal streaking, rendering the negatives useless for aureole application. Similarly, use of rewind processors produced objectional end-to-end development variations and localized turbulance effects. These problems have been largely overcome by use of spiral reel processors in combination with chemistry and techniques which are extremely tolerant to unavoidable procedural variations. The Kodak Plus-X film is developed in undiluted Kodak D-76 developer for 11 minutes at 68° F. Agitation is continuous for the first 30 seconds and 5 seconds every 30 seconds thereafter until development is complete. The remainder of the process is standard. Uniform and repeatable development to a gamma of about 1.0, low fog, and relatively fine grain are the results. An added bonus is extended dynamic range which assures that all densities fall well below the shoulder of the H-D curve over a variety of sky conditions and filter wavelengths.

(B) Densitometry

In the field of photographic densitometry and sensitometry, the concept of optical density, as a measure of the attenuation of radiant flux, is of fundamental importance. When the attenuation related to the flux transmitted by the developed image, the term transmission density is used.

The transmission density is defined, in general, as the logarithm to the base 10 of the opacitance (0) or reciprocal transmittance (τ) of the developed image, which is just the ratio of the radiant flux Φ_0 incident on the developed image to the radiant flux Φ_T transmitted by the image.

$$D = \log_{10}(0) = \log_{10}\left(\frac{1}{\tau}\right) = \log\left(\frac{\Phi_o}{\Phi_T}\right) \qquad (4)$$

Densitometry has been performed by both a Joyce-Loebl (J-L) Scanning Microdensitometer/Isodensity tracer (MDM) and a MacBeth transmission-type spot densitometer. The former not only provides a digitized magnetic tape output, but also a graphical plot of isodensity contours (Fig. 2.6 a)). Isodensities are lines of equal optical density in the image space; and isophotes are lines of equal brightness in the object space. By the use of photogrammetry and photometry relations described in later sections, one can obtain the solar aureole isophotes (Fig. 2.6 b)) from the MDM digital density data output an the optical density along the almucantar (Fig. 2.7) from the spot densitometer measurements; whereas the J-L Microdensitometer measures the specular density, the spot densitometer measures the diffuse density. The ratio of the specular to the diffuse densities is generally defined as the Callier factor (Ref. 19), which is typically larger than 1.0. In both cases, the almucantar or the sun vertical measurements, are made by the use of photogrammetric formulas (Ref. 22), which provide the x and y coordinates on the photograph, for points along the almucantar and sun-vertical projections. In the case of the spot densitometer positioning of the spot on the photograph is done manually, a process which is cumbersome and prone to error. However, after some experience, it is possible to obtain accurate density measurements. This is shown in Fig. 2.7 by a comparison between the almucantar optical density data, obtained by the two types of densitometers, plotted as a function of scattering angle. The plots show agreement to within 3 percent between the two sets of data. It should be pointed out that the H-D curves (Fig. 2.8) obtained by the two densitometers differ in slope, since one measures specular, and the other, diffuse densities. The detailed method for making accurate almucantar optical density measurements with a spot densitometer is described in Appendix I.

FIG. 2.6 a): Isodensity Contours of the Solar Aureole Photograph, Made with a Joyce-Loebl Microdensitometer Isodensitracer.

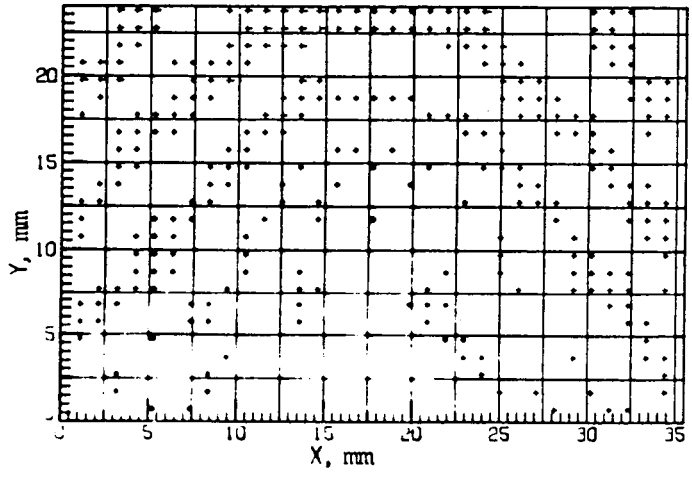

FIG. 2.6 b): Computer Isophotes Corresponding to the Photograph in Fig. 2.6 a)

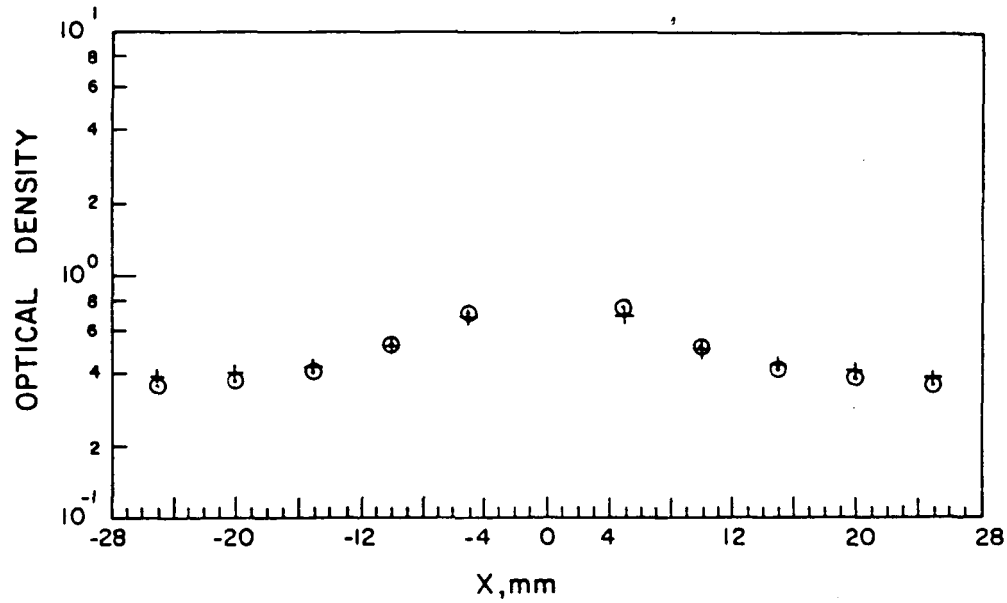

FIG. 2.7: Optical Density at Points Along the Film Projection of the Almucantar for for Photographs Taken with λ = 600 nm Filter. Circles Represent Joyce-Loebl Microdensitometer Measurements; Crosses, the Spot Densitometer Measurements

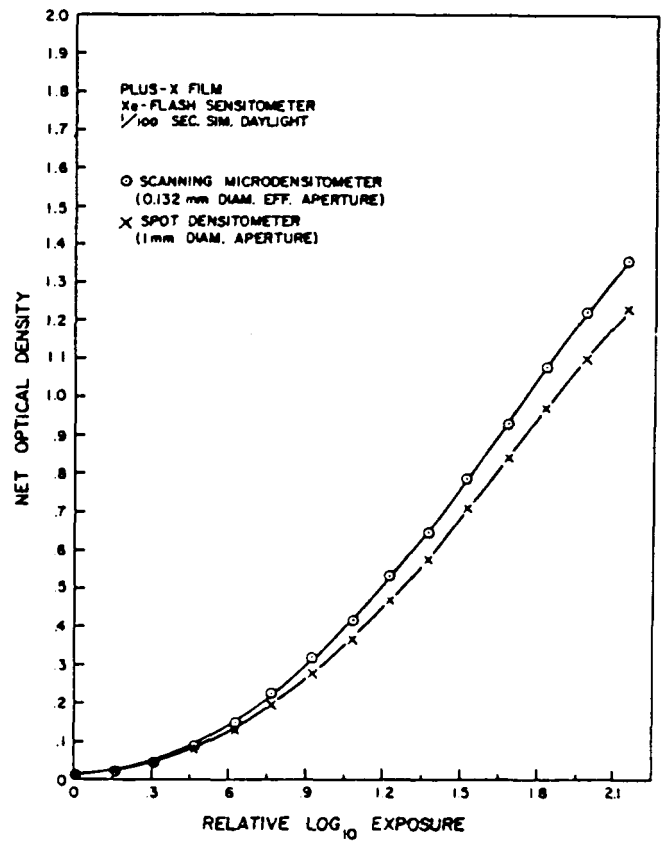

FIG. 2.8: H-D Curves Obtained by the Two Densitometers--Joyce-Loebl Microdensitometer and Spot Densitometer.

(C) Off-Axis Illumination Distribution

When a lens forms an image of an extended object, then the illumination for the off-axis image points, even where there is no vignetting, is usually lower than for the coaxial point. The intensity distribution at an angle θ in the image space is ideally given by $\cos^4 \theta$. The deviation from the "cosine fourth" relationship can be brought about by several means; for example, when the lens construction is such that the apparent size of the pupil increases for the off-axis points. In that case, the off-axis distribution may be given by some other power, α, of cosine θ. The determination of the off-axis distribution of intensity for the camera should be performed both with and without spectral filters mounted on the lens. Procedures for making such a determination are described in detail in Ref. 23, and so will not be presented here. The value of α varies with different spectral filters mounted on the lens (Ref. 23). A plausible explanation for this variation is that it results from the combined effects of spectral behavior of the wavelength filters as a function of incidence angle and the film.

(D) Spectral Response of the Film

Kodak Plus-X film has a spectral response which varies slightly about a uniform average over the entire visible range. Tests were performed to study the spectral dependence of the H-D curve for the film, by performing sensitometry on the film through Wratten filters placed inside the sensitometer. For Kodak Plus-X film, sensitometry was performed with three Wratten filters (Nos. 72B, 75, and 93) and the characteristic curves obtained therefrom were, for all practical purposes, identical in shape.

2.2.7 Photogrammetry Theoretical Relations

The formulas relating to the film projection of different points in the sky are given in Ref. 22. The almucantar scan projects as a conic on the

film (Fig. 2.9). If the sun's image is at the geometrical center of the photographic frame, then the film projection of the almucantar is a conic defined by the relation

$$\frac{(y_{pc} - a)^2}{a^2} + \frac{x_{pc}^2}{b^2} = 1$$

where $y_{pc} = y_p - y_c$, $x_{pc} = x_p - x_c$; (x_c, y_c), (x_p, y_p) are the coordinates of the center C and a point P on the frame; a and b are the

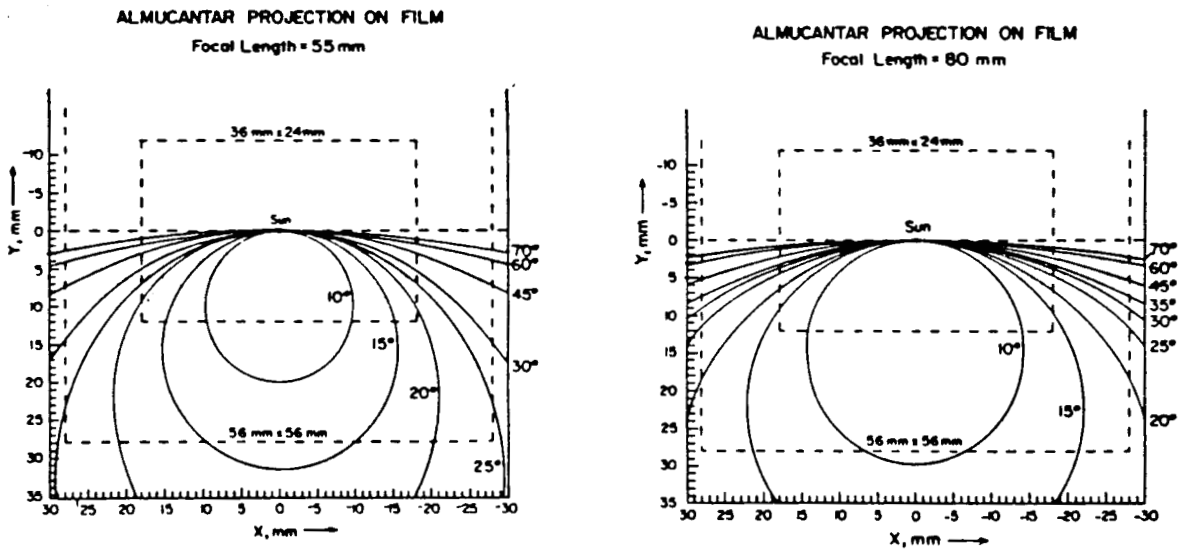

FIG. 2.9: Curves Represent Film Projections of Almucantar Scans for Sun at Various Solar Zenith Angles for a Camera Lens of Focal Length 80 mm.

characteristic distances of conics. If the solar zenith ϕ_s is 45^o, the conic is a parabola

$$y_p - y_c = \frac{1}{2F}(x_p - x_c)^2$$

where F is the lens focal length. If $\phi_s > 45^o$, the conic is a y-hyperbola, with a and b being the distances from center to vertex and covertex; $\phi_s < 45^o$, the conic is an ellipse, with a and b as the semimajor and semi-minor axes. This is illustrated in Fig. 2.9 for lens focal lengths 55mm and 80 mm. The details of formulations and results are given in Appendix 2.

2.2.8 Photometry Relations

Photographic-photometry is concerned with relations that exist between the radiation flux from the object space and the resultant optical density in the image space, the main problem being that of reconstructing intensity or radiance levels in object space by means of the image space optical density data. From the theories of photographic image (Ref. 21), off-axis illumination (Ref. 23) and photogrammetry (Ref. 22), we obtain various formulas that relate the density of each point on the photograph with radiance of a corresponding direction in the sky. The relations for the photometry are given in Refs. 1 and 19. They are recapitulated here for the sake of completeness.

The image irradiance, $I_p(\lambda)$, of a point P on the image plane at an angular distance δ_p from the geometrical center of the image is related to the radiance $B_p(\lambda)$ of the scene element in the sky by the formula (Ref. 24):

$$I_p(\lambda) = B_p(\lambda)\ F^2(\cos\delta_p)^{\alpha}\ T_g T_v/4V^2f^2 \tag{5}$$

where F = focal length, V = image distance, $f = F/d$ (the f-number), d = aperture diameter, T_g = transmission factor due to reflection and absorption by glass, T_v = transmission factor at points off-axis due to vignetting by the lens barrel, and α = exponent of cosine δ_p giving the off-axis illumination distribution for the lens.

If the object is at infinity, as it is in our case,

$$I_p(\lambda) = B_p(\lambda)\ T_g T_v(\cos\delta_p)^{\alpha}/4f^2 \tag{6}$$

But $I_p(\lambda)$ is related to the optical density D_p for the linear portion of the H-D curve by the photographic equation

$$I_p(\lambda)t\ \Delta\lambda = 10^{(D_p - D_F)/\gamma} \tag{7}$$

so that

$$B_p(\lambda) = K\ 10^{\ D_p/\gamma}\ (\cos\delta_p)^{-\alpha} \tag{8}$$

where

$$K = 10^{-D_F/\gamma}\left[\frac{4f^2}{T_v T_g\ \Delta\lambda t}\right] \tag{9}$$

This equation then relates the density, D, of the point P to the sky radiance at angle δ_p from the axis for the linear portion of the H-D curve.

If we know the spectral irradiance, $H(\lambda)$, measured in absolute units ($\mu W\ cm^{-2}\ \mu^{-1}$), which produces a certain density, D_s, for the sun's image, it may be possible to calibrate the photographic image in absolute units. The absolute calibration of the film requires that a known optical density on the film correspond to a known intensity of a direction in sky, the co-direction image point of which is at an angular distance δ_s from the geometrical center 0; then the radiance $B_s(\lambda)$ of sun's direct light is related to D_s by an equation similar to Eq. (8):

$$B_s(\lambda)10^{-D_{ND}} = 10^{D_s/\gamma}(\cos\delta_s)^{-\alpha} K \tag{10}$$

where D_{ND} is the density of the ND filter.

Since we photographed the sun and the aureole on the same photograph, the K factor is the same in Eqs. (8) and (10). Substituting K from Eq. (9) in Eq. (8), we obtain the radiance for any point P in the sky .

$$B_p(\lambda) = K\ 10^{D_p/\gamma}\ (\cos\delta_p)^{-\alpha} \tag{8}$$

where K is the calibration factor given by

$$K = B_s(\lambda)10^{-(D_s + D_{ND})/\gamma}(\cos\delta_s)^{\alpha} \tag{11}$$

It is easier and more accurate to obtain K from Eq. (11) than from Eq. (9).

2.2.9 Photographic Radiance Measurements

(A) Photographic solar almucantar radiance measurements

The problem of inversion of solar aureole data to determine aerosol characteristics can be made tractable, if we make the following reasonable

assumptions (Ref. 7), namely that, particles are spherical; polarization is neglected in the forward direction; absorption effects are ignored by selecting the appropriate wavelength filters to work with; zenith angles are kept less than 80^{o}, so that the spherical Earth corrections can be excluded. Under these assumptions, theory shows that the almucantar radiance becomes independent of aerosol altitude distribution and depends only on the (columnar) size distribution, n(r) (Refs. 1, 7, 25-27). In Refs. 1 and 7, the theory of solar aureole neglects multiple scattering (MS) and considers only single scattering (SS); in Refs. 26 and 27, we have shown how MS effects can be taken into account in order to obtain more accurate retrieved size distribution results. Almucantar radiance can easily be obtained from almucantar optical density measurements. The theoretical considerations regarding radiative transfer and multiple scattering problems will be discussed in Section 2.3 and those regarding inversion methods in Section 2.4.

(B) Isodensities and Isophotes

As defined earlier, isodensities are lines of equal optical density on a photographic image; and isophotes, lines of equal radiance in the object space. We have used two ways to obtain isodensity contours. One is by the J-L MDM isodensitracer which yields isodensity tracings on a sheet of paper (Fig. 2.6 a)). The other is by a video scanning color-coded TV system (Spatial Data Systems, Inc.), which gives multicolored isodensity contours, each color denoting a specific density value (Fig. 2.10). The contours are displayed on a TV screen that can be photographed. The contour mapping by the MDM takes about an hour per frame, while that by the video scanner is done instantaneously (1/30 sec.). The isophotes are produced by computer graphics from the radiance data obtained from the reduction of the digitized optical density data output of each photograph.

FIG. 2.10: Isodensity Contours of the Solar Aureole Photograph, Made with a Video Scanning, Color-Coded TV System

2.3 SINGLE AND MULTIPLE SCATTERING CONSIDERATIONS

Single and multiple scattering contributions to the circumsolar radiation along the almucantar and sun vertical have been computed by a Gauss-Seidel solution to the radiative transfer equation. In the near forward direction, the multiple scattering contributions are significant for optical depths of the order of 0.4. However, the shape of the angular distribution of almucantar radiance up to 10^{o} appears less sensitive to multiple scattering. The results have been compared against an existing radiative transfer code, and have also been discussed in Refs 28 and 29.

2.3.1 Single Scattering Theory of the Solar Aureole

In this section we consider the single scattering (SS) theory, in which we make the following reasonable simplifying assumptions:

(1) Particles are spherical so that results of the Mie theory can be used in computations.

(2) The atmosphere is horizontally homogeneous and vertically inhomogeneous.

(3) Absorption effects are ignored by selecting to work in spectral regions for which atmospheric absorption is nil.

(4) The polarization effects are small for forward scattered light and can be ignored.

(5) For relatively clear days (visibility > 15 km), the MS effects at the forward scattering angles are small compared with SS (Ref 30) and can be ignored.

(6) An average value for the refractive index of all atmospheric aerosols is assumed for forward scattering.

(7) The atmosphere is treated as plane-parallel; the spherical Earth effects, which become significant for zenith angles ϕ larger than 75°, are incorporated into the theory by the use of the generalized Chapman type functions $S(\phi)$ (Refs. 30 and 31) in place of the secant functions.

Figure 2.12 illustrates the geometry of the calculation. Shown is an acceptance cone $d\Omega$ originating at the detector and a solid angle $d\Omega'$ centered at the elemental scattering volume dV at altitude y(km). ϕ_s and ϕ are the zenith angles of the Sun and the narrow view cone and ω is the dihedral angle between the normals to the Sun zenith and view cone zenith planes intersecting at dV. The scattering angle ψ is then given by the relation

$$\cos \psi = \cos \phi \cos \phi_s - \sin \phi \sin \phi_s \cos \omega \qquad (12)$$

The element dV is given by

$$dV = R^2 \, d\Omega \, S(\phi) \, dy \qquad (13)$$

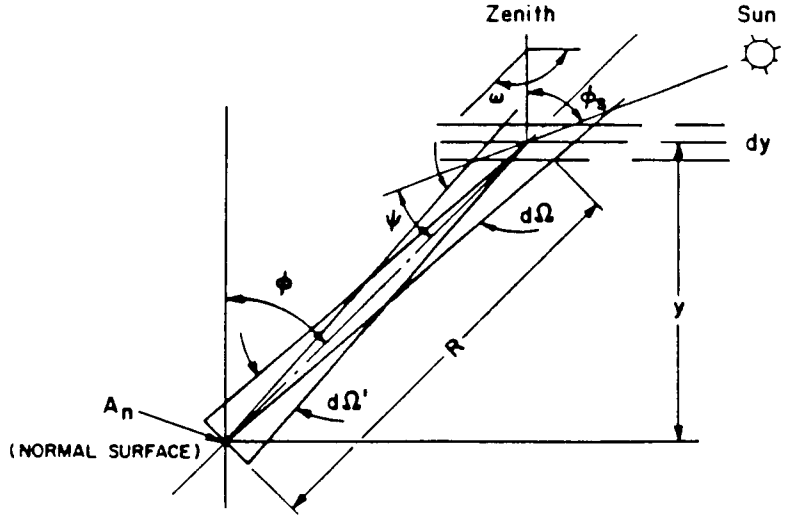

FIG. 2.11: The geometry of the sky single scattering problem.

where the generalized Chapman type functions

$$S(\phi) = \sec \phi \qquad (\text{for } \phi \leq 75^{\circ}) \tag{14}$$

The optical depth defined by

$$\tau_j(\lambda, y) = \int_y^{\infty} \beta_j'(\lambda, y) \qquad (j = M, A) \tag{15}$$

for a ray traversing the distance from the Sun to the air mass element dV is given by

$$\tau_1 = \Sigma_j \tau_j(\lambda, y) S_j(\phi_s) \qquad (j = M, A) \tag{16}$$

and from the air mass to the detector by

$$\tau_2 = \Sigma_j \{\tau_j(\lambda, 0) - \tau_j(\lambda, y)\} S_j(\phi) \tag{17}$$

where M denotes air molecules; A, the aerosol species; λ, the wavelength; and β' the volume scattering coefficient (VSC) (km^{-1}) at altitude y for the jth constituent. In this paper, all quantities represented by τ_A, β_A', β_A, F_A', F_A, P_A', and P_A are functions of $\tilde{m}$, even though their $\tilde{m}$ dependence is not indicated in their representation form. The primes denote the y-dependence of the quantities. β_A' and β_M' are defined by the following relations:

$$\beta_A'(\lambda, y) = \int_{r_2}^{r_1} n(r, y) \pi r^2 Q(x, \tilde{m}) dr \tag{18}$$

where $Q(x, \tilde{m})$ is the efficiency factor (Ref. 32), $x = 2\pi r/\lambda$ is the particle size parameter, r_1 and r_2 are minimum and maximum values of r and $\tilde{m} = m' - im''$ the complex refractive index of aerosols.

$$\beta'_M(\lambda, y) = \beta_M(\lambda)\rho_M(y) \tag{19a}$$

where the VSC for molecules is

$$\beta_M(\lambda) = \frac{8\pi^3(n^2 - 1)^2}{N\lambda^4} \frac{(4 + 3d)}{(4 - 3d)} \tag{19b}$$

In Eq. 19(b), N is the number of molecules cm^{-3}; n, the refractive index of the medium, $d = 4\Delta/(1 - \Delta)$; and Δ is the depolarization of scattered light at a scattering angle of 90^o for a linearly polarized incident radiation with its electric vector perpendicular to the scattering plane. For unpolarized incident light, Δ is replaced by $\xi = 2\Delta/(1 + \Delta)$. Then the volume scattering function (VSF) for air molecules (j = M) is

$$F'_M(\psi, \lambda, y) = \beta_M(\lambda)P_M(\psi)\rho_M(y), \quad km^{-1}sr^{-1} \tag{20}$$

where the molecular phase function is

$$P_M(\psi) = \frac{3}{16\pi}(1 + \cos^2\psi), \quad sr^{-1} \tag{21}$$

where $\rho_M(y)$ is the dimensionless function representing the altitude distribution of molecular density. The VSF for aerosols (j = A) is

$$F'_A(\psi, \lambda, y) = \beta'_A(\lambda, y)P'_A(\psi, \lambda, y) \tag{22}$$

where the aerosol volume phase function is

$$P'_A(\psi, \lambda, y) = \frac{1}{2k^2\beta'_A(\lambda, y)} \int_{r_1}^{r_2} \eta(r, y)\{i_1(\psi, \tilde{m}, x) + i_2(\psi, \tilde{m}, x)\}\, dr \tag{23}$$

and i_1 and i_2 are the Mie intensity functions and $k = 2\pi/\lambda$.

The sky radiance due to the molecules and aerosols in the volume element dV is then given by

$$dB(\phi, \phi_s, \omega, \lambda) = H_o(\lambda)\{S_M(\phi)F'_M(\psi, \lambda, y) + S_A(\phi)F'_A(\psi, \lambda, y)\} e^{-(\tau'_1 + \tau_2)} dy \quad (24)$$

Integrating over all such elemental volumes, the total single scattered sky radiance is

$$B(\phi, \phi_s, \omega, \lambda) = H_o(\lambda)\, e^{-\Sigma_j \tau_j S_j(\phi)} \left\{ S_M(\phi) \int_0^\infty e^{-\Sigma_j \tau_j(\lambda, y) D_j} F'_M(\psi, \lambda, y)\, dy + S_A(\phi) \int_0^\infty e^{-\Sigma_j \tau_j(\lambda, y) D_j} F'_A(\psi, \lambda, y)\, dy \right\} \quad (25)$$

where

$$D_j = S_j(\phi_s) - S_j(\phi) \qquad (j = M, A) \quad (26)$$

2.3.2 Multiple scattering contributions to circumsolar radiance

Questions have been raised as to whether multiple scattering (MS) contributions to the solar aureole have any significant effect on the retrieval of the SD. This question has been answered in two steps. The first step is to compare the contributions to the angular distribution of the almucantar radiance in the forward direction due to MS relative to those due to SS. The second step is to determine the effect of MS on the retrieval of the aerosol SD. In this section (2.3.2), only the first step will be considered; the second being left to section 2.4. Thus, for the purpose of calculating the SS and MS contributions, a computer code was developed which employed the Gauss-Seidel Interative approach to the solution of the radiative transfer equation for a plane

parallel atmosphere composed of air molecules, ozone and aerosol particles. Our code is essentially similar to the radiative transfer (RT) code written by J. V. Dave (Ref. 33) except in the construction of the source matrix. The difference in the two codes is outlined as follows.

Prior to utilizing our code in actual problems, we decided to check some results obtained by it for SS and MS radiance contributions in an aerosol atmosphere. But, unfortunately, we were unsuccessful in locating a set of standard tables of downwelling and upwelling radiance and polarization for atmospheres containing inhomogeneously distributed aerosol particles. Dave and Furukawa's tables (Ref. 34) and Coulson, Dave and Sekera tables (Ref. 35) are meant for only molecular atmospheres, with and without ozone, respectively. Therefore, the following strategy was adopted. First, it was decided to check the results obtained by ours and Dave's RT codes, using identical molecular data input, against the tables in Refs. 34 and 35. If the three sets of values agreed to within say 1% to 2%, then one could assume the two codes work correctly for both SS and RT in molecular atmosphere. Next step was to add aerosols into the molecular atmosphere, and use identical aerosol data input for the two codes and compare their results. If the two sets of results agreed with one another within 1%, then it would be safe to assume that our code was as accurate as Dave's RT code, which we treated as our standard against which to check. (Plans for checking our code against other codes were considered but abandoned in view of the high computer costs involved.)

(i) *The Gauss-Seidel Technique*

Before discussing the results of the aforementioned computations a brief description of the two codes and their similarities and differences

seems appropriate. Both codes are based on a Fourier decomposition method of solving the RT equation for downwelling and upwelling radiances and polarization. Following Herman's method (Ref. *36)*, the atmosphere is divided into a number of levels, and a Gauss-Seidel iterative scheme is employed, passing first in a downward direction, then upward, repeating the procedure until convergence is reached. In what follows we consider a downwards pass, the extension to upwards pass being similar.

The downwards intensity at level L (Fig. 2.12) is taken to be the downwards intensity at level L-1, attenuated by its passage through the intervening layer, plus the source matrix contribution from this layer. A layer is characterized by an optical thickness, τ, single scattering albedo, $\bar{\omega}_o$, and turbidity factor, T (= the ratio of particulate to total extinction coefficients), each assumed constant.

To obtain the source matrix for a given layer, one combines the optical properties of the layer with the average of the intensities of the levels which bound it. Using the Gauss-Seidel technique, the most recent values of the intensity are used at each iteration stage. Dave's code requires four subroutine calls: one each for the upward and downward intensities of each level involved; whereas, our code requires only two calls: The two levels being handled simultaneously, which results in a saving of about 20% in execution time.

(ii) *Comparison of the Computer Codes*

To illustrate the difference between codes, we have used the data set which Dave employed as his example in his documentation (Ref. 33). The important input data information is listed in Table 2.1. The vertical aerosol profile is that of Ref. 33 and the ozone absorption is ignored.

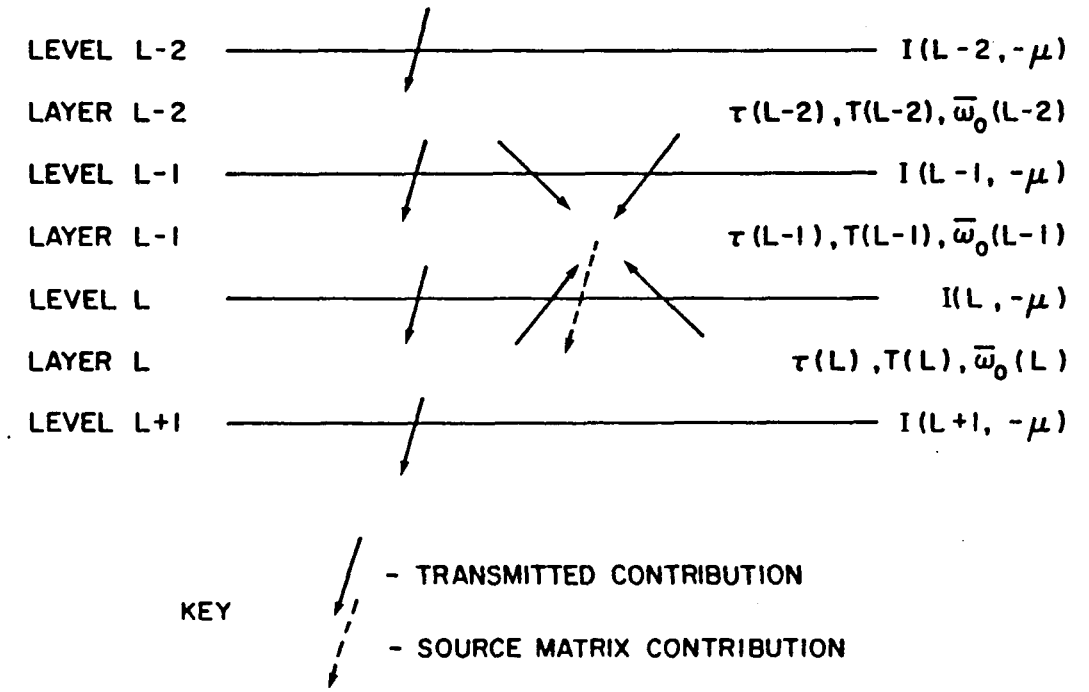

FIG. 2.12: Schematic Illustration of atmospheric layers, transmitted and source matrix contribution to sky radiance.

TABLE 2.1: Input Data

Wavelength	$\lambda = 0.55\ \mu m$
Rayleigh optical depth	$\tau_R = 0.1$
Particulate scattering optical depth	$\tau_{PS} = 0.01026$
Particulate absorption optical depth	$\tau_{PA} = 0.00236$
Ozone absorption optical depth	$\tau_{O_3} = 0.0$
Total optical depth	$\tau = 0.11262$
Solar zenith angle	$\phi_{SUN} = 60^{\circ}$
Unattenuated solar flux	$F = 100\pi$

Aerosol Characteristics:

Refractive index $m = 1.50 - i\ 0.03$

Size distribution

$$n(r) = C, \quad 0.03\ \mu m \leq r \leq 0.1\ \mu m$$
$$= C(r/0.1)^{-4} \quad 0.1\ \mu m \leq r \leq 2.0\ \mu m$$
$$= 0 \quad \text{otherwise}$$

The value of C is determined by τ_{PS}

Volume scattering coefficient $\beta_{scat} = 4.85 \times 10^{-10}\ cm^{-1}$ per particle

Volume absorption coefficient $\beta_{abs} = 1.12 \times 10^{-10}\ cm^{-1}$ per particle

Volume extinction coefficient $\beta_{ext} = 5.97 \times 10^{-10}\ cm^{-1}$ per particle

The output from Dave's code checks out to be in complete agreement with that published in Ref. 30. However, the output from our code differs from these results, most notably in the near forward direction. This is illustrated in Tables 2.2 and 2.3 and In Fig. 2.13.

Rather than reproduce the entire output of each code (a total of more than 3,000 numbers each), we give the results for the almucantar scan (observation zenith angle equal to solar zenith angle) in Table 2.2 and, the sun-vertical scan (observation azimuth angle equal to solar azimuth angle) in Table 2.3. In addition, the almucantar results for no ground reflectivity (A =)) are plotted in Fig. 2.13. Each table consists of five columns: the first two give Dave's results for ground reflectivities (A) of 0.0 and 0.25; the last two give results of our code; the middle column gives the single scattering (SS) results.

The most striking (and significant) result is contained in the very first row of Table 2.2 where we see that the SS contribution for scattering angle $\psi = 0^{\circ}$ is greater than Dave's RT results for both values of A. This can also be seen clearly in Fig. 2.13, where Dave's results are shown as a broken line. Turning to Table 2.3, we see that the SS contribution is higher than Dave's result with A = 0.0 for zenith angles of 50°, 60°, and 70°.

In order to make sure that our SS results are indeed correct, we compared them with Dave and Furukawa's tables (Ref. 34) for air, ozone but no aerosols, and found agreement between them to within 0.5%, for zenith angles up to 75°. For zenith angles of 80° and 85°, the discrepancy was only slightly greater. We feel the reason for this small discrepancy, is due to the Fourier decomposition of the phase function used in Box and Deepak's (and Dave's) code, which clearly must be truncated at some finite order.

TABLE 2.2: Almucantar Radiances I_{SS}, I_{RT}(Dave) and I_{RS}(BD) obtained by SS theory, Dave's and Our Codes, respectively

Azimuth Angle (Deg)	I_{RT} (Dave)		I_{SS}	I_{RT} (BD)	
	A = 0.0	A = 0.25	(A = 0.0)	A = 0.0	A = 0.25
0	15.556	16.627	17.015	18.003	19.056
30	7.864	8.935	7.209	8.142	9.195
60	5.450	6.522	4.655	5.452	6.506
90	4.086	5.158	3. 352	4.039	5.092
120	3.843	4.915	3.123	3.780	4.833
150	4.293	5.365	3.530	4.214	5.268
180	4.588	5.660	3.796	4.501	5.550

TABLE 2.3: Sun-vertical Radiances I_{SS}, I_{RT} (Dave) and I_{RT} (BD) obtained by SS theory, Dave's and Box and Deepak's (BD) RT Codes, respectively

Zenith Angle (Deg)	I_{RT} (Dave)		I_{SS}	I_{RT} (BD)	
	A = 0.0	A = 0.25	(A = 0.0)	A = 0.0	A = 0.25
0	2.486	3.044	2.157	2.471	3.017
10	2.903	3.470	2.553	2.905	3.459
20	3.514	4.107	3.141	3.553	4.132
30	4.407	5.048	4.030	4.526	5.152
40	5.812	6.532	5.500	6.112	6.816
50	8.574	9.423	8.613	9.388	10.220
60	15.556	16.627	17.015	18.003	19.056
70	15.225	16.730	15.283	16.624	18.110
80	20.889	23.495	19.720	21.892	24.482

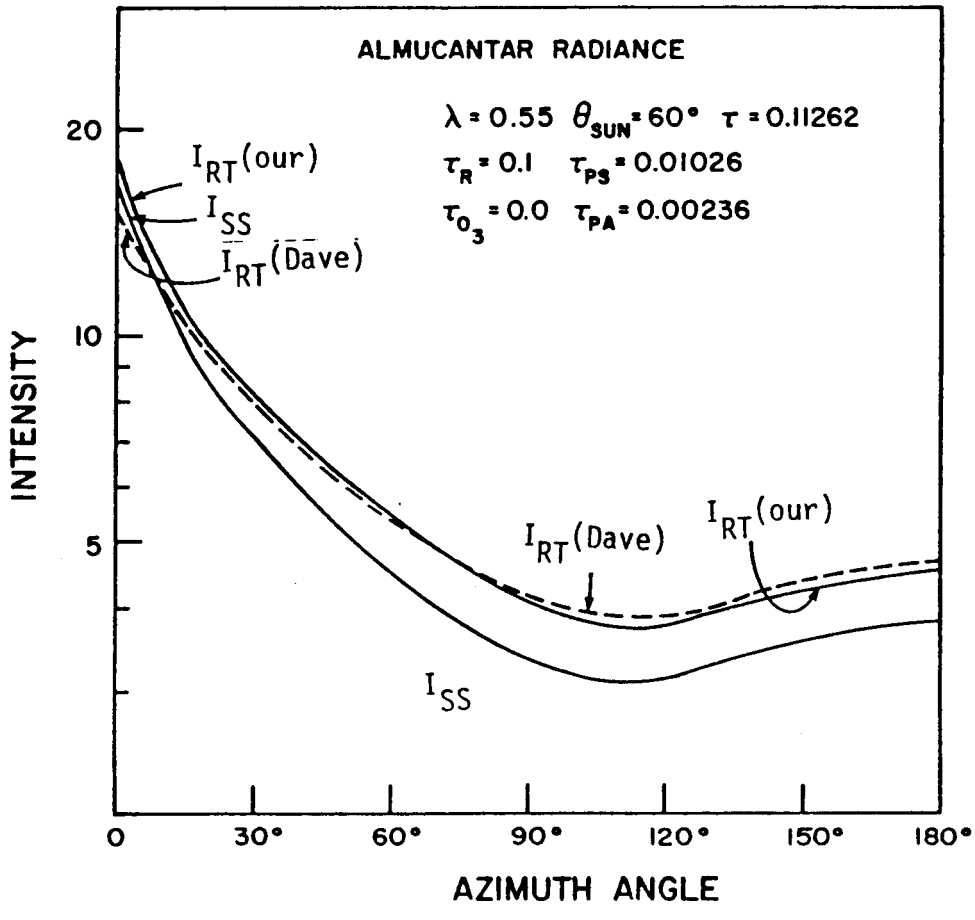

FIG. 2.13: Almacantar Radiance versus azimuth angle (0^{o}-180^{o}) for I_{SS}, I_{RT} (Dave) and I_{RT} (BD).

As an alternative verification, we have used the formula of Green, et al. (Ref. 1) for the almucantar SS radiance, viz.

$$I_{SS}(\psi) = F \sec \phi_s \, e^{-\tau \sec \phi_s} \, (\tau_R R(\psi) + \tau_{PS} P(\psi)) \Big/ 4\pi \qquad (27)$$

where R and P are the (normalized) Rayleigh and particulate phase functions, ψ is the scattering angle and ϕ_s is the solar zenith angle. Eq. (1) is a special case of the more general formula for SS scattering (Ref. 1), since for almucantar scan the observation angle is equal to Θ. To obtain the first value in Table 2.2, we choose $\psi = 0^o$, so that R(0) = 3/2. From earlier results in Dave's documentation (Ref. 5), P(0) = 26.94. Using these values along with the data in Table 2.1, yields $I_{SS}(0) = 17.2$, in excellent agreement with our result in Table 2.2.

Figure 2.13 shows that Dave's code gives a flatter almucantar radiance scan, than our code, implying a less forward-peaked phase function. The phase function is constructed as a linear combination of Rayleigh and particulate phase functions, and these results suggest that Dave's code incorporates too little of the particulate contribution to the total phase function.

In constructing the source matrix for, say layer L, it is necessary to combine the scattering properties of layer L with the intensities of levels L + 1 and L. It seems that in Dave's code, the intensities of level L + 1 are combined with the appropriate scattering properties of layer L, but the intensities of level L are combined with the turbidity factor of layer L - 1 (i.e., the layer above the correct layer). As the scale height of the aerosol profile is much smaller than that for the molecular profile (in the

troposphere), the turbidity factor decreases with height. Thus, by taking the turbidity factor for the layer above the required layer, Dave's code appears to include insufficient aerosol scattering.

Thus, we see from Tables 2.2 and 2.3, that whereas the results for SS and total radiance (I_{SS} and I_{RT}, respectively) obtained by the two codes (i.e., ours and Dave's) for the molecular atmosphere agree to within 1% to 2%, those for molecular plus aerosol atmosphere show a discrepancy. However, for the latter case, the values if I_{RT} obtained by Dave's code turn out to be less than I_{SS} values in the forward direction, which is obviously incorrect; whereas I_{RT} values obtained by our code are greater than the I_{SS} values for all angles, as they should be.

(iii) *Effects of Multiple Scattering*

We use our code to compute the SS and total radiance for different optical depths, solar zenith angles, aerosol characteristics and wavelengths of incident solar radiation. An example of a typical input data is as follows. The aerosol size distribution (Refs. 1 and 37) is a Modified Gamma Distribution (MGD) given by

$$n(r) = ar^2 e^{-br} \quad , \; 0.03 \leq r \leq 2.0\mu m \; , \; b = 10.0 \; \mu m^{-1} \tag{28}$$

the particle refractive index m = 1.55; volume scattering (and extinction) coefficients, β_{sc} (and β_{ext}), are given by $\beta_{ext} = \beta_{sc} = 1.116 \times 10^{-8}$ cm^{-1} per particle; and $\lambda = 0.55\mu m$. The results are given in Table 2.4, for solar zenith angles 30°, 45°, and 60°, and optical depth components for Rayleigh (τ_R) and Mie (τ_{PS}) particles, being (0.1, 0.2) and (0.2, 0.2), respectively.

Table 2.4: Normalized Almucantar Radiance Values I^N_{SS} and I^N_{RT} and for different ϕ_{sun}, τ_R and τ_{PS}.

Azimuth Angle (Deg)	Scattering Angle (Deg)	I^N_{SS}	I^N_{RT}		$(I^N_{RT}-I^N_{SS})/I^N_{SS}$	
			A = 0	A = 0.25	A = 0	A = 0.25
Solar Zenith Angle = 30°						
$\tau_R = 0.1$, $\tau_{PS} = 0.2$						
Normalization Constant =		1.0920	1.1406	1.1574	4.5	6.0
0	0.0	1.0000	1.0000	1.0000	0.0	0.0
4	2.0	0.9779	0.9787	0.9790	0.1	0.1
8	4.0	0.9161	0.9191	0.9202	0.3	0.4
12	6.0	0.8257	0.8318	0.8342	0.7	1.0
16	8.0	0.7211	0.7306	0.7344	1.3	1.8
$\tau_R = 0.2$, $\tau_{PS} = 0.2$						
Normalization Constant =		1.0003	1.0652	1.0904	6.5	9.0
0	0.0	1.0000	1.0000	1.0000	0.0	0.0
4	2.0	0.9785	0.9797	0.9802	0.1	0.2
8	4.0	0.9183	0.9227	0.9245	0.5	0.7
12	6.0	0.8303	0.8393	0.8430	1.1	1.5
16	8.0	0.7284	0.7426	0.7485	1.9	2.8
Solar Zenith Angle 60°						
$\tau_R = 0.1$, $\tau_{PS} = 0.2$						
Normalization Constant =		1.4679	1.5860	1.6026	8.0	9.2
0	0.0	1.0000	1.0000	1.0000	0.0	0.0
4	3.5	0.9360	0.9399	0.9405	0.4	0.5
8	6.9	0.7774	0.7908	0.7930	1.7	2.0
12	10.4	0.5932	0.6167	0.6207	4.0	4.6
16	13.9	0.4347	0.4658	0.4714	7.2	8.4
$\tau_R = 0.2$, $\tau_{PS} = 0.2$						
Normalization Constant =		1.2357	1.3683	1.3905	10.7	12.5
0	0.0	1.0000	1.0000	1.0000	0.0	0.0
4	3.5	0.9377	0.9429	0.9438	0.6	0.7
8	6.9	0.7833	0.8012	0.8043	2.3	2.7
12	10.4	0.6039	0.6343	0.6414	5.0	6.2
16	13.9	0.4494	0.4920	0.5001	9.5	11.3

Table 2.4: (Continued)

Azimuth Angle (Deg)	Scattering Angle (Deg)	I^N_{SS}	I^N_{RT}		$(I^N_{RT}-I^N_{SS})/I^N_{SS}$	
			A = 0	A = 0.25	A = 0	A = 0.25
Solar Zenith Angle = 45°						
$\tau_R = 0.1, \tau_{PS} = 0.2$						
Normalization Constant =		1.2373	1.3062	1.3231	5.6	6.9
0	0.0	1.0000	1.0000	1.0000	0.0	0.0
4	2.8	0.9566	0.9585	0.9590	0.2	0.3
8	5.7	0.8424	0.8492	0.8511	0.8	1.0
12	8.5	0.6942	0.7071	0.7108	1.9	2.4
16	11.3	0.5479	0.5663	0.5718	3.4	4.4
$\tau_R = 0.2$, $\tau_{PS} = 0.2$						
Normalization Constant =		1.1044	1.1911	1.2155	7.9	10.0
0	0.0	1.0000	1.0000	1.0000	0.0	0.0
4	2.8	0.9577	0.9605	0.9613	0.3	0.4
8	5.7	0.8466	0.8563	0.8592	1.1	1.5
12	8.5	0.7022	0.7207	0.7263	2.6	3.4
16	11.3	0.5597	0.5864	0.5946	4.8	6.2

The results presented in Table 2.4 have been arranged to illustrate two points: the MS contributions to the absolute *magnitude* of the almucantar radiance, and the MS contributions to the *shape* of the almucantar radiance curve. Thus the first row in each of the 6 sections of the Table gives the actual radiance for zero degree azimuth angle (and hence, zero degree scattering angle). Note that the incident flux was taken as $F = \pi$ for these computations. All other rows in each section give the normalized radiances, I^N_{SS} and I^N_{RT}, where

$$I^N \equiv I(\psi)/I(0) \tag{29}$$

Finally, in the two right-hand columns, we give the percentage differences $(I^N_{RT} - I^N_{SS})/I^N_{SS}$, which serves to indicate the deviation in the shape of the almucantar radiance curve due to MS.

(iv) *Concluding Remarks*

From the results given in Table 2.4, we see that MS contributes between 4.5% and 12.5% to the magnitude of the aureole radiance, within the range of parameters we have considered. Of more concern to the retrieval of the size distribution from almucantar radiances, however, is the MS contribution to the shape of the almucantar radiance curve. Table 2.4 suggests that provided we restrict ourselves to scattering angles of less than about 10°, the error in the shape of the curve is unlikely to exceed 3%. The azimuth range implied by this range of scattering angles is quite strongly dependent on solar zenith angle ϕ_{sun}.

2.3.3 An Approximation to Multiple Scattering in the Earth's Atmosphere: Almucantar Radiance Formulation

In our radiative transfer code (Section 2.3.2), based on the Gauss-Seidel approach, the particulate phase function P_p is expanded as a Legendre series so that as many as 100 or more terms may be involved compared to only three for the molecular phase function P_M. Thus with the inclusion of aerosols, the computation costs can be enormously increased. If such a code were used in an iterative inversion scheme, such as the nonlinear least squares method, the retrieval would become prohibitively expensive; hence, the necessity of making some simplifying approximations to the solutions of radiative transfer equation. Therefore, in order to make the inversion problem in aerosol remote sounding tractable, it becomes imperative to use extremely fast programs for computing the radiance fields in which MS is included. It is for this reason, that we developed our MS approximation, described in Refs. 27 and 28, the fast computation of the almucantar radiance field.

In this section, a phenomenological derivation of the MS approximation formula (Ref. 27) for the total almucantar radiance field, differing slightly from the expression in Ref. 28, will be given. Formulas for the correction factors which incorporate the effects of MS and nonzero ground albedo A will also be given. In addition, the use and accuracy of our MS approximation in direct problems of radiative transfer associated with almucantar radiance will be discussed with examples.

(i) *Theoretical Considerations*

The solar aureole theory and its use for determining aerosol size distributions has also been discussed in detail by Deirmendjian in Refs. 48 through 41. In the SS approximation, the almucantar radiance is given by

$$L^{SS}(\psi,\lambda) = H_o \sec \phi_s \, e^{-\tau_T \sec \phi_s} \left| \tau_M P_M(\psi) + F_{PC}(\psi,\lambda) \right| \qquad (30)$$

where H_o is the incident flux; ϕ_s is the solar zenith angle; τ_T is the total optical thickness; $_M$ is the molecular optical thickness (subscripts M and P denote molecules and particles, respectively); $P_M = \frac{3}{16\pi}(1 + \cos^2\psi)$ is the molecular phase function (sr^{-1}); ψ is the scattering angle given by

$$\cos \psi = \cos^2 \phi_s + \sin^2 \phi_s \cos \omega \qquad (31)$$

and ω is the azimuth angle measured in a counterclockwise direction relative to the sun vertical; and $F_{PC}(\psi,\lambda)$ is the columnar particulate scattering function (sr^{-1}) defined by

$$F_{PC}(\psi,\lambda) = \frac{1}{2k^2} \int_{r_1}^{r_2} (i_1 + i_2) \, N_C(r) \, dr \qquad (32)$$

$$\equiv \tau_{PS} \, P_p \, (\psi) \qquad (32a)$$

where N_C is the columnar size distribution ($cm^{-2}\ \mu m^{-1}$); i_1 and i_2 are Mie intensity coefficients; and r_1 and r_2 are lower and upper limits of radii. As indicated in Eq. (33a), F_{PC} is usually factored into a particulate scattering optical thickness, τ_{PS}, and a particulate phase function, P_p.

In Section 2.3.2 (Ref. 28), we compared the results of Eq. (30) with those obtained by our radiative transfer code, and showed that although Eq. (30) provided a reasonable approximation under relatively clear sky conditions, the MS contributions to the solar aureole were often non-negligible compared to the SS contributions. In addition, it was shown that the main MS contribution to almucantar radiance was due to molecules alone; the increase of aerosol loading had a relatively small effect on MS contributions. In Ref. 26, it was shown that size distributions retrieved in the SS approximation from radiance data for $\tau_M = 0.1$, showed relatively small discrepancy from true values; however, those from $\tau_M = 0.2$ showed considerably larger error, thereby suggesting that the MS effect due to aerosols is distinctly smaller than that due to molecules.

In our MS approximation, following Ref. 38, it was assumed that the solar aureole radiance was essentially due to SS by aerosols and molecules, and MS by molecules alone. The derivation of expressions for taking into account the effects of MS and ground albedo will be presented next.

(ii) Factorization of the Transfer Equation

Our MS approximation to the equation of radiative transfer in an aerosol-laden atmosphere follows the suggestion first made by Sekera (Ref.42) and subsequently developed by Diermendjian (Refs. 38, 39, 41), who referred to it as a perturbation approximation. (See also Ref. 40.) We start with the equation of radiative transfer in a plane-parallel, vertically inhomogeneous atmosphere, which we may write in the form

$$\mu \frac{\partial L(\tau;\xi)}{\partial \tau} = L - H_o e^{-\tau/\mu_o} \tilde{\omega}(\tau)\ P(\tau,\xi,\xi_o) - \int L(\tau,\xi')\ \tilde{\omega}(\tau)\ P(\tau,\xi,\xi')\ d\xi' \quad (33)$$

where $\mu = \cos\phi$, $\mu_o = \cos\phi_s$; ξ stands for (μ,ϕ)

$$0 \leq \tau \leq \tau_T$$

$$P(\tau) = \{\sigma_M P_M + \sigma_{PS} P_P\} / (\sigma_M + \sigma_{PS}) \quad (33a)$$

$$\sigma_i = - \frac{\partial \tau_i}{\partial z} \quad , \quad i = M,\ PS,\ TOT \quad (33b)$$

and

$$\tilde{\omega}(\tau) = (\sigma_M + \sigma_{PS}) / \sigma_{TOT} \quad (33c)$$

Equation (30) can be obtained from Eq. (33) by ignoring the integral on the right hand side, and setting $\mu = \mu_o$.

Following Sekera (Ref. 42) and Diermendjian (Refs. 40, 41), we may rewrite Eq. (33a) in the following form

$$P(\tau) = P_M + f(\tau)\ P_D \quad (34)$$

where

$$P_D = P_P - P_M \quad (35a)$$

and

$$f(\tau) = \sigma_{PS} / (\sigma_M + \sigma_{PS}) \quad (35b)$$

$f(\tau)$ is known as the turbidity coefficient, and $\omega(\tau)$ is the single scattering albedo, both being functions of the altitude

Similarly, we may separate the light field into two parts, viz.,

$$L(\tau,\xi) = L_M(\tau,\xi) + L_D(\tau,\xi) \quad (36$$

where L_M represents the radiance field produced by molecular scattering alone, and may be defined as the solution to the equation

$$\mu \frac{\partial L_M(\tau,\xi)}{\partial \tau} = L_M - H_o e^{-\tau/\mu_o} \tilde{\omega}(\tau) P_M(\xi,\xi_o) - \tilde{\omega}(\tau) \int L_M(\tau,\xi') P_M(\xi,\xi') d\xi' \quad (37)$$

Note that this equation is to be solved for a molecular atmosphere having an optical thickness equal to the total optical thickness τ_T of the actual molecular-plus-aerosol atmosphere, and not τ_M.

If we now substitute Eq. (36) into Eq. (33), and make use of Eqs. (34), (35), and (37), we obtain the following integrodifferential equation for L_D, which represents the departure from, or "perturbation" to a purely molecular radiance field:

$$\mu \frac{\partial L_D(\tau,\xi)}{\partial \tau} = L_D(\tau,\xi) - H_o e^{-\tau/\mu_o} \tilde{\omega}(\tau) f(\tau) P_D(\xi,\xi_o)$$

$$- \int \tilde{\omega}(\tau) \left[P_M(\xi,\xi') L_D(\tau,\xi') + f(\tau) P_D(L_M + L_D)\right] d\xi' \quad (38)$$

(a) Approximate Solution to Eq. (38)

Equation (38) is clearly more complex than the original Eq. (33). Sekera (Ref. 42) suggested that the method of successive scattering may be most appropriate for solving it (provided $L_M(\tau,\xi)$ is known throughout the atmosphere); as yet we know of no attempt to pursue this idea.

In the region of the solar aureole, Deirmendjian (Ref. 38, 41) employed a single scattering approach to the solution of Eq. (38). Thus, by neglecting the integral terms, we may obtain

$$L_D^{SS} = H_o \mu^{-1} e^{-\tau_T/\mu} P_D(\xi,\xi_o) \int_0^{\tau_T} \tilde{\omega}(\tau) f(\tau) e^{-\tau(\mu_o^{-1} - \mu^{-1})} d\tau \quad (39a)$$

Along the almucantar ($\mu = \mu_o$) this equation must be replaced by

$$L_D^{SS} = (H_o/\mu_o) \quad e^{-\tau_T/\mu_o} \quad P_D \int_0^{\tau_T} \tilde{\omega}(\tau)\ f(\tau)\ d\tau$$

$$= (H_o/\mu_o) \quad e^{-\tau_T/\mu_o} \quad \tau_{PS}(P_P - P_M) \tag{39b}$$

L_D represents the perturbation to the molecular radiance distribution L_M which the inclusion of aerosols requires. By adopting the SS approximation to L_D, our approximation corresponds to first-order perturbation theory.

(b) Parametrization of L_M

In a purely molecular atmosphere, there is no solar aureole, due to the nearly isotropic nature of the Rayleigh phase function. As a result, for visible or ultraviolet wavelengths, we cannot expect the single scattering approximation to Eq.(37) to prove particularly accurate. (In fact, if the single scattering approximation to Eq. (37) is combined with Eq. (39), the result would be Eq. (30), and nothing at all would have been gained.)

Instead, we followed a suggestion of McPeters and Green (Ref. 4). As is fairly well known (see for example, Ref. (35), the nature of the Rayleigh Phase function dictates that L_M must be expressible in the following form

$$L_M(\tau,\mu,\omega) = L_M^{(0)}(\tau,\mu,\mu_o) + L_M^{(1)}(\tau,\mu,\mu_o)\cos\omega$$

$$+ L_M^{(2)}(\tau,\mu,\mu_o)\cos 2\omega \tag{40}$$

A complete parametrization of L_M would require empirical formulae for $L_M^{(0)}$ $L_M^{(1)}$ and $L_M^{(2)}$ --three functions, each of 3 variables. Such a parametrization is beyond the scope of this paper. In this paper, we restrict our formulation and computations mainly to the almucantar, defined by $\mu = \mu_o$. This reduces the three functions $L_M^{(i)}$ to functions of only 2 variables. From a study of the tabulated results of Ref. 35 and 4, it was noted that, for a wide range of circumstances, L_M followed the angular pattern predicted by the single scattering approximation, except that it had been scaled up somewhat. Our own examination of Ref. 35 results confirm this idea, provided ϕ_s is not greater than 70^o. Thus we chose to write our parametrization of L_M along the almucantar as follows

$$L_M \simeq (H_o/\mu_o) \quad e^{-\tau_T/\mu_o} \qquad (\tau_{SS} + \tau_{MS})\ P_M \tag{41}$$

where

$$\tau_{SS} = \bar{\omega}\tau_T = \tau_M + \tau_{PS} \tag{42}$$

is the total scattering optical thickness, and τ_{MS}, an adjustable parameter dependent on τ_{SS} and μ_o, is the correction term due to multiple scattering.

Note that Eq. (41) implies a definite relationship between the three $L_M^{(i)}$ functions, a relationship which may not always be exactly satisfied. However, in the region of the solar aureole, $\cos\omega \simeq 1 \simeq \cos 2\omega$, so that small deviations from this relationship should have a minimal effect on the accuracy of Eq. (41).

Substituting Eqs. (39b) and (41) in Eq. (36), one obtains

$$L = L_M + L_D^{SS} \simeq (H_o/\mu_o) \quad e^{-\tau_T/\mu_o} \qquad \{t_{MS}\ P_M + \tau_{PS}\ P_P\} \tag{43a}$$

where

$$t_{MS} = \tau_M + \tau_{MS} \tag{43b}$$

is the effective molecular scattering optical thickness.

Equation (43) is, of course, formally identical to Eq. (30) differing from it only in the amount of molecular scattering it provides. Although such an equation could have been postulated directly from Eq.(30), we believe that the steps outlined in this section provide considerable insight into the nature of the correction term, τ_{MS}, and also suggests a procedure for calculating this factor. In the next section, we discuss this procedure, as well as the empirical formula which we have selected.

(iii) Formulation of Correction Factors for MS and Ground Albedo Effects

The most obvious way to obtain τ_{MS} would be to solve Eq.(37) each time as we require it; this, however, is contrary to our desire for simplicity. In paper A, we did solve Eq. (37) though we also expressed the opinion that it would be preferable to have some empirical formula for further use. We have since developed such a formula, which is discussed in this section.

Since we can assume that almucantar radiance L_M has the same ω dependence as obtained by the SS approximation L_M^{SS}, and that τ_{MS} is a function of μ_o and τ_{SS}, we may define τ_{MS} by setting $\omega = 0^o$ and $P_M(0^o) = \frac{3}{8\pi}$ in Eq. (41) as:

$$\tau_{MS} = L_M\ (\omega = 0^o)\ \ \mu_o\ \ e^{\tau_T \sec\theta_o}\ 8\pi/3\ H_o - \tau_{SS} \tag{44}$$

Here L_M and hence τ_{MS} has no ground albedo dependence (i.e., A = 0).

In order to obtain an empirical formula for τ_{MS}, we first produced a data base from the tables of Ref. 35 for optical thicknesses of 0.02, 0.05, 0.1, 0.15, 0.25 and 0.5, and zenith cosines 0.4, 0.92 and 1.0. To fill in some of the gaps, we supplemented these data with some further values generated by our own radiative transfer code. This data was all restricted to a conservative atmosphere, for which $\bar{\omega} = 1$, i.e., $\tau_T = \tau_M + \tau_{PS}$.

The final parameterized expression for τ_{MS} is restricted to three adjustable parameters, which were then iterated to obtain the best fit to the data base by using a non-linear least squares code, to give the relation

$$\tau_{MS} = 0.02\ \tau_{SS} + 1.2\ \tau_{SS}^2/\mu_o^{1/4} \tag{45}$$

This expression is, in general, accurate to within 1%, for optical thicknesses up to 0.6 and zenith angles up to 70^o. As a test of Eq. (45), we have compared its results, when inserted into Eq. (41), with the tables of Dave and Furukawa (Ref. 34), which include ozone absorption. This comparison is shown in Table 2.5, where we see that the biggest error is only 1.2%. Thus we see that Eq. (41), along with the empirical relation Eq. (45), provides a highly accurate approximation to the almucantar radiance, at least in the aureole region, for both conservative and non-conservative atmospheres.

Until now, our discussion has ignored the contribution from ground reflectivity or albedo, a deficiency we now proceed to rectify. As is well known (e.g., Refs. 43, 44, and 35), the radiance $L(A)$ in the presence of a ground albedo, $A > 0$, may be related to the zero ground albedo radiance $L(A = 0)$, and to certain auxiliary functions, as

$$L(A) = L(A = 0) + \left[\frac{A\ F(\tau_T,\mu)\ G(\tau_T,\mu_o)}{1 - A\ \bar{S}(\tau_T)}\right] H_o \tag{46}$$

where $G(\tau_T,\mu_o)$ is the transmission function of the atmosphere

$F(\tau_T,\mu)$ is the reflection function of the atmosphere for diffuse source at the ground

and $$\bar{S}(\tau_T) = 2\int_0^1 F(\tau_T,\mu)\ \mu\ d\mu \tag{47}$$

TABLE 2.5 : Comparison of Radiance Values from a Dust Free Atmosphere at a Scattering Angle of 0°.

λ (μm)	τ_M	τ_{O_3}	θ_o (deg)	Dave & Furukawa Results	Our MS Approximation
0.6550	0.04823	0.02016	0	0.01824	0.01821
			30	0.02089	0.02084
			60	0.03448	0.03435
0.6150	0.06224	0.03834	0	0.02316	0.02311
			30	0.02640	0.02634
			60	0.04249	0.04232
0.5750	0.08179	0.04048	0	0.03048	0.03035
			30	0.03465	0.03449
			60	0.05489	0.05460
0.5350	0.1098	0.0240	0	0.04177	0.04147
			30	0.04745	0.04711
			60	0.07474	0.07412
0.4950	0.1508	0.007143	0	0.05853	0.05799
			30	0.06636	0.06570
			60	0.10300	0.10187
0.3600	0.5634	0.004161	0	0.2014	0.2032
			30	0.2174	0.2180
			60	0.2507	0.2477

Here, we assume the Lambertian law of reflection, so that the contribution from ground-reflected photons is azimuth-independent, in contrast to all other photons, which are assumed to follow the azimuth dependence of the Rayleigh phase function. Therefore, for a Lambertian surface, one must add an azimuth-independent term to Eqs. (41) and (43), such that

$$L_M \simeq (H_o/\mu_o)\ e^{-\tau_T/\mu_o}\ \left[(\tau_{SS} + \tau_{MS})\ P_M + \tau_A\ P_M(0^o)\right] \tag{41'}$$

and

$$L = (H_o/\mu_o)\ e^{-\tau_T/\mu_o}\ \left[(\tau_M + \tau_{MS})\ P_M + \tau_{PS}\ P_P + \tau_A\ P_M(0^o)\right] \tag{43'}$$

where Eq. (44) and (46) suggest that τ_A is given as

$$\tau_A = \frac{A\ \tau_2(\tau_{SS},\mu_o)}{1 - A\ \tau_3(\tau_{SS})} \tag{48}$$

$$\tau_2 = F(\tau_{SS},\mu_o)\ G(\tau_{SS},\mu_o)\ \mu_o\ e^{\tau_T/\mu_o}\ 8\pi/3 \tag{49a}$$

and

$$\tau_3 = \bar{S}(\tau_{SS}) \tag{49b}$$

Again we have produced a sizeable data base, drawn from the tables of Ref. 35 and the results of our own code. By obtaining best least squares fits to the data base, the final expressions (with 3 adjustable parameters) for τ_2 and τ_3 are

$$\tau_2 = 1.34\ \tau_{SS}\ \mu_o\ (1.0 + 0.22\ (\tau_{SS}/\mu_o)^2) \tag{50a}$$

and

$$\tau_3 = 0.9\ \tau_{SS} - 0.92\ \tau_{SS}^2 + 0.54\ \tau_{SS}^3 \tag{50b}$$

Note that we often use the symbol τ_1 to denote τ_{MS} as given by Eq. (44), so that

$$\tau_1 \equiv \tau_{MS} = 0.02\ \tau_{SS} + 1.2\ \tau_{SS}^2 / \mu_o^{1/4} \tag{50c}$$

Let us now return to Eq. (43'), which we have built up in stages, and explain its implementation. In general, an atmosphere, or atmospheric model, will have at least 4 components to its optical thickness: τ_M, the molecular (Rayleigh) scattering component; τ_{O_3}, the ozone absorption component; τ_{PS}, the particulate scattering component; and τ_{PA}, the particulate absorption component. From τ_{SS}, cosine of the solar zenith angle, μ_o, and ground albedo, A (if non-zero), we may calculate both τ_{MS} and τ_A, using Eqs. (44), (48), and (50). The final evaluation of Eq. (43') is then straight-forward for any azimuth angle, or scattering angle (cf Eq. 31).

(iv) Computation of Almucantar Radiances

Rather than generate several new sets of data with our radiative transfer code (a rather expensive exercise), we have decided to utilize the data from existing runs, as this appears to give good coverage of the "parameter space" we wish to investigate. The existing data obtained with two size distribution models can be divided into the following two data groups.

The first data group, hereafter referred to as Data Group A, corresponds to a modified gamma-type aerosol size distribution, such as Deirmendjian's (Ref. 40) Haze H model:

$$n(r) = a\ r^2\ e^{-br} \tag{51}$$

We chose b = 10 μm^{-1}, a refractive index of m = 1.55 - i(0.0), and a wavelength of λ = 0.55 μm. The parameter a, which is related to the total number of particles, was determined by the value used for τ_p. The existing data base generated by the use of our radiative transfer code consisted of twenty-four data sets, each containing twenty radiance values for the azimuthal angles $\phi = 0^o(1^o)\ 19^o$, and obtained by using all possible combinations of the following values of the parameters θ_o, τ_M, τ_P and A:

$$\left.\begin{aligned} \theta_o &= 30^o,\ 45^o,\ 60^o \\ \tau_M &= 0.1,\ 0.2 \\ \tau_P &= 0.1,\ 0.2 \\ A &= 0.0,\ 0.25 \end{aligned}\right\} \qquad (52)$$

The second data group, hereafter referred to as Data Group B, corresponds to a log-normal aerosol size distribution, namely,

$$n(r) = N_o \exp\left\{-\frac{1}{2}\left[\log(r/r_m)/\sigma\right]^2\right\}/r\,\sigma\sqrt{2\pi} \qquad (53)$$

We chose r_m = 0.25 μm, σ = 1.0, and used the same value of refractive index as in the first group, namely, m = 1.55 - i(0.0). Here N_o is directly related to τ_p. Data Group B, in contrast to Group A, contains data that could be subdivided into two subgroups, hereafter referred to as Data Groups B1 and B2, corresponding to Model Atmospheres B1 and B2 defined in Table 2.6 by values of τ_M and τ_{O_3} at wavelengths of 0.4, 0.5, and 0.6 μm.

TABLE 2.6: Optical Thickness Values for Model Atmospheres B1 and B2 Correspond to a Log Normal Aerosol Size Distribution .

		Model Atmosphere B1		Model Atmosphere B2	
$\lambda(\mu m)$	τ_M	τ_P	τ_{O_3}	τ_P	τ_{O_3}
0.4	0.364	0.13984	0.0	0.18015	0.0
0.5	0.145	0.14400	0.01350	0.18480	0.01357
0.6	0.069	0.14778	0.05013	0.18910	0.04774

The Data Group B1 for Model Atmosphere B1 is based on $\theta_o = 45^o$, $\tau_P \simeq 0.14$, and A = 0.0 and 0.2; and Data Group B2 for Model Atmosphere B2 is based on $\theta_o = 30^o$, $\tau_P \simeq 0.18$, and A = 0.0, 0.2, 0.4, and 0.6. The exact values of all relevant parameters for the Model Atmospheres B1 and B2 are given in Table 2.2. In all, we have a total of eighteen data sets; six for Data Group B1 and twelve for Data Group B2.

Thus, altogether the radiative transfer data base, composed of two data groups A and B, contain 42 data sets, each containing 20 data points, generated by our radiative transfer code. It is against this data base, that checks on the accuracy of other approximations to the radiative transfer equation must be made. For this purpose, 42 data sets were obtained by using Eq. (14') for our MS approximation, and 21 data sets, by using Eq. (1) for the SS approximation (which is independent of A); with all relevant parameters being the same as the ones used to generate the radiative transfer data.

In order to bring out the salient features, instead of presenting the full data, we decided to present some judiciously selected data using a combination of tables and graphs. In Tables 2.7 and 2.8, data from Data Groups A and B, respectively, is presented for all the sets, but for only five of the twenty azimuth angles. In Figs. 2.14 and 2.15, we have plotted several selected data sets in full.

In Table 2.7, the computed radiance values for Data Group A are presented in five columns: the SS results are placed in the middle, flanked on either side by the true results from our radiative transfer code for the two values of ground albedo, with our MS approximation results on the outside of these. Between each pair of adjacent columns is a column giving the percentage errors involved when one of the approximations (SS or MS) is compared with the true radiative transfer values. To the left of these columns are five other columns giving the values of the parameters θ_o, τ_M, τ_p, ϕ, and ψ for which the computations were made. Note that $\Phi_o = \pi$ was used for all computations.

Table 2.8 presents similar data for Data Group B, which for convenience, has been divided into three parts: Table 2.8a gives the results for Model Atmosphere B1 and A = 0.0 and 0.2; Table 2.8b, results for Model Atmosphere B2 and A = 0.0 and 0.2; and Table 2.8c, results for Model Atmosphere B2 and A = 0.4 and 0.6.

Two points should be made regarding the error considerations. Firstly, the percentage error was obtained by dividing the larger by the smaller of the pair of numbers, subtracting unity, and multiplying by 100, so that the difference is always a positive number. The second point concerns the accuracy of the radiative transfer code results. Like all such programs,

TABLE 2.7: Data Group A Containing Radiative Transfer, SS, and Our MS Approximatio Radiances for the Modified Gamma Distribution, τ_M = 0.1 and 0.2, τ_p = 0.1 and 0.2, ϕ_s = 30°, 45° and 60°, and A = 0.0 and 0.25.

					A = 0.0					A = 0.25			
ϕ_s	τ_M	τ_p	ϕ (deg)	ψ (deg)	Our MS Approx..	% Error	Radiative Transfer	% Error	SS Approx.	% Error	Radiative Transfer	% Error	Our MS Approx.
30°	0.1	0.1	0	0.0	0.6480	0.23	0.6495	3.10	0.6300	5.32	0.6635	0.77	0.6686
			5	2.5	0.6270	0.24	0.6285	3.19	0.6091	5.48	0.6425	0.79	0.6476
			10	5.0	0.5704	0.23	0.5717	3.48	0.5525	6.01	0.5857	0.89	0.5909
			15	7.5	0.4932	0.18	0.4941	3.96	0.4753	6.90	0.5081	1.08	0.5136
			19	9.5	0.4277	0.19	0.4285	4.51	0.4099	7.90	0.4424	1.27	0.4480
	0.1	0.2	0	0.0	1.1280	1.12	1.1406	4.45	1.0920	5.99	1.1574	0.09	1.1564
			5	2.5	1.0908	1.13	1.1031	4.59	1.0547	6.17	1.1198	0.07	1.1190
			10	5.0	0.9899	1.16	1.0015	4.98	0.9540	6.73	1.0182	0.01	1.0181
			15	7.5	0.8524	1.22	0.8628	5.66	0.8166	7.71	0.8796	0.09	0.8804
			19	9.5	0.7358	1.26	0.7451	6.41	0.7002	8.80	0.7618	0.25	0.7637
	0.2	0.1	0	0.0	0.6280	0.05	0.6277	6.03	0.5920	9.92	0.6507	0.86	0.6563
			5	2.5	0.6093	0.07	0.6089	6.21	0.5733	10.22	0.6319	0.90	0.6376
			10	5.0	0.5587	0.09	0.5582	6.77	0.5228	11.17	0.5812	0.98	0.5869
			15	7.5	0.4896	0.14	0.4889	7.71	0.4539	12.78	0.5119	1.13	0.5177
			19	9.5	0.4310	0.23	0.4300	8.75	0.3954	14.57	0.4530	1.32	0.4590
	0.2	0.2	0	0.0	1.0574	0.74	1.0652	6.49	1.0003	9.01	1.0904	0.15	1.0920
			5	2.5	1.0241	0.74	1.0317	6.68	0.9671	9.29	1.0569	0.17	1.0587
			10	5.0	0.9341	0.75	0.9411	7.28	0.8772	10.16	0.9663	0.24	0.9686
			15	7.5	0.8113	0.74	0.8173	8.29	0.7547	11.63	0.8425	0.38	0.8457
			19	9.5	0.7072	0.72	0.7123	9.45	0.6508	13.32	0.7375	0.53	0.7414
45°	0.1	0.1	0	0.0	0.7546	0.73	0.7601	3.75	0.7326	5.66	0.7741	0.03	0.7743
			5	3.5	0.7071	0.75	0.7124	3.98	0.6851	6.03	0.7264	0.04	0.7267
			10	7.1	0.5904	0.81	0.5952	4.68	0.5686	7.14	0.6092	0.13	0.6100
			15	10.6	0.4566	0.88	0.4606	5.89	0.4350	9.10	0.4746	0.29	0.4766
			19	13.4	0.3635	0.88	0.3667	7.22	0.3420	11.32	0.3807	0.50	0.3826
	0.1	0.2	0	0.0	1.2802	2.03	1.3062	5.57	1.2373	6.93	1.3231	1.26	1.3067
			5	3.5	1.1978	2.11	1.2231	5.90	1.1550	7.36	1.2400	1.28	1.2247
			10	7.1	0.9954	2.33	1.0186	6.91	0.9528	8.69	1.0356	1.36	1.0217
			15	10.6	0.7634	2.66	0.7837	8.67	0.7212	11.01	0.8006	1.41	0.7895
			19	13.4	0.6019	2.92	0.6195	10.61	0.5601	13.62	0.6364	1.39	0.6277
	0.2	0.1	0	0.0	0.7137	0.55	0.7176	6.99	0.6707	10.29	0.7397	0.07	0.7403
			5	3.5	0.6724	0.55	0.6761	7.40	0.6295	10.91	0.6982	0.09	0.6987
			10	7.1	0.5707	0.58	0.5740	8.69	0.5281	12.90	0.5962	0.13	0.5977
			15	10.6	0.4541	0.57	0.4567	10.90	0.4118	16.29	0.4789	0.25	0.4801
			19	13.4	0.3726	0.56	0.3747	13.31	0.3307	19.99	0.3968	0.30	0.3981
	0.2	0.2	0	0.0	1.1706	1.75	1.1911	7.85	1.1044	10.06	1.2155	1.08	1.2021
			5	3.5	1.0990	1.81	1.1189	8.34	1.0328	10.70	1.1433	1.11	1.1301
			10	7.1	0.9229	1.97	0.9411	9.80	0.8571	12.65	0.9655	1.14	0.9541
			15	10.6	0.7210	2.18	0.7367	12.35	0.6557	16.07	0.7611	1.17	0.7527
			19	13.4	0.5802	2.33	0.5937	15.15	0.5156	19.88	0.6181	1.13	0.6117
60°	0.1	0.1	0	0.0	0.9517	1.82	0.9690	5.15	0.9215	6.63	0.9826	1.36	0.9694
			5	4.3	0.8643	1.93	0.8810	5.61	0.8342	7.25	0.8947	1.44	0.8828
			10	8.7	0.6683	2.27	0.6835	7.06	0.6384	9.21	0.6972	1.65	0.6857
			15	13.0	0.4757	2.77	0.4889	9.55	0.4463	12.61	0.5026	1.95	0.4933
			19	16.5	0.3612	3.18	0.3727	12.19	0.3322	16.32	0.3864	2.14	0.3786
	0.1	0.2	0	0.0	1.5233	4.12	1.5860	8.05	1.4679	9.18	1.6026	3.64	1.5467
			5	4.3	1.3804	4.40	1.4411	8.76	1.3250	10.02	1.4577	3.88	1.4031
			10	8.7	1.0597	5.23	1.1151	10.98	1.0048	12.64	1.1318	4.56	1.0820
			15	13.0	0.7449	6.47	0.7931	14.83	0.6907	17.23	0.8097	5.53	0.7677
			19	16.5	0.5579	7.55	0.5999	18.93	0.5045	22.22	0.6166	6.31	0.5800
	0.2	0.1	0	0.0	0.8513	1.74	0.8661	8.83	0.7958	11.37	0.8863	1.37	0.8743
			5	4.3	0.7795	1.85	0.7939	9.62	0.7242	12.50	0.8147	1.52	0.8024
			10	8.7	0.6184	2.13	0.6316	12.09	0.5635	15.67	0.6518	1.65	0.6414
			15	13.0	0.4598	2.52	0.4714	16.22	0.4056	21.20	0.4916	1.95	0.4821
			19	16.5	0.3650	2.85	0.3754	20.51	0.3115	27.00	0.3956	2.20	0.3873
	0.2	0.2	0	0.0	1.3164	3.94	1.3683	10.73	1.2357	12.53	1.3905	3.53	1.3431
			5	4.3	1.1991	4.20	1.2495	11.70	1.1186	13.69	1.2717	3.74	1.2257
			10	8.7	0.9360	4.94	0.9822	14.73	0.8561	17.32	1.0044	4.35	0.9621
			15	13.0	0.6773	5.96	0.7177	19.94	0.5984	23.66	0.7399	5.20	0.7031
			19	16.5	0.5232	6.82	0.5589	25.45	0.4455	30.44	0.5811	5.87	0.5487

TABLE 2.8a: Data Group B1 Containing Radiative Transfer, SS, and Our MS Approximation Radiances for Model Atmospheres B1, $\phi_s = 45^o$, and Ground Albedos 0.0 and 0.2

			A = 0.0					A = 0.2			
λ	ϕ (deg)	ψ (deg)	Our MS Approx.	% Error	Radiative Transfer	% Error	SS Approx.	% Error	Radiative Transfer	% Error	Our MS Approx.
0.4	0	0.0	11.2014	1.60	11.3810	2.63	11.0890	2.87	11.4070	1.58	11.2300
	5	3.5	2.5738	4.13	2.6800	7.88	2.4842	8.93	2.7060	3.98	2.6024
	10	7.1	0.7479	4.75	0.7834	19.11	0.6577	23.07	0.8094	4.26	0.7763
	15	10.6	0.4268	3.51	0.4418	30.98	0.3373	38.72	0.4679	2.86	0.4549
	19	13.4	0.3390	2.65	0.3480	38.92	0.2505	49.30	0.3740	1.94	0.3669
0.5	0	0.0	9.8073	1.26	9.9308	1.95	9.7404	2.10	9.9452	1.20	9.8273
	5	3.5	3.3711	2.94	3.4704	4.14	3.3323	4.57	3.4847	2.76	3.3911
	10	7.1	0.9307	4.53	0.9729	9.11	0.8916	10.73	0.9873	3.86	0.9506
	15	10.6	0.4602	4.22	0.4796	13.87	0.4212	17.28	0.4940	2.94	0.4799
	19	13.4	0.3062	3.20	0.3160	18.13	0.2675	23.51	0.3304	1.47	0.3256
0.6	0	0.0	7.3873	1.16	7.4732	1.75	7.3448	1.87	7.4819	1.07	7.4028
	5	3.5	3.3755	2.33	3.4541	3.04	3.3522	3.30	3.4627	2.12	3.3909
	10	7.1	0.9925	4.10	1.0332	6.63	0.9690	7.52	1.0419	3.38	1.0078
	15	10.6	0.4742	4.53	0.4957	9.86	0.4512	11.79	0.5044	3.06	0.4894
	19	13.4	0.3258	4.11	0.3392	11.98	0.3029	14.86	0.3479	2.08	0.3408

TABLE 2.8b: Data Group B2 Containing Radiative Transfer, SS, and Our MS Approximation Radiances for Model Atmospheres B2, $\phi_s = 30^o$, and Ground Albedos 0.0 and 0.2

			A = 0.0					A = 0.2			
λ	φ (deg)	ψ (deg)	Our MS Approx.	% Error	Radiative Transfer	% Error	SS Approx.	% Error	Radiative Transfer	% Error	Our MS Approx.
0.4	0	0.0	8.8335	0.57	8.8838	2.37	8.6783	2.69	8.9114	0.51	8.8665
	5	3.5	5.1108	1.64	5.1944	3.63	5.0125	4.18	5.2220	1.52	5.1437
	10	7.1	1.6108	3.32	1.6643	9.22	1.5238	11.03	1.6919	2.93	1.6437
	15	10.6	0.7912	3.13	0.8160	16.07	0.7030	20.00	0.8436	2.38	0.8240
	20	14.1	0.5035	2.16	0.5144	23.71	0.4158	30.38	0.5421	1.14	0.5360
0.5	0	0.0	7.2869	0.92	7.3543	1.94	7.2142	2.15	7.3695	0.81	7.3105
	5	3.5	5.0891	1.42	5.1616	2.52	5.0348	2.82	5.1768	1.26	5.1126
	10	7.1	2.0632	2.86	2.1222	4.90	2.0230	5.65	2.1374	2.42	2.0868
	15	10.6	0.9371	3.69	0.9717	8.39	0.8965	10.08	0.9869	2.74	0.9606
	20	14.1	0.5638	3.46	0.5833	11.49	0.5232	14.39	0.5985	1.96	0.5870
0.6	0	0.0	5.4628	1.27	5.5324	1.91	5.4289	2.08	5.5418	1.10	5.4817
	5	3.5	4.2361	1.65	4.3058	2.29	4.2095	2.51	4.3152	1.41	4.2550
	10	7.1	2.1395	2.77	2.1987	3.74	2.1194	4.19	2.2081	2.30	2.1584
	15	10.6	0.9981	3.96	1.0376	6.36	0.9756	7.32	1.0470	2.96	1.0169
	20	14.1	0.5995	4.17	0.6245	8.51	0.5755	10.15	0.6339	2.56	0.6181

TABLE 2.8c: Data Group B2 Containing Radiative Transfer, SS, and Our MS Approximation Radiances for Model Atmospheres B2, $\phi_s = 30^o$, and Ground Albedos 0.4 and 0.6

			A = 0.4					A = 0.6			
λ	ϕ (deg)	ψ (deg)	Our MS Approx.	% Error	Radiative Transfer	% Error	SS Approx.	% Error	Radiative Transfer	% Error	Our MS Approx.
0.4	0	0.0	8.9041	0.43	8.9422	3.04	8.6783	3.44	8.9768	0.33	8.9473
	5	3.5	5.1813	1.38	5.2528	4.79	5.0125	5.48	5.2873	1.20	5.2245
	10	7.1	1.6811	2.47	1.7227	13.05	1.5238	15.31	1.7572	1.91	1.7242
	15	10.6	0.8612	1.53	0.8744	24.38	0.7030	29.30	0.9090	0.54	0.9041
	20	14.1	0.5730	0.02	0.5729	37.78	0.4158	46.08	0.6074	1.35	0.6156
0.5	0	0.0	7.3364	0.67	7.3856	2.38	7.2142	2.61	7.4028	0.52	7.3648
	5	3.5	5.1385	1.06	5.1929	3.14	5.0348	3.48	5.2101	0.84	5.1669
	10	7.1	2.1125	1.94	2.1535	6.45	2.0230	7.30	2.1707	1.40	2.1408
	15	10.6	0.9862	1.70	1.0030	11.88	0.8965	13.80	1.0202	0.57	1.0144
	20	14.1	0.6125	0.34	0.6146	17.47	0.5232	20.76	0.6318	1.38	0.6405
0.6	0	0.0	5.5020	0.90	5.5516	2.26	5.4289	2.45	5.5618	0.68	5.5241
	5	3.5	4.2754	1.16	4.3250	2.74	4.2095	2.99	4.3352	0.88	4.2974
	10	7.1	2.1786	1.80	2.2179	4.65	2.1194	5.13	2.2281	1.25	2.2006
	15	10.6	1.0371	1.89	1.0567	8.31	0.9756	9.37	1.0670	0.76	1.0589
	20	14.1	0.6382	0.86	0.6437	11.85	0.5755	13.62	0.6539	0.92	0.6599

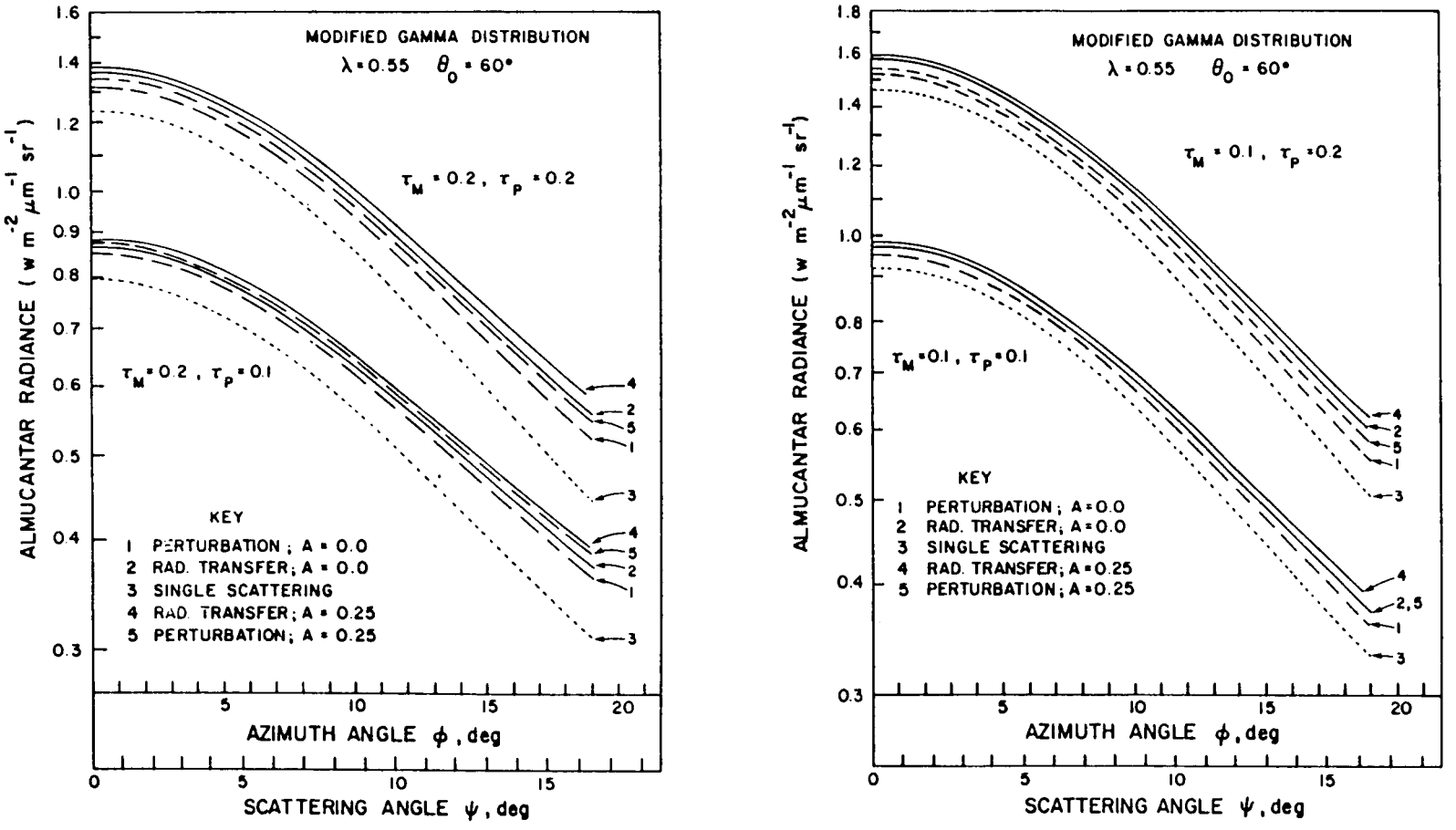

FIG. 2.14: Almucantar radiances for the modified gamma size distribution and $\theta_o = \phi_s = 60^o$.

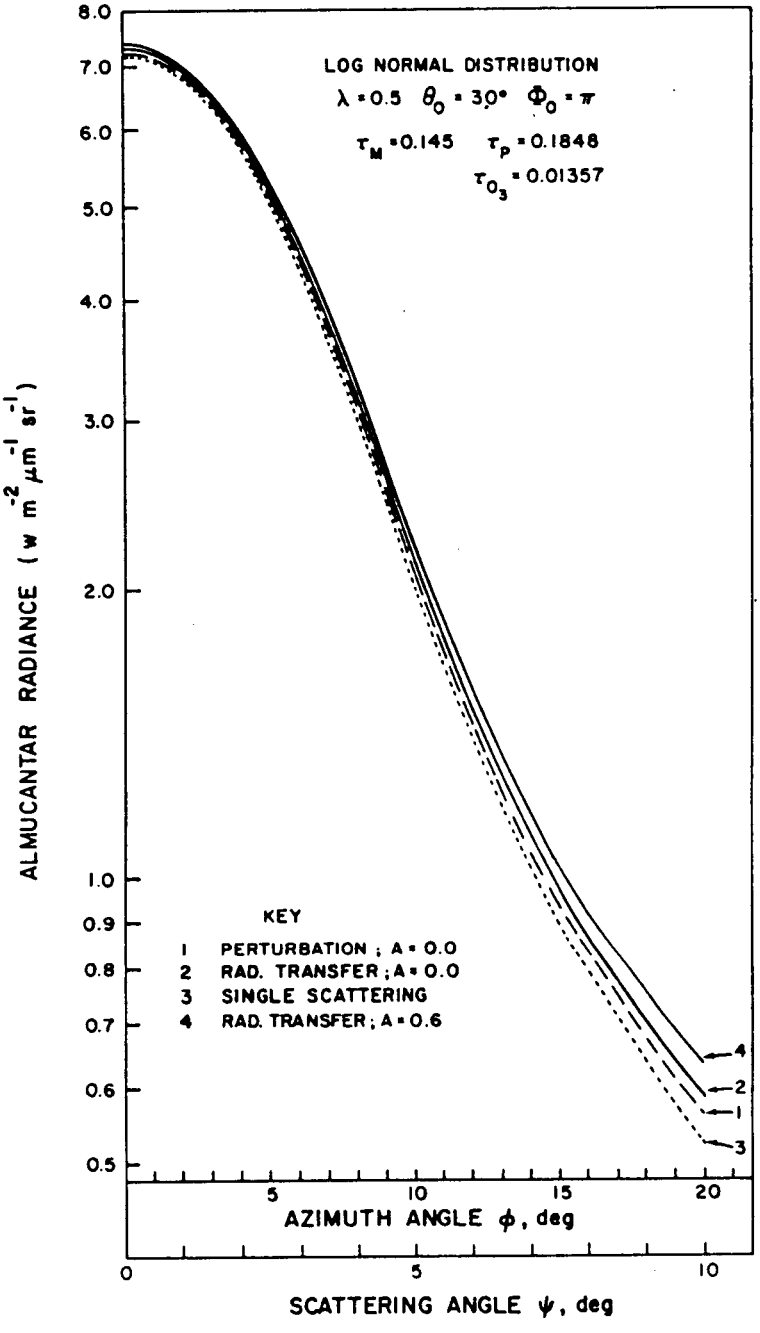

FIG. 2.15: Almucantar radiances for model atmosphere B2, and λ = 0.5 μm. Here $\theta_o = \phi_s = 30^o$.

our code is numerical, and, thus, can never be exact. Consequently, we are not able to guarantee our radiative transfer results to better than about 1% although we believe that they are more accurate than this. Since very few published results exist, it is virtually impossible to compare our results with results of known accuracy.

In order to illustrate these results, we have selected a few data sets for graphical presentation. Originally, it had been our intention to show both the "best" and "worst" cases for comparison. But, in a great many cases, it was nearly impossible to distinguish the various curves, especially in the case of Data Group B. Thus, the graphs presented in Figs. 2.14 and 2.15 are, essentially, "worst" cases, which, we feel, adequately illustrate the relative accuracy of the SS and MS approximations.

In Fig. 2.14, we plot the four data sets for $\phi_s = 60^\circ$, which illustrate the effect of varying τ_M and τ_p. In Fig. 2.15, we plot the results for Model Atmosphere B2, and $\lambda = 0.5$ μm. Clearly, it was not possible to plot all the data, so we have plotted the three curves for A = 0.0 (to indicate the relative accuracy of MS and SS approximations), and the radiative transfer results for A = 0.6 (to indicate the effect of ground albedo). The location of the missing lines may be inferred from Table 2.8.

So far, we have only considered results obtained using the one refractive index, m = 1.55. It is generally accepted that the real part of the refractive index has little effect on the differences in scattered radiances (obtained by MS and SS approximation and RT calculations) in the aureole region where diffraction scattering predominates. We wanted to know how our MS approximation was effected by the inclusion of aerosol absorption. In order to study its effects, we have repeated the calculations for Haze H (Eq. (51)) with $\tau_p = \tau_M = 0.2$, but using a refractive index of m = 1.55 - i 0.02. (Note that

τ_p now has two components, namely, $\tau_{PS} = 0.16718$, and $\tau_{PA} = 0.03282$.) We have also extended these calculations to include some higher azimuth angles. These results are presented in Table 2.9.

(v) Discussion of Results

The most significant parameters to be considered in this analysis are probably τ_M and τ_p, closely followed by ϕ_s, A, and the shape of the aerosol phase function $P_p(\psi)$ at small angles ψ. The effects of aerosol refractive index and ozone absorption are most certainly small for the visible wavelength region. Even if we restrict our considerations to the aforementioned five parameters, a complete study of all the possible combinations would be exceedingly costly, and is well beyond the scope of this investigation. Nevertheless, the data which we have shown here will be sufficient to draw several important conclusions concerning the accuracy and utility of our MS approximation.

We will start our investigation with a study of the first group of data sets, which will permit an analysis of the effects of four of the five principal parameters (θ_o, τ_p, τ_M, A). Table 2.7 shows that, for $\tau_M = \tau_p = 0.1$, our MS approximation is highly accurate, and provides a significant improvement over SS, for both values of A and all three values of ϕ_s. The SS and MS approximation results both decline in accuracy as ϕ_s increases; for which there are two reasons. Firstly, as ϕ_s increases, so does the air mass, and with it the amount of higher-order scattering. Secondly, as ϕ_s increases, so does the scattering angle corresponding to a given azimuth angle. In the region of the aureole, Eq. (2) may be approximated by

$$\psi \simeq \phi \sin \phi_s \tag{54}$$

Thus, as ϕ_s increases, the data presented in Table 2.7 are seen to extend to larger values of ψ, where the dominance of the single scattering contribution is decreased.

TABLE 2.9: Radiative Transfer, SS, and Our MS Approximation Radiances for the Modified Gamma Distribution, $m = 1.55 - i0.02$, $\tau_M = 0.2$, $\tau_{ps} = 0.167$, and $\tau_{PA} = 0.033$

			A = 0.0					A = 0.25			
ϕ_s (deg)	ϕ (deg)	ψ (deg)	Our MS Approx.	% Error	Radiative Transfer	% Error	SS Approx.	% Error	Radiative Transfer	% Error	Our MS Approx.
30	0	0.0	1.0205	0.74	1.0281	5.43	0.9723	7.27	1.0485	0.33	1.0520
	5	2.5	0.9874	0.74	0.9948	5.59	0.9392	7.49	1.0152	0.36	1.0189
	10	5.0	0.8979	0.74	0.9046	6.06	0.8498	8.13	0.9250	0.45	0.9292
	15	7.5	0.7755	0.73	0.7812	6.86	0.7276	9.24	0.8017	0.62	0.8067
	20	10.0	0.6462	0.69	0.6507	7.99	0.5987	10.80	0.6712	0.89	0.6772
	30	14.9	0.4319	0.44	0.4338	11.20	0.3852	15.19	0.4542	1.78	0.4623
	45	22.1	0.2581	0.62	0.2565	16.84	0.2133	23.00	0.2770	3.75	0.2874
	90	41.4	0.1257	3.80	0.1211	27.33	0.0880	37.85	0.1416	6.14	0.1503
45	0	0.0	1.1294	1.56	1.1473	6.44	1.0734	8.00	1.1667	0.72	1.1583
	5	3.5	1.0582	1.61	1.0755	6.82	1.0022	8.47	1.0949	0.72	1.0870
	10	7.1	0.8828	1.74	0.8984	7.93	0.8272	9.88	0.9179	0.71	0.9114
	15	10.6	0.6812	1.92	0.6945	9.83	0.6262	12.28	0.7139	0.60	0.7096
	20	14.1	0.5104	2.02	0.5209	12.46	0.4560	15.60	0.5403	0.35	0.5384
	30	21.1	0.3050	1.77	0.3105	18.65	0.2526	23.43	0.3299	0.63	0.3320
	45	31.4	0.1884	0.58	0.1895	26.12	0.1400	32.98	0.2089	2.15	0.2134
	90	60.0	0.0943	0.84	0.0951	37.64	0.0593	48.25	0.1146	1.92	0.1124
60	0	0.0	1.2693	3.34	1.3132	8.55	1.2009	9.73	1.3303	2.78	1.2933
	5	4.3	1.1526	3.55	1.1950	9.26	1.0844	10.54	1.2122	2.95	1.1765
	10	8.7	0.8903	4.13	0.9287	11.41	0.8227	13.02	0.9458	3.36	0.9140
	15	13.0	0.6321	4.95	0.6650	14.96	0.5655	17.11	0.6822	3.91	0.6555
	20	17.3	0.4487	5.72	0.4759	19.44	0.3834	22.23	0.4930	4.32	0.4717
	30	25.9	0.2679	6.23	0.2857	27.86	0.2061	31.96	0.3029	4.36	0.2897
	45	38.7	0.1737	5.90	0.1846	36.70	0.1187	41.15	0.2017	4.31	0.1930
	90	75.5	0.0855	10.47	0.0955	48.48	0.0492	56.34	0.1127	12.78	0.0983

When τ_p is increased from 0.1 to 0.2, a deterioration of both the MS and SS approximation results is noticed. This is hardly surprising, as both of these approximations ignore all MS events involving aerosols, which will increase significantly when τ_p is doubled. By contrast, when τ_M is increased from 0.1 to 0.2, we notice that, while the SS results continue to deteriorate, the MS results generally improve in accuracy, for all values of A and ϕ_s. Again, this result is hardly surprising, as the MS approximation is designed specifically to take account of the multiply-scattered molecular contribution.

Thus, in summary, from Table 2.7, one can see that the MS approximation is quite accurate for small values of τ_p, τ_M, and ϕ_s, and that this accuracy tends to reduce somewhat as either τ_p or ϕ_s is increased. However, in contrast to the SS approximation, the accuracy of the MS approximation tends to increase when τ_M is increased, thereby leading to the conclusion that the MS approximation improves in accuracy as the ratio τ_M/τ_p is increased.

Next, with the help of Group B data presented in Table 2.8, we may discuss the effects of the aerosol phase function--firstly because the phase function for Group B is quite different from that for Group A, and secondly because variation of wavelength, λ, implies a variation of effective particle size, which, in turn, affects the phase function.

In order to understand the wavelength dependence of the MS approximation, we study Tables 2.8a, 2.8b, and 2.8c. As λ increases, the ratio of molecular to particulate scattering decreases by a factor of five, thereby decreasing the accuracy of the MS approximation, and increasing that of the SS approximation. This is due to the systematic reduction in the total MS contribution. Nevertheless, even for λ = 0.6 μm, our MS approximation is generally twice as accurate as the SS approximation, while for λ = 0.4 μm, the former is far more accurate than the latter.

When we compare the results in Tables 2.8a and 2.8b for the two Model Atmosph B1 and B2, we see that the MS approximation errors are quite similar. This is not really surprising, as the factor $\tau_p \sec \phi_s$, a good indicator of the amount of particulate multiple scattering (which our MS approximation ignores) is very similar for both. On the other hand, the SS approximation errors are significantl higher for Model Atmosphere B2, due to the higher values of $\tau_M \sec \phi_s$.

Perhaps the most significant difference between the two data groups A and B is the particulate phase function. Thus, for example, let us compare the data set from Group A for $\phi_s = 30^\circ$, $\lambda = 0.5$ μm and $\tau_p = 0.1848$, with the set from Group value. This is entirely due to the phase functions for the log normal and modified gamma distributions used in this study, which are in the ratio of 200 to 26. In contrast to the behavior in the forward direction, we see that for large values of ϕ the order has been reversed. This, again, is due to the fact that the phase function is normalized: more photons scattered in the near forward direction leaves fewer to be scattered at larger angles.

As the particulate contribution to the solar aureole increases, the molecular contribution remains constant, and, thus, its relative contribution is decreased. This observation accounts for the somewhat lower accuracy of the MS approximation in accounting for the Group B data: the fraction of the multiple scattering it provides for has been reduced.

With a strongly forward-peaked phase function, such as that for the Group B data, the contribution of particulate single scattering relative to all other contributions is significantly increased by comparison with the situation for a flatter phase function. Thus, we see that the SS approximation is most accurate for the Group B data in the near forward direction. However, by the time we reach azimuth angles of 15° to 20°, the accuracy of the SS approximation falls off significantly, as we move out of the aerosol diffraction peak. The continued accuracy of the MS approximation indicates that it remains capable of accounting for much of the MS at these angles.

From Data Group A (Table 2.7) we concluded that the MS approximation was most useful when the ratio of molecular to particulate scattering was high. The Data Group B results (Table 2.8) are in agreement with this conclusion. although we must now appreciate that this ratio depends not only on the ratio τ_M/τ_p, but also on the shape of the particulate phase function.

For two of the three wavelengths included in the Group B studies, ozone absorption is present. Since we have not made parallel computations with this factor removed, we cannot make any categorical statements of its effects. Nevertheless, there is nothing in the data in Table 2.8 to suggest that the presence of ozone absorption is likely to reduce the utility of our MS approximation.

So far, we have made only passing remarks concerning the effects of ground albedo. The results we have presented suggest that, in general, the contribution from ground-reflected photons is small. The only exception is likely to occur in those cases where the ratio of molecular to particulate scattering is excessive. The reason for this is that, in the angular range from 90° to 150°, the region most responsible for re-scattering ground-reflected photons back to earth, the molecular phase function dominates the particulate by as much as an order of magnitude. Thus, we note that an albedo of 0.25 in Table 2.7 contributes about as much additional intensity as an albedo of 0.4 in Table 2.8, and considerably more if we consider the fractional increase.

One of the obvious advantages of our MS approximation, over the SS approximation, is that it is able to make allowance for a non-zero ground

albedo. It is, therefore, instructive to examine the variation in the percentage errors as the albedo is increased. The results of Tables 2.7 and 2.8 show that, not only does our MS approximation retain its accuracy as albedo increases, but, in general, its accuracy improves. We may even observe instances where the MS approximation over-estimates the actual radiance. This can be understood from an examination of the omitted terms in Eq. (9) for L_D. Since, P_M is significantly larger than P_P over an important angular region (when ground reflection is present), we see that P_D will be negative under such circumstances. Thus, these two omitted integrals are likely to be of opposite sign, implying that the correction to L_D may be either positive or negative.

All the results presented in this paper have been obtained with one value (namely, m' = 1.55) of the real part of the aerosol refractive index, and, thus, we cannot really comment on the effect of this parameter. However, it is generally accepted that the real part of the refractive index has little effect on the differences in scattered radiances (obtained by the MS and SS approximation and RT calculations), especially in the aureole region where diffraction scattering predominates. Also, we cannot comment much on the influence of aerosol absorption, since results of only one value (m" = 0.02) of the imaginary part of the aerosol refractive index have been obtained (Table 2.9). However, when the results in Table 2.9 are compared with those in Table 2.7, we see that the percentage errors (between the three sets of results) are rather similar, at least up to azimuth angles of 15° to 20° from the sun. Thus, we feel confident in concluding that the inclusion of aerosol absorption in no way diminishes the utility of our MS approximation.

When the results for higher azimuth angles are examined, we see that the accuracy of our MS approximation remains high (errors < 6%) at least out to 45^{o}, and is quite acceptable (< 13%) for azimuth angles of 90^{o}. By contrast, SS approximation deteriorates much more rapidly for high azimuth angles.

Finally, there is another way in which our results may be viewed. It is clear that measured radiances are composed of both SS and higher order scattering. The general success of the SS approximation in explaining much of the data demonstrates that SS is the most significant component. The data presented in this paper indicate that, in almost all cases, use of our MS approximation reduces by half, and often much more, the errors that occur due to the SS approximation. Thus, we see that the multiply-scattered molecular component is perhaps the next most important contribution to the aureole intensity, under relatively clear sky conditions.

(vi) Application of MS Approximation to Size Distribution Retrievals

Box and Deepak (Ref. 26) have discussed in detail a systematic investigation of errors in the retrieved results for aerosol size distributions obtained from simulated almucantar radiance data generated by our radiative transfer code. Results were retrieved by using the SS approximation, our MS approximation (also referred to as the modified Deirmendjian-Sekera (D-S) approximation) and the McPeters and Green (M-G) method. (See Tables I and III in Ref. 26 where d_{DS} stands for t_{MS}.) It was demonstrated that the retrievals

of aerosol size distributions can be considerably improved by using the MS formulation described here; the largest errors occur for the case of solar zenith angle $\phi_s = 60^o$, $\tau_A = 0.2$, $\tau_p = 0.2$ and A = 0.25, namely, about 2% error in retrieved results for b, the mode radius parameter in the Haze H model. We believe that these errors are due largely to the neglect of particulate multiple scattering. By contrast, the errors in b results retrieved from the same data by the use of the SS approximation were over 9%. Thus by the use of our MS approximation, the retrieval accuracy can be improved by a factor of about four.

(vii) Summary and Conclusions

From the results in Tables 2.7, 2.8 and 2.9, and the previous discussions, we are able to conclude that our MS approximation provides a significant improvement over SS approximation, with essentially no extra computational effort. Thus, it is our opinion that such SS calcualtions should be supplemented with the MS contribution discussed in this section.

Our results have shown that, in almost all instances, inclusion of this molecular MS contribution reduces the errors obtained with SS approximation by a factor of at least two, and usually more. In particular, our MS approximation will provide greatest improvement in those cases where the ratio of Rayleigh to particulate scattering is high, and/or where the ground albedo contribution is significant.

We may conclude, therefore, that the MS approximation, as outlined in Eqs. (43), (48) and (50), is of considerable value in providing details of

the aureole radiance pattern in a hazy atmosphere, with relatively high accuracy, at a fraction of the cost of a full, radiative transfer calculation. In addition, it can improve the accuracy of retrievals by a factor of at least four, compared to the SS approximation.

2.3.4 The Finite Sun Effect on the Interpretation of Solar Aureole

Although it is usually assumed that solar radiation falls on the earth's atmosphere in the form of plane waves, the finite angular size of the solar disk contradicts this assumption. For most purposes, this finite sun effect on computed or measured radiation quantities is negligible. However, in the region of the solar aureole, which is dominated by aerosol diffraction scattering, measurable effects may be obtained. In Ref. 45, we have shown that the finite sun effect is related to derivatives of the scattering phase function and that a 1 percent effect may be obtained close to the sun if enough large particles are present in the atmosphere.

In the past, when measurement techniques were not too precise (Ref. 3), it was feasible to interpret these data using the simplest possible model, namely, single scattering by molecules and aerosols from a point-source sun. As measurement accuracy has improved, however, more attention has been devoted to the removal of as many sources of error as possible from the inversion process.

Most of these sources of error are associated with the physical process of radiative transfer: absorption by trace gases such as ozone, and multiple scattering. Recently, King and Byrne (Ref. 46) have shown how to make a fairly accurate allowance for the ozone Chappius band, and we have shown how to make at least a partial accounting for multiple scattering. More work in this area is undoubtedly needed, especially in regard to multiple scattering in relatively hazy conditions.

One source of possible error in the analysis of solar aureole data is concerned not with the problem of the transfer of solar radiation through the

terrestrial atmosphere but with the source of that radiation, the sun itself. In all analyses that we are aware of, it has been assumed that the sun is a point source at infinite distance, and that solar radiation falls on the top of the atmosphere in plane waves. While the small angular size of the sun ensures that the error involved in using this approximation is quite small, it is nevertheless important to have a clear understanding of the magnitude of this error, and more especially of any special circumstances which could significantly increase it. In Ref. 45, we examine this effect in detail, both qualitatively and quantitatively. The results are discussed here.

In the single-scattering approximation, photons arriving at a detector along a given direction may have originated from different points on the sun's disk and thus been scattered through different scattering angles. If the scattering phase function is varying slowly with angle in this angular range, the effect will be negligible. Thus, in a purely Rayleigh scattering atmosphere, the finite sun effect can be safely ignored.

By contrast, if the phase function is varying rapidly, as is the case in the forward diffraction peak of typical aerosol phase functions, the effect may not be insignificant. Thus we have seen that a fairly typical aerosol size distribution leads to an effect of the order of half a percent within a degree of the sun and of several tenths of a percent out to a 5^{o} scattering angle. Beyond this angle, the effect was less than 0.1 percent. The presence of additional large particles would undoubtedly increase these numbers. Thus, we believe that if it is desired to make measurements of 0.1 percent accuracy close to the sun's disk, for the purposes of determining the aerosol phase function and/or size distribution, then some attempt

ought to be made to account for the finite sun effect, even if only after the fact.

The effect of multiple scattering is, of course, to smear out the details of the phase function, and thus we can see no need to include the finite sun effect in radiative transfer calculations for moderate to thick atmospheres. In fact, the only time when the finite sun effect is likely to have any possible significance is in the solar aureole, which is dominated by the diffraction peak of the aerosol phase function. It was for just such a situation that the analysis in this paper was developed.

2.4 INVERSION OF SIMULATED SOLAR AUREOLE RADIANCE DATA

2.4.1 Retrieval of Aerosol Size Distributions by Inversion of Simulated Multiple Scattered Aureole Data

Inversion of solar almucantar radiance data is a simple and practical method of obtaining aerosol size distributions. In this section, similar to Ref. 26, we have inverted a number of sets of simulated data, using the standard single scattering approximation, to test the errors involved in ignoring multiple scattering. We have also inverted the data using two techniques: one, Box and Deepak's modification of the method proposed by Deirmendjian and Sekera; and the other that of McPeters and Green.

In section 2.3 (and Ref. 28), we compared the relative contributions of multiple scattering (MS) and single scattering (SS) to the solar aureole almucantar radiance distribution, as obtained by a radiative transfer (RT) code. In this section, we shall determine the effects of multiple scattering on the retrieval of the aerosol size distribution from the almucantar radiance data.

The results of section 2.3 indicate that, although the single scattering approximation is reasonable for most visible wavelengths, multiple scattering contributions may not be negligible even in clear sky conditions, and may introduce significant errors in the retrieved size distribution, especially with regard to its absolute magnitude. In this section, first, we invert a number of sets of almucantar radiance data to obtain size distribution, using the single scattering approximation; and then consider two other approximations in which multiple scattering due to a molecular atmosphere alone is taken into account. As will be seen later on, the results obtained in the first case show significant errors in some cases, whereas in the latter two cases there are improvements in the retrieved size distribution.

The symbols adopted in this section follow those recommended by the International Radiation Commission (Ref. 47), except for the optical depth, which will be denoted by τ.

(i) *Single Scattering Radiance in Solar Aureole Almucantar*

We have run the Box and Deepak code (Ref. 28) for a series of molecular and particulate optical thicknesses, τ_M and τ_p, and a series of solar zenith angles, ϕ_s. The aerosol size distribution employed was a modified gamma distribution (Refs. 37 and 40) of the form

$$n(r) = ar^2 e^{-br}, \quad (0.03 \text{ m} \leq r \leq 3.0 \text{ m}) \tag{55}$$

We chose $b = 10\ \mu m^{-1}$; parameter a was given by $a = 4.5 \times 10^{3}\tau_p$. We used a wavelength ($\lambda$) of 0.55 μm, and a real refractive index (m) of 1.55. As ozone absorption was ignored, the single scattering albedo ($\tilde{\omega}$) throughout the model atmosphere was 1.0.

Using these inputs, the code generates a considerable amount of radiance data, at ground level, the top of the atmosphere and at one or two intermediate levels. In this paper, we will be concerned with only the ground level radiances along the almucantar (i.e., a scan for which observation zenith angle equals solar zenith angle).

In Ref. 28, we compared these radiative transfer radiances with radiances given by the very simple formula for the single scattering radiance L_{SS}. In the almucantar, this formula reduces to the form (Ref. 1)

$$L_{SS} = (H_o/\mu_o)\ e^{-\tau/\mu_o} \{\tau_M P_M(\psi) + \tau_P P_P(\psi)\}/4 \tag{56}$$

(ii) *Inversion in the Single Scattering Approximation*

Since the problem of inverting scattered radiance data is simplest in the single scattering approximation and in the forward angles (less than 20^{o}), we shall treat this case first. Here, the simulated radiative transfer data, L_{RT} in the almucantar in the forward direction will be inverted using the single scattering relation in Eq. (56) to determine the size distribution.

In order to do this, L_{RT} is substituted for L_{SS} in Eq. (56), which is rearranged to give

$$F_P(\psi) = L_{RT} 4\pi e^{\tau/\mu_o} (\mu_o/H_o) - \tau_M P_M(\psi) \tag{57}$$

where by definition $F_P(\psi)$, the column scattering function, is given by the relation

$$F_P(\psi) = \lambda^2/2\pi \int_0^\infty \int_0^\infty \eta(r,y) (i_1 + i_2) \, dr \, dy \tag{58}$$

where $\eta(r,y)$ is the aerosol altitude-size distribution function (Ref. 37), y is the altitude (km), and i_1 and i_2 are the Mie intensities (Ref. 32 and 40).

Since Eq. (56) is only the single scattering approximation to the radiative transfer equation, we refer to $F_P(\psi)$ as obtained from Eq. (57) as an effective column scattering function. Hence, the size distribution

obtained by inverting Eq. (58) is referred to as an effective size distribution. A question of considerable importance is then: how close is this effective size distribution to the original distribution which actually produced the observed (or in the case here, simulated) scattering pattern?

To answer that question, we have inverted a series of sets of simulated data using Eqs. (57) and (58). We assumed a size distribution of the form in Eq. (55), with a and b as adjustable parameters, and used a non-linear least squares inversion code to determine their best fit values. These values can then be compared with the original values, to provide us with an indication of the agreement between the retrieved and the actual size distribution.

It should be pointed out that by assuming the functional form of Eq. (55) for our unknown size distribution, rather than performing a point-by-point inversion of Chahine- or Twomey-type (Ref. 48), we are not biasing the results. The main thrust of this paper is to compare different methods of making allowance for multiple scattering, not different methods of inverting the integral equation, Eq. (58). In this regard, to compare the original size distribution with those obtained from a point-by-point inversion may not lead to any definite conclusions. On the other hand, we feel that the retrieved values of the two adjustable parameters, a and b (in the size distribution model, Eq. (55)), which are related to the total number of particles, and the mode radius, respectively, provide a precise quantitative test of the methods we are examining.

Using the single scattering approximation, we have inverted eight sets of data obtained from the eight combinations of the parameters τ_M = 0.1 or 0.2, τ_p = 0.1 or 0.2 and ϕ_s = 30° or 60°. For each data set, we obtained simulated radiance data for three cases: (1) single scattering only; (2) radiative transfer with ground albedo A = 0.0; and (3) radiative transfer with A = 0.25. Each of the twenty-four sets of radiance data consisted of 20 values, corresponding to azimuth angles from 0° to 19°. Inversion was performed on each set of radiance data. Table 1 gives the retrieved values of a, b and mode radius r_m (r_m = 2/b) for each of the 24 sets of data.

As expected, when we inverted the single scattering radiance data, (shown in Case 1, Table 10), we got back the original values of a and b.

Consideration of the other two cases (namely, 2 and 3) in Table 10 shows that, as suggested in Paper I, the retrieved size distribution parameters a and b obtained from the inversion of the radiative transfer data agree reasonably well with the input data for b (or r_m), but show large discrepancies for a, which is related to the absolute normalization. For small values of ϕ_s τ_M, τ_p and A = 0.0, the retrieved size distribution shows the best agreement, with this agreement deteriorating steadily as any of the four parameters is increased. These trends are just as would be expected, since an increase in any of these parameters will clearly lead to an increase in the multiple scattering contribution relative to the single scattering contribution.

TABLE 2.10: Retrieved Size Distribution Parameters a and b Using the Single Scattering Approximation

ϕ_s	τ_M	τ_P	CASE	Single Scattering Approximation			
				a	b (μm^{-1})	$r_m = 2/b$	% Error i
30°	0.1	0.1	1	44986	10.000	0.2000	0.00
			2	51590	10.169	0.1967	1.69
			3	57404	10.308	0.1940	3.08
	0.2	0.1	1	44983	10.000	0.2000	0.00
			2	60083	10.367	0.1929	3.67
			3	72418	10.616	0.1884	6.16
	0.1	0.2	1	89986	10.000	0.2000	0.00
			2	107680	10.219	0.1957	2.19
			3	115630	10.312	0.1939	3.12
	0.2	0.2	1	89981	10.000	0.2000	0.00
			2	119130	10.350	0.1932	3.50
			3	133750	10.504	0.1904	5.04
60°	0.1	0.1	1	44986	10.000	0.2000	0.00
			2	59451	10.373	0.1928	3.73
			3	65161	10.504	0.1904	5.04
	0.2	0.1	1	44971	9.999	0.2000	0.01
			2	76021	10.725	0.1865	7.25
			3	88741	10.955	0.1826	9.55
	0.1	0.2	1	89978	10.000	0.2000	0.00
			2	132900	10.516	0.1902	5.16
			3	141960	10.612	0.1885	6.12
	0.2	0.2	1	89996	10.000	0.2000	0.00
			2	157270	10.760	0.1859	7.60
			3	174230	10.912	0.1833	9.12

A. Influence of Optical Thickness

When τ_M increases from 0.1 to 0.2, we see a marked deterioration in the accuracy of the inversion, with the error in b roughly doubling. On the other hand, when τ_P increases from 0.1 to 0.2, we see very little deterioration, and in some cases, a small improvement in the value of b. The most obvious explanation is that it is molecular scattering which is most responsible for multiple scattering. Thus, we may regard the contribution due to Rayleigh scattering (which is small in the aureole) as noise, which distorts the signal due to particulate scattering. The better the ratio of τ_P to τ_M, the better the signal to noise ratio and the more accurate, in general, is the retrieved parameter b.

B. Influence of Solar Zenith Angle

Increasing ϕ_s has two effects. First, the optical path length or air mass is increased, and we may refer to the earlier discussion of this effect. Second, the scattering angle, ψ, becomes closer to the corresponding azimuth angle, ω. Thus, for $\omega = 19^\circ$, $\psi = 9.5^\circ$ when $\phi_s = 30^\circ$; $\psi = 16.4^\circ$ when $\phi_s = 60^\circ$. The greater the value of ψ, the greater is the contribution from molecular scattering since the Rayleigh phase function is close to isotropic and the particulate phase function is usually strongly forward-peaked. This implies a deterioration of the above-mentioned signal to noise ratio.

The above discussions and the results shown in Table 10 strongly suggest that it is multiple scattering due to atmospheric molecules, rather than aerosols, which is the main cause of the poor size distribution retrievals.

In order to improve the accuracy of our retrieved size distribution, the next best approach to an exact solution of the radiative transfer equation is to take into account multiple scattering due to molecules, along with single scattering due to both aerosols and molecules. A survey of the literature indicates that such a strategy for retrieving aerosol size distributions from diffuse (i.e., single plus multiple scattering) radiance data was proposed by Sekera (Ref. 42) and Deirmendjian (Refs. 38, 39, and 41). Their method is essentially a perturbation approach. However, so far to the best of our knowledge, it has not been applied to any inversion problem. McPeters and Green (Ref. 4) take account of the molecular multiple scattering in deducing the aerosol size distribution from solar aureole data. Malchow and Whitney (Ref. 49) have also included the multiple scattering due to molecules in their inversion technique for application to sunlit horizon radiance profiles as might be measured from satellites.

In this paper, we shall demonstrate how the retrievals of aerosol size distributions can be improved when we use a modification of the Deirmendjian-Sekera Perturbation method (Ref. 41) to invert our simulated data for solar aureole almucantar radiance. For the sake of comparison, the size distribution results by the McPeters and Green scheme will also be obtained. Both these methods are explained next.

(iii) *Description of the Approximate Methods*

A. Dermendjian-Sekera (D-S) Perturbation Method

The equation of radiative transfer in a plane parallel atmosphere with scattering but no absorption can be written as

$$\mu \frac{\partial L(\tau, \xi)}{\partial} = L - H_c e^{-\tau/\mu_o} P_{TOT}(\tau; \xi, \xi_o)/4\pi - \int_\Omega L(\tau, \xi') P_{TOT}(\tau; \xi, \xi') d\xi'/4\pi \quad (59)$$

where

$$P_{TOT}(\tau) = \{\sigma_M P_M + \sigma_P P_P\}/\sigma_{TOT} \quad (60a)$$

where $$\sigma_i = -\frac{\partial \tau_i}{\partial z}, \quad i = M, P, TOT \quad (60b)$$

Equation (56) can be obtained from Eq. (59) by ignoring the integral on the right hand side and setting $\phi = \phi_s$.

Following Sekera (Ref. 42) and Deirmendjian (Refs. 39, 41), we may re-express Eq. (60) in the form

$$P_{TOT}(\tau) = P_M + f(\tau) P_D \quad (61)$$

where $$P_D = P_P - P_M \quad (62a)$$

and $$f(\tau) = \sigma_P / \sigma_{TOT} \quad (62b)$$

is known as the turbidity factor, or turbidity coefficient.

Similarly we may separate the light field into two parts, viz.,

$$L(\tau, \xi) = L_M(\tau, \xi) + L_D(\tau, \xi) \quad (63)$$

where by definition L_M represents the radiance field produced by Rayleigh scattering alone, and L_D, the departure from this case due to the difference in scattering patterns between molecules and aerosols, as expressed in Eq. (62a).

If we substitute Eqs. (62) and (63) into Eq. (59), and remember that L_M satisfies Eq. (59) with P_{TOT} replaced by P_M, we find that four terms cancel, leaving the following integrodifferential equation for L_D.

$$\mu \frac{\partial L_D(\tau,\xi)}{\partial \tau} = L_D(\tau, \xi) - \Phi_o e^{-\tau/\mu_o} f(\tau) P_D(\tau; \xi, \xi_o)/4\pi$$

$$- \int_\Omega P_M(\xi, \xi') L_D(\tau, \xi') d\xi' /4\pi - f(\tau) \int_\Omega P_D(L_M + L_D) d\xi' /4\pi \qquad (64)$$

This equation is probably best solved by the successive scattering method, provided that Rayleigh radiation field, L_M, is known throughout the atmosphere. As yet we know of no serious attempt to actually pursue this line to its logical conclusion.

In the region of the solar aureole, Deirmendjian (Ref. 41) employed a single scattering approach to Eq. (64), by neglecting both the integral terms. Solution of Eq. (64) is then quite straightforward. Along the almucantar, the single scattering solution, L_D^{SS}, is particularly simple, and takes the form

$$L_D^{SS} = (H_o/\mu_o)\ e^{-\tau/\mu_o}\ P_D \int f(\tau) d\tau/4\pi$$

i.e., $$L_D^{SS} = (H_o/\mu_o)\ e^{-\tau/\mu_o}\ \tau_P\ (P_P - P_M)/4\pi \qquad (65$$

B. McPeters and Green (M-G) Method

From a study of the tabulated results of Coulson, et al. (Ref. 35) for molecular atmospheres, McPeters and Green observed that the shape of the radiative transfer radiance was very similar to that of the

single scattering pattern (at least in the aureole region), but differed from it in absolute value. Similar conclusions were drawn by us for an aerosol plus molecular atmosphere in Paper I and discussed in the following sections. Therefore, McPeters and Green proposed to introduce a correction factor, C_{MG}, to the Rayleigh optical depth τ_M that would increase the single scattering radiance values to match the radiative transfer radiance values. We may express their results as follows:

$$L_{MG} = (H_o/\mu_o)\ e^{-\tau/\mu_o}\ \{d_{MG}\ P_M + \tau_P\ P_P\}\ /4\pi \qquad (66)$$

where d_{MG} $(= C_{MG}\ \tau_M)$ is the effective Rayleigh optical depth, and C_{MG} is adjusted to give a suitable fit to L_M data for a molecular atmosphere (i.e., for $\tau_P = 0$).

C. Box and Deepak Modification to the D-S Method

To obtain the Rayleigh field contribution to the almucantar radiance in the D-S method, it is necessary to solve the radiative transfer equation for L_M in terms of P_M--a relatively straightforward task. However, instead of following this procedure, we model the L_M part of the radiance field after Eq. (66), such that

$$L_R = (H_o/\mu_o)\ e^{-\tau/\mu_o}\ d_{DS}\ P_M/4\pi \qquad (67)$$

where d_{DS} is referred to as the effective Rayleigh optical thickness. Here d_{DS} can be adjusted to give an exact fit to the true molecular radiance data, either at some scattering angle, ψ, (e.g., $\psi = 0^o$), or to give the best fit (in a least squares sense) over a range of angles. In our studies so far, we have found these two approaches to yield d_{DS} values that agree within 1%, for

azimuth angles out to 20°, optical thicknesses as high as 0.6, zenith angles as large as 70°, and ground albedos as high as 0.8. This implies that in the solar aureole region, the shape of the molecular-scattered almucantar radiance pattern, L_M follows the functional form of the molecular phase function, P_M, very closely. Thus, the approximation involved in Eq. (67) is highly accurate, at least for the data we have examined. This modification of the original D-S approach represents a considerable simplification with no loss of accuracy.

d_{DS} is a function τ, ϕ_s and ground albedo, A. Note that in the single scattering approximation, $d_{DS} = \tau$, not τ_M. It can be obtained from tables (Ref. 18) or the results of separate computations. We feel that a phenomenological formula for these effective optical thicknesses, d, as a function of τ, ϕ_s and A would be of considerable value and is currently being investigated. These results will be discussed in a subsequent publication.

We may now combine Eqs. (63), (65), and (67) to get the total radiance L_{DS} in the Deirmendjian-Sekera approximation:

$$L_{DS} = (H_o/\mu_o)\, e^{-\tau/\mu_o} \{d_{DS} P_M + \tau_P (P_P - P_M)\} /4\pi$$

$$= (H_o/\mu_o)\, e^{-\tau/\mu_o} \{(d_{DS} - \tau_P) P_M + \tau_P P_P\} /4\pi \qquad (68)$$

We see now that Eq.(68) is structurally identical to Eq.(56) (and also Eq. (66)), and in particular, can be inverted after the manner of Eq. (57) to obtain the scattering function, $F_P(\psi)$ and, thence, the aerosol size distributic Equations (56) and (68) differ in only one point: the multiple scattering

contribution due to molecules. Since d_{DS} is larger than τ, $(d_{DS} - \tau_p)$ is larger than τ_M, and so Eq. (68) provides for more molecular scattering than Eq. (56), although each contains the same amount of particulate scattering. This is precisely what we require.

Strictly speaking, L_{DS}, as given by Eq. (68), is not exactly the same as would be given in the original Deirmendjian-Sekera formulation. We should, of course, have replaced the Rayleigh phase function in Eq. (67) by a different function, to give the correct angular distribution for the Rayleigh radiance, L_M. However, as has been suggested by the discussion in the paragraph immediately following Eq. (67), this function differs very little from P_M, at least within the range of parameters we have examined. As an illustration of the basic veracity of Eq. (68), Fig. 2.16 shows the single scattering radiance, L_{SS}, as well as the full radiative transfer radiance, L_{RT}, for two values of the ground albedo, A. Also shown on the same graph are the corresponding column scattering functions, F_p, obtained from the radiances using Eq. (57). It is clear that all six curves are essentially identical, differing only in vertical displacement. (Within the angular range shown, P_M is essentially constant.) Thus, we conclude that, within the aureole region, we can make allowance for molecular multiple scattering simply by using an effective Rayleigh optical thickness. The errors involved in this approximation are, in general, considerably less than the errors involved in ignoring all multiple scattering events involving aerosols.

(iv) *Retrievals by M-G and Modified D-S Methods*

In their studies, McPeters and Green (Ref. 4) employed a phenomenological formula for d_{MG} as a function of μ_o and λ (and, hence, τ_M) based on the published results of Coulson, et al. (Ref. 35), with ground albedo ignored.

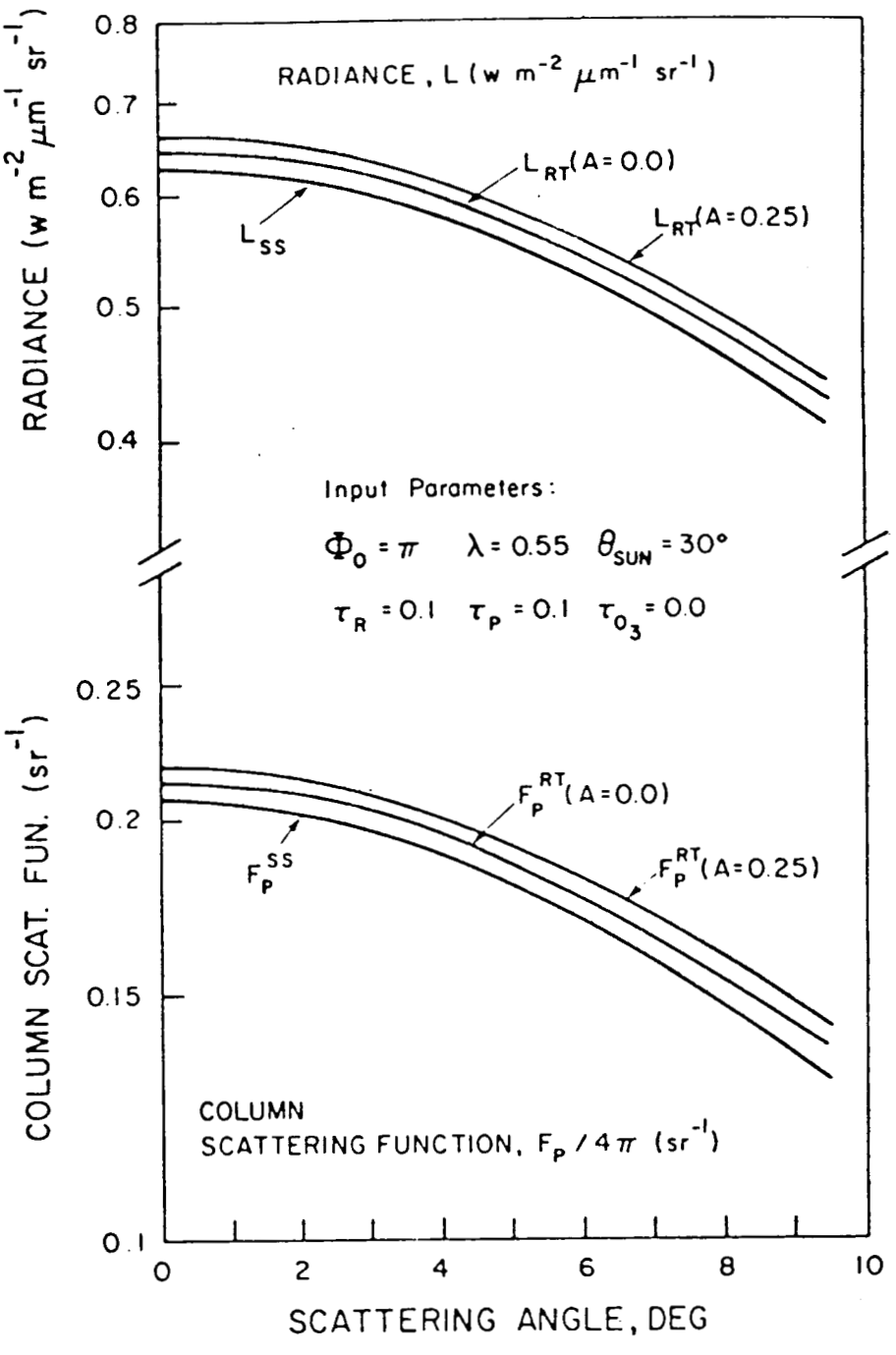

FIG. 2.16: Illustrations of Almucantar Radiance and Corresponding Columnar Scattering Functions Computed from Radiative Transfer Code and Single Scattering Approximations.

In this paper, we have obtained all the required d values from a separate series of runs of our radiative transfer code for a purely molecular atmosphere. These values are listed in Table 2.11.

In the modified D-S method, the effective Rayleigh optical thickness, d_{DS}, is obtained by considering a Rayleigh atmosphere with the optical thickness equal to the total optical thickness τ (i.e., molecular plus particulate). In the M-G method, the effective Rayleigh optical thickness, d_{MG}, is obtained by considering a Rayleigh atmosphere with just the Rayleigh optical thickness. Since the effective Rayleigh optical thickness d, for both methods is always larger than τ, and in fact the ratio d/τ increases with increasing τ, we can conclude that $(d_{DS} - \tau_P) > d_{MG}$, and thus the modified D-S method provides for more molecular scattering than that of McPeters-Green. This difference will be most pronounced for larger values of τ_P (as well as larger values of τ_M) so that the inversion of these data sets will provide the most critical comparative test of these two methods.

We have re-inverted our 16 data sets, using both Eqs. (12) and (14) plus the data from Table 2.10. (There was obviously no need to repeat the inversion of the single scattering data sets.) These results are presented in Table 2.12.

The results of these new inversions are, in all cases, more accurate than the results presented in Table 2.10. Also, one notices that whereas the M-G method yields somewhat more accurate results than the single scattering approximation (c.f. Table 2.10 and Table 2.12), the modified D-S method turns out to be much more accurate. The McPeters-Green method does not seem to provide for sufficient molecular scattering.

When the modified D-S results are examined, we see that the largest

TABLE 2.11: Effective Optical Thicknesses Used in the Modified Deirmendjian-Sekera, and McPeters-Green Inversions

τ_M	τ_P	τ	ϕ_s	A	d_{DS}	$d_{DS} - \tau_P$	d_{MG}
0.1	0.1	0.2	30°	0.0	0.255	0.155	0.114
				0.25	0.315	0.215	0.144
			60°	0.0	0.262	0.162	0.116
				0.25	0.298	0.198	0.133
0.2	0.1	0.3	30°	0.0	0.420	0.320	0.255
				0.25	0.512	0.412	0.315
			60°	0.0	0.437	0.337	0.262
				0.25	0.493	0.393	0.298
0.1	0.2	0.3	30°	0.0	0.420	0.220	0.114
				0.25	0.512	0.312	0.144
			60°	0.0	0.437	0.237	0.116
				0.25	0.493	0.293	0.133
0.2	0.2	0.4	30°	0.0	0.609	0.409	0.255
				0.25	0.736	0.536	0.315
			60°	0.0	0.642	0.442	0.262
				0.25	0.721	0.521	0.298

DS - Modified Deirmendjian-Sekera method
MG - McPeters-Green method

TABLE 2.12: Retrieved Size Distribution Parameters a and b Using Modified Deirmendjian-Sekera and McPeters-Green Approximation

Θ_o	τ_M	τ_P	A	a		b (μm^{-1})		$r_m = 2/b$		% Error in b	
				Modified D-S	M-G	Modified D-S	M-G	Modified D-S	M-G	Modified D-S	M-G
30°	0.1	0.1	0.0	44613	49693	9.985	10.121	0.2003	0.1976	-0.15	1.21
			0.25	42489	51349	9.925	10.164	0.2015	0.1968	-0.75	1.64
	0.2	0.1	0.0	44086	52289	9.970	10.187	0.2006	0.1963	-0.30	1.87
			0.25	42297	54686	9.920	10.247	0.2016	0.1952	-0.80	2.47
	0.1	0.2	0.0	92147	105720	10.020	10.195	0.1996	0.1962	0.20	1.95
			0.25	87803	10945	9.960	10.241	0.2008	0.1953	-0.40	2.41
	0.2	0.2	0.0	91100	111220	10.006	10.261	0.1999	0.1949	0.06	2.61
			0.25	87257	116240	9.953	10.319	0.2009	0.1938	-0.47	3.19
60°	0.1	0.1	0.0	48242	56373	10.083	10.298	0.1984	0.1942	0.83	2.98
			0.25	47123	58534	10.052	10.352	0.1990	0.1932	0.52	3.52
	0.2	0.1	0.0	48730	62486	10.098	10.444	0.1981	0.1915	0.98	4.44
			0.25	47946	65791	10.078	10.519	0.1985	0.1901	0.78	5.19
	0.1	0.2	0.0	106460	129550	10.205	10.480	0.1960	0.1908	2.05	4.80
			0.25	104040	134800	10.174	10.538	0.1966	0.1898	1.74	5.38
	0.2	0.2	0.0	107170	142980	10.215	10.622	0.1958	0.1883	2.15	6.22
			0.25	105360	150520	10.193	10.698	0.1962	0.1870	1.93	6.98

errors occur for $\phi_s = 60^o$ and $\tau_p = 0.2$, namely, about 2% error in b. We believe that these discrepancies are due largely to the neglect of particulate multiple scattering, which will clearly be largest under such circumstances. For all other data sets, the errors in the retrieved value of b are all under 1%. Thus, we feel that use of the modified D-S method will lead to a more accurate determination of the mode radius of the aerosol size distribution. Similarly, although the errors in the retrieved values of a are larger than the errors in b, they nevertheless represent a significant improvement over the large errors in the original retrieval (Table 2.10). We therefore feel confident in recommending this method for more accurate retrievals of aerosol size distribution from solar aureole data.

(v) *Concluding Remarks*

So far, the simulated almucantar radiance data that we have studied have been generated by only one set of aerosol parameters for refractive index and size distribution. Also, ozone absorption and experimental errors have been ignored. Until a larger data base has been examined, we are unable to draw any absolute conclusions. However, the results presented so far give us considerable confidence in stating that use of the modified Deirmendjian-Sekera technique leads to more accurate inversion of aureole data than performed by using the single scattering approximation or the M-G approximation. This holds true especially for larger optical thicknesses. Further study needs to be performed in extending the modified D-S method for larger optical depths and more realistic experimental situations.

2.5 EXPERIMENTAL VALIDATION OF THE SOLAR AUREOLE TECHNIQUE

In this section, we intercompare the retrieved results for the columnar size distribution of aerosols obtained by inverting the multispectral (400, 500, and 600 nm), multiangle (3^o to 15^o) measurements of almucantar radiance made on May 6, 1977, at Tucson, Arizona, and the ground truth measurements (Ref. 50,51) obtained by two optical sizing counters. In the following sections, we shall briefly recapitulate the inversion formulations for the SS and MS approximations, and discuss the results of retrievals in the two approximations using different size distribution models. It is shown that size distributions retrieved by using our MS approximation are more accurate than those obtained by the SS approximation by comparing them with ground truth measurements of size distributions, in order to validate that the solar technique is a viable, simple and accurate method for determining the columnar aerosol size distribution.

In Section 2.3, we compared the relative contributions of MS and SS to the solar aureole almucantar radiance (SAAR) distribution--MS values having been generated by a computer code based on our Gauss-Seidel iterative approach to the solution of the radiative transfer equation. One important result that emerged was that for scattering angles ψ within 10^o from the sun, the MS plus the SS contributions to almucantar radiance exceed the SS contributions by a small constant factor. It was also shown that under ordinary sky conditions, the MS contribution due to molecules is much greater than that due to aerosols, so that one can use an MS approximation to the radiative transfer by including contributions due to SS by aerosols and molecules and MS by molecules alone; while ignoring MS events in which aerosols are involved.

2.5.1 SS and MS Approximations

(i) In the SS Approximation. The SS radiance L_T^{SS} in the almucantar is given by:

$$L_{SS} = (H_o/\mu_o)\ \exp(-\tau/\mu_o)\,[F_{MC}(\psi) + F_{PC}(\psi,\lambda)] \tag{69}$$

where

$$F_{PC}(\psi) = \frac{1}{2k^2} \int_0^{\infty} \int_{r_1}^{r_2} \eta(r,y)\ (i_1 + i_2)\ dr\ dy$$

$$= \frac{1}{2k^2} \int_{r_1}^{r_2} N_C(r)\ (i_1 + i_2)\ dr \qquad (70)$$

and

$$F_{MC}(\psi) = \tau_M P_M(\psi) \qquad (71)$$

where $\eta(r,y)$ is the aerosol altitude-size distribution ($cm^{-3}\ \mu m^{-1}$); y is the altitude (km); N_C is the columnar size distribution ($cm^{-2}\ \mu m^{-1}$),

Thus, we can obtain the data for the columnar particulate scattering function $F_{PC}(\psi)$ in the SS approximation by replacing L_{SS} in Eq. (1) by the actual radiance measurements, $L(\psi,\lambda)$, rearranging:

$$F_{PC}^{SS}(\psi) = L \exp(\tau/\mu_o)\ \ \mu_o/\Phi_o - F_{MC}(\psi) \qquad (72)$$

(ii) <u>*In the MS Approximation*</u>. In our MS approximation, the MS effect for a nonzero ground albedo A is taken into account in the total almucantar radiance field by replacing $(F_{MC} + F_{PC})$ in Eq. (69) by an effective columnar total scattering function $F_{ECT}(\psi)$, such that

$$L_{MS} = (H_o/\mu_o) \exp(-\tau/\mu_o)\ F_{ECT}(\psi) \qquad (73)$$

where

$$F_{ECT}(\psi) = \left[(\tau_{MS} + \tau_M)\ P_M(\psi) + \tau_{PS} P_P(\psi) + \tau_A P_M(0^o)\right] \qquad (74)$$

In our MS approximation, particulate scattering is treated as a small perturbation over the molecular scattering. Here, τ_{MS} and τ_A are the correction (optical depth) terms due to MS and surface albedo A, respectively; τ_{PS} is the optical depth due to particulate scattering, as opposed to particulate absorption; $\tau_{PS}P_P = F_{PC}$; $\bar{\omega}$, the SS albedo (averaged); and $\mu = \cos \phi$.

The expressions for τ_{MS} and τ_A are given as follows (Ref. 27)

$$\tau_{MS} (\equiv \tau_1) = 0.02\ \tau_{SS} + 1.2\ \tau_{SS}^2/\mu^{1/4} \tag{77}$$

$$\tau_A = A\ \tau_2(\tau_{SS}, \mu_o)/\{1 - A\ \tau_3(\tau_{SS})\} \tag{78}$$

$$\tau_{SS} = \omega\ \tau = \tau_M + \tau_{PS} \tag{79}$$

$$\tau_2 = 1.34\ \tau_{SS}\ \mu_o\{1.0 + 0.22(\tau_{SS}/\mu_o)^2\} \tag{80}$$

$$\tau_3 = 0.9\ \tau_{SS} - 0.92\ \tau_{SS}^2 + 0.54\ \tau_{SS}^3 \tag{81}$$

Equations (69) and (73) differ in only one point: the MS contributions due to molecules. Note that Eq. (5) is structurally identical to Eq. (69), and can therefore be rearranged to obtain the columnar aerosol size distribution $N_C(r)$ [$cm^{-2}\ \mu m^{-1}$], in the same manner as in the SS approximation.

In the MS approximation, we can obtain the experimental data for the columnar scattering function by replacing L_{MS} in Eq. (73) by the experimental L data and rearranging to get

$$F_{PC}^{MS}(\psi) = L \exp(\tau/\mu_o)\ (\mu_o/H_o) - \{(\ _{MS} + \ _M)\ P_M(\psi) + \ _A P_N(0^o)\} \tag{82}$$

It is from the experimental data for F_{PC}^{SS} or F_{PC}^{MS}, obtained as a function of scattering angle ψ and wavelength λ, that we retrieve the columnar size distributions $N_C(r)$ in the SS and MS approximations. The coefficients i_1 and i_2 were calculated using J. V. Dave's (Ref. 52) computer code. The retrievals are performed using the nonlinear least squares (NLLS) method. (The theory of NLLS inversion method is described in Refs. 53 and 54.)

In view of the fact that the parameters τ_{MS} and τ_A both involve the particulate optical depth, τ_{PS}, which is usually not known with sufficient accuracy, Eq. (12) cannot, in general, be used as it stands. Instead, we may define a new function $G(\psi)$ by

$$G(\psi) = L \exp(\tau/\mu_o) \cdot (\mu_o/H_o) - {}_M P_M (\psi) \tag{83}$$

In the SS approximation, of course,

$$F_{PC}^{SS} (\psi) = G (\psi) \tag{84}$$

whereas in the MS approximation

$$F_{PC}^{MS} (\psi) + \tau_{MS} P_M (\psi) + \tau_A P_M (0^o) = G (\psi) \tag{85}$$

Thus, in this approximation, the integral equation we must solve is

$$G(\psi) = \frac{1}{2k^2} \int_{r_1}^{r_2} (i_1 + i_2) N_C(r) dr + \tau_{MS} P_M(\psi) + \tau_A P_M(0^o) \tag{86}$$

As well as N_C both τ_{MS} and τ_A must now be considered (at least partially) as unknowns, via their dependence on τ_{PS}.

The NLLS inversion procedure involves assuming an analytical model for N_C (see below), with a number of adjustable parameters, which are iterated until a "best fit" to the data is obtained. One consequence of the structure of Eq. (86) is that the "scaling parameter" is no longer an overall multiplicative constant.

2.5.2 Size Distribution Models for $N_C(r)$

A number of different analytic size distribution models were used during the course of this analysis. In this paper, however, we will report results for only one of these. This model has two terms (to allow for bimodality), both of which are modified gamma distributions (refs. 45, 40) of haze M type:

$$N_C(r) = p_1 p_5 r \{\exp(-p_2 \sqrt{r}) + p_3 \exp(-p_4 \sqrt{r})\} \quad (87)$$

A word needs to be said about the apparently superfluous parameter p_5. As indicated above, data were obtained at three different wavelengths, 400, 500 and 600 nm. Unfortunately, due to a problem with the neutral density filter at 400 nm, the calibration of this data set was somewhat uncertain. The parameter p_5 was defined to be 1.0 for the 500 and 600 nm data, but permitted to vary for the 400 nm data.

2.5.3 Retrievals in the SS Approximation

A total of five sets of results will be presented in this paper: test runs S3 (data for all three wavelengths inverted using the SS approximation), M3 (data for all three wavelengths inverted using our MS approximation,) M3A (as for M3, but with the ground albedo treated as a free parameter - p_6), S2 (data for 500 and 600 nm only, inverted using the SS approximation) and M2 (data for 500 and 600 nm, inverted using our MS approximation). The S2 and M2 runs were an attempt to circumvent the calibration problem at 400 nm; however, they also served the purpose of checking to see how the results obtained by use of the 2 wavelength data compared with those obtained by the use of the 3 wavelength data.

In the retrievals presented here, the multiplicative factor for 400 nm (p_5) was held fixed. Attempts to vary this parameter along with the others were not successful. A better approach proved to be to use the best estimate available for this parameter, update the parameter in the light of inversion results, and rerun the inversion program. Generally it was found that the F_{PC} data for 400 nm was consistently too high or too low by some factor so that the 400 nm scaling factor was updated by this multiplicative factor.

Because of the slight changes in the model which were necessary to account for the differences in scale between the 400 nm, 500 nm and 600 nm data, inversions were performed using both the SS and MS approximations. This ensured the validity of comparisons between SS and MS retrievals. The retrieved parameters and the statistics of the retrievals for the various test runs are summarized in Tables 2.13 and 2.14, respectively.

TABLE 2.13. Summary of the Different Test Runs for Size Distribution Retrievals using the NLLS Code and Mie Theory Results

Test run	RT approx imation	Data	Itera-tions	Retrieved Parameters						Mode radius r_m		Figures	
				$p_1 \pm \Delta p_1$	$p_2 \pm \Delta p_2$	$p_3 \pm \Delta p_3$	$p_4 \pm \Delta p_4$	$p_5 \pm \Delta p_5$	$p_6 \pm \Delta p_6$	mode	mode	F_p	$n(r)$
S3	SS	3-λ	20	4.100(+3)* ±265.00	16.700 ±0.112	7.496(-6) ±0.363	4.660 ±0.285	0.463 (fixed)		0.014	0.184	1	4
M3 (albedo fixed)	MS	3-λ	3	1.856(+3) ±192.00	16.000 ±0.219	2.868(-5) ±1.927(-5)	4.950 ±0.406	0.452 (fixed)	0.250 (fixed)	0.016	0.163	2	4
M3A (albedo varied)	MS	3-λ	6	1.890(+3) ±129.00	15.800 ±0.292	4.040(-5) ±1.884(-5)	5.140 ±0.287	0.400 (fixed)	-0.196 ±0.336	0.016	0.151	3	
S2	SS	2-λ	20	7.779(+3) ±23.42	17.900 ±5.44	1.124(-5) ±2.919	5.34 ±0.820			0.012	0.146	5	4
M2	MS	2-λ	20	7.103 ±25.530	18.000 ±6.510	1.254(-5) ±3.979(-5)	4.350 ±0.852		0.200 (fixed)	0.012	0.140	6	4

*Arguments in parentheses denote powers of 10.

TABLE 2.14. Summary of the Statistics for Fits to Experimental Data

Run No.	Test run	Wavelength (nm)	Standard Deviation σ		% Fit	
			Individual	Total	Individual	Total
1	S3	400	0.02470		93.31	
		500	0.03100		98.44	
		600	0.02590			
				0.0202		98.48
2	M3	400	0.04750		75.80	
		500	0.04350		96.96	
		600	0.02500		98.94	
				0.0295		96.63
3	M3A	400	0.02800		95.83	
		500	0.03140		98.81	
		600	0.02710		99.05	
				0.0180		99.05
4	S2	500	0.09530		94.30	
		600	0.06625		92.56	
				0.0494		93.20
5	M2	500	0.06480		93.26	
		600	0.07020		91.65	
				0.0530		92.66

(i) Test Runs (S3, M3 and M3A) Using Three-Wavelength Data:

The fits to the F_{PC} data for 400 nm and 500 nm using the SS approximation (Run S3) were good (Fig. 2.17). The fits for 600 nm (Fig. 2.17) were not good, although the final estimate is a definite improvement on the initial estimate. The final estimate is far too high at large scattering angles.

The first of the MS runs to be discussed is the one with albedo fixed at 0.25 (Run M3). The shape of the 400 nm (Fig. 2.18) scattering function is good, although the actual values are consistently too high. The multiplicative factor used for this data was 0.452 and the results obtained here suggest that 0.40 would have been a better value.

The fit to the F_{PC}^{MS} nm data (Fig. 2.18) was not as good as in the SS case (Fig. 2.17), the calculated F_{PC} values being too low for most scattering angles. The fit to the 600 nm data (Fig. 2.18), on the other hand, is very good and is a marked improvement over the SS approximation (Fig. 2.17).

In the test run M3A, the albedo parameter (p_6) was allowed to vary, and the multiplicative factor (p_5) for the 400 nm data was set at 0.4 on the basis of the results of the M3. The fit to the F_{PC}^{MS} 400 nm data (Fig. 2.19) was very good. For 500 nm (Fig. 2.19), there was a slight improvement over the run M3 although the calculated values at large scattering angles are still too low. For 600 nm (Fig. 2.19), there was a definite improvement over the SS case, but the fit was not as good as for the case (M3) when the albedo was held fixed. When the albedo was allowed to vary the calculated values at large scattering angles were much lower than measurements. The parameters retrieved for the above inversions are given in Table 2.13), and the corresponding statistics of the fits to the data, in Table 14. The parameters for the two MS approximation runs are very similar, but differ a little from those for the SS approximation, especially for the first mode of the size distribution.

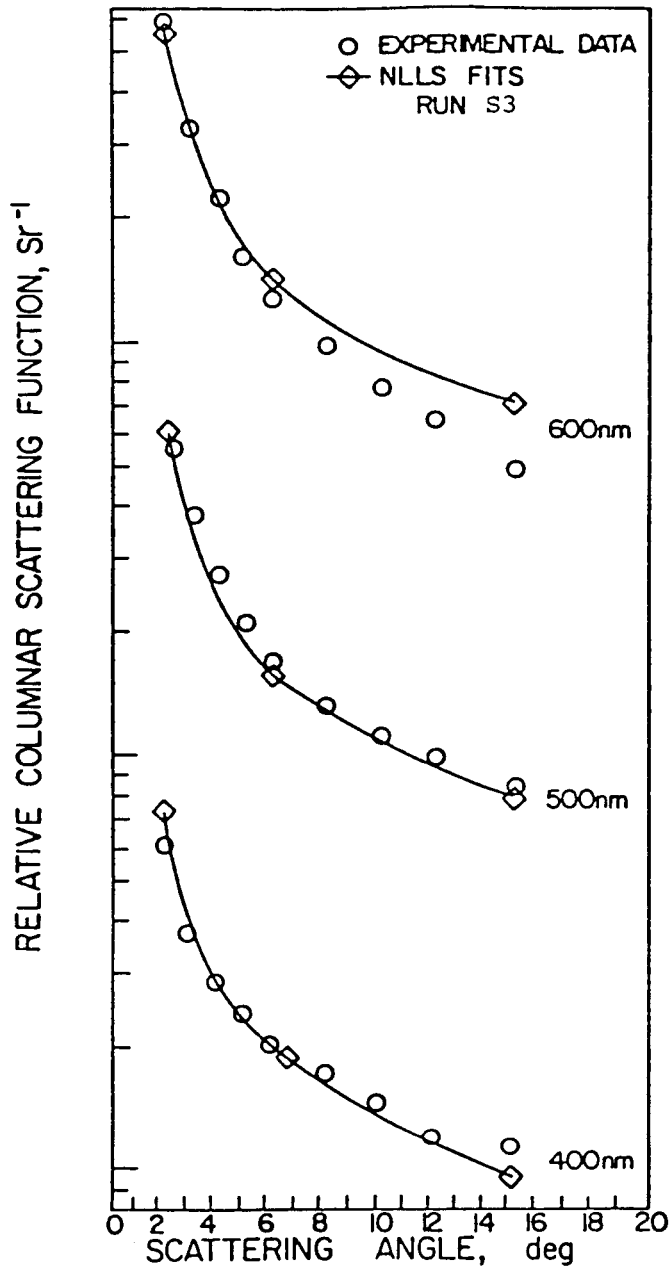

FIGURE 2.17. NLLS fits to F_{PC} versus ψ data for run S3.

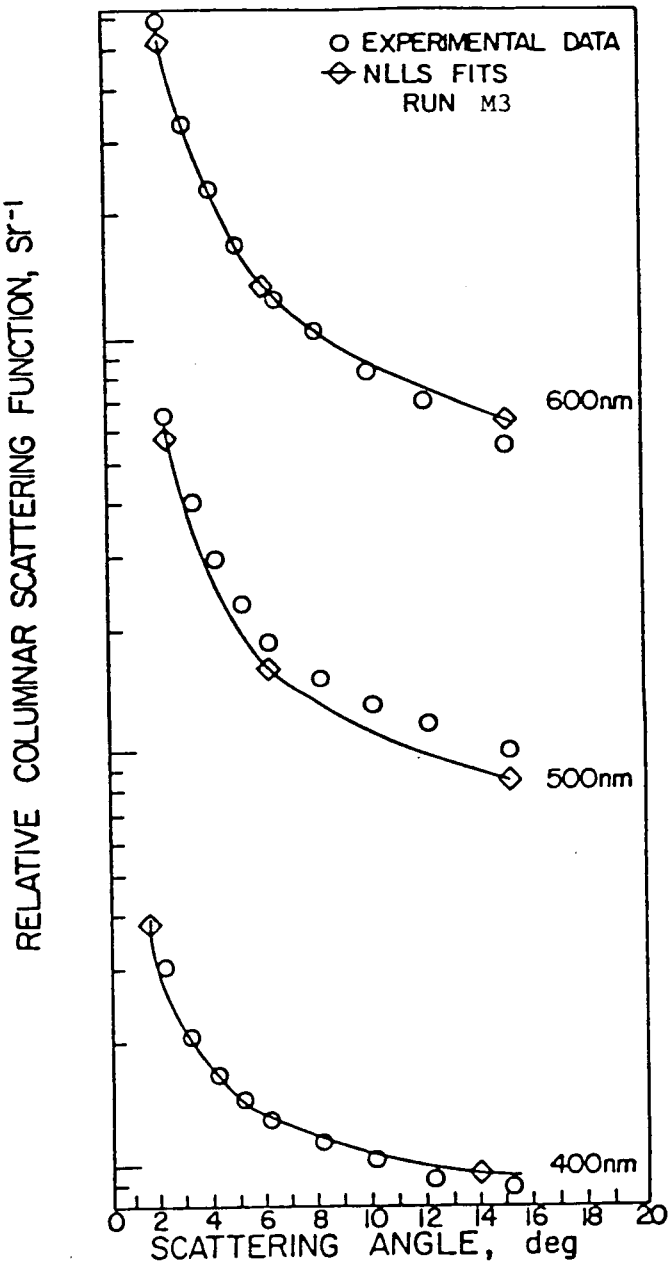

FIGURE 2.18. NLLS fits to F_{PC} versus ψ data for run M3, with A = 0.25 (fi

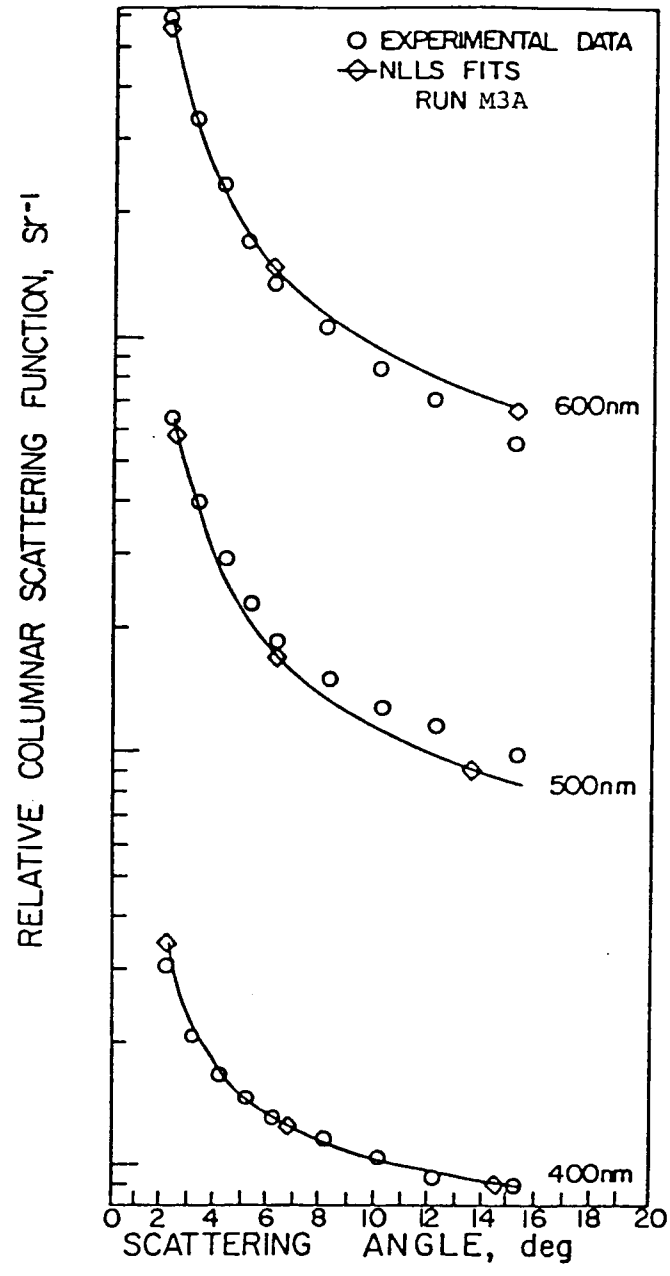

FIGURE 2.19. NLLS fits to F_{PC} versus ψ data for run M3A.

The significance of the negative albedo retrieval is not clear but the results from other runs in which the albedo was allowed to vary suggest that it may not always be possible to retrieve the albedo from the solar aureole measurements. Instead, it is suggested that for inversion work, the albedo be held fixed, and several different values tried to determine which gives the best results. With the data considered here it was found that the same results were obtained when albedos of 0.20 and 0.25 were used.

Comparison of the size distributions for the SS and MS approximations (Fig. 2.20) shows that they are identical, except for the radii range $r < 0.2$ μm, for which it shows that $N_C(r)$ has higher values for the SS case then for the MS case. These differences for low radii are due to the MS corrections and are reflected in the differences between the parameters for the two approximations for the first mode. The retrieved size distributions agree very well with the ground truth measurements for May 7, 1977, obtained by Whitby and Royco counters, as shown in Fig. 2.20.

As shown in Table 2.13, the mode radii for the two modes are very similar for the three inversion runs discussed above. From Table 2.14 it can be seen that the standard deviations for the fits to the F_{PC} data for the SS case (S3) tend to be slightly lower than for the MS case, but the only case in which this is statistically significant at the 90% level of confidence is when the overall fit for the MS case (M3), with the albedo fixed, is compared with the SS case.

In general, it seems that applying the MS corrections does result in an overall improvement in the fit to the F_{PC} data. It is sometimes a compromise in that a marked improvement for one wavelength over the SS results may be accompanied by a poorer fit at another wavelength.

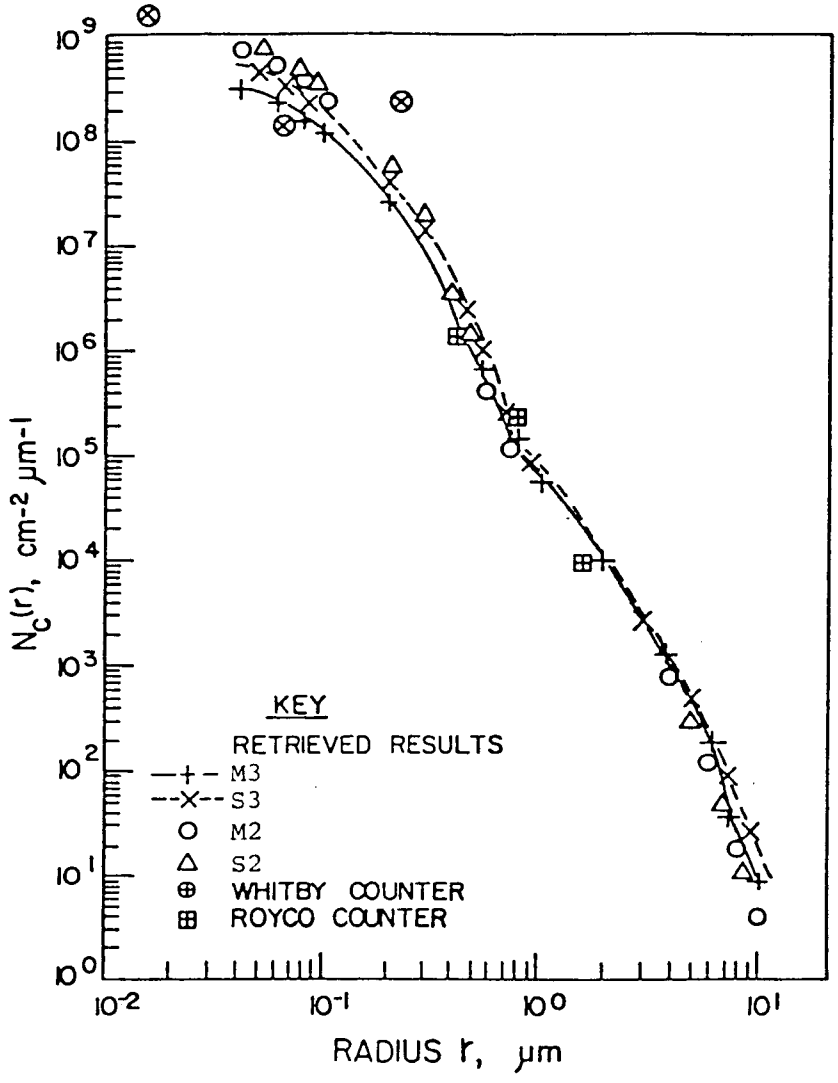

FIGURE 2.20. Measured $N_C(r)$ and retrieved $N_C(r)$ for runs M3, S3, M2, and S2.

(ii) Test Runs S2 and M2 using Two-Wavelength Data:

Here, data for only 500 nm and 600 nm wavelengths were inverted. These inversions were done to determine whether or not the inclusion of the 400 nm data, with its calibration problem, was having any effect on the inversions. Using the SS approximation in Run S2, good fits to the F_{PC} data at 500 nm (Fig. 2.21) were obtained, but the calculated values for 600 nm (Fig. 2.21) were too high at large scattering angles.

Using the MS approximation in Run M2, in which an albedo of 0.20 was used, the fit to the F_{PC} data at 500 nm (Fig. 2.22) obtained was good, whereas for 600 nm (Fig. 2.22), the calculated values were still too high but were better than those for the SS approximation.

Table 2.13 shows that the parameters for the test runs S2 and M2 are essentially the same but the errors are high, especially for p_1 and P_3 which are multiplicative scaling factors. Comparison with S3, M3, and M3A results shows that the percentage errors are much higher when data for only two, instead of three, wavelengths were inverted simultaneously.

It should be noted that neither of the inversions discussed above had reached convergence even after 20 iterations. However, differences between the variances for successive iterations were constant after the 10th or 12th iteration, and the percentage errors in the parameters did not change after this stage either, so it is unlikely that convergence would be obtained with more iterations. Probably, the convergence criteria were too stringent. This problem has been encountered on other occasions and suggests that some improved convergence criteria might be required; work on the solution of this problem is in progress.

The statistics for the S2 and M2 retrievals are given in Table 2.14. As in the three wavelength case, there is no significant difference between the standard deviation of the residuals for the SS approximation and that for the MS approximation.

The two size distributions retrieved by the SS and MS approximations (Fig. 2.20) are almost identical. There is no difference

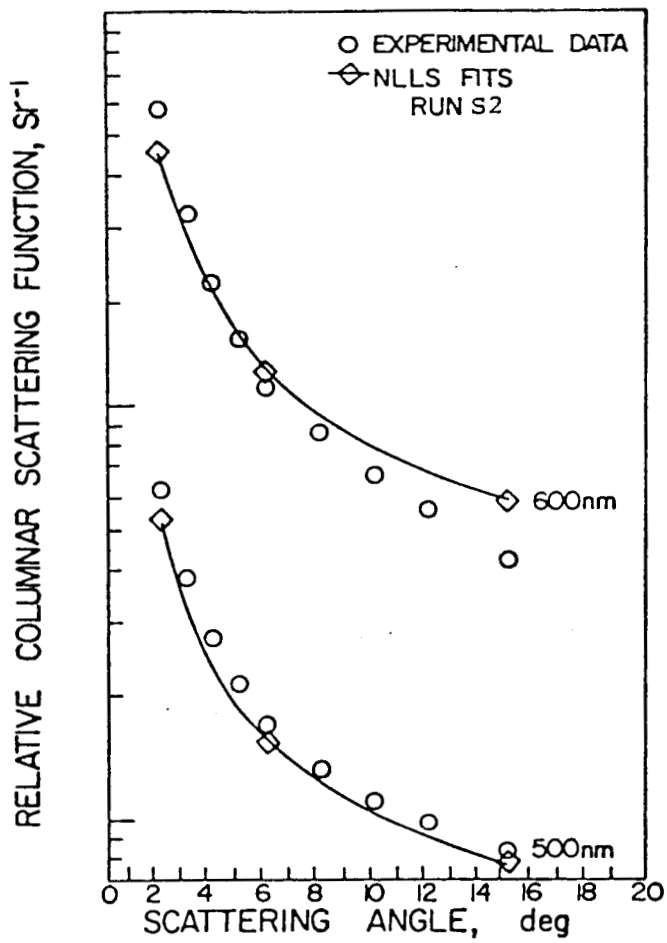

FIGURE 2.21. NLLS fits to F_{PC} versus ψ data for S2.

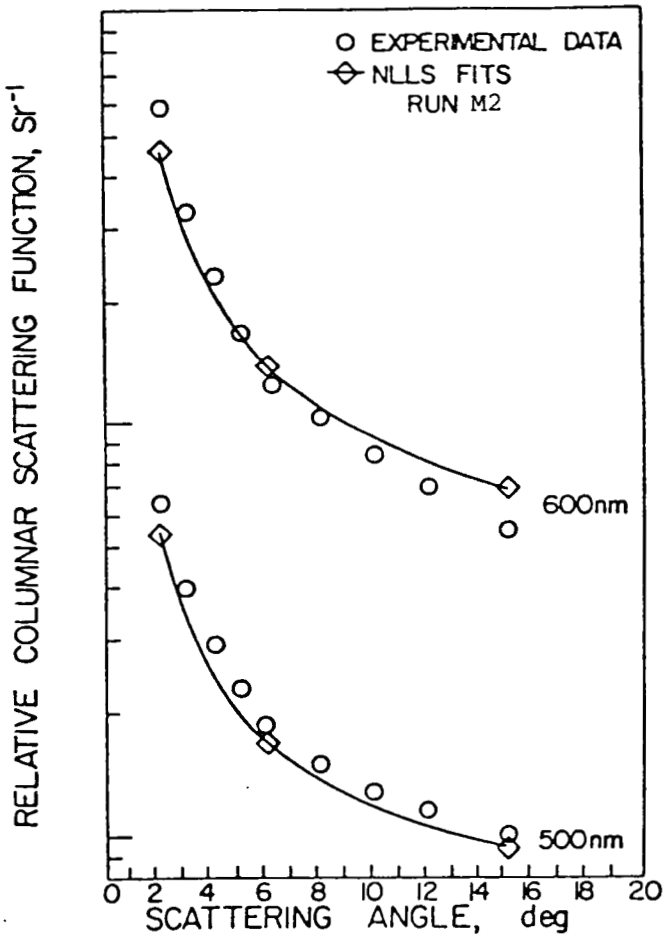

FIGURE 2.22. NLLS fits to F_{PC} versus ψ data for run M2 with A = 0.2 (fix

between the two size distributions at small radii.

The size distributions obtained by using only the two wavelength data simultaneously are very similar to those obtained using three wavelength data, and agree with the ground truth data for May 7, 1977. Comparison of the results obtained in the two cases suggests that although good results can be obtained by using only two wavelength data, the addition of data for another wavelength should result in faster convergence and smaller uncertainties in the retrieved parameters.

2.5.3 Concluding Remarks

(i) Improvement in retrievals by using simultaneous inversion of 3-λ instead of 2-λ data.

The work done using the SS approximation showed that even though better fits to the columnar scattering function data were obtained by inverting the data for each wavelength individually, as in Ref. 28, than by inverting data for the three- or two-wavelengths simultaneously, they usually yield slightly different size distributions, one for each data set. On the other hand, simultaneous inversion of data for all the wavelengths, results in a single size distribution, that which gives the best fit to all the data in the least squares sense.

The use of MS corrections did result in an overall improvement in agreement between measurements and final estimates of $F_{PC}(\psi,\lambda)$. In some instances, a marked improvement in the agreement between measurements and calculations for one wavelength in the MS case over that in the SS case was accompanied by a poorer fit at another wavelength. This is probably because of the different size distributions for each of the wavelengths. The compromise obtained in the MS case gives a reasonably good fit to F_{PC} data for all wavelengths rather than good fits for two wavelengths and a bad fit for the third as obtained often in the SS case.

The uncertainties in the parameter estimates were not improved by the use of MS corrections. The percentage errors in the retrieved

parameters were much the same for all the results presented here, except when data for only two wavelengths was considered, in which case they were slightly increased.

Comparison of the results obtained for both the two- and three-wavelength data sets, suggests that the extra wavelength in the latter case does lead to more rapid convergence and lower uncertainty in the parameters. Further work, however, is needed to confirm this result.

(ii) Suitability of the two-term bimodal model for $N_C(r)$.

The results presented here suggest that Model for $N_C(r)$ is a suitable mo for representing aerosol size distributions. The model gave good fits to the F_{PC} data and the retrieved size distributions agree rather well with the ground truth data. It should be pointed out that the ground truth measurements were for May 7, whereas the retrieved results were for May 6. Here the assumption that there was no significant change in the aerosol size distribution between May 6 and May 7, appears to be consistent with conditions of clear sky prevailing during those two days.

(iii) Difficulty in retrieving surface albedo from solar aureole data.

The poor results obtained for the albedo, when it was treated as an adjustable variable, suggest that it may not always be possible to get good estimates for the albedo by inversion of the solar aureole data. However, it does appear that a reasonable fix on the albedo could be obtained by trying several different estimates of A, and selecting the final retrieved A value which gives the best fit to the F_{PC} data.

(iv) Validation of the solar aureole method.

Thus, in spite of the fact that work still needs to be done in further improving the accuracy of retrievals, we have been able to

show that the solar aureole technique is a simple, practical, and accurate method for determining atmospheric aerosol size distributions. One concludes, therefore, that measurements of angular distribution of forward scattered (aureole) radiation - at one or more wavelengths - provide an accurate means of obtaining the columnar size distributions of atmospheric aerosols. Since the solar aureole measurements were ground-based, the columnar size distributions obtained were essentially those of tropospheric aerosols, as they constitute the bulk of atmospheric aerosols.

(v) Recommendation for using satellite-based solar aureole technique.

Inasmuch as the objective of this work was to develop a viable simple and accurate technique for measuring the average size distribution of atmospheric aerosols from solar aureole measurements, this effort was part of a research program, under NASA support, to develop a satellite-based technique for measuring aerosol size distributions and concentrations from multispectral measurements of scattered radiance of the sunlit atmosphere in both the horizon-viewing or downward-viewing modes, with the sun in any known position with respect to the satellite. An obvious question, therefore, arises, namely, can we use the forward scattering technique for satellite-based measurements of size distribution of atmospheric aerosols -- especially stratospheric — on a global basis? The answer is decidedly yes. Forward scattered limb radiance would then be those that are made close to the sun during the satellite sunrise or sunset events. It should be pointed out that retrievals of aerosol size distribution from scattered radiance can be achieved with the sun in any angular position with respect to the satellite but the forward scattered radiance measurements provide the most accurate size distribution retrievals.

(a) Advantages of satellite-based scattered radiance technique.
Following are some of the advantages of the scattered radiance technique:

(1) No restrictions are placed on the sun's location, so that continuous or intermittent measurements can be made of the aerosol size distribution during the entire sunlit portion of the orbit, which will shed information on the temporal behavior of stratospheric aerosols and their sources and sinks. However, the most accurate informatic about aerosol size distributions, we believe would be obtained from forward scattered (aureole) limb radiance measurements when the sun's disk is close to the horizon.

(2) Because of the measurements of angular distribution of the scattered radiance, it will be possible to make accurate retrievals of aerosol size distribution, which are presently not available on a global basis.

(3) In addition, by making polarization measurements of scattered radiance, it should be possible to retrieve the aerosol refractive index, which is sensitive to polarization.

(b) Inversion codes for satellite-based radiance measurements. The computer codes needed for inverting the scattered radiance measurements have been developed over the last six years under NASA support (Refs. 20 and 21) for retrieving profiles of the size distribution, concentration, and total loading of aerosols from simulated satellite-based multi-spectral scattered radiance measurements. Also, the technology for making scattered radiance measurements exists, as evidenced by the highly successful measurements of the direct solar radiation made by the SAM, SAM II, and SAGE radiometers during satellite sunset/sunrise events (Ref. 22). The one thing that is lacking is a set of well-defined, calibrated, multispectral, satellite measurements of scattered radiance.

It is, therefore, strongly recommended that forward scattered (solar aureole) multispectral measurements be performed with the help of satellite-based radiometers and photographic cameras to obtain vertical profiles of the size distribution, in addition to the concentration, of atmospheric aerosols.

SECTION 3

MULTISPECTRAL SOLAR EXTINCTION MEASUREMENTS TO DETERMINE AEROSOL CHARACTERISTICS

In a recent paper, Box and Lo (Ref. 57) first proposed the use of an approximate method for the fast retrieval of aerosol size distributions from multispectral optical depth measurements. The method has subsequently been used by Russell et al. (Ref. 58) for on-line data analysis. The motivation behind the work reported in this paper was twofold--one to determine the sensitivity of the approximate method to the differences in the two sets of wavelengths (one used for measurements, and the other for computing the data base of optical depth values); and two, to determine the accuracy of size distribution results obtained by the use of the approximate method by comparing the retrievals with those obtained by a numerical nonlinear least squares (NLLS) method. The development of fast retrieval algorithms is of great importance to the efficient handling of large quantities of optical depth data. In this paper, we discuss the results of applying the two retrieval methods--the approximate and the NLLS--to multispectral aerosol optical depth data to retrieve the aerosol columnar size distribution.

(i) Multispectral solar extinction measurements

The solar extinction measurements were made with the help of a multispectral solar radiometer during the University of Arizona's Aerosol and Radiation Experiment (UA-ARE), May 6-19, 1977 (Ref. 51) The total optical depths $\tau_T(\lambda)$ were obtained for seven wavelengths given in Set No. 3 in Table 3.1, by the Langley plot method for 8 days

TABLE 3.1. Wavelength Filter Sets (Nos. 1, 2, and 3)

Wavelength set no.	Wavelengths λ (μm)
1	0.3 (0.05) 0.8
2	0.387, 0.501, 0.590, 0.677, 0.849, 1.060, 1.228
3	0.44, 0.5217, 0.5556, 0.6120, 0.6708, 0.7797, 0.8717

during May 6-19, 1977. The scattering optical depth $\tau_M(\lambda)$ for the molecular atmosphere was obtained with the help of tables and surface pressure measurements; and $\tau_{O_3}(\lambda)$, that for ozone absorption was computed by the King and Byrne (Ref. 49) method. Then the particulate optical depth $\tau_p(\lambda)$ can be obtained from the relation

$$\tau_p(\lambda) = \tau_T(\lambda) - [\tau_M(\lambda) + \tau_{O_3}(\lambda)] \tag{1}$$

Eight sets of data for $\tau_p(\lambda)$, shown in Table 3.2 were provided to us by Professor John Reagan, University of Arizona. The aerosol optical depth $\tau_p(\lambda)$ is related to the altitude-size distribution $\eta(r,z)$ [cm^{-3} μm^{-1}] and the columnar size distribution $N_C(r)$ [cm^{-2} μm^{-1}] by the following relations

$$\tau_p(\lambda) = \int_0^\infty \sigma_p(\lambda,z)\, dz$$

$$= \int_0^\infty \int_0^\infty \pi r^2\, Q_{EXT}(x,m)\, \eta(r,z)\, dr\, dz$$

$$= \int_0^\infty \pi r^2\, Q_{EXT}(x,m)\, N_C(r)\, dr \tag{2}$$

TABLE 3.2. Optical Depth Measurements Obtained with Wavelength Set No. 3 (Table 3.1)

Observation Sets	Dates in 1977	Optical Depth τ_p Measurement						
	λ (μm)	0.4400	0.5217	0.5556	0.6120	0.6708	0.7797	0.8717
I	5/6	0.0308	0.0367	0.0353	0.0354	0.0341	0.0375	0.0372
II	5/7	0.0852	0.0756	0.0676	0.0649	0.0629	0.0613	0.0648
III	5/10	0.0362	0.0375	0.0388	0.0341	0.0355		0.0351
IV	5/14	0.0734	0.0556	0.0503	0.0433	0.0386	0.0375	0.0380
V	5/15	0.0360	0.0389	0.0390	0.0370	0.0373	0.0331	0.0351
VI	5/17	0.1042	0.0835	0.0813	0.0747	0.0699	0.0659	0.0612
VII	5/18	0.0603	0.0527	0.0507	0.0490	0.0459	0.0425	0.0364
VIII	5/19	0.0850	0.0829	0.0687	0.0728	0.0658	0.0683	0.0577

where Q_{EXT} is the extinction efficiency factor, $x = 2\pi r/\lambda$ is the size parameter, λ is the radiation wavelength, r is the particle radius (μm), z is the altitude (km), σ_p is the particulate volume extinction coefficient (km^{-1}) at altitude z, and m is the complex aerosol refractive index.

Next we shall discuss the retrieval of the columnar aerosol size distribution $N_C(r)$ from the seven channel $\tau_p(\lambda)$ data, by the use of the approximate and NLLS methods.

(ii) Retrieval of the size distribution from $\tau_p(\lambda)$ data

In both the retrieval techniques--the approximate and the NLLS--one assumes that the general characteristics of the atmospheric aerosol size distribution can be represented by an analytic model. Eight such analytic models, that have often appeared in literature, have been discussed in Ref. 46. The analytic model selected for this work is the popular Deirmendjian modified gamma (Haze H) distribution, which is written as

$$N_C(r) = \frac{1}{2} p_1 p_2^3 r^2 e^{-p_2 r} \quad (cm^{-2} \mu m^{-1}) \tag{3}$$

with p_1 and p_2 as the two adjustable parameters. The mode radius of the size distribution is $r_m = 2/p_2$ and concentration of particles is equal to p_1. $N_C(r)$ is related to $\tau_p(\lambda)$ by Eq. (2). It is assumed that the aerosol refractive index is m = 1.5 - i(0) and remains esentially constant for the near UV, visible and near IR wavelengths being considered in this paper.

The two retrieval methods and their results are briefly described as follows.

A. Approximate Method. The approximate method of Box and Lo is essentially a table look-up method, with a difference. The table is constructed by calculating τ_p at each selected wavelength, and then approximating this data set with a power fit, i.e.,

$$\tau(\lambda) \simeq \beta(\lambda/\lambda_o)^{-\alpha} \quad , \quad \lambda_o = 1 \ \mu m \tag{4}$$

p_1 is merely a scaling parameter, which we set to unity, and then allow p_2 to vary over a suitable range of values. Thus $\alpha = \alpha(p_2)$, $\beta = \beta(p_2)$. A different table is produced for each refractive index of interest. (Note that we could also have used an exponential function in place of the power law of Eq. (4), but have chosen the power law form because of its universal acceptance.) Note that, since we only extract two parameters from the data, we are only able to infer two parameters of the size distribution. Thus, we have selected a two-parameter model--Haze H (Ref. 57).

When a set of experimental data is obtained, it is approximated by the power law form, Eq. (4), and the experimental α and β values obtained. From the tabulated values of α, the optimum value of p_2 is extracted. Next the value of β for that value of p_2 is obtained from its table. Finally, the value of p_1 is obtained from the relation (Ref. 57).

$$p_1 = \beta(\text{experiment}) \ / \ \beta(p_2) \tag{5}$$

In Fig. 3.1, we plot α vs p_2 for the three wavelength sets of Table 3.1, and for a refractive index of m = 1.5 - i0.0. Such graphs

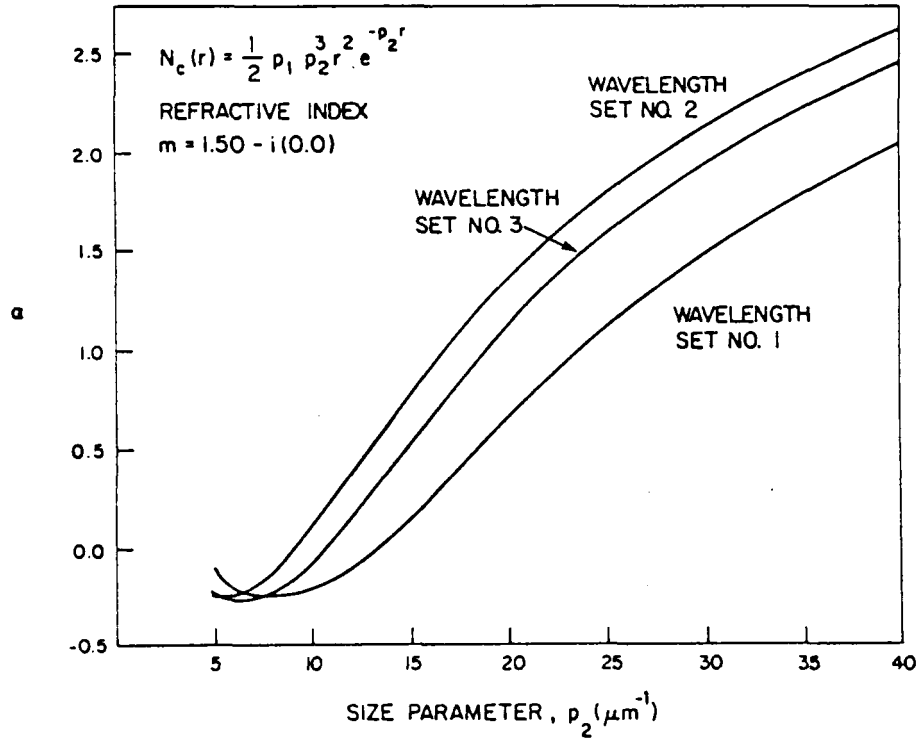

FIG. 3.1. Plots of α as a function of p_2 for the three wavelength sets.

are suitable for hand analysis: for automatic analysis (e.g., Ref. 58), a tabular form is required. In this plot, set no. 1 corresponds to Box and Lo's original wavelength set, set no. 2 corresponds to the wavelengths used in the work of Russell et al (Ref. 58) and set no. 3 corresponds to the wavelengths used in UA-ARE experiment (see Table 3.1).

B. Nonlinear Least Squares (NLLS) Method. The nonlinear least squares (NLLS) method assumes a suitable analytic form for $N_c(r)$, with a number of undetermined parameters, p, and attempts to find that set of parameters which minimizes the sum of squares of the differences between the observed and calculated τ_p values. In order to compare these results with those

from the approximate method, we have assumed the functional form of Eq. (3), with p_1 and p_2 as the parameters to be determined. Because τ_p is linear in p_1, leaving p_2 the only nonlinear parameter, it is always possible to find a global minimum.

Since the NLLS method is iterative, it is necessary to start with an initial guess for the unknown parameters: the NLLS code then provides successively better estimates of the optimum parameter set, along with their uncertainties and correlation coefficient (see Ref. 54). One suitable source of the initial guess is, of course, the approximate method of Box and Lo. However, with the simple functional form of Eq. (3) virtually any set of initial parameters will suffice: for a more complicated function, this may not be the case.

(iii) Results

In this paper, we analyze 8 data sets taken in Tucson, Arizona in May of 1977. These data sets are presented in Table 3.2, along with the resulting α and β values, and the correlation coefficient, C, (Table 3.3) which indicates the accuracy of the power-law fit. These data sets were analyzed using the tables generated by using the 3 wavelength sets of Table 3.1 (see Fig. 3.1), as well as using our NLLS code. The results are presented in Table 3.4.

If we assume that the answers corresponding to wavelength set 3 are "correct", then we see that the answers obtained from the other two wavelength sets show systematic errors. This, of course, is just what would be expected from an examination of Fig. 3.1, and confirms our suggestion that the approximate method can only return reliable results

TABLE 3.3. Values of α, Δα, β, Δβ and Correlation Coefficient C associated with the $\tau_p(\lambda)$ measurement sets in Table 3.2

Observation Sets	Dates in 1977	α	Δα	β	Δβ	C
I	5/6	-0.206	0.090	3.89(-2)*	0.18(-2)	0.718
II	5/7	0.421	0.119	5.60(-2)	0.35(-2)	0.844
III	5/10	-0.092	0.072	3.45(-2)	0.13(-2)	0.496
IV	5/14	0.980	0.176	2.93(-2)	0.27(-2)	0.928
V	5/15	-0.143	0.090	3.42(-2)	0.16(-2)	0.579
VI	5/17	0.732	0.071	5.38(-2)	0.20(-2)	0.977
VII	5/18	0.677	0.050	3.45(-2)	0.09(-2)	0.987
VIII	5/19	0.511	0.113	5.57(-2)	0.33(-2)	0.897

*Arguments in parenthesis denote powers of 10.

TABLE 3.4. Retrieved Results for (p_1,p_2) Obtained from τ_p vs. λ Measurements (Table 3.2) taken at Wavelength Set No. 3, by the Approximate Method using Look-up Tables 1, 2 and 3 Generated for Wavelength Set Nos. 1, 2 and 3 (Table 3.1), respectively, and by means of NLLS Program

Observation Sets*	Dates in 1977	Approximate Method Retrievals using Look-up Table No. 1		Look-up Table No. 2		Look-up Table No. 3			NLLS Retrievals			
		p_2 (μm^{-1})	$\pm\Delta p_2$ (μm^{-1})	p_2 (μm^{-1})	$\pm\Delta p_2$ (μm^{-1})	p_2 (μm^{-1})	$\pm\Delta p_2$ (μm^{-1})	p_1	p_2 (μm^{-1})	$\pm\Delta p_2$ (μm^{-1})	p_1	$\pm\Delta p_1$
I	5/6	10.1	1.5	6.6	1.0	8.7	1.0	8.00	8.8	1.1	8.45	5.0
II	5/7	17.6	1.5	12.3	0.8	14.2	0.9	183.46	14.6	1.7	212.00	133,0
III	5/10	13.1	1.0	9.0	0.7	10.0	0.7	14.60	11.5	0.8	32.40	11.4
IV	5/14	23.5	2.0	16.7	1.4	18.8	1.6	593.64	21.9	3.0	1553.00	1287.0
V	5/15	11.4	1.2	7.7	0.7	9.5	0.7	10.90	12.1	0.6	42.70	11.3
VI	5/17	20.8	0.8	14.7	0.5	16.7	0.5	507.23	17.7	1.6	696.00	358.0
VII	5/18	20.2	0.5	14.2	0.4	16.2	0.5	265.72	16.5	0.8	298.00	85.3
VIII	5/19	18.5	1.0	13.0	0.8	14.9	0.9	249.00	15.1	1.3	271.00	123.0

*For which optical depth τ_p measurements are shown in Table 3.2.

if the analysis table is constructed using essentially the same wavelengths as the ones used for measurements.

We now compare the results of the approximate method, using wavelength set 3, with the results from the NLLS method. For data sets I, II, VI, VII and VIII the agreement is good to very good. (Note that we have decided not to quote the uncertainties in p_1 as given by the approximate method, as these uncertainties compound rapidly, as discussed in Ref. 57.) For data sets III and IV the agreement is reasonable, while for data set V the agreement is only fair.

In order to understand the reason for the discrepancies we return to Table 3.3, and take note of the correlation coefficient C for the fits. For data sets III and V, these values are quite low, indicating that a power law fit to the data was not very satisfactory. For data set IV, although the correlation coefficient C is quite high, the uncertainty in the value of α is somewhat larger than usual. This is reflected in the large uncertainty in p_2 as produced by both methods.

It should be noted that in Ref. 59 plots are shown of columnar size distributions (i.e., $dN_C/d \log r$) retrievals for 3 of the 8 sets, namely, sets I, V, and VIII for May 6, 15 and 18, 1977, respectively. The plots appear to be bimodal, with the first mode for sets I and V having p_2 values of about 8.0 and 2.5, respectively. The set VIII plot is practically a straight line with a slight curvature and an inflexion point, indicating the presence of a mode. Comparison between our results and those of King, et al. shows that for set I the p_2 values agree reasonably well. For set II, the p_2 values differ by a factor of 4, our value being

the higher one. For set III, simular comparison of the p_2 values is not possible. One explanation for these discrepancies is that the approximate and the NLLS methods depend on the choice of an analytical model, such as Haze H, whereas King et al.(Ref. 59) employ a form of the constrained linear inversion approach proposed by Phillips (Ref. 60) and Twomey (Ref. 61). Discrepancies arising due to the use of different inversion approaches do not detract from the intent and the conclusions of this paper. Information about the Ref. 59 results are included here for the sake of completeness.

(iv) Conclusions

The results of this analysis make it clear that the results of the approximate method can only be considered reliable if the wavelengths used to construct the analysis table are the same as (or at least close to) the wavelengths at which the measurements are made. As the computational effort to construct such a table is quite small using a modern computer, this should not prove an impediment to the use of the approximate method.

When we compare the results of the approximate method, using wavelength set 3 (the "correct" set) with those from the NLLS method, we find that, in general, the two show good agreement. However, when the correlation coefficient of the power-law fit to the data drops, or the uncertainty in the computed value of α rises, we usually note a discrepancy between these two results. This is not altogether surprising, as it indicates that the Haze H model is almost certainly not an accurate description of the true aerosol size distribution.

Overall then, we may conclude that if an appropriate wavelength set is used to generate the analysis table, the approximate method is capable of producing reasonably accurate size distribution retrievals (mode radius to within 10% to 15%, for example), at least in those cases where the actual distribution is approximately of the Haze H form. An abnormally low value for the correlation coefficient of the power law fit to the data, or an abnormally large uncertainty in the experimental value of α (or β), are probably good indicators of cases where this model is not suitable.

SECTION 4

FORWARD SCATTERING CORRECTIONS TO AEROSOL EXTINCTION MEASUREMENTS

4.1 FORWARD SCATTERING CORRECTIONS TO TRANSMISSOMETRY MEASUREMENTS OF EXTINCTION IN POLYDISPERSE AEROSOLS

In Ref. 62 results were presented of a parametric study of the forwardscattering correction factor R and the complementary error factor E for monodispersions. In this section the results of a similar study carried out for spherical *polydispersions* of size distribution $n(r)\ [cm^{-3}\mu m^{-1}]$, r being the radius in μm, will be presented. For the sake of clarity, only the results obtained with the use of simple unimodal size distributions of the modified Gamma type, such as Deirmendjian models (Ref. 40) Haze M, Haze H and Cloud C3 (referred to as Haze C in this section), are presented here. Results for other real size distributions can easily be obtained in a similar manner. The behavior of both correction and error factors, i.e., R and E, averaged over each of the three size distributions, will be discussed here as functions of each of the following parameters: the mode radius r_m, the polydispersity or the spread of the size distribution, and the real (m') and imaginary (m") parts of the complex refractive index m = m' - im". The computations have been carried out with both the exact Mie theory solutions in explicity closed form and the Rayleigh diffraction theory approximation, as explained in Ref. 62. The results of such a study are extremely useful in obtaining the optimum experimental design parameters for the measurement of extinction coefficients in particulate media (Ref. 63).

(i) The Transmission Law (Bouguer's Law)

The transmission law for an electromagnetic plane wave passing through a homogeneous polydisperse aerosol medium (Fig. 4.1) is given

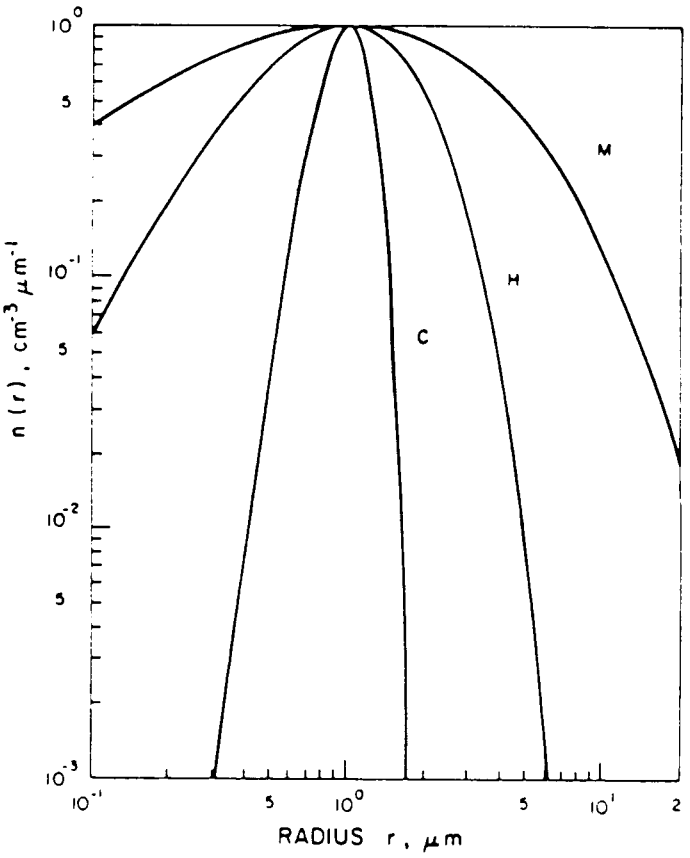

FIG. 4.1. Plots of the three Deirmendjian size-distribution models, Hazes M, H and C, for a mode radius of 1 μm.

by Bouguer's Law, namely

$$I(\lambda) = I_o(\lambda)\ e^{-\tau(\lambda)} \tag{1}$$

where

$$\tau(\lambda) = \beta_{ext}(\lambda)\ L \tag{2}$$

and

$$\beta_{ext}(\lambda) = \beta_{scat}(\lambda) + \beta_{abs}(\lambda) \tag{3}$$

As in Ref. 58, for the sake of clarity, the molecular contributions to β_{ext} will be ignored here. Then for polydisperse aerosols of size distribution $n(r)$, $cm^{-3}\mu m^{-1}$, the coefficients are defined by

$$\beta_j(\lambda) = \int_{r_1}^{r_2} \pi r^2 Q_j(x,m)\, n(r)\, dr,\ j = \text{ext, scat and abs} \tag{4}$$

All the quantities in Eq. (4) are the same as defined in Ref. 62, except that the factor $N_p(r)$ for monodisperse particles has been replaced here by the operator $\int_{r_1}^{r_2} n(r)dr$, where r_1 and r_2 are lower and upper limits of radii. Aerosol size distributions are discussed in a later section.

(ii) Forward Scattering Corrections

A. Exact Mie Theory Formulation

Because of the fact that forwardscattered light invariably enters the detector view cone, Bouguer's law, as defined in Eq. (1), cannot be used to obtain the true optical depth τ in a transmission experiment. But instead, one obtains the apparent optical depth τ' related to the apparent volume extinction (β'_{ext}) and scattering (β'_{scat}) coefficients, which are distinguished from the true quantities β_{ext} and β'_{scat} respectively; here, β_{abs} is clearly not affected by the

forwardscattering. Thus,

$$\beta'_{ext} = \beta'_{scat} + \beta_{abs} \text{ (apparent)} \tag{5}$$

The Mie efficiency factor Q_{scat} is based on the total amount of light lost from the beam by scattering by a particle in all directions; and Q'_{scat}, on the amount of light lost by scattering in all directions except within a cone of half-angle θ in the forward direction, so that their difference is given by

$$Q_{ext} - Q'_{ext} = Q_{scat} - Q'_{scat} = \frac{1}{x^2}\int_0^{\theta}(i_1 + i_2)\sin\theta' d\theta'$$

$$= \frac{I}{x^2}(x,m,\theta) \tag{6}$$

where $I(x,m,\theta)$ is defined in Eqs. (28) and (29) in Ref. 62.

From Eqs. (3) and (5), one obtains

$$\beta_{ext} - \beta'_{ext} = \beta_{scat} - \beta'_{scat}$$

$$= \pi\int_{r_1}^{r_2} r^2 n(r)\,(Q_{ext} - Q'_{ext})\,dr$$

$$= \pi\int_{r_1}^{r_1} r^2 n(r) Q_E\,dr$$

$$= \frac{\pi}{k^2}\int_{r_1}^{r_2} n(r)\,I(x,m,\theta)dr \tag{7}$$

where E (and R) are defined in Eqs. (10) and (9) of Ref. 62.

Then a correction factor $\bar{R}$ and an error factor $\bar{E}$, averaged over the particle size distribution between the limits r_1 and r_2, may be defined by

$$\bar{R} = \beta'_{ext} / \beta_{ext} = 1 - \bar{E} \tag{8}$$

where

$$\bar{E} = \frac{\pi}{\beta_{ext} k^2} \int_{r_1}^{r_2} n(r)\, I(x,m,\theta)\, dr \tag{9}$$

Note that $\bar{R} = \bar{R}\,(n(r),m,\theta)$.

B. The Approximate Rayleigh Diffraction Formulation

From Eq. (12) in Ref. 62 and Eqs. (6) and (8), the Rayleigh diffraction approximation to the forwardscattering correction for a polydispersion is given by

$$\bar{R} = \frac{\pi}{\beta_{ext}} \int_0^\infty r^2 n(r) Q(x,m) \frac{1}{2} \{1 + J_o^2(x\theta) + J_1^2(x\theta)\}\, dr \tag{10}$$

where J_o and J_1 are Bessel functions of the first kind and of orders zero and one, respectively.

(iii) Corrected Transmission Law

By inserting the correction factor $\bar{R}$ into the transmission equation, one can account for both the direct and forwardscattered radiation. Thus

$$I(\lambda) = I_o(\lambda) e^{-\tau'(\lambda)} \tag{11}$$

where

$$\tau'(\lambda) = \int_0^L d\ell\ \beta'_{ext}$$

$$= \int_0^L d\ell\ \beta_{ext}\ \bar{R}\ (n(r),\theta)$$

$$= \int_0^L d\ell \int_{r_1}^{r_2} dr\ \pi r^2 Q(x,m)\ n(r) R(x,\theta) \qquad (12)$$

From the discussion in Ref. 62, it is clear that for parallel beam transmission systems with an open-detector, the half-cone angle $\theta = \theta(\ell)$, so that

$$\tau'(\lambda) = \pi L \int_{r_1}^{r_2} dr\ r^2 Q(x,m) n(r) \hat{R}(x,L) \qquad (13)$$

where

$$\hat{R}(x,L) = \frac{1}{L} \int_0^L d\ell\ R(x,\theta(\ell)) \qquad (14)$$

And for a lens-pinhole system θ = constant, so that $R = R(x,\theta)$, independent of ℓ. For the discussion of the experimental design considerations of the two detector systems, see Ref. 62.

(iv) Aerosol Size Distributions

Several analytic representations of aerosol size distributions appear in the literature. In this paper, the behavior of $\bar{R}$ and $\bar{E}$ is investigated as a function of the mode radius r_m, the spread of the size distribution and the complex refractive index $m(= m' - im")$, the upper and lower limits of radii being 10^{-2} and 20 μm. For the sake of simplicity, three of the Deirmendjian models (Ref. 46), namely, Haze M, Haze H and Cloud C3 (referred to here as Haze C), were selected for representing different polydispersities of aerosol size distribution n(r). Since r_m is varied between

the radii limits 10^{-1} and 10 μm, the three models are used here in a more general way than was their original intent. It is in that sense that model Cloud C3 is referred to as Haze C. The limits of integration over r are 10^{-2} and 20 μm.

The expressions for the n(r) models and their corresponding mode radii r_m are given as follows:

(a) Haze M: $$n(r) = r\, e^{-\sqrt{br}}, \quad r_m = 4/b \tag{15}$$

(b) Haze H: $$n(r) = r^2 e^{-br}, \quad r_m = 2/b \tag{16}$$

(c) Haze C: $$n(r) = r^8 e^{-(br)^3}, \quad r_m = \left(\frac{8}{3}\right)^{1/3} b^{-1} \tag{17}$$

Note that any normalization or scale factor in the size distribution will cancel when $\bar{E}$ and $\bar{R}$ are evaluated. Thus, although $\bar{E}$ and $\bar{R}$ do depend on the *shape* of the size distribution, they do not depend on the total *number* of particles.

The difference in the shape of these three models is illustrated in Fig. 4.1, where each has r_m = 1.0 μm and $n(r_m)$ = 1.0 $cm^{-3}\mu m^{-1}$. For want of a better terminology, the "spread" of a size distribution will also be referred to as "polydispersity" of the size distribution in this paper. For example, Haze H will be referred to as more "polydisperse" than Haze C, and in the same vein it will be stated that Haze M has a higher "polydispersity" than Haze H. It should be noted here that there exist other terms in the theory of distribution functions to express the same quantity.

Perhaps the major disadvantage of the Deirmendjian models is that their fall-off behavior for large radii is too sharp: many experimentally measured distributions show a power law behavior, at least in the optically active region. For this reason, we have also considered a power law distribution, given by

$$n(r) = r^{-\nu}, \quad 10^{-2}\mu m \leq r \leq 15\ \mu m$$

and allowed ν to vary between 2 and 4. Note that one cannot talk about either mode radius or polydispersity for a power law haze, only slope, ν.

(v) Computational Considerations

A parametric study of the correction factor $\bar{R}$ and the corresponding error factor $\bar{E}$ was carried out as functions of different combinations of r_m, θ, m' and m", whose values occur within the ranges $0.1 < r_m < 10\mu m$, $0^o < \theta < 10^o$, $1.33 < m' < 1.65$ and $0.0 < m" < 0.1$.

The computations of $\bar{R}$ (and $\bar{E}$) in Eq. (8) (and Eq.(9)) are made by using the closed form relations given in Ref. 58 for $I(x,m,\theta)$. The computations of $\bar{R}$ for the approximate method are made by using Eq. (10).

(vi) Discussions and Conclusions

The parametric study of $\bar{R}$ was carried out as a function of many different combinations of r_m, θ, m' and m", but for the sake of clarity the results of only a few judiciously selected combinations are presented in the following sub-sections. As the Deirmendjian models are so different from the power law model, we shall treat each separately, starting with the Deirmendjian models.

A. Results for R and E as functions of r_m and m

Figures 4.2 (a, b, and c) and 4.3 (a, b, and c) illustrate the behavior of $\bar{R}$ and $\bar{E}$ respectively, as functions of r_m in the range 0.1 to 10.0 μm, for three different half-cone angles (1^o, 4^o, and 10^o) and five different refractive indices (1.33, 1.65, 1.55 - i(.05), 1.55 - i(0.1)), for each of the three models: (a) Haze M, (b) Haze H, and (c) Haze C, respectively. The computations were made for λ = 0.55 μm.

For Haze M (Fig. 4.2a), the values of $\bar{R}$ rapidly decrease as r_m increases from 0.1 μm to about 1 μm and then tend to level off to a nearly constant value. The percentage error (Fig. 4.3a) for Haze M shows that for small r_m the error $\bar{E}$ increases fairly rapidly and then quickly levels off to a constant value which is different for each set of θ and m values. The smaller the θ the higher is the value of r_m beyond which the leveling of the values for $\bar{E}$ takes place.

For Haze H and Haze C, the plots of $\bar{R}$ make an inverted integral sign ($\rfloor$) within the r_m range of 0.1 μm to 10.0 μm, their steepness increasing with the decrease in polydispersity of the size distribution. From Figs. 4.2 and 4.3, we see that for $\theta = 1^o$, there is virtually no m-dependence for any of the hazes. For this reason, very few symbols have been drawn on these lines. For $\theta = 4^o$, we see that a small m-dependence has started to appear, being most clearly visible in Fig. 4.3, due to the logarithmic scale for $\bar{E}$. However, for $\theta = 10^o$, a clear m-dependence can be distinguished, especially in Fig. 4.2. We see, in general, that $\bar{R}$ is lowest for m = 1.33, and that there is little difference between the

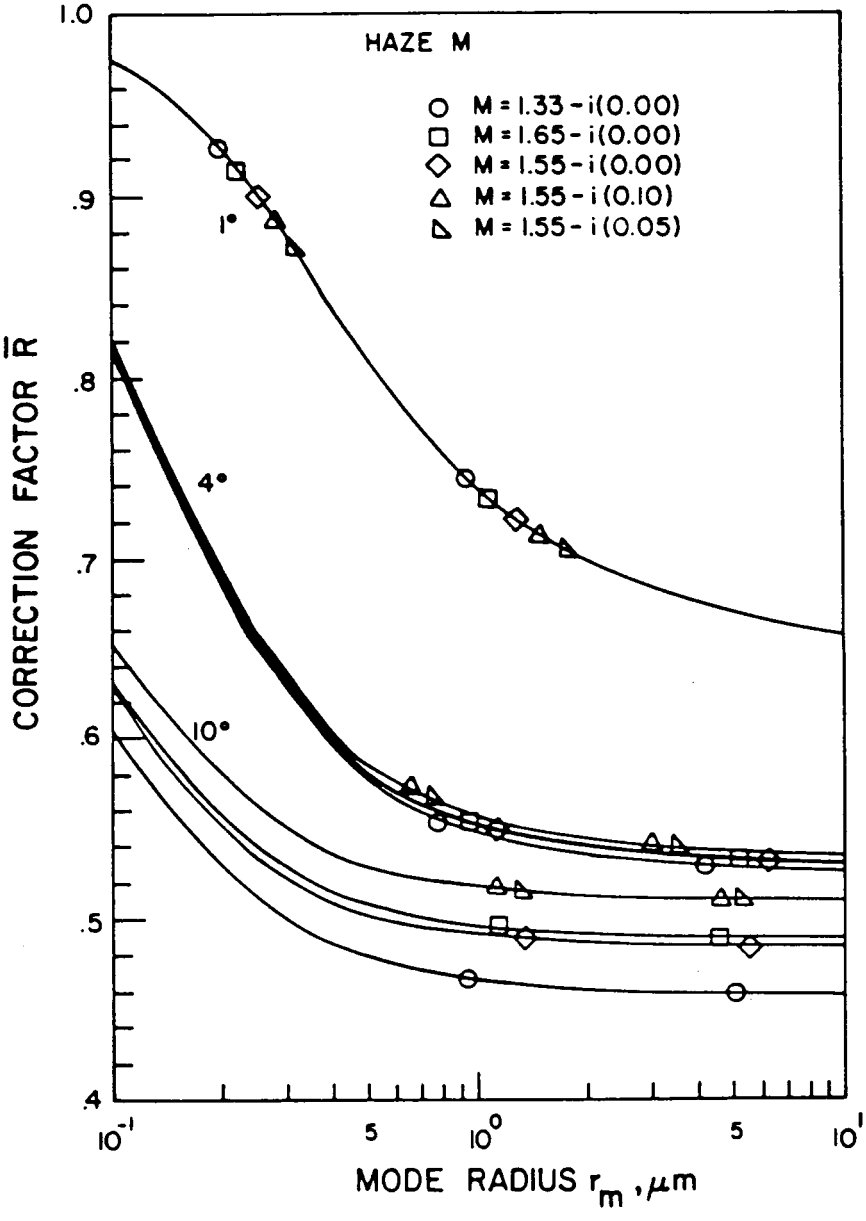

FIG. 4.2a. Plots of the correction factor $\bar{R}$ versus mode radius for three values of θ and five refractive indices: Haze M

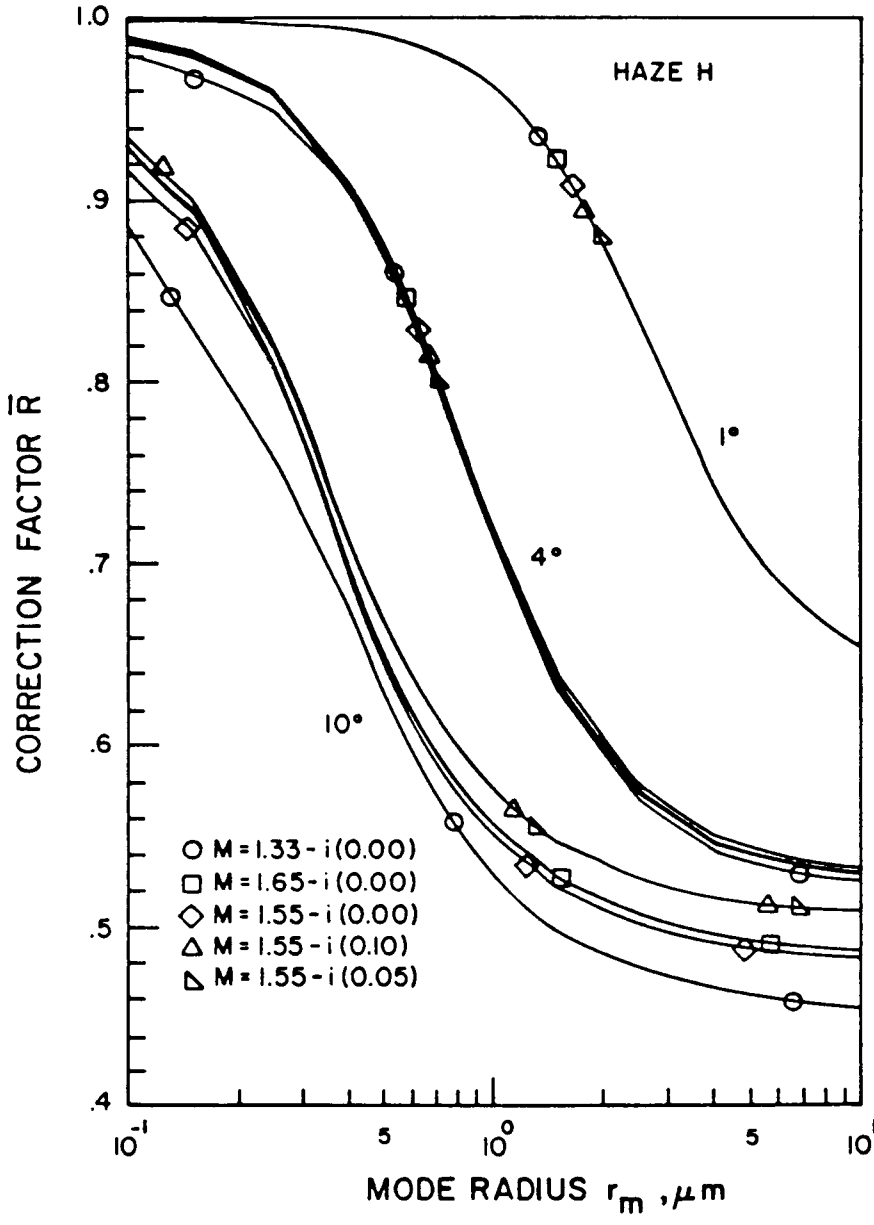

FIG. 4.2b. Plots of the correction factor $\bar{R}$ versus mode radius for three values of θ and five refractive indices: Haze H

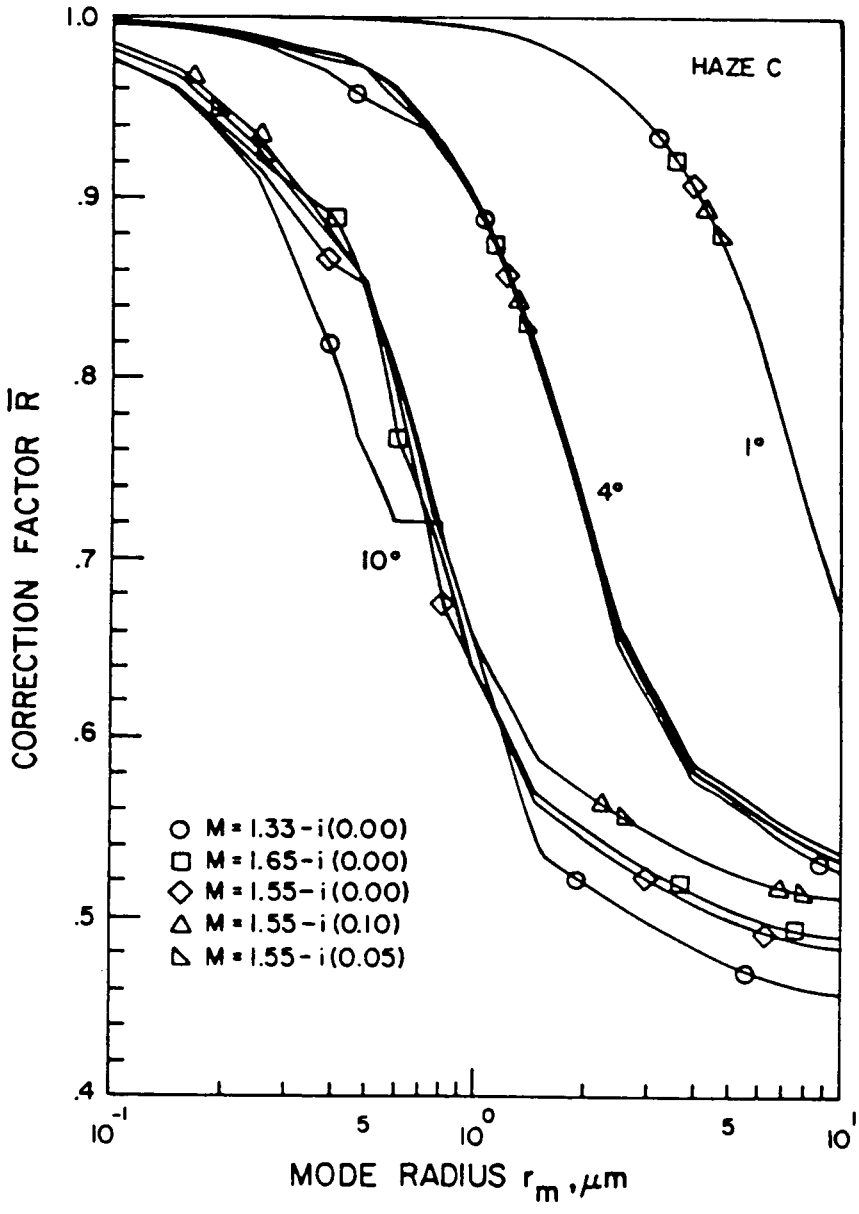

FIG. 4.2c. Plots of the correction factor $\bar{R}$ versus mode radius for three values of θ and five refractive indices: Haze C

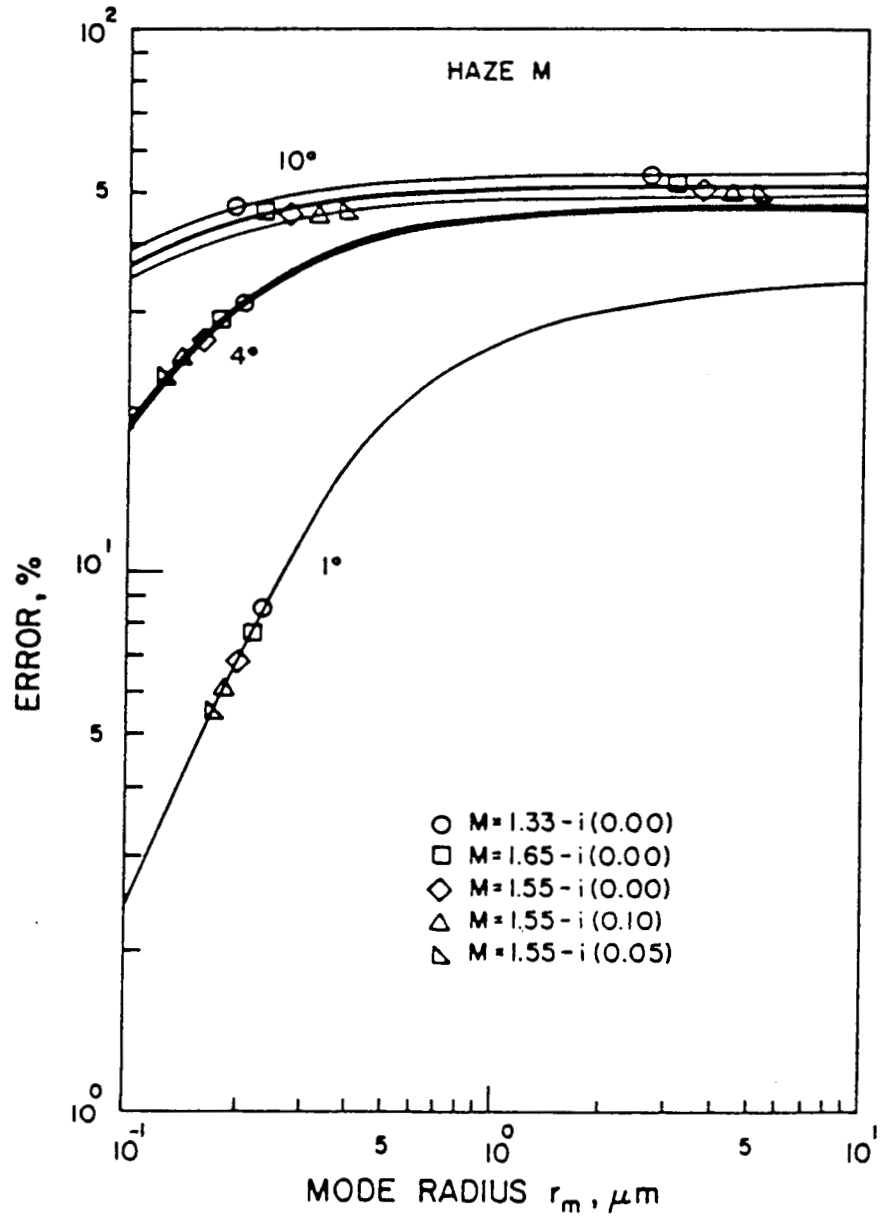

FIG. 4.3a. Plots of percentage error ($100\overline{E}$) versus mode radius for three values of θ and five refractive indices: Haze M

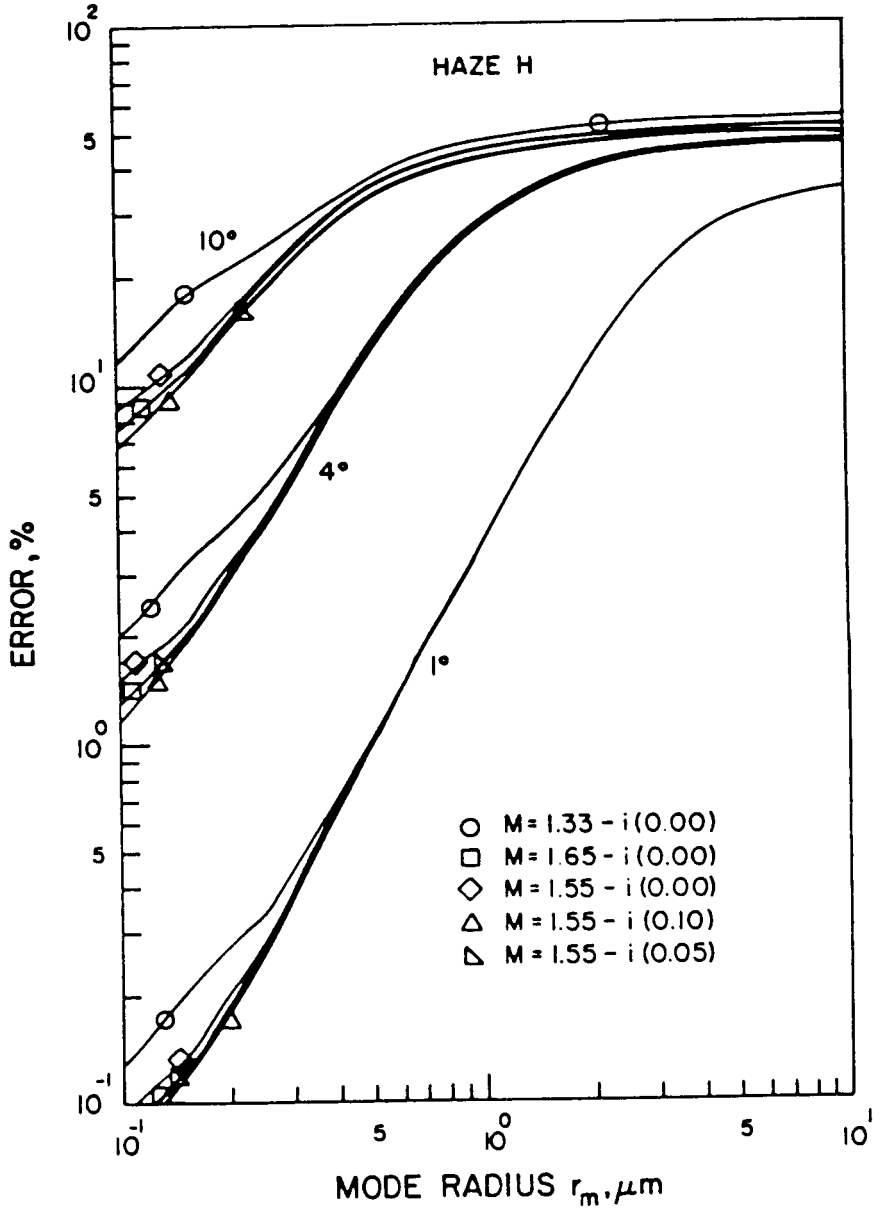

FIG. 4.3b. Plots of percentage error ($100\overline{E}$) versus mode radius for three values of θ and five refractive indices: *Haze H*

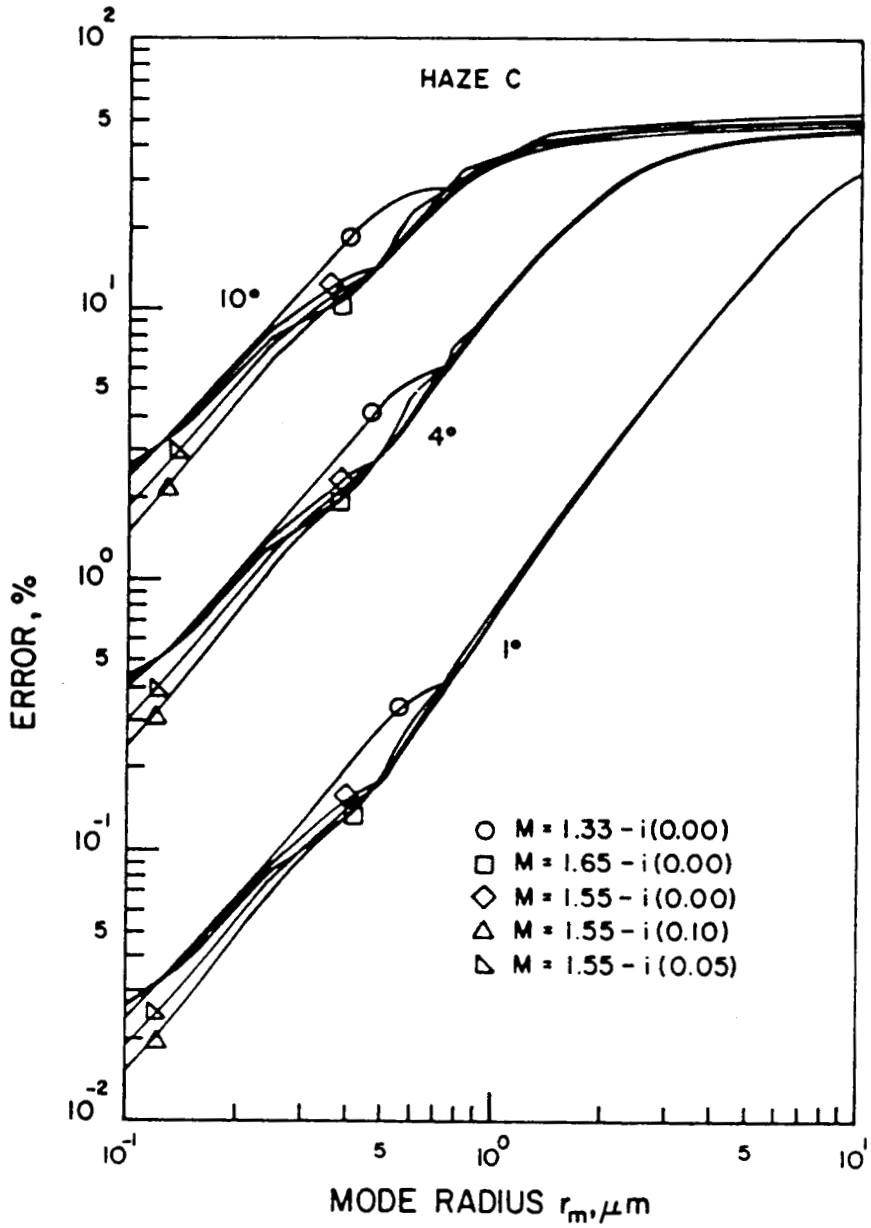

FIG. 4.3c. Plots of percentage error ($100\bar{E}$) versus mode radius for three values of θ and five refractive indices: Haze C

curves for m = 1.55 and 1.65. However, the presence of a small amount of absorption immediately raises $\bar{R}$, although the actual value of this absorption appears to have little effect.

Effect of Polydispersity: Comparing the $\bar{R}$ (and $\bar{E}$) vs r_m plots for the three models, one can reach the following conclusions:

It can be seen from the plots presented here that, in general, for given values of θ and r_m, the higher the polydispersity the higher the error, $\bar{E}$. This is due to the predominant forward scattering of the large particle component, implied by the increased polydispersity. We should note, however, that the saturation values of $\bar{E}$ and $\bar{R}$ (both $\simeq 0.5$) are not affected by polydispersity, but that these values are reached "sooner" for a more polydisperse haze than for a less polydisperse haze. A saturation value of $\bar{E} \simeq 0.5$ implies a Q'_{ext} value of 1.0. An explanation for this is as follows. For the same value of θ, the amount of scattered radiation collected at the detector increases as the large particle component increases which, in effect, reduces Q' from a value of about 2.0 (assumed for large particles) to a minimum value of 1.0. The saturation value for $\bar{E}$ tends to be about 50% for $\theta = 10^{\circ}$ and 45% for $\theta = 4^{\circ}$ for Haze M, a difference of about 5%. This difference however, tends to decrease as aerosol size distributions become less polydisperse, implying smaller number of large particles, so that the saturation value of $\bar{E}$ approaches 50%.

B. Results for $\bar{R}$ and $\bar{E}$ as a function of θ

Figures 4.4 (a, b, and c) show the behavior of $\bar{E}$ as a function of θ for six values of mode radius (0.1, 0.15, 0.50, 1.0, 2.5, and 10.0 μm) and m = 1.55 for each of the three size distribution models, respectively. Again, the effects of polydispersity are quite apparent in the increasing spread of the $\bar{E}$ vs θ plots for lower r_m values (below 1.0 μm) as the polydispersity decreases.

Figure 4.5 (a, b, and c) illustrate the behavior of $\bar{R}$ as a function of θ for five values of r_m (0.1, 0.4, 1.0, 4.0, and 1.0 μm). Symbols without a cross represent the Mie theory results and those with a cross represent the approximate results. The discussion of their comparison will be presented in the next section. Only the Mie theory results will be discussed here. The choice of different r_m values for the cases shown in Figs. 4.4 and 4.5 was merely for the sake of the clarity of the graphical display. The plots in Figs. 4.5 (a, b, and c) also show that the correction factor $\bar{R}$ falls rapidly with increasing θ for large r_m values and then levels off quickly to a value close to 0.5. For large particles, the plots are practically identical for all the three models. However, for small values of r_m, there is a considerable spread in the values of $\bar{R}$.

C. Comparison between the Mie Theory and Diffraction Formulation

Consider Figs. 4.5 (a, b, and c) and 6(a, b, and c) representing the $\bar{R}$ vs θ results for nonabsorbing (m - 1.55) and absorbing (m = 1.55 - i 0.05) aerosols, respectively. Symbols with cross represent the

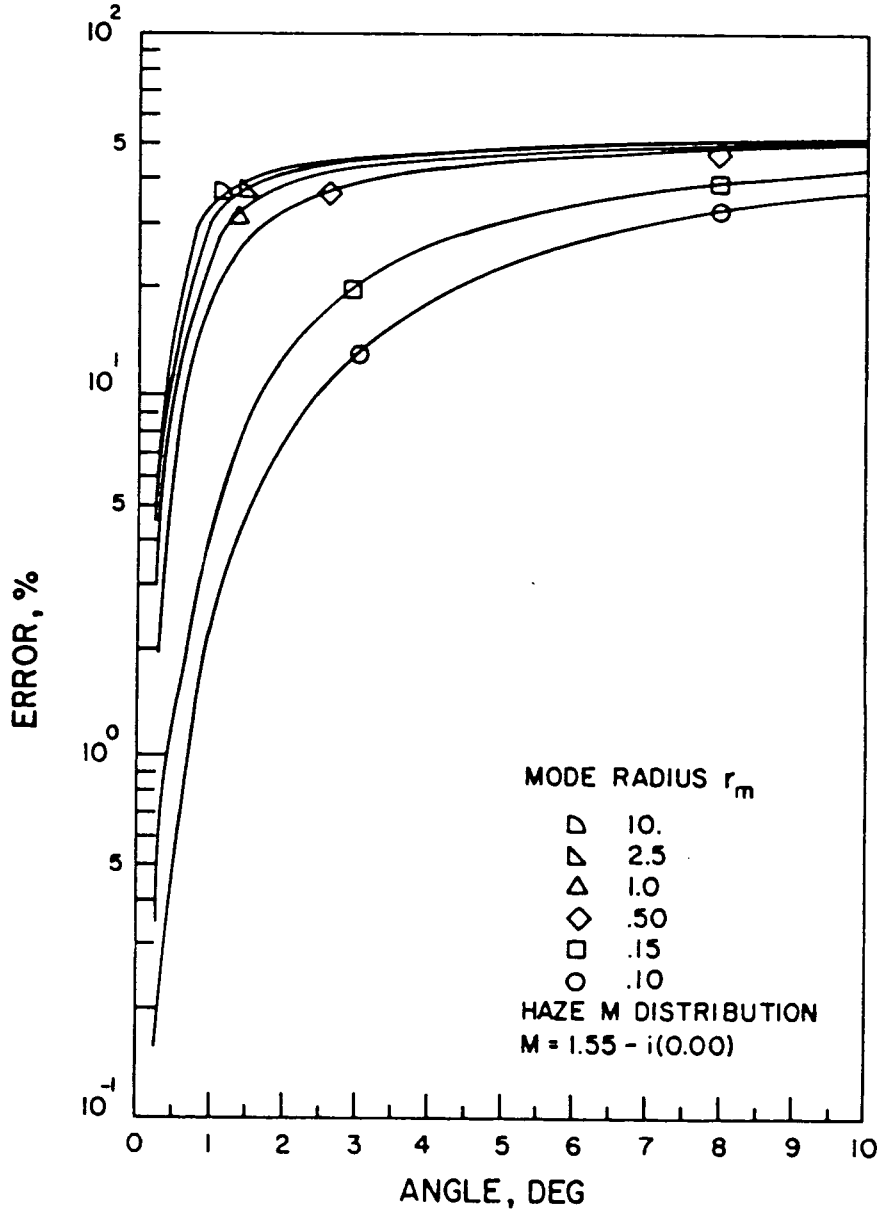

FIG. 4.4a. Plots of percentage error ($100\bar{E}$) versus half-angle θ, for six mode radii (m = 1.55): Haze M

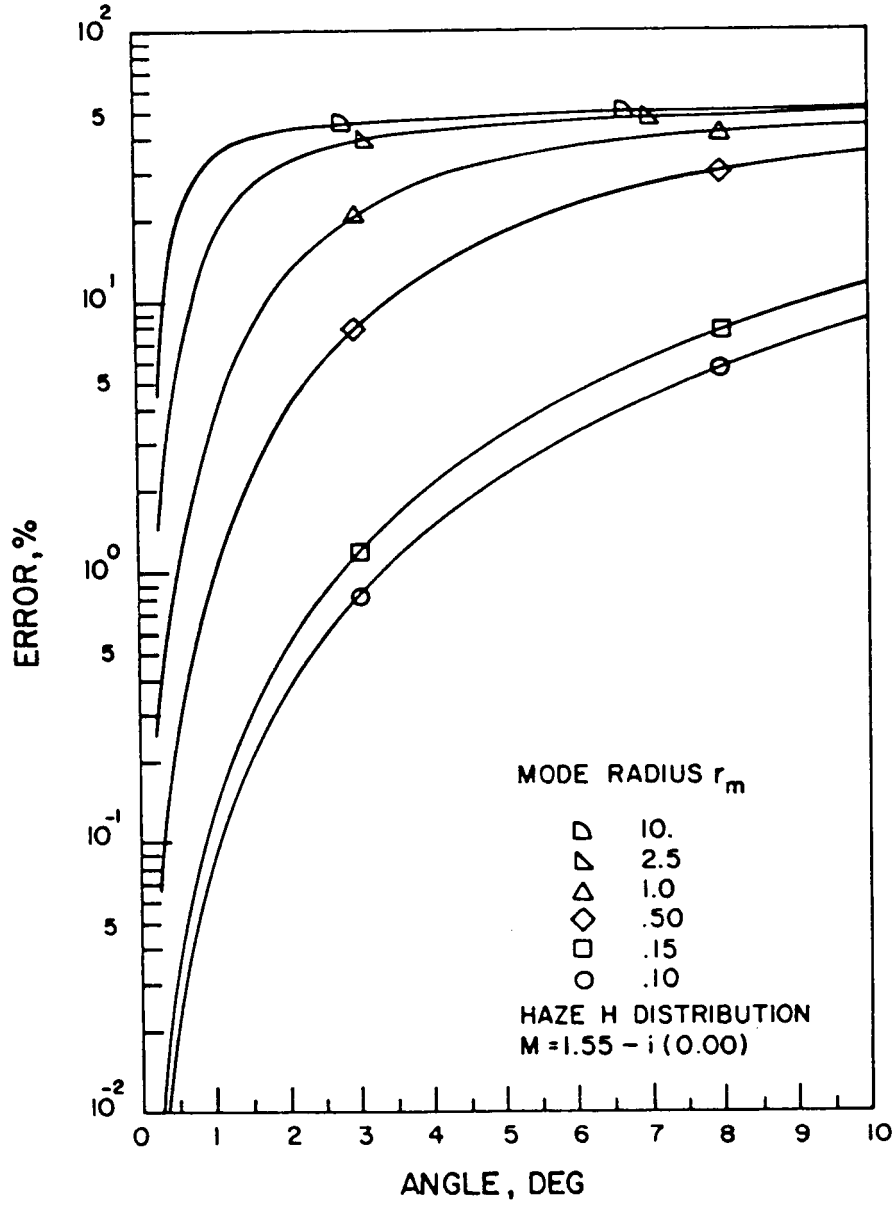

FIG. 4.4b. Plots of percentage error ($100\bar{E}$) versus half-angle θ, for six mode radii (m = 1.55): Haze H

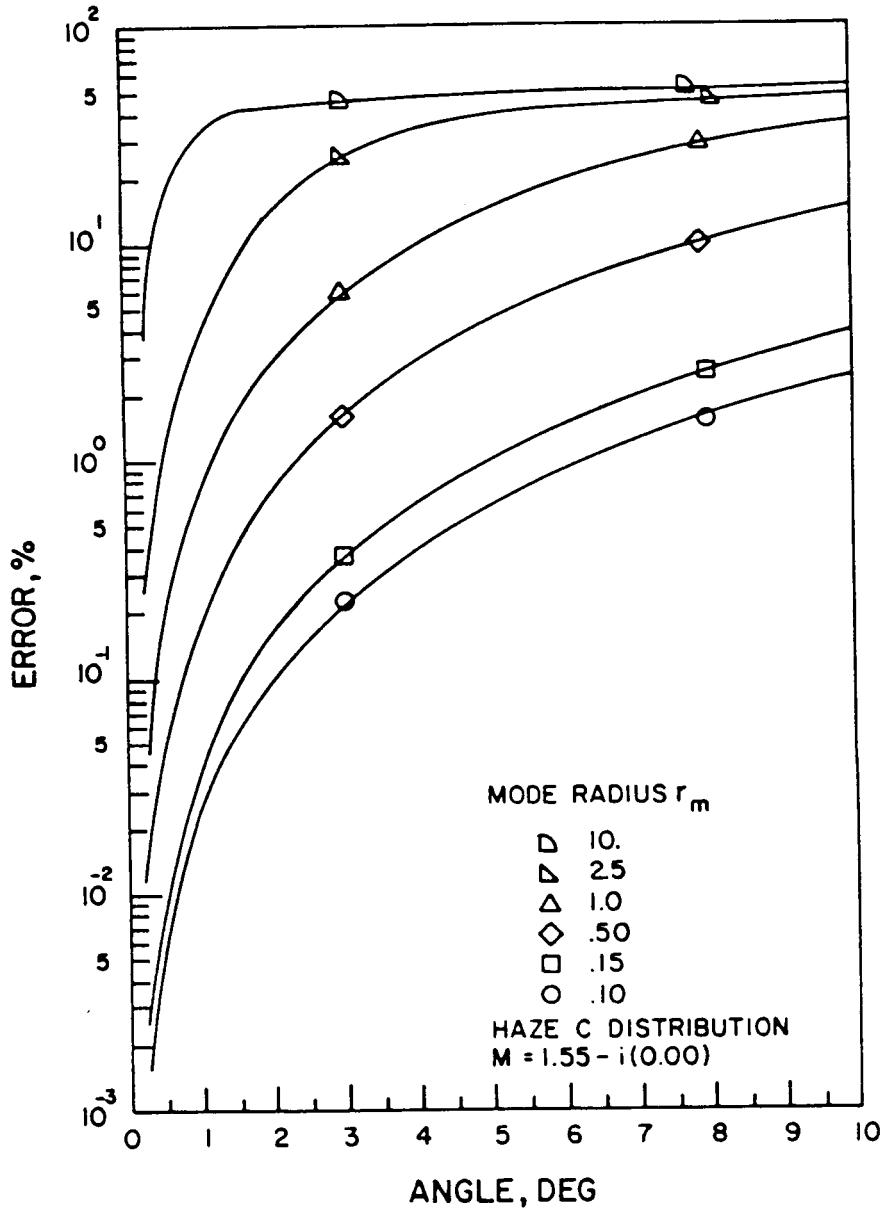

FIG. 4.4c. Plots of percentage error ($100\bar{E}$) versus half-angle θ, for six mode radii (m = 1.55): Haze C

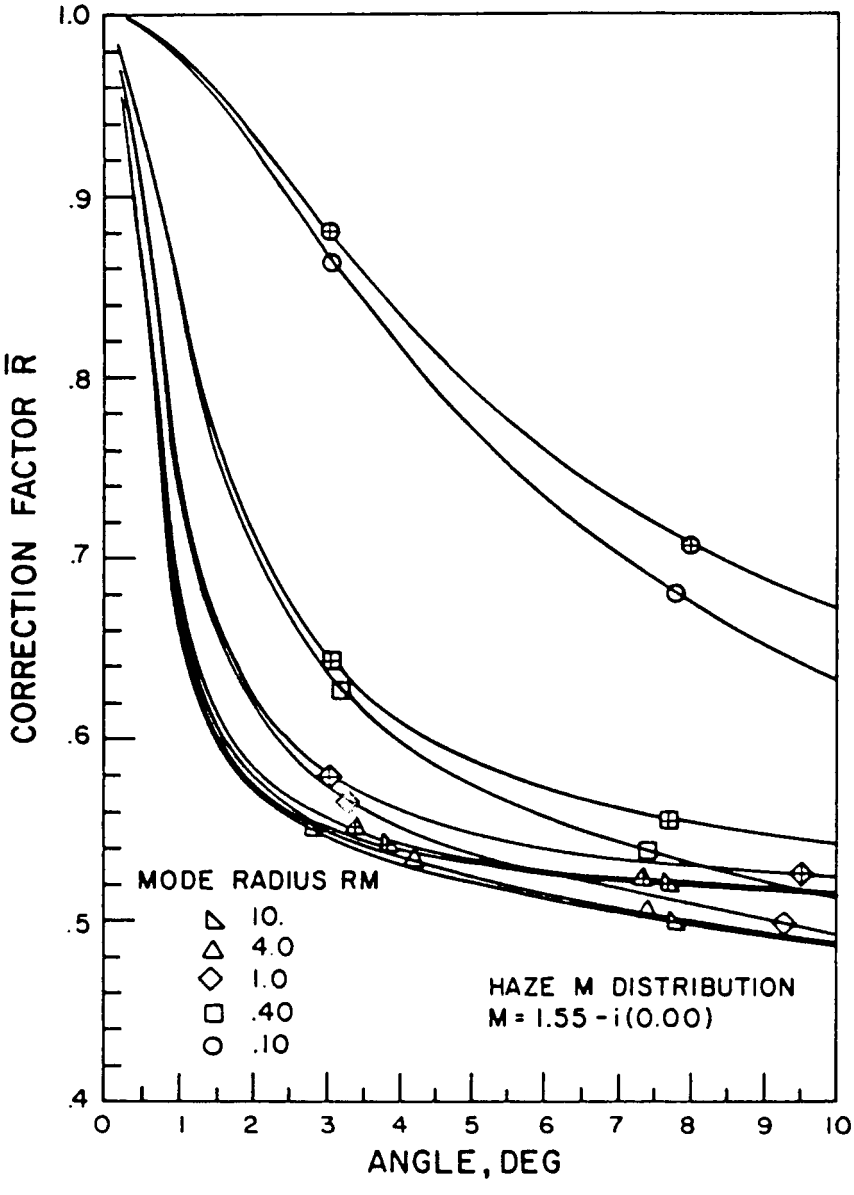

FIG. 4.5a. Plots of correction factor $\bar{R}$ versus θ for $m = 1.55$, $\lambda = 0.55$ μm, and five mode radii: Haze M. (Symbols without cross represent Mie results; symbols with crosses, approximate results.)

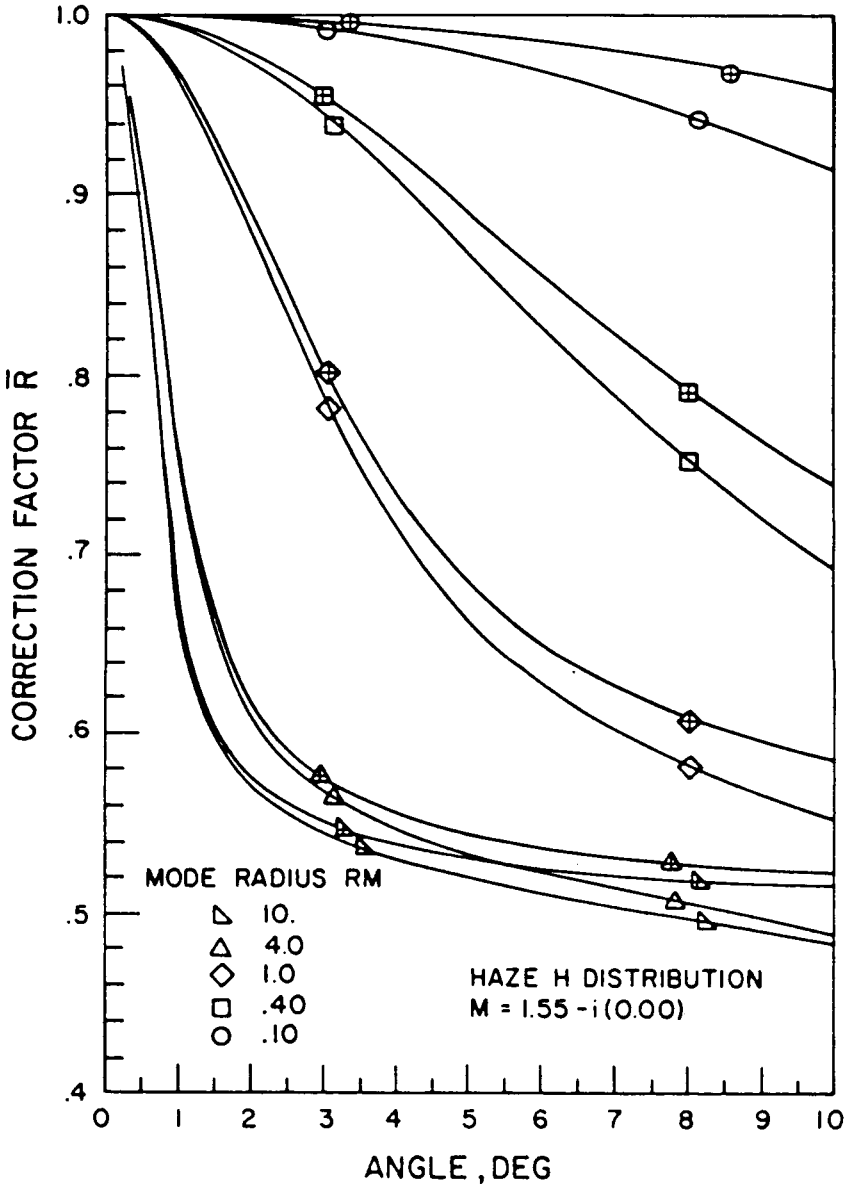

FIG. 4.5b. Plots of correction factor $\bar{R}$ versus θ for $m = 1.55$, $\lambda = 0.55$ μm, and five mode radii: Haze H. (Symbols without cross represent Mie results; symbols with cross, approximate results.)

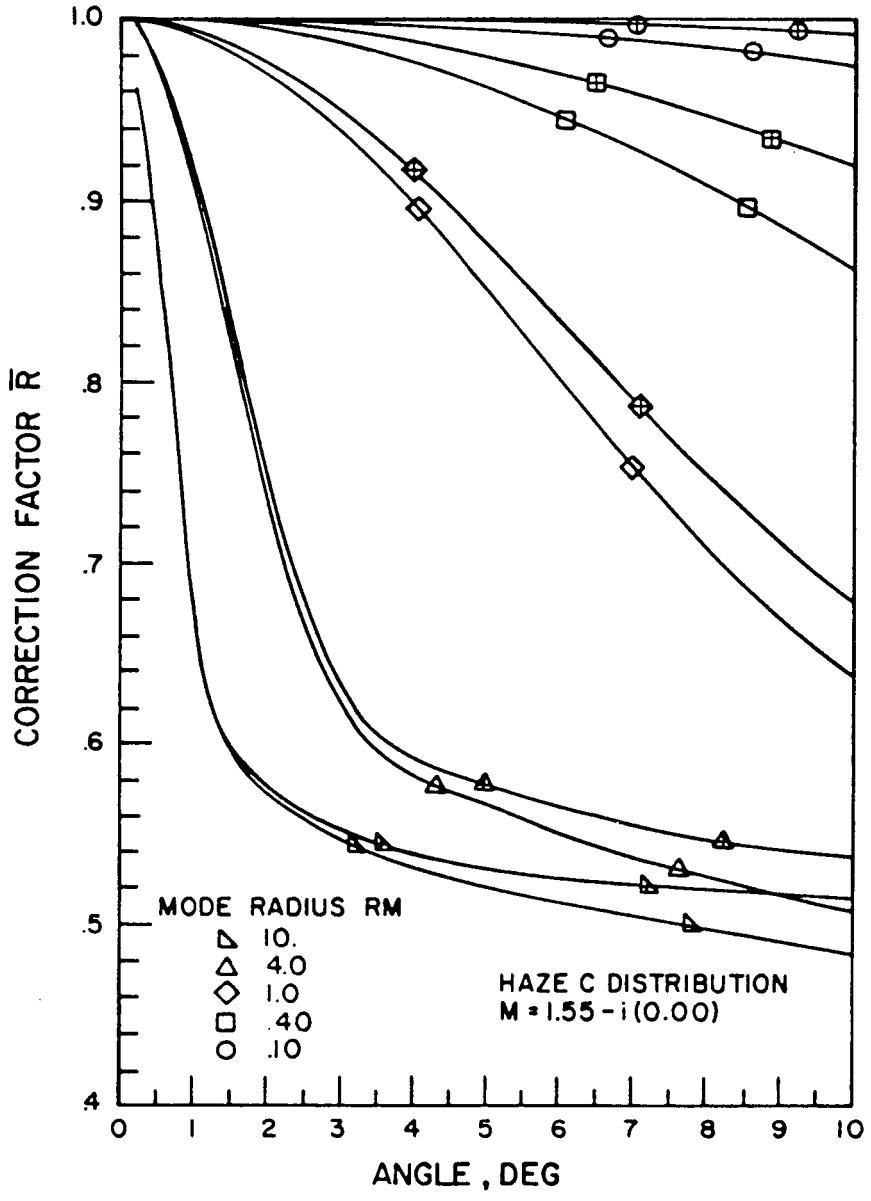

FIG. 4.5c. Plots of correction factor $\bar{R}$ versus θ for m = 1.55, λ = 0.55 μm, and five mode radii: Haze C. (Symbols without cross represent Mie results; symbols with cross, approximate results.)

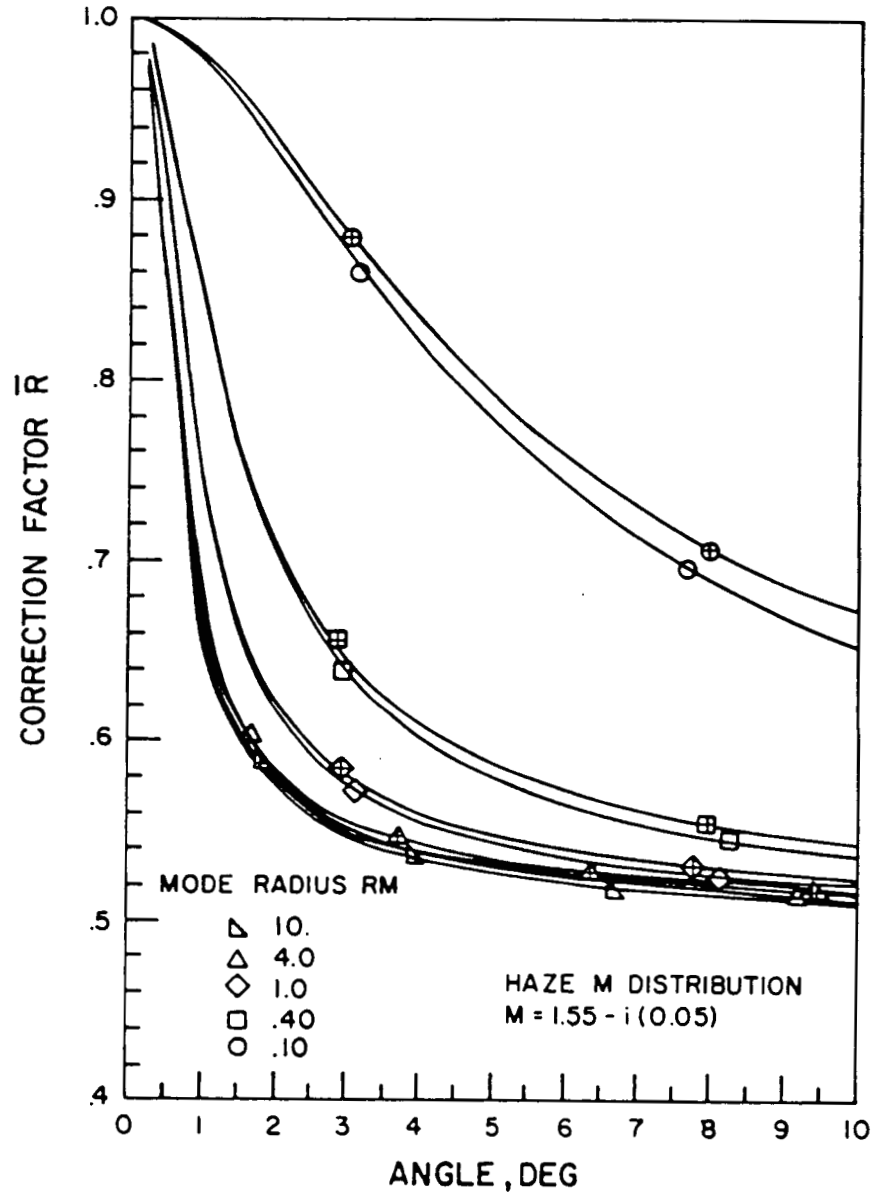

FIG. 4.6a. Plots of correction factor $\bar{R}$ versus θ for m = 1.55 - i(0.0 λ = 0.55 μm, and five mode radii: Haze M. (Symbols without cross represent Mie results; symbols with cross, approximate results.)

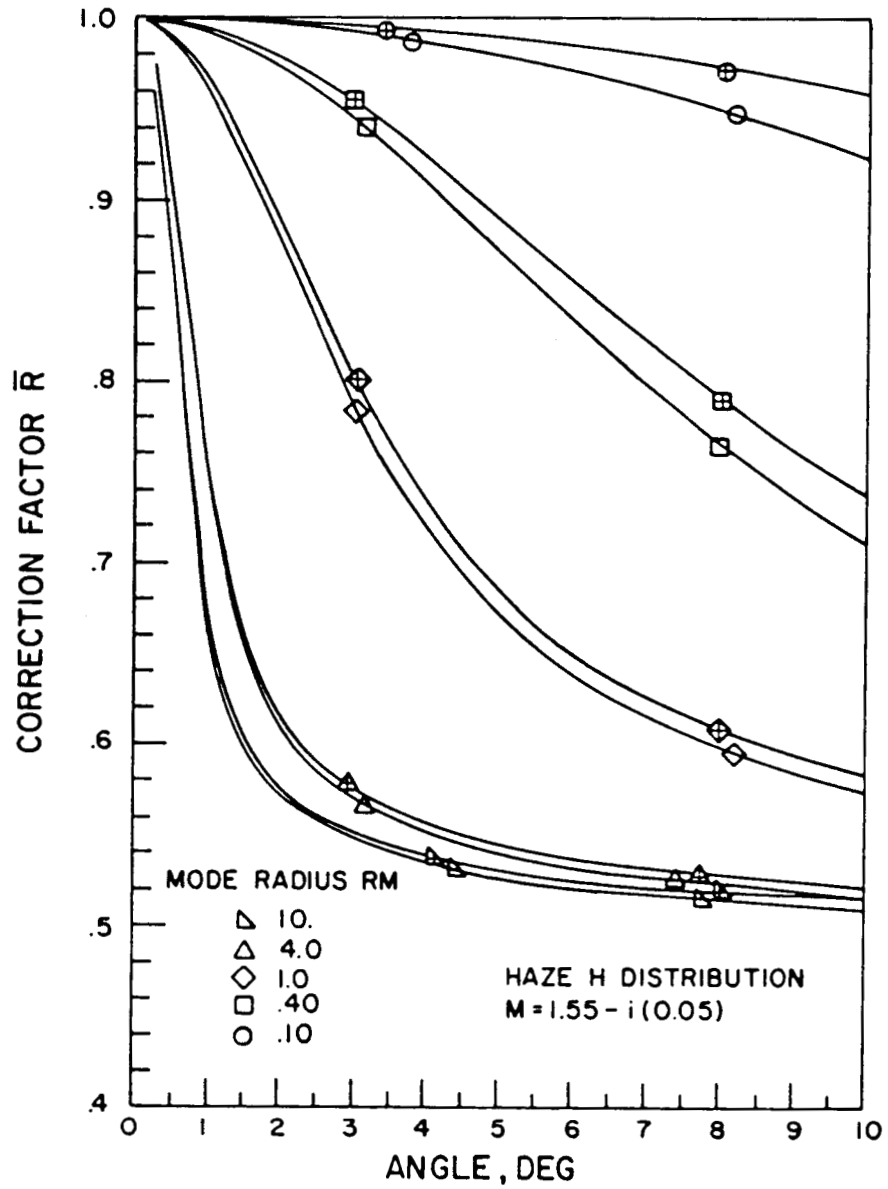

FIG. 4.6b. Plots of correction factor $\bar{R}$ versus θ for m + 1.55 - i(0.05), λ = 0.55 μm, and five mode radii: Haze H. (Symbols without cross represent Mie results; symbols with cross, approximate results.)

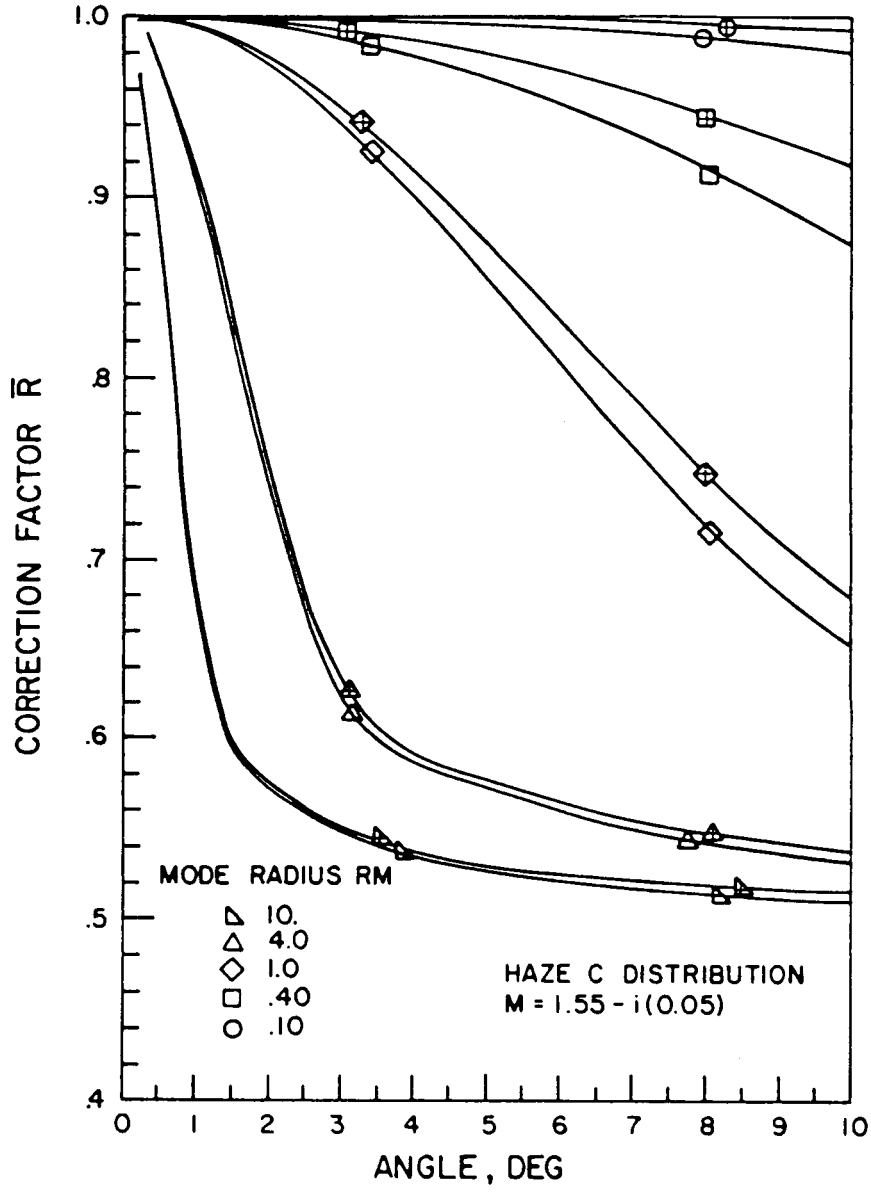

FIG. 4.6c. Plots of correction factor $\bar{R}$ versus θ for $m = 1.55 - i(0.05)$, $\lambda = 0.55$ μm, and five mode radii: Haze C. (Symbols without cross represent Mie results; symbols with cross, approximate results.)

results due to Rayleigh formulation and those without cross the results due to Mie theory. Figures (a), (b) and (c) represent the models: Haze M, Haze H, and Haze C, respectively.

Figures 4.5 (a, b, and c) show that, for nonabsorbing aerosols, the agreement between the Mie and the Rayleigh approximation is not as good for small r_m as it is for large r_m, for all three models. This is to be expected since the Rayleigh diffraction formula Eq. (13) is only valid for large particles. On the other hand, the agreement for both large and small r_m appears to be better for Haze M (more polydisperse aerosol) than for Haze C, indicating that for more polydisperse size dispersions the agreement between the Rayleigh formulation and the exact formulation tends to improve. Comparison of these results with those for monodispersions in Ref. 62 also substantiates the trend. The remarks for the case of nonabsorbing aerosols apply to the case of absorbing aerosols ($m = 1.55 - i0.05$) as well, except for the additional conclusion that the agreements between the Rayleigh and Mie results for all models are considerably better for the absorbing aerosols than for the nonabsorbing (see Figs. 4.6 (a, b, and c)). The latter conclusion is again in line with the one made for monodispersions in Ref. 62.

D. The Error Contours Diagram in r_m - θ plane

Figure 4.7 shows the error contours for 10% (dashed line) and 5% error (solid line) for $m = 1.55$ and the models M, H and C. The curves indicate an inflection point in Haze M (10%) curve and Haze H (5%) at about $\theta = 1.5^{\circ}$ and $\theta = 6^{\circ}$, respectively, in the range $r_m \sim 0.1$ μm.

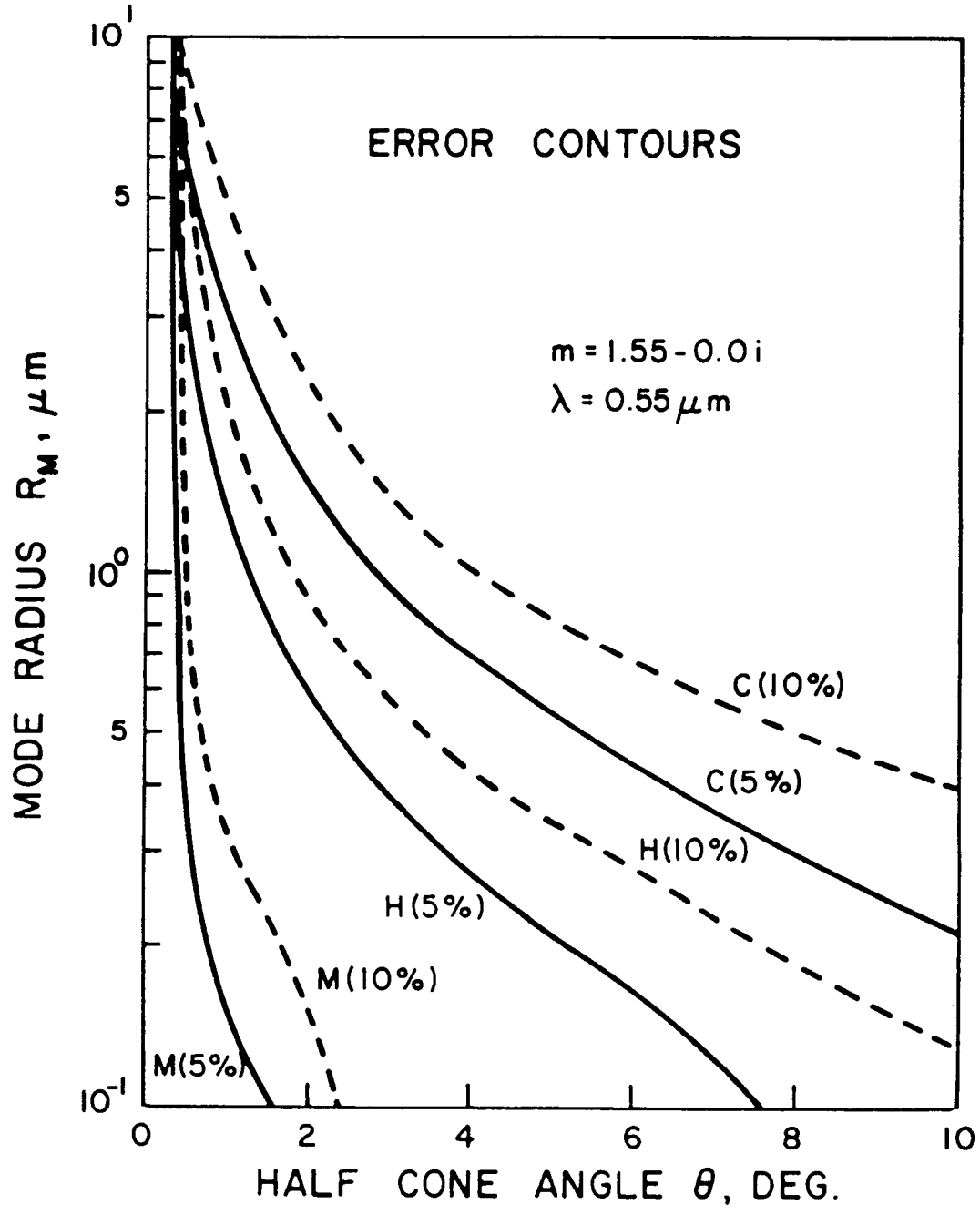

FIG. 4.7. Error contours in the r_m - θ plane for m = 1.55, λ = 0.55 μm, for models Haze M, Haze H and Haze C.

E. Experimental Design Considerations

Equation (14a) shows how the forwardscattering correction factor is included in the transmission law to obtain the measured (or apparent) optical depth τ'. Comments about the two aforementioned experimental geometries, discussed in Ref. 62, also apply to the case of polydisperse aerosols, in addition to the following comments regarding the effects of the polydispersity on the experimental design.

In Ref. 62 (Fig. 4.6), results were plotted for $\hat{R}$ as a function of $x\theta$ for the two aforementioned experimental geometries. For the polydisperse case, however, $\hat{R}(x\theta)$ has to be further averaged over the volume extinction coefficient, to yield $\hat{\bar{R}}$, the "path-averaged correction factor" for polydisperse aerosols, defined by the equation

$$\hat{\bar{R}} = \int_{r_1}^{r_2} dr\, r^2 n(r/r_m) Q(kr) \hat{R}(kr\theta) \Big/ \int_{r_1}^{r_2} dr\, r^2 n(r/r_m) Q(kr) \qquad (18)$$

The symbols cap(^) and bar(-) denote averaging over the path length and particle size distribution, respectively.

As expressed by Eq. (18), it is not possible to express R as a function $x_m\theta \equiv kr_m\theta$, which would enable one to make some sort of comparison with the results for the monodisperse case. However, such a comparison becomes possible if we make the further assumption that $Q = 2$, which is a reasonable one for the case of large particles for which the Rayleigh formulation is valid. Then, Eq. (18) reduces to

$$\hat{\bar{R}} = \hat{\bar{R}}(kr_m\theta) = \int_{z_1}^{z_2} dz\ z^2\ n(z)\hat{R}(k\,r_m\,\theta z) \Big/ \int_{z_1}^{z_2} dz\ z^2\ n(z)dz \qquad (19)$$

where

$$z = r/r_m,\ z_1 = r_1/r_m,\ z_2 = r_2/r_m \qquad (20)$$

$\hat{\bar{R}}$, obtained by using Eq. (19), can easily be plotted as a function of $y(= kr_m\theta)$, for the three size distributions for each of two detector systems, as shown in Fig. 4.8. The resulting plots are similar in shape to those for the monodisperse aerosols in Paper I, with the values of R converging to 1 and 0.5 for $y \to 0$ and ∞, respectively. However, a comparison between the two sets of plots easily shows that increasing the polydispersity results in a translation of the curves toward the lower y values, or, in other words, maximum gradients for R occur at lower values of y.

In order to make accurate transmission measurements, it is important that the experimental design be based on those values of y for which either $R \to 1$ or $R \to 0.5$. But to be able to do so, some reasonable prior knowledge of both the mode radius r_m and the polydispersity is required.

F. λ-Dependence of R and E

All the results shown in the various plots were computed for $\lambda = 0.55$ μm. For any other value λ', these same results are valid for the three models, Haze M, Haze H, and Haze C, provided r_m is replaced by r_m' such that

$$r_m'/\lambda' = r_m/\lambda \qquad (21)$$

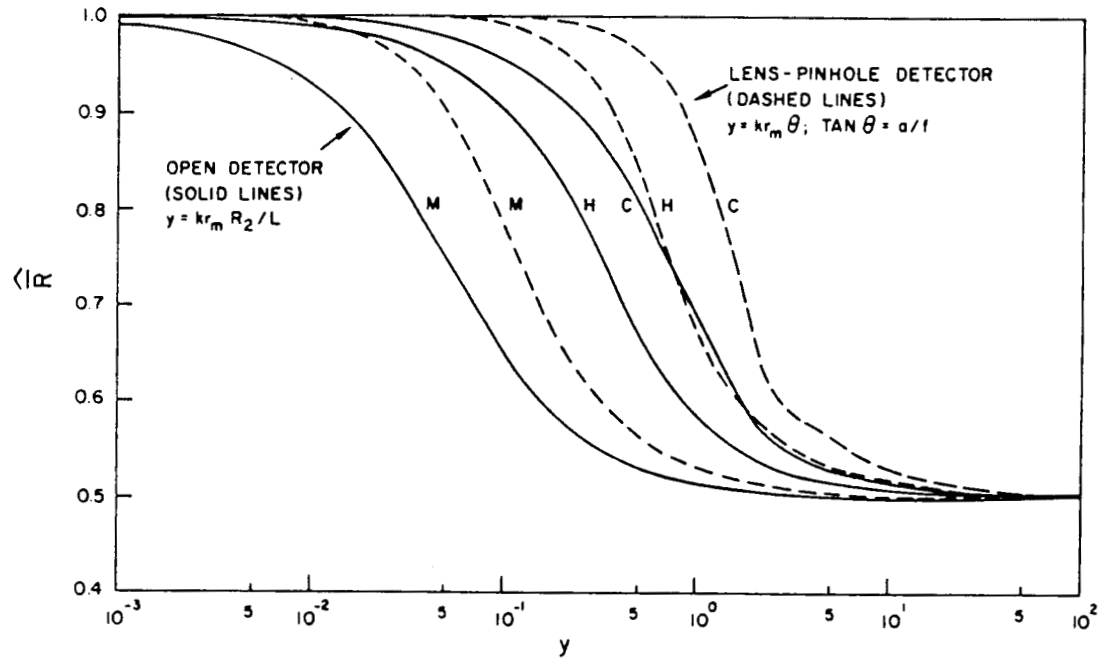

FIG. 4.8. Plots of the "path-averaged correction factor" $\hat{\hat{R}}$ versus y, where $y = kr_m\, a/f$ and $kr_m\, R_2/L$ for the lens-pinhole detector and open detector systems, respectively for models Haze M, Haze H and Haze C. $\lambda = 0.55$ μm.

A more detailed parametric study of the behavior of the forwardscattering effects involved in different transmission measurement experiments designed to measure optical extinction and visibility in the atmosphere will be presented in a separate publication.

G. Results for Power Law Size Distributions

In Fig. 4.9 (a, b, and c), we present a few selected results for the case of a power law size distribution. Figures 4.9a and 4.9b show a series of error contours in θ - ν plane, for refractive indices of 1.33 - i0.0 and 1.55 - i0.05, respectively. These two refractive indices usually produced the largest and smallest errors (respectively) for a given θ - ν combination. Since an increase in ν leads to a reduction in large particle content, the shape of these plots is inverted compared to those in Fig. 4.7.

Figure 4.9c shows plots of $\bar{E}$ vs θ for a refractive index of 1.55 - i0.05, and for five selected values of ν. The Rayleigh approximation results are included for comparison. (Again, symbols without a cross represent Mie results; those with a cross represent Rayleigh results. The shape of these curves is simular to those in Figs. 4.5 and 4.6. We see from Fig. 4.9c that the Rayleigh approximation is good for this complex refractive index over the full range of ν values considered. As in the case of the Deirmendjian models, the Rayleigh approximation is not as good for a real refractive index.

(vi) Summary Remarks

From the foregoing discussion, it is obvious that the transmission law as expressed by Eq. (1) cannot be used except in the case of small

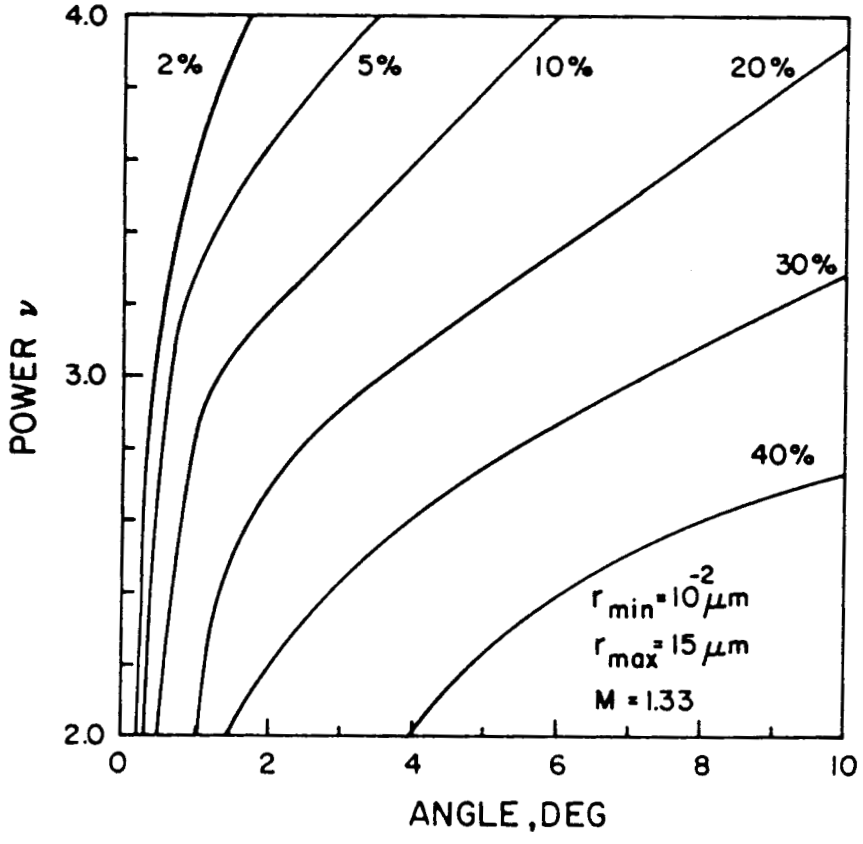

FIG. 4.9a. Error contours in the ν - θ plane for m = 1.33, λ = 0.55 μm, for the power law size distribution.

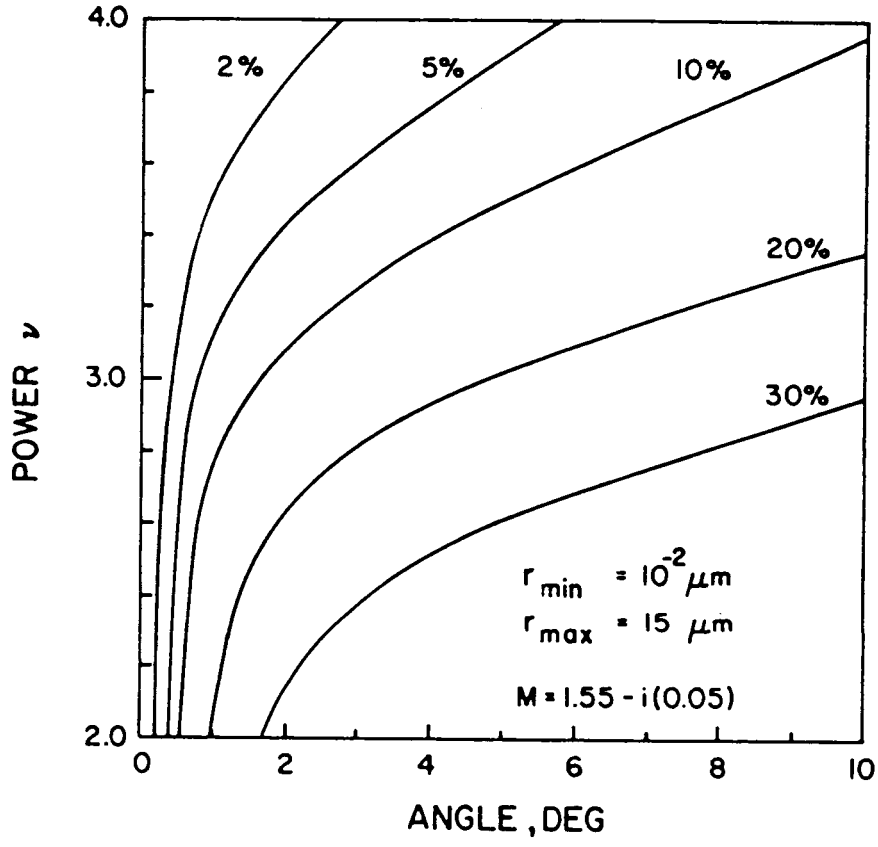

FIG. 4.9b. Error contours in the ν - θ plane for m = 1.55 - i(0.05), λ = 0.55 μm, for the power law size distribution.

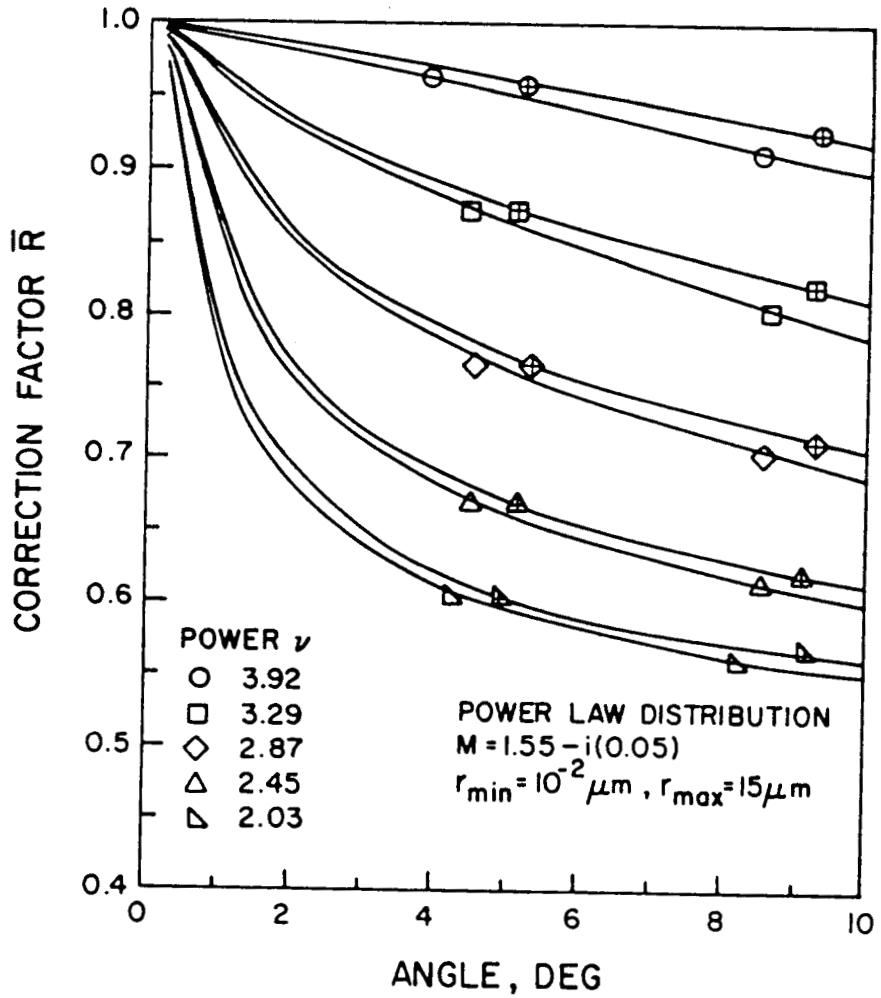

FIG. 4.9c. Plots of correction factor $\bar{R}$ versus θ for m = 1.55 - i(0.05), λ = 0.55 μm, and five values of the power, ν, for a power law size distribution. (Symbols without cross represent Mie results; symbols with cross, approximate results.)

particles, for which it is merely a good approximation. The effect of not only the particle size distribution, refractive index and shape but also the geometry of the optical system on the apparent volume scattering and extinction coefficients must be considered.

This study shows that the $\bar{R}$ ($\bar{E}$) decreases (increases) as the size distribution becomes more polydisperse. This result can be explained by the fact that as the polydispersity becomes greater, the relative proportion of larger particles increases, resulting in an increase in forwardscattered radiation within narrower angles. The results are valid for conditions in which multiple scattering effects can be neglected, and only single scattering predominates.

The lens-pinhole detector geometry yields the most accurate transmission/extinction results, provided the design conforms to the prescription that the value of y in Fig. 4.8 should be such that $\bar{R}$ is close to either 1.0 or 0.5.

4.2 FORWARD SCATTERING CORRECTIONS TO SOLAR RADIOMETRY

Following the extensive discussions of Angstrom (Refs. 64 and 65 and) others (Ref. 66), it is well known that measurements of attenuated direct solar radiation by pyrheliometers and sun photometers are subject to errors due to the presence of diffuse sky radiation within the detector's field of view (FOV). Diffuse radiation consists of both singly- and multiply-scattered radiation. The amount of diffuse radiation depends on the instrument aperture and the characteristics (amount and kind) of the scatterers in the atmosphere. The results discussed by Angstrom (Refs. 64 and 65) were based on a summary of a great number of measurements of circumsolar radiation; and those by Shaw (Ref. 66), were based on computations of diffuse sky intensity using the Deirmendjian-Sekera perturbation approach (Ref. 41). In this section, we show how, for relatively clear atmospheres, these results can be understood in terms of the so-called forward scattering corrections to optical extinction measurements discussed in two earlier papers (Refs. 62 and 67), and the multiple scattering contributions due to molecules alone. Under moderately clear sky conditions, the major contribution to the diffuse sky radiation entering the FOV of the detector at the ground-level is single scattering (SS) by aerosol particles and molecules and multiple scattering (MS) by molecules. Following the perturbation approach, we shall assume here that the MS contributions due to aerosols are negligible. Discussions of these SS and MS contributions will be presented for several typical aerosol size distributions. It will be shown that for clear sky conditions, errors due to molecular scattering may be neglected for many practical purposes.

(i) *Scattering Contributions*

Consider a radiometer with a circular aperture having a view cone of solid angle Ω_D, and its axis centered on the solar disk. Figure 4.10 shows (schematically) the geometry involved. The detector FOV is assumed to be circular, with a half-angle ψ_D. Angstrom and Rodhe (Ref. 64) have shown how to obtain an effective aperture half-angle in the case of a rectangular field-of-view, and it will be assumed that such a procedure has been performed in the case of such a non-circular field-of-view.

The total spectral irradiance $I(\lambda)$ at wavelength λ, measured by the receiver, is composed of contributions $I_{DIR}(\lambda)$, due to attenuated, direct solar radiation, and $I_{DIF}(\lambda)$, due to diffuse sky radiance entering the FOV, so that

$$I(\lambda) = I_{DIR}(\lambda) + I_{DIF}(\lambda) \tag{22}$$

where $I_{DIR}(\lambda)$ is given by Bouguer's law, namely

$$I_{DIR}(\lambda) = I_o(\lambda)\ e^{-\tau(y_o)\ \sec\ \theta_s} \tag{23}$$

and $I_{DIF}(\lambda)$, by the integral of sky radiance over the FOV,

$$I_{DIF}(\lambda) = \int_{\Omega_D} B(\lambda)\ d\Omega_D \tag{24}$$

Here, $I_o(\lambda)$ is the unattenuated solar spectral irradiance incident on top of the atmosphere; θ_s is the solar zenith angle; $\tau(y_o)$ is the total optical thickness above the point of observation (at altitude y_o km), and $B(\lambda)$ is the diffuse sky radiance within the elemental solid angle $d\Omega_D$.

In this paper, we restrict our discussions to the case of clear to low turbidity sky conditions, so that the major contributions to diffuse

sky radiation entering the FOV can, for all practical purposes, be assumed to be due to single scattering by particulates and molecules (I_{SS}) and multiple scattering by molecules (I^M_{MS}) alone. Thus,

$$I_{DIF}(\lambda) = I_{SS}(\lambda) + I^M_{MS}(\lambda) \tag{25}$$

A. Single Scattering Contribution

Fig. 4.10 illustrates the SS geometry. Following Green et al (Ref. 1), the SS contribution to the sky radiation is given by the expression (with the λ-dependence suppressed):

$$I_{SS} = I_o \int_{y_o}^{\infty} dy \int_o^{\psi_D} \sin\psi \, d\psi \int_o^{2\pi} d\phi \; e^{-\tau(y)\sec\theta_s} \sec\theta \; * \left\{ F_P(\psi,y) + F_M(\psi,y) \right\} e^{-(\tau(y_o) - \tau(y))\sec\theta} \tag{26}$$

where the volume scattering functions for molecules and particulates (subscripts M and P) are defined by

$$F_M(\psi,y) = \beta_M(y) \frac{3}{16\pi} (1 + \cos^2\psi), \qquad [km^{-1} \; sr^{-1}] \tag{27a}$$

$$F_P(\psi,y) = \int_o^{\infty} dr \; \eta(r,y) \; \{i_1(\psi, kr, m) + i_2(\psi, kr, m)\} / 2k^2, \qquad [km^{-1} \; sr^{-1}] \tag{27b}$$

the volume scattering coefficients, by

$$\beta_M(y) = \frac{8\pi^3 (m_S^2 - 1)^2}{3\lambda^4 N_S^2(o)} N_S(y) \qquad [km^{-1}] \tag{28a}$$

$$\beta_P(y) = \int_o^{\infty} dr \; \pi r^2 \; \eta(r,y) \; Q_{ext}(kr, m) \qquad [km^{-1}] \tag{28b}$$

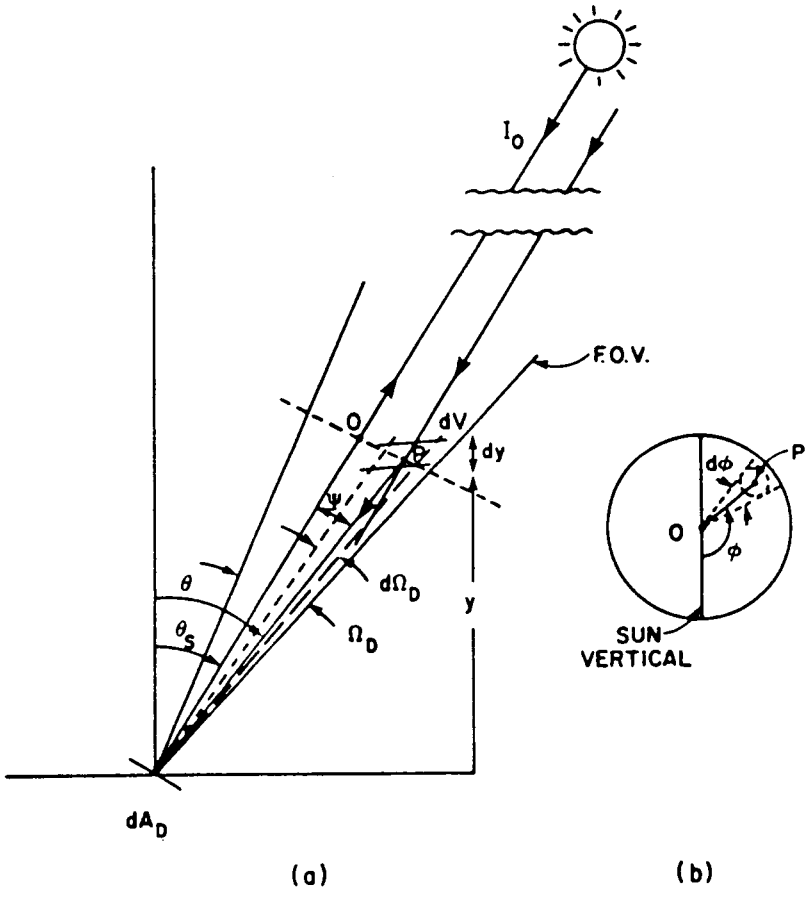

FIG. 4.10 Scattering Geometry for a Radiometer

and the optical depths by

$$\tau(y) = \int_y^\infty \{\beta_M(y') + \beta_p(y')\}\, dy' \tag{29}$$

In the above equations, $k = 2\pi/\lambda$ is the wavenumber; i_1 and i_2 are the Mie intensities (Ref. 32); m_S is the refractive index of air at 15°C and 1013 mb pressure (Ref. 68); $N_S(y)$ is the molecular number density at altitude y; m is the aerosol refractive index; θ is the zenith angle of an element of solid angle, and is given by the relation

$$\cos\phi_s = \cos\phi_s \cos\psi - \sin\phi_s \sin\psi \cos\omega \tag{30}$$

Finally, $\eta(r,y)$ is the aerosol number density per unit radius at radius r and altitude y ($cm^{-3}\ \mu m^{-1}$). It will prove useful to define the over-altitude distribution, N(r,y), by

$$N(r,y) = \int_y^\infty \eta(r,y')\, dy' \tag{31}$$

Hence, for example, we have

$$\tau_p(y) = \int_0^\infty \pi r^2\, Q_{ext}(kr, m)\, N(r,y)\, dr \tag{32}$$

B. Approximate Analytical Solution

Equation (26) involves a triple integral, and in general would require numerical computation. However, since most modern sun radiometers are designed to have small fields of view ($\psi_D < 8^\circ$), it seemed worth exploring the possibility of making some reasonable approximations, and performing

analytically as many of the integrals as possible. Although this leads to a small loss of accuracy, we feel this loss is more than outweighed by the insight that may be gained into the dependence of I_{SS} on the different parameters and variables. The details of these manipulations, along with a discussion of the results to be presented here.

Provided that ψ_D is reasonably small and ϕ_s not too large ($\phi_s \lesssim 60^o$), we may perform the integrations over ω and y to arrive at the following expression:

$$I_{SS} = I_o \sec \phi_s \, e^{-\tau(y_o)\sec\phi_s} \, 2\pi \int_0^{\psi_D} \sin\psi \, d\psi \{F'_P(\psi,y_o) + F'_M(\psi,y_o)\} \qquad (33)$$

where the columnar scattering functions are defined by

$$F'(\psi,y_o) = \int_{y_o}^{\infty} F(\psi,y) \, dy \qquad (3$$

The integral over $F'_p(\psi,y_o)$ depends on the particulate phase function and, hence, on the particulate size distribution which, in general, may be altitude dependent, i.e., $\eta(r,y)$. However, in Refs. 62 and 67, we have shown how to perform such integrations, at least formally, by introducing an error factor, E, or correction factor, R, which will be denoted here by E_p and R_p, and defined as:

$$E_p = \frac{\pi}{\tau_p k^2} \int_0^{\infty} dr \int_0^{\psi_D} d\psi \sin\psi \, N(r,y_o) \, (i_1 + i_2)$$

$$= \frac{2\pi}{\tau_p(y_o)} \int_0^{\psi_D} \sin\psi \, F'_p(\psi,y_o) \, d\psi \qquad (35a$$

and $$R_P = 1 - E_P \tag{35b}$$

An explanation of Eq. (35a), defining the error factor, is briefly described in Appendix 4B. In Refs. 62 and 67 (and Appendix 4B), a bar (-) and a tilde (~) over E and R, are used to denote the respective averaging with respect to size distribution (i.e., integration over r) and path length (i.e., integration over y). For notational convenience, we omit both these symbols from E_P and R_P in the main body of this paper; though it must be kept in mind that both integrations are clearly implied here. Thus, in Eq. (33),

$$2\pi \int_0^{\psi_D} \sin\psi \, d\psi \, F'(\psi, y_o) = \tau_P(y_o) \, E_P \tag{36}$$

In the molecular case, the integral over $F'_M(\psi, y_o)$ can be performed exactly to yield

$$2\pi \int_0^{\psi_D} \sin\psi \, F'_M(\psi, y_o) \, d\psi = 2\pi \int_0^{\psi_D} \sin\psi \, d\psi \, \frac{3}{16\pi} (1 + \cos^2\psi) \int_{y_o}^{\infty} \beta_M(y) \, dy$$

$$= \tau_M(y_o) \, E_M \tag{37a}$$

where

$$E_M = \frac{1}{2} - \frac{3}{8} \cos\psi_D - \frac{1}{8} \cos^3\psi_D \tag{37b}$$

where $\tau_M(y_o)$ is the molecular optical depth and E_M is the error factor for extinction measurements due to forward scattering in a pure molecular atmosphere. For

$$\psi_D < 10^o, \quad E_M \simeq 3\psi_D^2/8 \tag{37c}$$

Using Eqs. (36) and (37a) in Eq. (38), one obtains

$$I_{SS} = I_o \sec \phi_s \, e^{-\tau(y_o) \sec \phi_s} \, (\tau_P(y_o) E_P + \tau_M(y_o) E_M) \qquad (38)$$

C. Molecular MS Contribution

In his paper, Shaw (Ref. 66) made use of the perturbation method of Deirmendjian (Ref. 41) to include multiply-scattered light due to molecules alone. Recently, we have examined (and slightly modified) this method (Refs. 26, 27, and 50), and shown that most of the multiply-scattered light in the aureole region can be accounted for by this approach, at least for aerosol optical depths $\tau_P \leq 0.2$. (For $\tau_P > 0.2$, the neglect of particulate MS may lead to errors, which may require a much more complete and complicated analysis).

In Ref. 26, we showed that, at least within the aureole region, we may use the perturbation method by simply replacing the molecular optical depth, τ_M, by an effective molecular optical depth $t_M(y_o)$ which depends on $\tau(y_o)$, θ_s and on ground albedo, A. (This dependence is discussed in detail in Ref. 27.) Alternatively, we may include molecular multiple scattering by adding a second molecular term of the form $t_{MS} E_M$. Implicit here is the assumption that the shape of the angular distribution of the multiply scattered light in the region of the solar aureole (i.e., scattering angles $\leq 10^o$) is similar to that of the singly scattered Rayleigh contribution, only the magnitude differs by a factor f. For moderately clear skies, this is a reasonably accurate approximation. Thus, we may write

$$I_{MS}^M = I_o \sec \phi_s \, e^{-\tau(y_o) \sec \phi_s} \, t_{MS}(y_o) E_M \qquad (38')$$

and, hence, we get for the total diffuse radiation

$$I_{DIF} = I_{SS} + I_{MS}^{S} = I_o \sec \phi_s \, e^{-\tau(y_o)\sec\phi_s} \{\tau_P(y_o)E_P + (\tau_M(y_o) + t_{MS}(y_o))E_M\} \quad (39)$$

t_{MS} is related to the effective molecular optical depth t_M introduced in Ref. 26 by $t_M = \tau_M + t_{MS}$. t_{MS}, t_M and the ratio, $f = t_M/\tau_M$, are given in Table 4.1 for a series of values of τ_M (covering the full visible spectrum) and τ_P up to 0.2. A solar zenith angle of 45^o was chosen, and ground albedo was assumed to be zero. In general, these results are not sensitive to ϕ_s, unless the sun is quite low ($\phi_s > 70^o$) in the sky, in which case spherical earth corrections have to be taken into account and most of our approximations break down. It is possible to make allowance for ground reflection by multiplying t_M (or f) by a factor of (1 + A). Also shown in Table 4.1 is the ratio $F = t_M/\tau_P$, which will prove useful in the following discussion.

(ii) *Total Measured Intensity*

From the above discussion, we see that the total irradiance recorded by the detector is then simply the sum of Eq.(23) and Eq.(39) (c.f., Eq. (22)), i.e.,

$$I = I_o \, e^{-\tau(y_o)\sec\theta_s} \{1 + \sec\theta_s(\tau_P(y_o)E_P + t_M(y_o)E_M)\} \quad (40)$$

For $\tau_P(y_o) \sim 0.2$, $t_M(y_o) \sim 0.5$, and $\psi_D \sim 9^o$, E_M is about 0.01 (c.f., Eq. (37)), and for typical aerosols, E_P is about 0.1 (see below). So, for $\theta_s \leq 60^o$, the second term in Eq. (40) is $\lesssim 0.05$--i.e., the diffuse light contributes roughly 5% to the total. For a solar radiometer with $\psi_D \approx 4^o$, the diffuse contribution is roughly 1%. Since the values of τ_P, t_M and θ_s used in

TABLE 4.1: Effective Molecular Optical Depths and Related Multiple Scattering Factors, for θ_s and 45^o and A = 0.0

τ_M	τ_P	t_{MS}	t_M	$f \equiv t_M/\tau_M$	$F \equiv t_M/\tau_P$
0.02	0.02	0.002	0.022	1.110	1.110
	0.05	0.007	0.027	1.338	0.535
	0.10	0.020	0.040	1.993	0.349
	0.20	0.067	0.087	4.338	0.434
0.05	0.02	0.007	0.057	1.135	2.838
	0.05	0.014	0.064	1.276	1.276
	0.10	0.031	0.081	1.621	0.810
	0.20	0.086	0.136	2.724	0.681
0.10	0.02	0.020	0.120	1.199	5.993
	0.05	0.031	0.131	1.310	2.621
	0.10	0.055	0.155	1.552	1.552
	0.20	0.124	0.224	2.242	1.121
0.20	0.02	0.067	0.267	1.334	13.338
	0.05	0.086	0.286	1.431	5.724
	0.10	0.124	0.324	1.621	3.242
	0.20	0.221	0.421	2.104	2.104
0.40	0.02	0.243	0.643	1.608	32.167
	0.05	0.279	0.679	1.698	13.587
	0.10	0.345	0.745	1.862	7.449
	0.20	0.497	0.897	2.242	4.483

these examples are probably a little bit on the high side, and since most solar radiometers have view-cone half-angles of less than 5^{o}, it is clearly reasonable to conclude that, in general, the diffuse contribution to the total measured irradiance will be less than, or of the order of, 1%.

With these results in mind, we may now re-write Eq. (40) as follows:

$$I = I_o \, e^{-\sec \phi_s \{\tau(y_o) - (\tau_P(y_o) E_P + t_M(y_o) E_M)\}} \tag{41}$$

(iii) *Corrected Optical Thickness and Sensitivity Analysis*

Much of the spectral solar radiometry is performed to determine the total atmospheric optical thickness, and therefrom, for example, the aerosol optical thickness. Although we have just seen that the diffuse contribution to the total measured intensity is only about 1%, we now show that the error in the aerosol optical thickness obtained from such measurements may suffer somewhat greater error.

(a) Corrected Optical Thickness

The apparent, or measured, optical thickness $\tau'(y_o)$ is defined according to Bouguer's law, viz.,

$$I = I_o \, e^{-\tau'(y_o) \sec \phi_s} \tag{42}$$

Then, by comparing Eqs. (41) and (42), one can obtain the following relation between the measured optical thickness and the true optical thickness:

$$\tau'(y_o) = \tau(y_o) - \{\tau_P(y_o) \; E_P + t_M(y_o) \; E_M\} \tag{43}$$

Omitting the y dependence, one can rewrite Eq. (43) as

$$\tau' = \tau - \tau_P E_P - t_M E_M \tag{44}$$

As will be shown below, E_P is generally larger than E_M by a factor of 10 or so. Thus, under circumstances in which the ratio $F = t_M/\tau_P$ is no larger than, say, 2, we may neglect the molecular term in Eq. (44). (This will clearly depend on both the radiation wavelength, and the atmospheric haziness.) In this case, we may write Eq. (44) as

$$\tau' = \tau - \tau_P E_P \tag{45}$$

And further if $\tau = \tau_M + \tau_P + \tau_{O_3}$, then from Eq. (45) one obtains:

$$\tau' = \tau_M + \tau_{O_3} + \tau_P R_P \tag{46}$$

Assuming that τ_M and τ_{O_3} are known, then the experimental value for the particulate optical depth, τ_P', which may be obtained by subtraction from τ' (i.e., $\tau' = \tau_M + \tau_P' + \tau_{O_3}$), will be in error by a factor of R_P, i.e.,

$$\tau_P' = \tau_P R_P \tag{47}$$

Thus, we see that the correction factor, R_P, represented by $\hat{\hat{R}}$ in our earlier papers (Refs. 62 and 67), is precisely the factor we need to correct experimentally-determined values of aerosol optical depth, in many cases. In the cases where molecular contribution cannot be ignored, the following relation should be used

$$\tau_P' = \tau_P R_P - t_M E_M \tag{48}$$

i.e.,

$$\tau_P = (\tau_P' + t_M E_M)/R_P \tag{48'}$$

(b) Sensitivity Analysis

In this section, we shall try to obtain some idea of the behavior of E_P or R_P for different size distributions and aperture half-angles, and compare our results (Eq. (48)) with those of Angstrom and Shaw. Although the integrals in Eq. (35) cannot be performed analytically for any real case, it is possible to gain considerable insight by a brief consideration of the Henyey-Greenstein phase function, which is usually written as

$$P(\mu,g) = \frac{1 - g^2}{4\pi(1 - 2g\,\mu + g^2)^{3/2}} \tag{49}$$

where g is the asymmetry factor, and $\mu = \cos\psi$. In this case, we obtain for E_P

$$E_P(\mu_D,g) = \frac{(1 + g)\,\{(1 - 2g\,\mu_D + g^2)^{1/2} - 1 + g\}}{2g\,(1 - 2g\,\mu_D + g^2)^{1/2}} \tag{50}$$

Note that $E_P(1,g) = 0$ and $E_P(-1,g) = 1$, as required.

For small values of ψ_D (say $\psi_D \lesssim 10^\circ$), and g not too close to unity, we may expand Eq. (50) to give

$$E_P(\psi_D,g) \simeq \frac{1 + g}{(1 - g)^2}\,\frac{\psi_D^2}{4} \tag{51}$$

c.f., Eq. (37c) for E_M. Note that for g = 2/3, Eq. (51) gives $E_P = 3.75\,\psi_D^2$, which is just 10 times E_M.

In. Fig. 4.11, we plot E_P against Ψ_D, for a number of values of g. Also plotted on Fig. 4.11 is E_M multiplied by 10. As can be seen, this curve lies

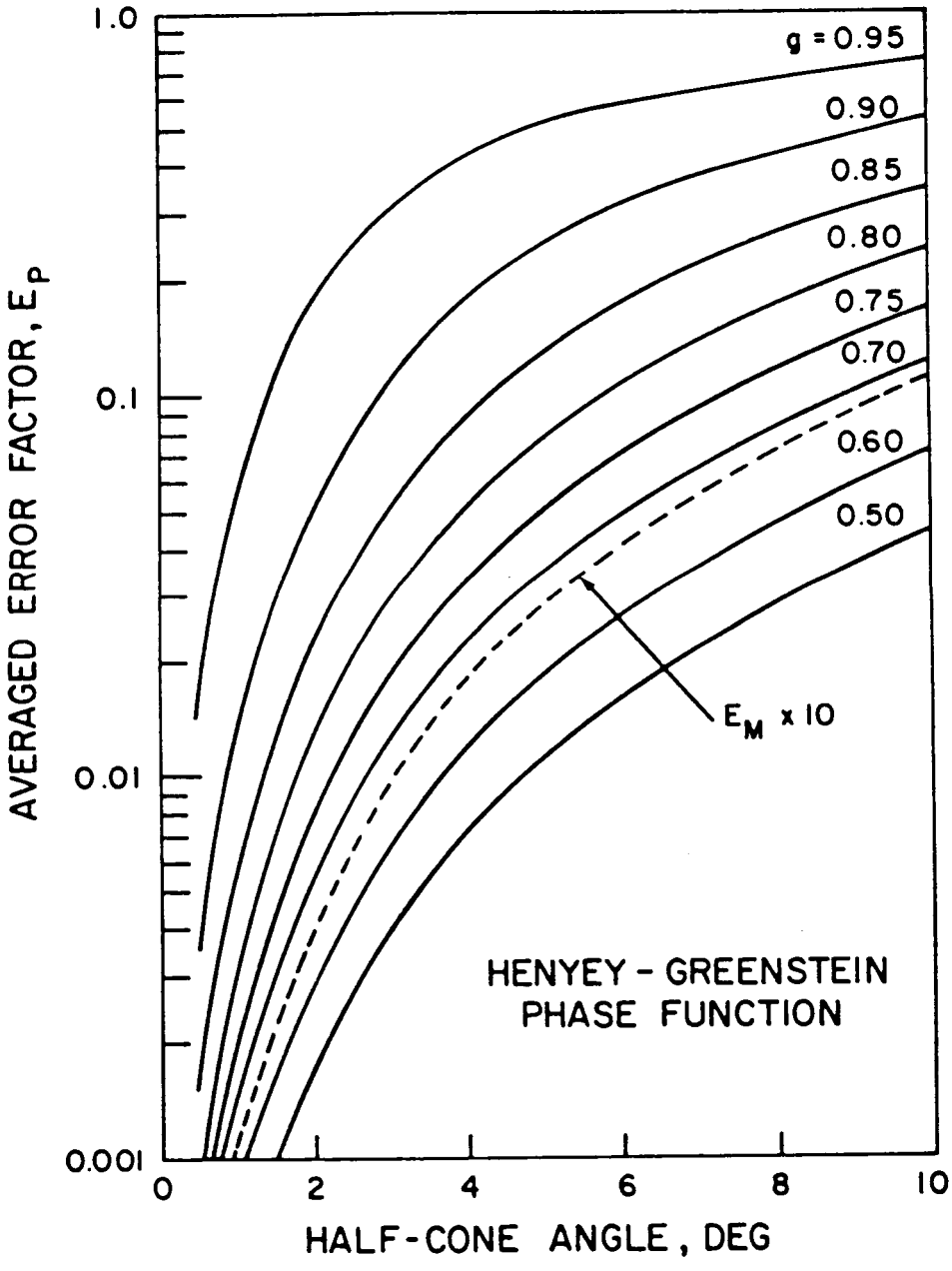

FIG. 4.11 Error Factor for the Henyey-Greenstein Phase Function

approximately where the curve for g = 0.67 might be expected to lie. Since most tropospheric aerosols, and virtually all fogs and clouds, have asymmetry factors of around 0.7 or higher (Refs. 69, 70), our earlier statement that E_P should normally exceed E_M by an order of magnitude is seen to be correct for a wide range of view-cone half-angles, ψ_D.

In Ref. 67, presented a number of graphs depicting the behavior of E_P and R_P as functions of both view-cone angle and size distribution parameters, for a number of modified-gamma-type size distributions, and also for a power law size distribution. Here, in Figs. 4.12 and 4.13, we give some further examples of R_P to illustrate the magnitude of the effect.

In Figs. 4.12 a) and b), we consider the size distribution $n(r) = C\, r^{-\nu}$ for $0.01 \leq r \leq 15$ μm, and plot R_P against ν for a number of view-cone half angles and R_P against ψ_D for a number of ν values. (Being ratios, R_P and E_P are independent of scaling parameters such as C.) We see that, even for small view cone angles, R_P deviates from unity quite significantly, if ν is sufficiently small. (Small values of ν imply a higher percentage of large particles.) For larger view-cone angles, even $\nu = 3$ implies a significant effect.

In Fig. 4.13, we consider the size distribution $n(r) = ar^2\, e^{-br}$, and plot R_P against view-cone angle, for several values of b. Again, we see that for small values of b, a significant correction is required even for small view-cone angles. (Small b, again, implies more large particles, as the mode radius of this size distribution is given by $r_m = 2/b$ μm.) With larger view-cone angles, even moderate b-values imply a significant correction.

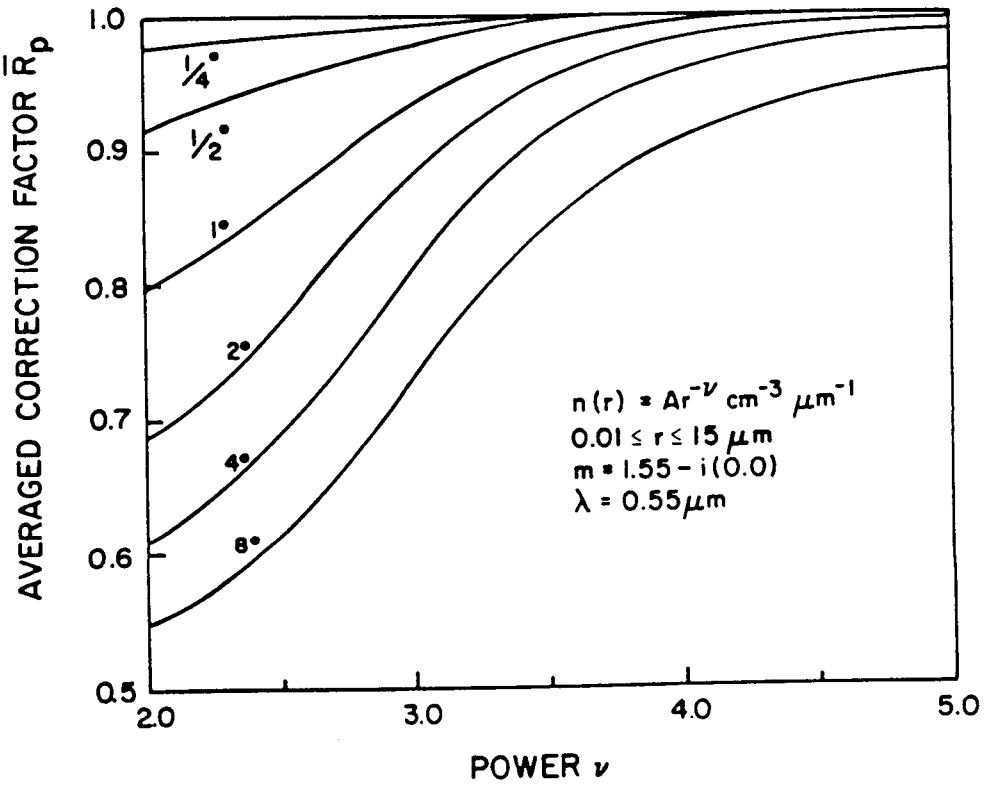

FIG. 4.12 a): Correction Factor as a Function of the Exponent γ for a Power-Law Size Distribution

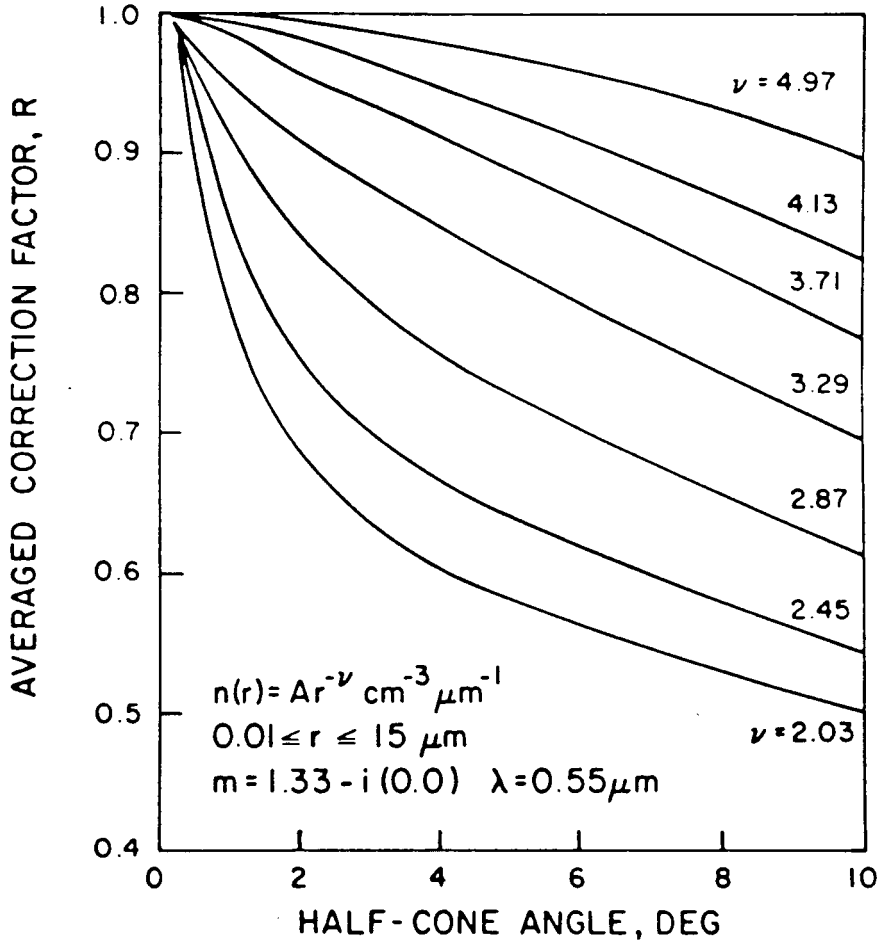

FIG. 4.12 b): Correction Factor as a Function of Half-Cone Angle for a Power-Law Size Distribution

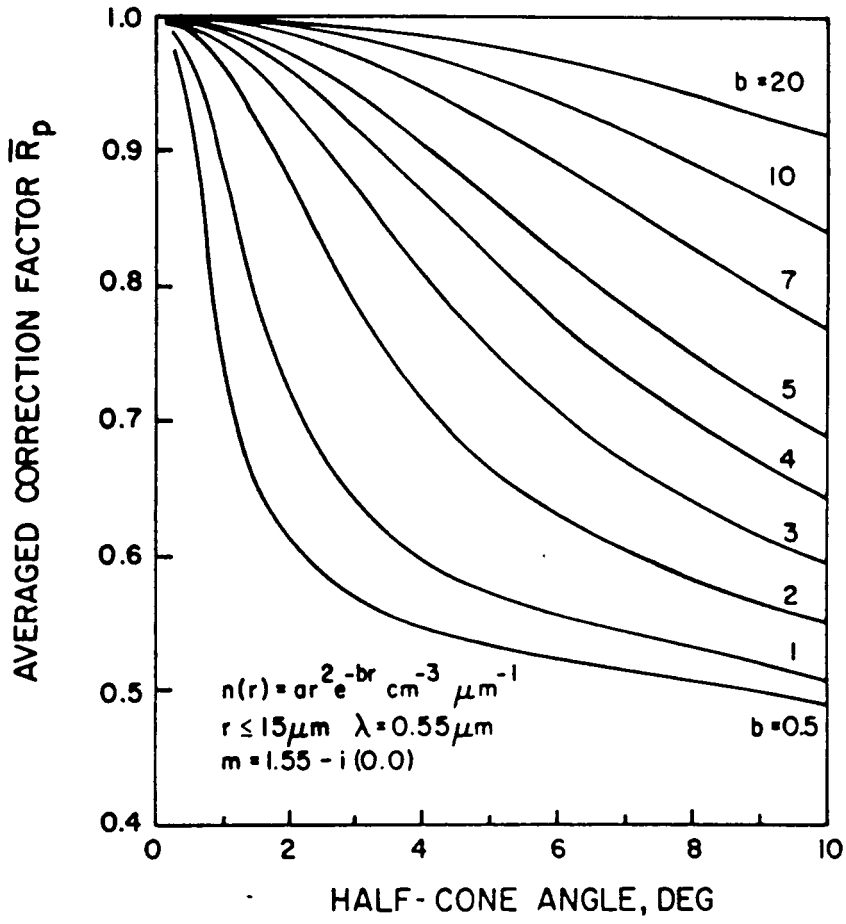

FIG. 4.13 Correction Factor as a Function of Half-Cone Angle for Modified Gamma Type Size Distribution (Model Haze H)

(iv) *Retrieval Algorithms for Aerosol Size Distribution*

The question arises: Can we use the results presented in this paper to determine the true optical thickness or extinction coefficient without an *a priori* knowledge of the aerosol size distribution (often the object of the extinction measurements in the first place)? The answer is in the affirmative; we shall explain, in this section, the strategies and the algorithms adopted for the retrieval of aerosol size distributions from the measured optical quantities.

Many tropospheric aerosols follow power-law size distributions (Ref. 71), and thus the results presented in Fig. 4.12 are applicable. To this end, we note that for a power-law distribution, E_p and R_p are independent of wavelength, and E_p is given by

$$E_p(n(r) \sim r^{-\nu}) = \frac{\int_0^{\infty} \int_0^{\psi_D} x^{-\nu} \sin\psi \, (i_1 + i_2) \, d\psi \, dx}{\int_0^{\infty} x^{2-\nu} \, Q(x) \, dx} \tag{52}$$

where the size parameter, $x = kr$.

Thus, if the underlying size distribution is of power-law form, which leads, as is well known (Refs. 71, 72), to power-law behavior for τ_p as a function of λ, then the measured τ_p' values will still exhibit power-law behavior, with the same power. Hence a simple procedure is available in such cases: to the measured τ_p' values, fit the power-law curve

$$\tau_p'(\lambda) \simeq \beta_p' \lambda^{-\alpha} \tag{54}$$

Then, since $\nu = \alpha + 3$, go to Fig. 4.12 and read off the value of R_p for this ν and view-cone half angle ψ_D. Finally, correct all values of τ_p' by multiplying by R_p^{-1} (or alternatively, multiply β_p' by R_p^{-1}).

For other size distributions, R_p is not independent of wavelength, and this simple procedure is not available. However, it is easy to modify inversion algorithms to include the forward scattering correction, as follows. Standard algorithms to obtain $N(r,y_o)$ from a series of multispectral extinction measurements are based on the numerical inversion of the integral equation (Refs. 73, 74, 57).

$$\tau_p(\lambda) = \int_0^\infty \pi r^2 N(r,y_o) Q(kr) dr \tag{54}$$

However, we now know that it is not τ_p, but τ_p' that we measure, and thus the integral equation to be inverted should be

$$\tau_p'(\lambda) = \int_0^\infty \pi r^2 N(r,y_o) Q'(kr) dr$$

$$= \int_0^\infty \int_{\psi_D}^\pi \pi N(r,y_o) (i_1 + i_2) \sin\psi \, d\psi \, dr/k^2 \tag{55}$$

(c.f. Eqs. (B1), (B3) and (B4))

Although it is true that

$$Q' = \int_{\psi_D}^\pi (i_1 + i_2) \sin\psi \, d\psi / x^2 \tag{56}$$

is more difficult to compute than Q, we have shown in Ref. 58 that the recent formulation by Wiscombe and Chylek (Ref. 75) makes the computation of Q' considerably easier than it might at first appear. We also note that, since for a given instrument the value of ψ_D is fixed, there is no increase in the number of kernal values that must be computed and stored, so that storage on disk is still practical. Finally, we note that inversion of Eq. (55) should prove no more difficult than inversion of Eq. (54), so that the same algorithms may be used; only the kernal functions will be slightly modified.

In those cases where it is not possible to ignore the molecular contribution to I_{DIF}, then the integral equation to be inverted will become

$$\tau_P'(\lambda) + t_M(\lambda)\ E_M = \int_0^\infty \pi\ r^2\ Q'(kr)\ N(r,y_o)\ dr \qquad (57)$$

Again, the inversion of this equation is no more difficult than inversion of Eq. (54).

(v) *Discussion of Assumptions*

The result presented in Eq. (47) is particularly simple and elegant, and it is worth considering carefully, the conditions under which it is valid. A discussion of the simplifying approximations made in its derivation is given as follows.

The first approximation which was needed to analytically perform the integration over the equatorial angle, ϕ, is considered in Appendix 4A. This made the integration over altitude fall out; thus, leaving only the

C-3

integration over scattering angle, ψ, which was performed by introducing the error factor E. The accuracy of this approximation is shown in Table 4.2. Essentially, one may conclude that this approximation will be accurate for most modern radiometers, except for the case of large zenith angles ($> 70^{o}$), in which case one must take account of spherical earth corrections.

The second approximation involved the neglect of the scattering contribution of molecules relative to that of aerosols. As the particulates are much larger than air molecules, they scatter most of the photons in the near forward direction. For this reason, E_p is, in general, larger than $E_M = 3\ \psi_D^2 / 8$, by an order of magnitude or more. Thus, neglect of the molecular contribution would seem to be reasonable, unless the aerosol optical depth happens to be exceptionally low, in which case Eq. (47) should be replaced by Eq. (48).

The third approximation involves the use of the Deirmendjian perturbation technique to account for the MS light. This technique, which we have examined via numerical experiments in Refs. 47 and 48, and applied successfully to the analysis of experimental aureole data (Ref. 71), appears to account for most of the details of the radiance distribution in the solar aureole region. Under this approximation, all the MS radiation results from the molecules alone, and can be accounted for by replacing τ_M by an effective optical depth, t_M. Since the effect of this procedure is to roughly double the molecular contribution to I_{DIF}, the arguments for ignoring this contribution should remain valid. If necessary however, we may employ Eq. (48) to include this contribution.

TABLE 4.2: Percentage Errors Involved in Using Eq. (A5)

	Solar Zenith Angle				
ψ	30°	40°	50°	60°	70°
1°	0.0	0.0	0.0	0.1	0.1
2°	0.1	0.1	0.1	0.2	0.5
3°	0.2	0.2	0.3	0.6	1.2
4°	0.3	0.4	0.6	1.0	2.1
5°	0.5	0.7	0.9	1.6	3.4
6°	0.7	0.9	1.3	2.3	5.0
7°	1.0	1.3	1.8	3.1	7.0
8°	1.3	1.7	2.4	4.1	9.5
9°	1.7	2.2	3.1	5.3	12.5
10°	2.1	2.7	3.9	6.6	16.1

The main approximation in using the perturbation technique, however, is that we have ignored all MS events which involve aerosols. The results of our previous investigations (Refs. 26, 27, 30) suggest that this assumption is highly accurate for aerosol optical depths of about 0.1, and still quite accurate upto $\tau_p = 0.2$. Furthermore, the experimental results compiled by Angstrom and Rodhe (Ref. 64) indicate that the diffuse radiation contribution is directly proportional to τ_p, which is in complete agreement with our results.

The fourth approximation was outlined between Eqs. (40) and (41), and can be expressed as

$$1 + \sec\theta_s(\tau_P E_P + t_M E_M) \simeq e^{\sec\theta_s(\tau_P E_P + t_M E_M)} \qquad (58)$$

This is a valid approximation (i.e., $\lesssim$ 2% error), provided $\sec\theta_s(\tau_P E_P + t_M E_M)$ is small ($\lesssim 0.2$), and clearly depends on solar zenigh angle, haziness, and ψ_D: E_P and E_M increase roughly as ψ_D^2. Again, as discussed earlier, an instrument with a small view-cone half-angle, ψ_D, may be used at larger solar zenith angles, and also under more turbid conditions, before the approximation (Eq. (58)) breaks down. It is worth commenting that the terms neglected in Appendix 4A are of similar form to the next term in the above series expansion, and so these two errors will tend to compensate. The results of Shaw's numerical study (Ref. 66), which employs only our third approximation, shows that $\tau_p - \tau_p'$ is independent of θ_s until θ_s reaches a large value (~ 75°), whereupon this independence breaks down rapidly. (The higher the value of τ_p, the sooner the breakdown occurs, as would be expected, although the range of zenith angles involved is quite

narrow.) Again we must add that for such large solar zenith angles, spherical-earth corrections are required, adding further complications.

And, finally, it has been assumed here that the sun is a point source at infinite distance, and that, as a result, solar radiation falls on the atmosphere as parallel rays. In reality, the sun has an angular diameter of 1/2 degree, so that all scattering angles, ψ (see Fig. 4.10) should be blurred a little, i.e., averaged over ± 1/4 degree. This so-called blurring effect is complicated, due to the three-dimensional geometry, solar limb-darkening (see Ref. 76) and the wavelength-dependence of the latter. We shall refer to this as the "finite-sun effect." One result of this effect is that even for a radiometer with a minute field of view, such as is used in the SAM-II and SAGE satellite missions (Ref. 76), the effective value of ψ_D will still be 1/4 degree. However, this situation is quite complex and will not be discussed here. This and other effects of the finite angular size of the sun (such as in aureole measurements close to the sun), are being given careful examination and will be discussed in a separate paper.

(vi) *Discussion of Results and Concluding Remarks*

In his 1976 paper, Shaw (Ref. 66) considered just one size distribution and plotted $\delta\tau_p \equiv \tau_p - \tau_p'$ against $\mu_s (= \cos\theta_s)$ for three values of τ_p. His results show that $\delta\tau_p$ is essentially independent of μ_s, unless $\mu_s \lesssim 0.2$ i.e., $\sec\theta_s \gtrsim 5$ or $\theta_s \gtrsim 75^o$. It is just for these large zenith angles that the exponential approximation involved in going from Eq. (41) to Eq. (42) is liable to prove invalid, and so this aspect of Shaw's results is in complete agreement with our own conclusions.

The second observation to be made from Fig. 4.10 in Ref. 66 is that $\delta\tau_p$ i directly proportional to τ_p - in complete agreement with our Eq. (47)-- except for a small offset (i.e., $\delta\tau_p \neq 0$ when $\tau_p = 0$). This offset can easily be understood in terms of the molecular contribution which we have chosen to ignore for moderately turbid skies, but which should be included in cases of extremely low τ_p.

Shaw also plotted I_{DIF} / I_{DIR} against μ_s for the same values of τ_p. His results suggest that this ratio is inversely proportional to μ_s - i.e., directly proportional to sec ϕ_s - which is clearly in agreement with our equations.

The results presented by Angstrom (Refs. 64 and 65) for pyroheliometer measurements are actually experimental, based on a synthesis of a great many measurements. He shows plots of the ratio of diffuse to direct, as a function of ψ_D, for four different values of the "turbidity parameter" τ_p sec ϕ_s, and their shape as a function of ψ_D is consistent with our plots of E against view-cone angle in Ref. 67. Both of these conclusions are consistent with our results.

We may conclude from these studies, that under most relative clear sky conditions, the diffuse contribution to the total intensity will be small-- say 1% or less. A larger effect will result if the optical thickness, the radiometer half-cone angle, or the solar zenith angle, is particularly large, and especially if several of the factors pertain simultaneously. This conclusion will remain essentially unchanged, regardless of whether the instrument is operating in a broad band or a narrow band mode.

However, if multispectral extinction measurements are made, with the object of studying the wavelength variation of the aerosol optical thickness, then such results may well contain significant errors. Programs designed for this purpose, clearly should make allowance for this effect.

Often, the object of such multispectral extinction programs, is the determination, using varying levels of approximation, of the aerosol size distribution. The simplest such approximation, that of extracting only the Junge power, ν, requires essentially no modification at all. Even more complicated algorithms may be corrected using the relatively simple modifications discussed above. In view of the importance of the effects discussed in this paper, it is our opinion that all retrieval algorithms should be so modified, in order to minimize such errors.

APPENDIX 4A

Here, an outline is given of the steps taken, and the approximations employed, in going from Eq. (26) to Eq. (33).

First consider the integration over the equatorial angle, ω. Collecting all terms which involve ϕ (see Eq. (9)) we come to the following integral:

$$I_\phi = \int_0^{2\pi} d\phi \; e^{-(\tau(y_o) - \tau(y))} \; f(\phi,\psi,\phi_s) \qquad f(\phi,\psi,\phi_s) \tag{A1a}$$

where

$$f(\omega\,\psi,\phi_s) \equiv (\cos\phi_s \cos\psi - \sin\phi_s \sin\psi \cos\omega)^{-1} \tag{A1b}$$

Now if ψ is small, which it should be for a good photometer, and ϕ_s is not too large ($< 75^o$), then we may expand f to second order in ψ-(note that the first order term will integrate to zero when I_ϕ is evaluated)-giving

$$f \simeq \sec\phi_s \; (1 + \psi \tan\phi_s \cos\phi + \psi^2 \tan^2\phi_s \cos^2\omega + \frac{1}{2}\psi^2) \tag{A2}$$

After tedious, but straightforward manipulations, I_ω may now also be evaluated to second order in ψ, yielding

$$I_\phi \simeq 2\pi \sec\phi_s \; e^{-t \sec\phi_s} \{1 + \psi^2 \, g(t,\phi_s)\} \tag{A3}$$

where

$$g(t,\phi_s) = \frac{1}{2}\sec^2\phi_s - t\sec\phi_s\left(\tan^2\phi_s + \frac{1}{2}\right) + \frac{1}{4}t^2\tan^2\phi_s\sec^2\phi_s \qquad (A4)$$

and

$$t = \tau(y_o) - \tau(y)$$

The approximation we now wish to make is to ignore $\psi^2 g$, and all higher terms. Provided that neither ψ_D nor θ_s is too large, this would appear to be a perfectly reasonable step. Note that an instrument with a small view-cone angle may be used at larger zenith angles than one with a larger view-cone angle, before the approximation breaks down. The approximation we thus intend to make is to write

$$I_\phi \simeq 2\pi\sec\phi_s\, e^{-(\tau(y_o) - \tau(y))\sec\phi_s} \qquad (A5)$$

To test the accuracy of this approximation, we have evaluated Eq. (A1) numerically, and compared the results with those from Eqs. (A3) and (A5), for $\phi_s = 30^\circ\ (10^\circ)\ 70^\circ$, $\psi = 1^\circ\ (1^\circ)\ 10^\circ$, and $t = 0\ (0.2)\ 1.0$. For the smaller values of θ_s and ψ, Eq. (A5) proved to be a highly accurate approximation to Eq. (A1), and Eq. (A3) proved to be extremely accurate. As either ϕ_s or ψ approached the limits of their allotted ranges, the accuracies of both Eq. (A3) and Eq. (A5) started to fall off, and especially (as expected) when both limits were being approached.

As an indication of the accuracy of Eq. (A5), Table A2 contairs the percentage errors it entails, for a variety of ϕ_s-ψ combinations. In each case, we

have listed the error corresponding to t = 0, which is invariably the largest. (Remember that we still have an integration over y (i.e., t) to perform. This will reduce the actual errors involved, by an amount which will depend on $\tau(y_o)$.) The errors involved in using Eq. (A3) are not tabulated, but in most cases they are lower by a decade or more.

When Eq. (A5) is used instead of Eq. (A1) in Eq. (5), the latter reduces to

$$I_{SS} = I_o \sec \phi_s \, 2\pi \int_o^{\psi_D} \int_{y_o}^{\infty} dy \, e^{-\tau(y) \sec \phi_s} \, e^{-(\tau(y_o) - \tau(y)) \sec \phi_s} \{F_p + F_M\} \sin \psi \, d\psi \qquad \text{(A6)}$$

which leads immediately to Eq. (12).

If the $\psi^2 g$ term is retained, it is still possible, at least in principle, to perform the integration over altitude. However, the integration over ψ becomes much more complex, and nothing seems to be gained by the inclusion of these terms. We point out though, that there is some slight resemblance between these terms, and the next couple of terms in the expansion of the exponential in Eq. (42). Thus the approximation of ignoring $\psi^2 g$, and the approximation in going from Eq. (41) to Eq. (42), should tend to cancel, rather than reinforce, one another.

APPENDIX 4B

Described here is an alternate derivation of the scattering correction factor R to optical extinction measurements, that follows the approach described in Refs. 62 and 67.

First, consider extinction measurements in monodisperse aerosols. Due to the finite size of the detector, some of the light scattered by the particles will be intercepted by the view cone, so that the measured extinction coefficient (β') will differ from the true extinction coefficient, β. Then one may define a correction factor, R, for monodispersions as

$$R = \frac{\beta'}{\beta} = \frac{Q'}{Q} = \int_{\psi_D}^{\pi} (i_1 + i_2) \sin\psi \, d\psi \; / \; Q \, k^2 \, r^2 \qquad \text{(B1a)}$$

where ψ_D is the acceptance angle of the detector and r is the particle radius; and the corresponding error factor, E, as

$$E = 1-R = \frac{Q - Q'}{Q} = \int_{o}^{\psi_D} (i_1 + i_2) \sin\psi \, d\psi \; / \; Q \, k^2 \, r^2 \qquad \text{(B1b)}$$

Although these definitions apply strictly only to aerosols with real refractive indices, they may easily be extended to absorbing aerosols, as shown in Ref. 62.

For polydisperse aerosols, these two factors should be averaged over the size distribution as well as the path length. Thus the size distribution averaged correction factor $\bar{R}$ is

$$\bar{R} = \frac{\bar{\beta}'}{\bar{\beta}} = \frac{\pi}{\beta k^2} \int_{\psi_D}^{\pi} \int_{o}^{\infty} (i_1 + i_2) \, n(r) \, dr \sin\psi \, d\psi$$

and the corresponding error factor is

$$\bar{E} = 1-\bar{R} \tag{B2}$$

A further averaging over the path length needs to be performed, to yield $\hat{\bar{R}}$ and $\hat{\bar{E}}$. In Ref. 67, we assumed that aerosol was uniformly distributed along the beam path, whereas in the case of sun radiometry, for a constant acceptance half angle ψ_D, the aerosol number density varies with altitude. Then, we may define the altitude-averaged correction factor, $\tilde{\bar{R}}$, as

$$\tilde{\bar{R}} = \frac{\tau'}{\tau} = \frac{\pi}{\tau}\int_{\psi_D}^{\pi}\int_{o}^{\infty}\int_{y_o}^{\infty} \rho(y)\ n(r)\ (i_1 + i_2)\ dy\ dr\ \sin\psi\ d\psi\ /\ k^2 \tag{B3}$$

with $\tilde{\bar{E}} = 1 - \tilde{\bar{R}}$.

Although Eq. (B3) has been written on the assumption that the total aerosol altitude-size distribution is separable (i.e., $\eta(r,y) = n(r)\ \rho(y)$), this assumption is really unnecessary in our treatment, as we are concerned with altitude averaged results. We may define $\tilde{\bar{E}}$, for example, by

$$\begin{aligned}\tilde{\bar{E}} &= \frac{\pi}{\tau k^2}\int_{o}^{\psi_D}\int_{o}^{\infty}\int_{y_o}^{\infty} \eta(r,y)\ (i_1 + i_2)\ dy\ dr\ \sin\psi\ d\psi \\ &= \frac{\pi}{\tau k^2}\int_{o}^{\psi_D}\int_{o}^{\infty} N(r,y_o)\ (i_1 + i_2)\ dr\ \sin\psi\ d\psi\end{aligned} \tag{B4}$$

which is nothing but Eq. (36a). Here, use has been made of Eq. (32).

For notational convenience, the bar (-) and tilde (~) have both been omitted throughout the main body of this paper. However, no confusion should arise, as we shall always be concerned only with the altitude-averaged polydisperse correction and error factors.

SECTION 5

REPRESENTATION OF AEROSOL SIZE DISTRIBUTION DATA BY ANALYTIC MODELS

Even though atmospheric aerosols are known to possess a variety of shapes, the description of their physical structure is immensely simplified if they are assumed to be spherical. The size spectrum of atmospheric aerosols is, in general, continuous and may cover over four decades in radii, namely, 10^{-3} to 20 μm (Ref. 71). Of the basically four ways in which the empirical size distribution (SD) data can be represented, namely, tabular, histogram, graphical and analytical (Ref. 77), the last one is usually employed due to the fact that there exist regularities in the gross structure of atmospheric aerosols which exhibit behavior similar to that of a variety of mathematical functions. An analytic function generally encompasses in a smooth way the main features of the aerosol structure. While admittedly unrealistic in its smoothness, the analytical representation has the following advantages, namely those of convenient adjustability to obtain a best fit to the experimental data; compact representation of the dependent variable (the SD) in the form of estimated parameters of the fitted distribution; construction of reasonable and convenient models; and, carrying out parametric modeling studies of aerosol optical properties in a systematic manner.

The success of the analytic representation approach depends upon the selection of an appropriate mathematical function to approximate the actual size distribution data. This may not always be possible (Ref. 78); often a linear sum of mathematical functions may provide a good representation. Thus, there seems to be no "special" analytic function that can be said to be unique in representing aerosols SD's. The choice of the function is to some extent dictated by the modeler's taste. However, ultimately, it is

only when the fitted analytic function leads to results that closely fit the experimental optical (scattering/extinction) data and at the same time falls within the typical physical domain of atmospheric aerosols, that the analytic function may be assumed to represent the aerosol SD.

This paper summarizes the main results of a parametric study of eight mathematical functions, with up to four parameters, that are commonly used as models for representing aerosol size distributions; and describes, as an example, the method of obtaining best-fit parameter estimates of one of these models. Others are discussed in detail in Ref. 37. In this connection this paper presents a set of graphical plots depicting the parametric behavior of the model. These plots are a subset of the catalog of plots (for eight SD models) described in Ref. 37.

(i) *Terminology for Aerosol Size Distributions*

The physical structure of aerosols (atmospheric or artificial) can be represented, in general, in terms of the number, area, volume or mass of aerosol particles per unit volume per unit radius at radius r. However, in this paper the discussion will be restricted to the SD representation in terms of the particle number and radius, so that only the radius-number distribution, log radius-number distribution and cumulative size distribution will be considered. Their definitions follow those given in Ref. 37. (The dependence of the SD on factors such as, altitude, and composition, etc., will be considered here.)

The radius-number distribution n(r), ($cm^{-3}\mu m^{-1}$) is defined as the number of particles per unit volume (cm^3) within a unit radius range at r measured in μm. Thus,

$$n(r) = -dN(r) / dr = dN_u(r) / dr, \ (cm^{-3}\mu m^{-1}) \qquad (1)$$

where N(r) [$N_u(r)$] is the cumulative oversize [undersize] distribution function (Ref. 1).

The log radius-number distribution $n_L(r)$, (cm^{-3}), is defined by

$$n_L(r) = -dN(r) / d(\log_{10} r) = 2.3026\ r\ n(r),\ (cm^{-3}). \qquad (2)$$

Junge found it conventient to handle the wide range of atmospheric aerosol size distribution data by plotting $n_L(r)$ as a function of r, on a log-log scale. This method of plotting has the advantage that it represents the particle concentration as well as the size distribution.

The cumulative size distribution represents the total number of particles per cm^3 that have radii greater [less] than r, is represented by N(r) [$N_u(r)$] and is called the cumulative oversize [undersize] distribution function (Ref. 79). In essence

$$N(r) = \int_r^\infty n(r'')dr'' = \int_{\log_{10}(r)}^\infty n_L(r')\ d\ \log_{10}(r'),\ (cm^{-3}) \qquad (3a)$$

$$N_u(r) = \int_0^r n(r'')dr'' = \int_{-\infty}^{\log_{10}(r)} n_L(r')\ d\ \log_{10}(r'),\ (cm^{-3}) \qquad (3b)$$

In this paper, only the cumulative oversize distribution (COSD) will be discussed. Note that N(0) would then be the total number density (cm^{-3}) of the particles.

(ii) *Distribution Functions and Selection Criteria*

Given some empirical aerosol size distribution data, the problem is to find an analytic function that will most closely represent this data. Examples of mathematical functions of up to two parameters are the normal, gamma, binomial and exponential distribution functions; and of those with more than two parameters are: The Weibull, Johnson and Pearson distribution families. These distributions are discussed in detail in many books on

probability (see Ref. 77). These functions admit almost every type of probability distribution, except composite distributions made up of several distinct populations, such as multi-modal distributions. In addition, there is another versatile distribution, referred to as the generalized distribution function (GDF) (Refs. 80 and 81) which is derived from the Wood-Saxon function.

In the selection of an analytic function to represent the size distribution n(r), the following criteria must be taken into account:

1. The function is not singular for $0 \leqslant r \leqslant \infty$;
2. It is easily integrable over r;
3. It can represent the main features of the gross structure of the aerosols by a minimum number of adjustable parameters.

(iii) *Size Distribution Models and Their Mathematical Properties*

Analytic models suitable for representing aerosol size distributions include the following mathematical functions:

1. Power Law Distribution (PLD)
2. Regularized Power Law Distribution (RPLD)
3. Modified Gamma Distribution (MGD)
4. Inverse Modified Gamma Distribution (IMGD)
5. Log-normal Distribution (LND)
6. Normal Distribution (ND)
7. Generalized Distribution (GD)
8. Power Law Generalized Distribution (PLGD)

The expressions and the mathematical properties of the functions will be described in this section. Here the model distributions represent the radius-number distribution n(r), from which the corresponding expressions for $n_L(r)$ and N(r) are derived. The properties of interest are: the mode

radii for n(r) and $n_L(r)$; lower limit, asymptotic, and parametric behavior of the functions; and the kth moment of the models. The mode radius r_m for n(r) is given by the solution of

$$\frac{d\ n(r)}{dr} = 0$$

and that for $n_L(r)$, by the solution of

$$\frac{d\ n_L(r)}{dr} = 0$$

the kth moment is given by:

$$M_k = \int_0^\infty r^k\ n(r)dr$$

The moments are useful for calculating properties of the distribution such as number density (N(0)), average radius ($\bar{r}$), average area ($\bar{\bar{A}}$) and average volume ($\bar{V}$) of aerosol particles in a unit volume, as shown here:

$$N(0) = M_0$$

$$\bar{r} = M_2/M_0$$

$$\bar{A} = \pi M_2/M_0$$

$$\bar{V} = \frac{4}{3}\ \pi\ M_3/M_0$$

In all SD models, adjustable parameters are represented by p_1, p_2, p_3, ..., where p_1 is the scaling parameter and is chosen so that the maximum value of the function is unity.

A. Model 1: The Power Law (PL) Model. This model, known as Junge power law, was proposed by Junge to represent his continental aerosol SD data and is given by

$$n(r) = p_1\ r^{-p_2},\ r_1 \leq r \leq r_2 \qquad (4a)$$

or, alternately, by

$$n_L\ (r) = 2.3\ p_1 r^{(1-p_2)},\ r_1 \leq r \leq r_2 \qquad (4b)$$

It has a COSD of the form

$$N(r) = \frac{p_1}{p_2-1}\left(r^{1-p_2} - r_2^{1-p_2}\right), \quad r_1 \leq r \leq r_2 \qquad (4c)$$

Junge used 0.01 μm for r_1 and 1.0 μm for r_2; but other values could be used.

The kth moment for the distribution is given by

$$M_k = p_1\left(r_1^{1+k-p_2} - r_2^{1+k-p_2}\right) / (p_2 - k-1) \qquad (4d)$$

This model becomes singular at r = 0, if $r_1 = 0$; has all its moments infinite if $r_1 = 0$ and $r_2 = \infty$; and has no mode radius (r_m). Even though this model may not always represent a real situation, and does not meet the selectio criteria, it is popularly used as it readily gives analytically tractable results. The model is graphically presented in Ref. 37.

B. Model 2. The Regularized Power Law (RPL) Model. In order to eliminate the singularity at r = 0 that occurs in Model 1, without losing its power law behavior at large r, one may use a regularized form of the power law,

$$n(r) = \left(\frac{p_1}{p_2}\right) \frac{(r/p_2)^{p_3-1}}{\left[1 + (r/p_2)^{p_3}\right]^{p_4}} \qquad (5a)$$

The mode radius is given by

$$r_m = p_2 \left(\frac{p_3-1}{1 + p_3(p_4-1)}\right)^{1/p_3} \qquad (5b)$$

and the maximum value is

$$n(r_m) = \frac{p_1}{p_2} \frac{(p_3-1)^{1-\frac{1}{p_3}} (1+p_3(p_4-1))^{\frac{1+p_3(p_4-1)}{p_3}}}{(p_3p_4)^{p_4}} \qquad (5c)$$

The limiting behavior of the function is as follows

$$\text{As} \quad r \to 0, \; n(r) \simeq \frac{p_1}{p_2} (r/p_2)^{p_3-1} \tag{5d}$$

$$\text{and, as} \quad r \to \infty, \; n(r) \sim \frac{p_1}{p_2} (r/p_2)^{-(1+p_3(p_4-1))} \tag{5e}$$

The log radius number distribution is

$$n_L(r) = \frac{2.3 \; p_1 (r/p_2)^{p_3}}{(1+(r/p_2)^{p_3})^{p_4}} \tag{5f}$$

Its maximum value occurs at

$$r_{lm} = p_2 \; (p_4-1)^{-1/p_3} \tag{5g}$$

$$\text{so that} \quad n_L(r_{lm}) = 2.3 \; p_1 \frac{(p_4-1)^{p_4-1}}{(p_4)^{p_4}}$$

The limiting behavior for this form of the distribution is as follows

$$\text{As} \quad r \to 0, \; n(r) \simeq 2.3 \; p_1 \; (r/p_2)^{p_3} \tag{5h}$$

$$\text{and, as} \quad r \to \infty, \; n(r) \sim 2.3 \; p_1 \; (r/p_2)^{-p_3(p_4-1)} \tag{5i}$$

The COSD is given by (Ref. 81, No. 3.194/2 and 9.121/1).

$$N(r) = \frac{p_1}{p_3(p_4-1)} \quad \frac{1}{(1 + (r/p_2)^{p_3})^{p_4-1}} \tag{5j}$$

The limiting behavior for this function is as follows,

$$\text{As} \quad r \to 0, \; N(r) \simeq \frac{p_1}{p_3(p_4-1)} \quad (1 - (p_4-1) \; (r/p_2)^{p_3}) \tag{5k}$$

$$\text{and as} \quad r \to \infty, \; N(r) \quad \frac{p_1}{p_3(p_4-1)} \quad (r/p_2)^{-p_3(p_4-1)} \tag{5l}$$

The moments M for the RPL are given by (Ref. 82, No. 3.194/3 and Ref. 83, p. 103):

$$M_k = \frac{p_1 \, p_2^{\,k}}{p_3} \; \frac{\Gamma\left(1+\frac{k}{p_3}\right) \Gamma\left(p_4 - 1 - \frac{k}{p_3}\right)}{\Gamma(p_4)}, \quad k < p_3(p_4-1) \qquad (5m)$$

where Γ is the gamma function.

The parameter p_2 has the main effect on mode radius, being a multiplicative factor, while p_3 and p_4 control the positive and negative gradients, and hence polydispersity. The parameter p_3 controls the positive gradient while both p_3 and p_4 influence the negative gradient. The model is graphically presented in Figs. 5A.1 - 5A.3. A more complete set of graphs is given in Ref. 37.

C. Model 3: Modified Gamma Distribution (MGD) Model. Model 3 is the modified gamma distribution function. Deirmendjian (Ref. 40) has shown that this function can be used to describe various types of realistic aerosol distributions. For instance, by assigning different values to the parameters p_2 and p_4 one obtains models such as Haze H, Haze M, Haze L, Cloud C3, etc.

$$n(r) = p_1 \, r^{p_2} \, \exp\left(-p_3 r^{p_4}\right) \qquad (6a)$$

Its mode radius is

$$r_m = \left(\frac{p_2}{p_3 p_4}\right)^{1/p_4} \qquad (6b)$$

and its maximum value is

$$n(r_m) = p_1 \left(\frac{p_2}{p_3 p_4}\right)^{p_2/p_4} \exp\left(-p_2/p_4\right) \qquad (6c)$$

The limiting behavior of the distribution is as follows

As $r \to 0$, $n(r) \simeq p_1 \, r^{p_2}$ (6d)

and as $r \to \infty$, $n(r) \to 0$ as $p_1 \exp\left(-p_3 r^{p_4}\right)$ (6e)

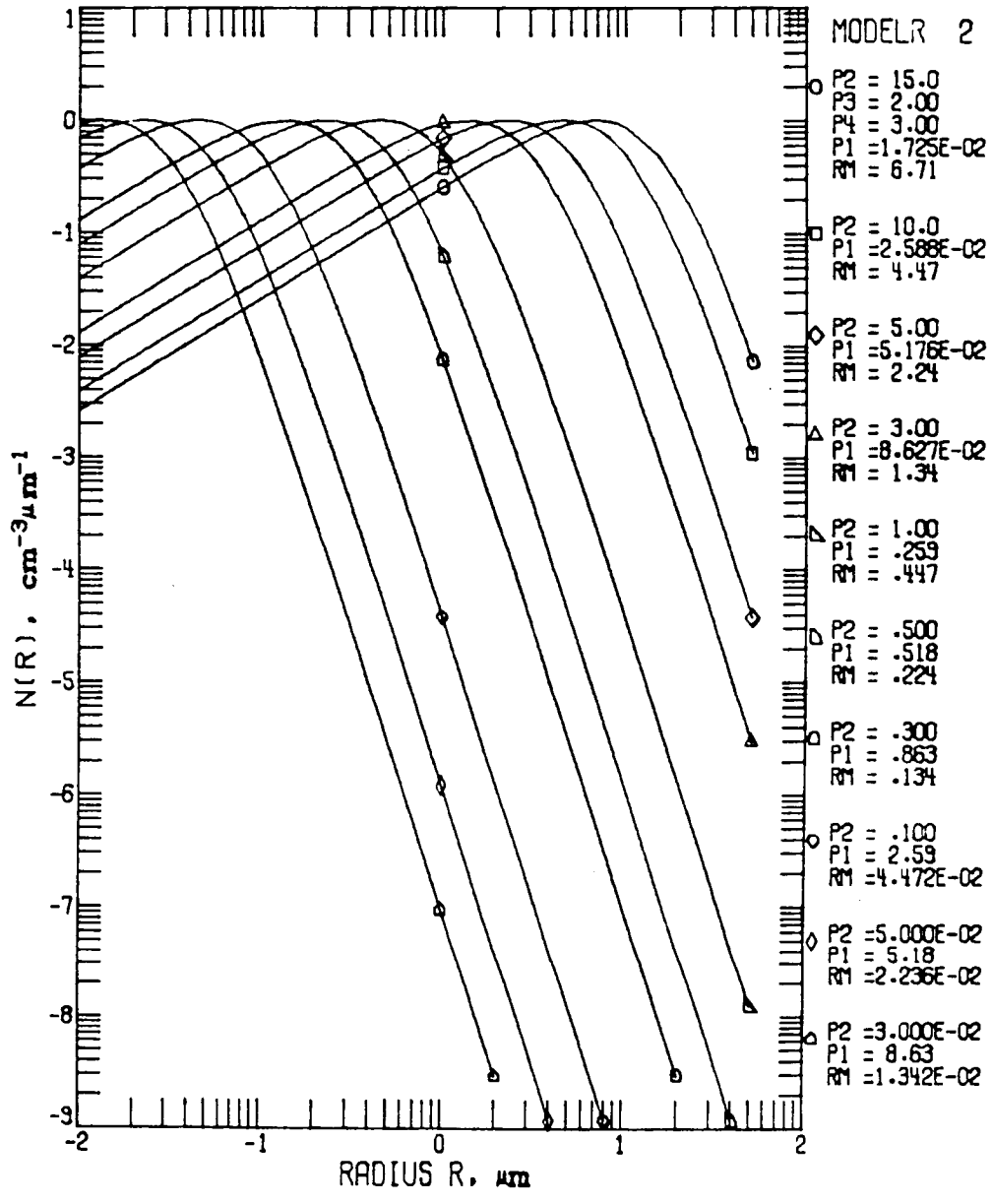

FIG. 5A.1. Model 2 (Regularized Power Law) for n(r). Parameter Set 2.1: p_2 variable, p_3 = 2.0, p_4 = 3.0.

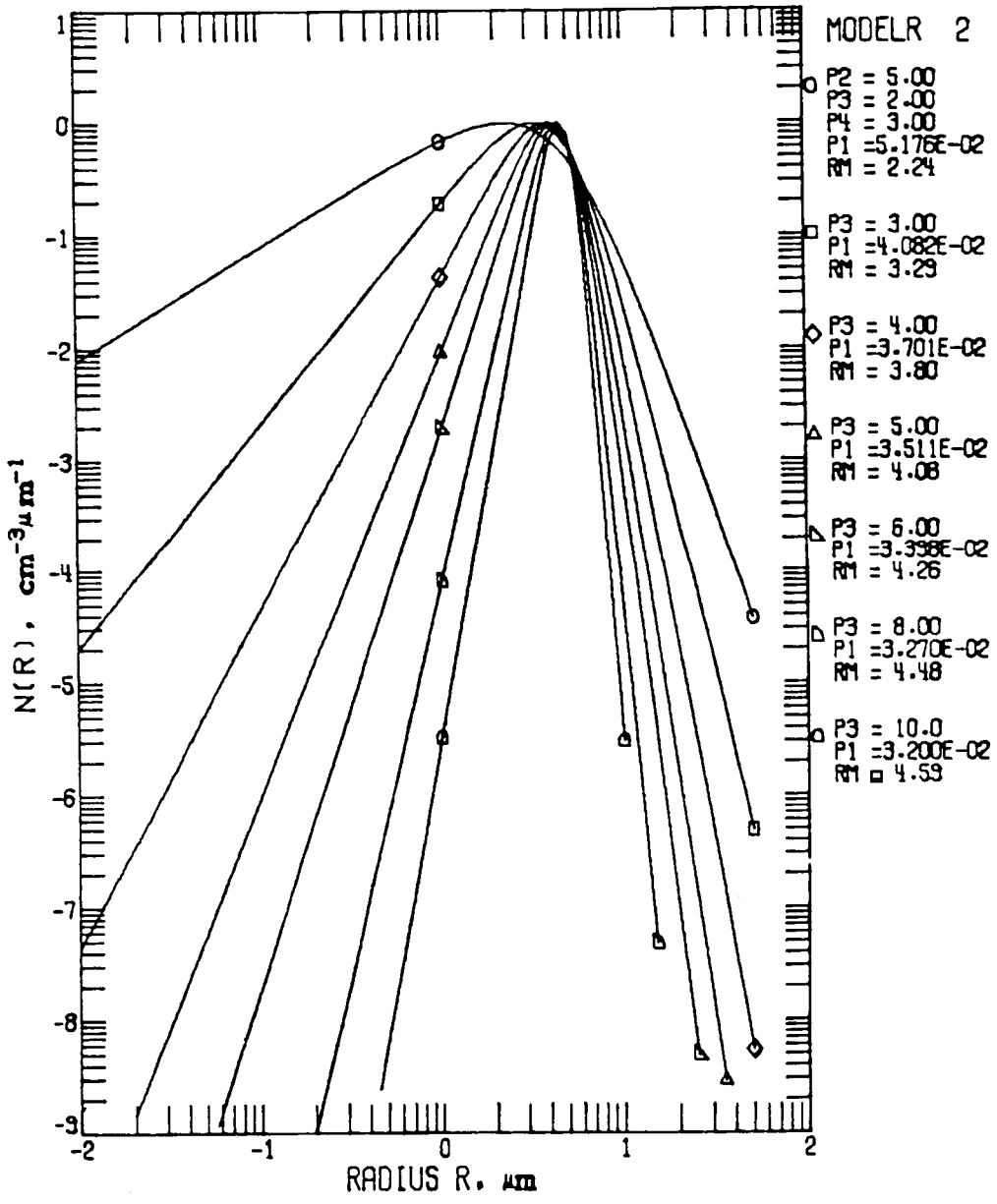

FIG. 5A.2. Model 2 for n(r). Parameter Set 2.3: p_3 variable, $p_2 = 5.0$, $p_4 = 3.0$.

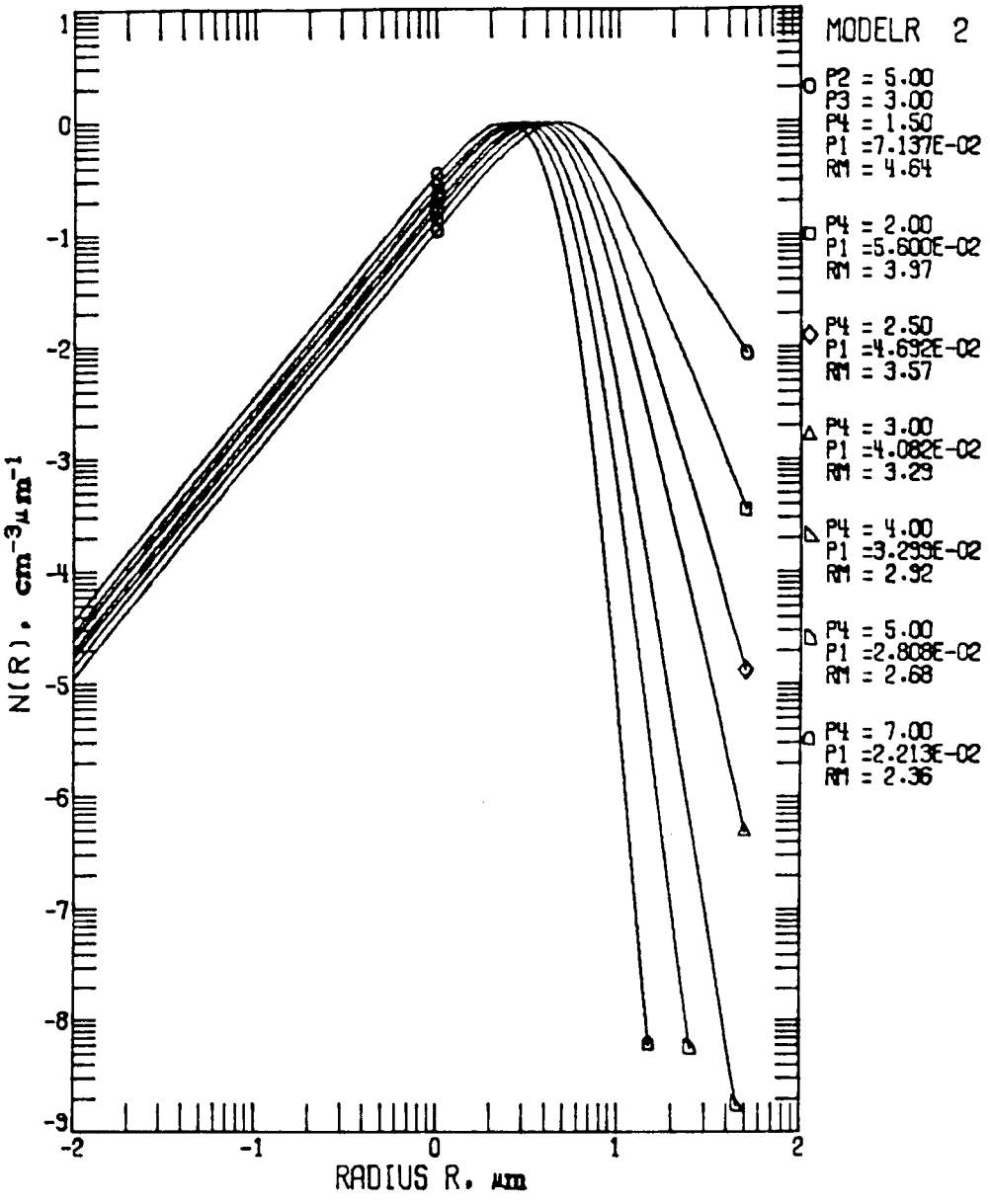

FIG. 5A.3. Model 2 for n(r). Parameter 2.4: p_4 variable, p_2 = 5.0, p_3 = 3.0.

The log radius-number distribution is given by

$$n_L(r) = 2.3 \quad p_1 r^{p_2+1} \quad \exp\ (-p_3 r^{p_4}) \tag{6f}$$

It has a maximum value at

$$r_{lm} = (p_{24}/p_3)^{1/p_4} \text{ where } p_{24} = (p_2+1)/p_4 \tag{6g}$$

so that

$$n_L(r_m) = 2.3\ p_1\ (p_{24}/p_3)^{p_{24}}\ \exp\ (-p_{24}) \tag{6h}$$

The limiting behavior of the function is as follows,

As $r \to 0$, $n_L(r) \simeq 2.3\ p_1\ r^{p_2+1}$ (6i)

and as $r \to \infty$, $n_L(r) \to 0$ as $2.3\ p_1 \exp(-p_3 r^{p_4})$ (6j)

The COSD is given by (Ref. 82, No. 3.381/3),

$$N(r) = p_1\ \Gamma(p_{24},\ p_3 r^{p_4})\ /\ p_4 p_3^{p_{24}} \quad p_3 > 0 \tag{6k}$$

The limiting behavior for the COSD is as follows (Ref. 84, 6.5.3, 6.5.12, 6.5.32),

$$\text{As } r \to 0,\ N(r) \simeq p_1\ (\Gamma(p_{24}) - p_3^{p_{24}} r^{p_2+1}/p_{24})/p_4 p_3^{p_{24}} \tag{6l}$$

$$\text{and, as } r \to \infty,\ N(r) \sim \frac{p_1}{p_3 p_4}\ r^{p_2-p_4+1}\ \exp\ (-p_3 r^{p_4}) \tag{6m}$$

The k^{th} moment for the distribution is given by (Ref. 82 No. 3.381/4),

$$M_k = (p_1/p_4)\ p_3^{-(p_{24}-k/p_4)}\ \Gamma(p_{24}+k/p_4),\ p_2+k+1 > 0 \tag{6n}$$

The parameter p_3 controls the mode radius and the parameters p_2 and p_4 control the polydispersity. The parameter p_2 determines the limiting behavior as $r \to 0$ while the parameter p_4 determines the limiting behavior as $r \to \infty$. The model is graphically presented in Ref. 37.

D. Model 4. Inverse Modified Gamma Distribution. This distribution has the same form as Model 3 except that the inverse radius is used. This results in an exponential fall-off at the small size and the power law behavior at the large-radius end. Twomey (Ref. 85) suggests this form of the modified gamma distribution for dry aerosols.

The radius number distribution is given by

$$n(r) = p_1 \exp(-p_3/r^{p_4}) \; / \; r^{p_2} \tag{7a}$$

Its mode radius is given by

$$r_m = \left[\frac{p_3 p_4}{p_2}\right]^{1/p_4} \tag{7b}$$

and the maximum value is

$$n(r_m) = p_1 \left[\frac{p_2}{p_3 p_4}\right]^{p_2/p_4} \exp(-p_2/p_4) \tag{7c}$$

The limiting behavior of the distribution is as follows,

$$\text{As} \quad r \to 0, \; n(r) \to 0 \text{ as } p_1 \exp(-p_3/r^{p_4}) \tag{7d}$$

$$\text{and, as} \quad r \to \infty, \; n(r) \sim p_1 r^{-p_2} \tag{7e}$$

The log-radius number distribution is given by

$$n_L(r) = 2.3 \; p_1 \exp(-p_3/r^{p_4}) \; / \; r^{(p_2-1)} \tag{7f}$$

Its mode radius is given by

$$r_{lm} = (p_3/p_{42})^{1/p_4}, \quad p_{42} = (p_2-1)/p_4 \tag{7g}$$

and the maximum value is

$$n_L(r_{lm}) = 2.3\ p_1\ (p_{42}/p_3)^{p_{42}}\ \exp(-p_{42}) \qquad (7h)$$

The limiting behavior of the distribution is as follows,

$$\text{as} \quad r \to 0,\ n_L(r) \to 0 \quad \text{as} \quad 2.3\ p_1\ \exp(-p_3/r^{p_4}) \qquad (7i)$$

$$\text{and, as } r \to \infty,\ n_L(r) \sim 2.3\ p_1 r^{-(p_2-1)} \qquad (7j)$$

The COSD is given by (Ref. 82, No. 3.381/1)

$$N(r) = \frac{p_1}{p_4}\ (p_3)^{-p_{42}}\ \gamma\ (p_{42},\ p_3\ r^{-p_4}),\ p_{42} > 0 \qquad (7k)$$

where γ is the incomplete gamma function.

The limiting behavior of this distribution is as follows (Ref. 84, No. 6.1.1, 6.5.2, 6.5.12).

$$\text{As} \quad r \to 0,\ N(r) \simeq \frac{p_1}{p_4}\ [p_3^{-p_{42}}\ \Gamma(p_{42}) - \exp(-p_3/r^{p_4})/p_3$$

$$r^{p_4(p_{42}-1)}] \qquad (7\ell)$$

$$\text{and, as} \quad r \to \infty,\ N(r) \sim p_1\ r^{-(p_2-1)} / (p_2-1) \qquad (7m)$$

The moments of the distribution are given by (Ref. 82, No. 3.381/4)

$$M_k = \frac{p_1}{p_4}\ p_3^{-(p_{42}-k/p_4)}\ \Gamma\ (p_{42}-k/p_4)\ ,\ k < p_2-1 \qquad (7n)$$

The parameters p_2 and p_4 control the rate of fall-off at large and small radii, respectively, and hence control the polydispersity. The parameter p_3 controls the mode radius. This model is graphically presented in Ref. 37.

E. Model 5. The Log Normal Distribution (LND) Model. The log normal distribution generally provides a better description of particle size distribution (discussed later on) because particle sizes, like many naturally

occurring populations, are often asymmetric. In this distribution it is lnr rather than r which is normally distributed. An excellent discussion of this distribution is given by Kerker (Ref. 78).

The radius number distribution is given by

$$n(r) = \frac{p_1}{\sqrt{2\pi}\, p_3 r} \exp\left\{-\frac{1}{2}\left[\frac{\ln r - \ln p_2}{p_3}\right]^2\right\} \tag{8a}$$

The mode radius is

$$r_m = p_2 \exp(-p_3^2) \tag{8b}$$

and its maximum value is

$$n(r_m) = \frac{p_1}{\sqrt{2\pi}\, p_2 p_3} \exp(p_3^2/2) \tag{8c}$$

The parameter p_2 is the geometric mean of r and $\ln p_2$ is the mean of nr. No series expansion could be found for the limiting behavior of this distribution which tends rapidly to zero at both extremities.

The log radius-number distribution is

$$n_L(r) = \frac{2.3\ p_1}{\sqrt{2\pi}\, p_3} \exp\left\{-\frac{1}{2}\left[\frac{\ln r - \ln p_2}{p_3}\right]^2\right\} \tag{8d}$$

It has a maximum at

$$r_{lm} = p_2 \tag{8e}$$

so that

$$n_L(r_{lm}) = 2.3\ p_1/(\sqrt{2\pi}\, p_3) \tag{8f}$$

No series expansion could be found for the limiting behavior of this distribution which tends rapidly to zero at both extremities.

The COSD is given by (Ref. 82, p. 183)

$$N(r) = \frac{p_1}{2}\ \mathrm{erfc}\left[\frac{\ln r - \ln p_2}{\sqrt{2}\ p_3}\right] \tag{8g}$$

where erfc is the complementary error function.

The limiting behavior of this function is as follows

As $r \to 0$, $N(r) \to p_1$ (8h)

and, as $r \to \infty$, $N(r) \to 0$ (8i)

The parameter p_2 is the median for the COSD, i.e.,

$N(p_2)/N(0) = 0.5$

The moments for the distribution are given by (Ref. 82, No. 3.323/2)

$$M_k = p_1 p_2^k \exp\ (p_3^2\ k^2/2) \tag{8j}$$

The parameter p_3 controls the polydispersity of the model and the parame p_2 has a multiplicative effect on mode radius. This model is graphically presented in Ref. 37.

F. Model 6. The Normal Distribution (ND). The normal distribution is a symmetric distribution which is finite at r = 0 and, thus, strictly speaking cannot be used to represent aerosol SDs at small r. It can be used to represent SDs at other ranges of r, and since it is a Gaussian distribution, which has well known properties, such a model can be very useful in certain applications. It is given by

$$n(r) = \frac{p_1}{\sqrt{2\pi}\ p_3} \exp\ \{-\frac{1}{2}\left[\frac{r-p_2}{p_3}\right]^2\} \tag{9a}$$

Its mode radius is given by

$$r_m = p_2 \tag{9b}$$

and the maximum value is

$$n(r_m) = \frac{p_1}{\sqrt{2\pi}\ p_3} \tag{9c}$$

$$\text{As} \quad r \to 0, \; n(r) \simeq \frac{p_1}{\sqrt{2\pi}\, p_3} \exp\left\{-\frac{1}{2}\left(\frac{p_2}{p_3}\right)^2\right\} (1 + r p_2/p_3^2) \qquad (9d)$$

No series expansion could be found for the asymptotic behavior of this function which tends rapidly to zero.

The log radius-number distribution is given by

$$n_L(r) = \frac{2.3 \quad p_1 \, r}{\sqrt{2\pi}\, p_3} \exp\left\{-\frac{1}{2}\left[\frac{r-p_2}{p_3}\right]^2\right\} \qquad (9e)$$

Its mode radius is given by

$$r_{lm} = \frac{p_2 + \sqrt{p_2^2 + 4\, p_3^2}}{2} \qquad (9f)$$

and the maximum value is

$$n_L(r_{lm}) = \frac{2.3\; p_1}{\sqrt{2\pi}\; p_3}\left(\frac{p_2 + \sqrt{p_2^2 + 4p_3^2}}{2}\right) \exp\left\{-\frac{1}{2}\left[\frac{p_2^2 + 4p_3^2}{p_3^2}\right]\right\} \qquad (9g)$$

The limiting behavior of the distribution is as follows

$$\text{As} \quad r \to 0, \; n_L(r) \simeq \frac{2.3\; p_1 r}{\sqrt{2\pi}\; p_3} \qquad (9h)$$

$$\text{and, as} \quad r \to \infty, \; n_L(r) \to 0 \qquad (9i)$$

The COSD is given by (Ref. 86, p. 183)

$$N(r) = \frac{p_1}{2} \operatorname{erfc}\left[\frac{r-p_2}{\sqrt{2}\; p_3}\right] \qquad (9j)$$

The limiting behavior of the distribution is as follows (Ref. 86, p. 183),

$$\text{As} \quad r \to 0, \; N(r) \approx (p_1/2)\left[1 - \frac{\sqrt{2}}{\pi}\left(\frac{r-p_2}{p_3}\right)\right] \tag{9k}$$

$$\text{and, as} \quad r \to \infty, \; N(r) \sim \frac{p_1}{\sqrt{2\pi}} \left(\frac{p_3}{r-p_2}\right) \exp\left\{\left[\frac{r-p_2}{\sqrt{2}\, p_3}\right]\right\} \tag{9ℓ}$$

The moments of the distribution are given by (Ref. 82, No. 3.462/1).

$$M_k = \frac{p_1}{\sqrt{2\pi}} p_3^{\,k} \, (k!) \exp\left(-p_2^{\,2}/4p_3^{\,2}\right) D_{-k-1}(-p_2/2) \tag{9m}$$

where D_{-k-1} is a parabolic cylinder function.

In the normal distribution, the parameter p_2, controls the mode radius and the parameter p_3 controls the polydispersity. The model is graphically presented in Ref. 37.

G. Model 7. The Generalized Distribution Function (GDF). This distribution is finite at r = 0 and, thus does not, strictly speaking, represent particle size distributions at small r. However, it is a versatile function with a wide variety of applications, including altitude distributions (Refs. 1 and 80), and is therefore included here as a potential representation of aerosol SDs.

The radius-number distribution is given by

$$n(r) = \frac{p_1 \, (1+p_2)^2 \exp\,(r/p_3)}{\{p_2 + \exp\,(r/p_3)\}^2} \tag{10a}$$

Its mode radius is given by

$$r_m = p_3 \ln p_2 \tag{10b}$$

and the maximum is

$$n(r_m) = \frac{p_1 \, (1+p_2)^2}{4\, p_2} \tag{10c}$$

The limiting behavior of the distribution is as follows

$$\text{As} \quad r \to 0, \; n(r) \simeq p_1 \left(1 + r/p_3 \left(\frac{p_2 - 1}{p_2 + 1}\right)\right) \tag{10d}$$

$$\text{and, as} \quad r \to \infty, \; n(r) \to 0 \text{ as } p_1 (1+p_2)^2 \exp(-r/p_3) \tag{10e}$$

The log radius-number distribution is given by

$$n_L(r) = 2.3 \; p_1 \; (1+p_2)^2 \; r \exp(r/p_3) \; / \; (p_2 + \exp(r/p_3))^2 \tag{10f}$$

Its mode radius r_{1m} is given by the solution of the equation

$$p_2(1 + r_{1m}/p_3) = (r_{1m}/p_3 - 1) \exp(r_{1m}/p_3) \tag{10g}$$

and the maximum is given by

$$n_L(r_{1m}) = 2.3 \; p_1 \; (1+p_2)^2 \; (r_{1m} - p_3) \; (r_{1m} + p_3) \; / \; (4 \; p_2 r_{1m}) \tag{10h}$$

The limiting behavior of the distribution is as follows

$$\text{As} \quad r \to 0, \; n(r) \simeq 2.3 \; p_1 \; (1+p_2)^2 \; r \tag{10i}$$

$$\text{and, as} \quad r \to \infty, \; n(r) \to 0 \text{ as } 2.3 \; p_1 \; (1+p_2)^2 \exp(-r/p_3) \tag{10j}$$

The COSD is given by

$$N(r) = \frac{p_1 \; (1+p_2)^2 \; p_3}{\left(p_2 + \exp(r/p_3)\right)} \tag{10k}$$

The limiting behavior of the distribution is as follows

$$\text{As} \quad r \to 0, \; N(r) \simeq p_1 \; (1+p_2) \; p_3 \; (1 - r/p_3(p_2+1)) \tag{10ℓ}$$

$$\text{and, as} \quad r \to \infty, \; N(r) \to 0 \text{ as } p_1 p_3 \; (1+p_2)^2 \exp(-r/p_3) \tag{10m}$$

The analytic expression for the moments of the distribution could not be evaluated.

The parameter p_3 can be considered as a scale radius and the parameter p_2 determines the type of function. For $p_2 = 0$ the distribution becomes an exponential, and for small p_2 the function initially falls off more slowly than the exponential. As the parameter p_3 increases, the spread or polydispersity of the function increases. The model is graphically presented in Ref. 37.

H. Model 8. Power Law Generalized Distribution Function (PLGDF). This model is a versatile function which is most useful when the data to be fitted have broad peaks. The radius-number distribution is given by

$$n(r) = \frac{p_1 \exp\ (p_2/r^{p_4})}{r^{p_4+1}\ [1+p_3\{\exp\ (p_2/r^{p_4}) - 1\}]^2} \tag{11a}$$

There is no analytic expression for the mode radius.

The limiting behavior of the distribution is as follows

$$\text{As} \quad r \to 0,\ n(r) \to 0 \text{ as } p_1 \exp\ (-\frac{p_2}{r^{p_4}}) \tag{11b}$$

$$\text{and, as} \quad r \to \infty,\ n(r) \sim p_1\ r^{-(p_4+1)} \tag{11c}$$

The log radius-number SD is given by

$$n_L(r) = \frac{2.3\ p_1 \exp\ (p_2/r^{p_4})}{r^{p_4}\ [1+p_3\ \{\exp(p_2/r^{p_4}) - 1\}]^2} \tag{11d}$$

There is no analytic expression for the mode radius.

The limiting behavior of the distribution is as follows

$$\text{As} \quad r \to 0,\ n_L(r) \to 0 \quad \text{as} \quad 2.3\ p_1 \exp\ (-p_2/r^{p_4}) \tag{11e}$$

$$\text{and, as} \quad r \to \infty,\ n_L(r) \sim 2.3\ p_1\ r^{-p_4} \tag{11f}$$

The COSD is given by

$$N(r) = \frac{p_1\ \{\exp\ (p_2/r^{p_4}) - 1\}}{p_2 p_4\ [1+p_3\ \{\exp(p_2/r^{p_4}) - 1\}]} \tag{11g}$$

The limiting behavior of the distribution is as follows

$$\text{As} \quad r \to 0,\ N(r) \simeq p_1/p_2p_3p_4\{1+1/p_3(e^{p_2/r^2}-1)\} \tag{11h}$$

$$\text{and, as} \quad r \to \infty,\ N(r) \to 0 \quad \text{as} \quad \frac{p_1}{p_2p_4} \left\{ \frac{\exp(p_2/r^{p_4})-1}{1+p_3\{\exp(p_2/r^{p_4})-1\}} \right\} \tag{11i}$$

The moments, other than the zeroth moment (N(0)), cannot be calculated for this distribution. However, there is a special form of the function, referred to as Model 8B, for which higher moments can be calculated, but it has no analytic form for the COSD. The radius-number SD for this function is given by

$$n(r) = \frac{p_1 \exp(p_2/r^2)}{r^{p_4}(1+p_3(\exp(p_2/r^2)-1))^2} \tag{12a}$$

Its mode radius is obtained from the solution of the equation. There is no analytic expression for the mode radius.

The limiting behavior of this distribution is as follows

$$\text{As} \quad r \to 0,\ n(r) \to 0 \quad \text{as } p_1 \exp(-p_2/r^{p_4}) \tag{12b}$$

$$\text{and, as} \quad r \to \infty,\ n(r) \sim p_1 r^{-p_4} \tag{12c}$$

The log radius-number distribution is given by

$$n_L(r) \quad \frac{2.3\ p_1 \exp(p_2/r^2)}{r^{p_4-1}(1+p_3(\exp(p_2/r^2)-1))^2} \tag{12d}$$

There is no analytic expression for the mode radius.

The limiting behavior of the distribution is as follows

$$\text{As} \quad r \to 0,\ n_L(r) \to 0 \quad \text{as} \quad 2.3\ p_1 \exp(-p_2/r^2) \tag{12e}$$

$$\text{and, as} \quad r \to \infty,\ n_L(r) \sim 2.3\ p_1 r^{-(p_4-1)} \tag{12f}$$

The moments for this distribution are given by (Ref. 86)

$$M_k = \frac{p_1}{2p_3^{\,2}\, p_2^{\,p_{4k}}} \left| p_{4k} \sum_{i=0}^{\infty} \left(1 - \frac{1}{p_3}\right)^i (i+1)^{-(p_{4k}-1)} \right. \quad (12g)$$

where $p_{4k} = \frac{p_4-(k+1)}{2}$, $p_4 > k + 1$.

The parameter behavior for both functions (Eqs. (11a) and (12a)) is similar. The parameter p_2 controls the rate of fall-off at small radii where the parameter p_4 controls the rate of fall-off at large radii. The parameter p_3 controls the spread of the distribution, the breadth of the peaks increasing with large values of p_3. The model is graphically presented in Ref. 37.

(iii) Graphical Representation of Size Distribution Models

The parametric behavior of a size distribution model can be illustrated graphically by plotting the size distributions corresponding to several values of one of the parameters on the same graph, while other parameters remain constant. An example of the parametric variation of n(r) in the case of Model is given in Figs. 5A.1 through 5A.3. A complete catalog of plots illustrating the parametric behavior of n(r), $n_L(r)$, and N(r) for all of the eight models is given in Ref. 37.

For each set of plots in Figs. 5A.1 through 5A.3, the values of the four parameters (p_1, ..., p_4) are given for the first plot, along with the mod radius r_m. For subsequent distributions only the parameter being varied, the scaling parameter p_1 and the mode radius are given. The scaling parameter is chosen here such that the distribution maximum is equal to one.

(iv) Determination of Model Parameters from Plots

The graphical catalog of plots can be easily used to estimate the values of the different parameters for size distribution measurement data. This is done by first plotting the data on the transparency of a blank log-log graph which has the same x-y scale as the graphs in the catalog; then after selecting a suitable model, overlaying the data transparency on the parametric plots, one at a time, to determine which value of the plots gives the best fit to the data.

Vertical translation of the transparency relative to the parametric plot will generally be necessary because the range of values covered by the experimental data will differ from that of the parametric plot. Horizontal translation may also be necessary if the parameter being determined controls the fall-off as $r \to 0$ or $r \to \infty$ or the curvature near the peak. Horizontal translation cannot be used if the parameter controls the location of the mode radius.

Graphical determination of model parameters can be illustrated using Mdoel 2 to represent Junge's data (Fig. 5.2). Model 2 was chosen because, similar to the data, it has a power law fall-off as $r \to \infty$.

The Junge data was plotted on a transparency which was overlayed on Fig. 5A.3 and then translated vertically until the data points as large r ($r >>$ mode radius r_m) coincided with one of the catalog plots, in this case that corresponding to $p_4 = 2.0$, thus the combination $p_3 = 3.0$, $p_4 = 2.0$, thus the combination $p_3 = 3.0$, $p_4 = 2.0$ fits the slope of the curve as $r \to \infty$.

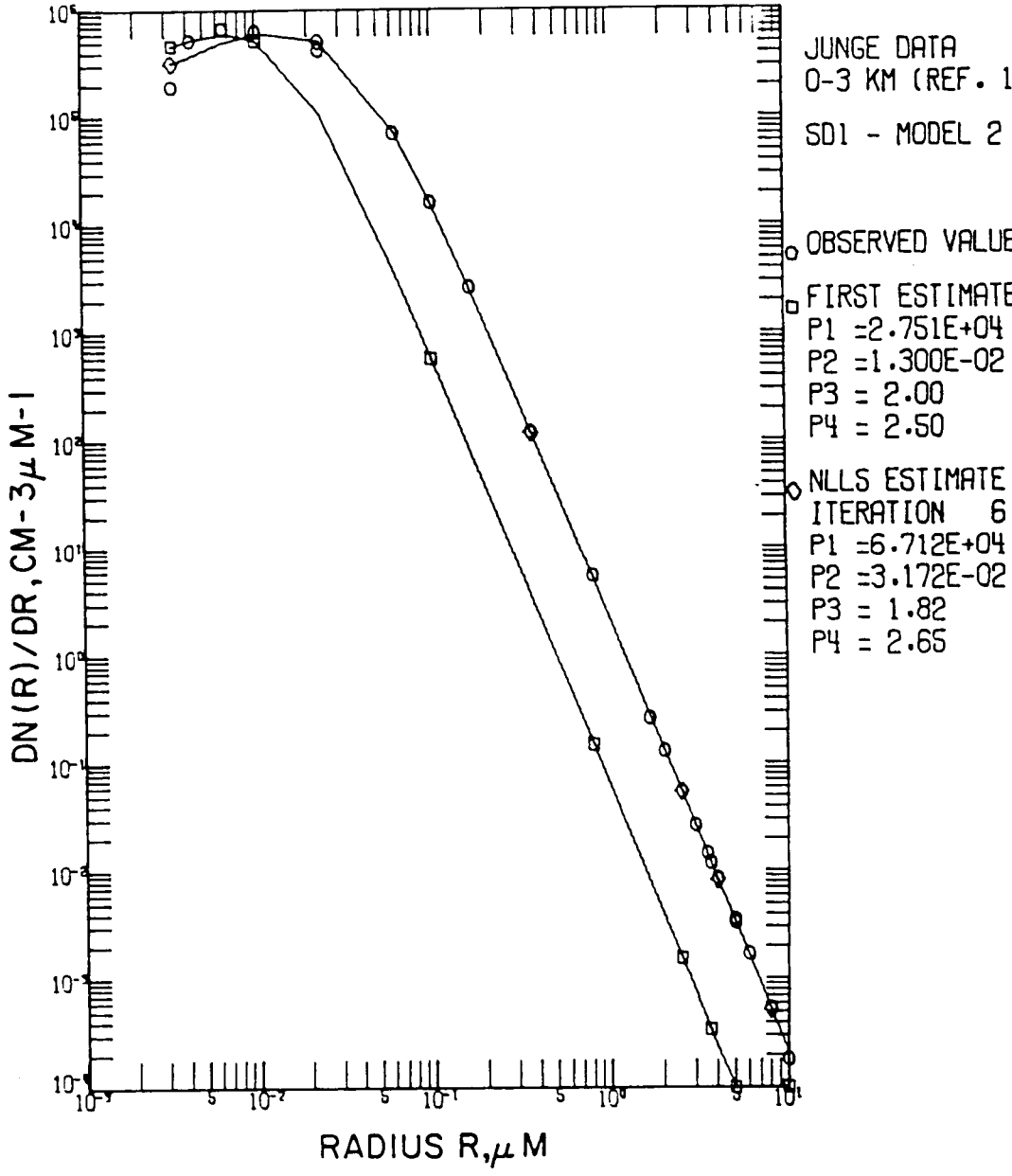

FIG. 5.2: Example of Fit to Junge Data Using Model 2 (Regularized Power Law).

Since there are only a few data for small r ($r << r_m$), concentrate on the region around the peak in determining p_3. The transparency was overlayed on Fig. 5A.2 and translated vertically and horizontally until the curve which best matched the data in the region of the peak was found. In this case it turned out to correspond to $p_3 = 2.0$, which falls off too steeply as $r \to \infty$. Remembering that the initial estimates for p_3 and p_4 were 3.0 and 2.0, respectively, which gives a slope of -4 when substituted in $-[1 + p_3(p_4 - 1)]$ (see Eq. 5e) we see that for $p_2 = 3.0$, a value of 2.5 is needed for p_4.

The final parameter to be determined from the plots is p_2, which controls the mode radius r_m. This is done by overlaying the transparency on Fig. 5A.1 and translating vertically until the data maximum coincided with 1.0 on the vertical plot scale. This showed that $p_2 < 0.05$. Substitution of the mode radius, 6.5×10^{-3}, and the estimates for p_3 and p_4 in Eq. (5b) gives $p_2 = 0.013$.

Once the estimates for p_2, p_3, p_4 were found, p_1 was obtained from the relation

$$p_1 = \frac{\sum_{j=1}^{N} y_j^o \, y_j^c}{\sum_{j=1}^{N} (y_j^c)^2}$$

where y_j^o is the observed size distribution at r_j, y_j^e is the calculated distribution value and N is the total number of data points.

These estimates of parameters were used to initial estimates of p in a nonlinear least squares program to obtain the best fit. The results

are given in Fig. 5.2. The initial estimate had the right shape but was too far to the left of the data points because the initial estimate for p_2 was too low. The initial estimates for p_3 and p_4 agree quite well with the final estimate and a better initial estimate of p_2 could have been obtained by taking the midpoint of the peak region as the mode radius rather than the actual maximum.

The description and use of the graphical catalog were confined to the radius number distribution n(r) alone. For similar details regarding $n_L(r)$ and N(r), see Ref. 37. These plots can be used to estimate the parameters for multimodal distributions (Ref. 37) by visually sketching in the most probable behavior for each mode and then determining the parameters for each mode separately.

(v) Concluding Remarks

The uses of the graphical catalog are twofold. First, it provides a catalog of the shapes of the different distributions, illustrating such properties as the locations of mode radii, rates of fall-off and polydisperse By providing a means for comparing distributions, it aids in selecting the model(s) most likely to give a good description of the experimental data to be fitted. Second, the catalog provides a means of estimating the likely values of the model parameters. Parameter estimates thus obtained can then be used as initial guess parameters in nonlinear least squares or other optimization codes to obtain the best-fit values of the parameters.

It is important that the model chosen to fit the size distribution data be an appropriate one if useful results are to be obtained. A model is considered appropriate, if properties such as the mode radius, rates of fall-off and polydispersity of the model are similar to that of the

experimental size distribution data. A summary table for the different analytical models and their properties is given in Appendix 5A.

It is worth mentioning that in the literature on this subject one often finds experimental size distributions being represented by other analytic functions or their sums, such as, exponential function, "truncated" power law, and Chebyshev coefficients. But they do not qualify for inclusion in our scheme on the basis of the selection criteria in Section (ii). It is quite likely that some other analytic representations may have been inadvertently overlooked.

APPENDIX 5A

TABLE 1: Summary Table for Size Distribution Models

	Model 1 Power Law	Model 2 Regularized Power Law	Model 3 Modified Gamma Distribution
$n(r)$	$p_1 r^{-p_2}$	$\frac{p_1 (r/p_2)^{p_3-1}}{p_2[1+(r/p_2)^{p_3}]^{p_4}}$	$p_1 r^{p_2} \exp(-p_3 r^{p_4})$
r_m	not applicable	$p_2 \left(\frac{p_3-1}{p_{34}+1} \right)^{1/p_3}$, $[p_{34} = p_3(p_4-1)]$	$\{p_2/(p_3 p_4)\}^{1/p_4}$
$n(r_m)$	not applicable	$\frac{p_1}{p_2} \frac{(p_3-1)^{(p_3-1)/p_3} \quad (1+p_{34})^{(p_{34}+1)/p_3}}{(p_3 p_4)^{p_4}}$	$p_1 \left(\frac{p_2}{p_3 p_4} \right)^{p_2/p_4} \exp(-p_2/p_4)$
As $r \to 0$, $n(r) =$	$p_1 r^{-p_2}$	$\frac{p_1}{p_2}(r/p_2)^{p_3-1}$	$p_1 r^{p_2}$
As $r \to \infty$, $n(r) \approx$	$p_1 r^{-p_2}$	$\frac{p_1}{p_2}(r/p_2)^{-(p_{34}+1)}$	0
$N(r)$	$\frac{p_1(r^{1-p_2} - r_1^{1-p_2})}{p_2-1}$	$\frac{p_1[1+(r/p_2)^{p_3}]^{(1-p_4)}}{p_{34}}$	$p_1 \Gamma(p_{24}, p_3 r^{p_4})/(p_4 p_3^{p_{24}})$, $(p_{24} = \frac{p_2+1}{p_4})$
As $r \to 0$, $N(r) \approx$	$\frac{p_1 r^{1-p_2}}{p_2-1}$	$\frac{p_1[1-(p_4-1)(r/p_2)^{p_3}]}{p_{34}}$	$p_1 \Gamma(p_{24})/p_4 p_3^{p_{24}}$
As $r \to \infty$, $N(r) \sim$	$\frac{p_1 r^{1-p_2}}{p_2-1}$	$\frac{p_1 (r/p_2)^{-p_{34}}}{p_{34}}$	0
M_k	$\frac{p_1(r_1^{1+k-p_2} - r_2^{1+k-p_2})}{(p_2-k-1)}$	$\frac{p_1 p_2^k}{p_3} \frac{\Gamma(1+k/p_3)\Gamma(p_4-1-k/p_3)}{\Gamma p_4}$	$(p_1/p_4) p_3^{-(p_{24}+k/p_4)} \Gamma(p_{24}+k/p_4)$

TABLE 1 (Continued)

	Model 4 Inverse Modified Gamma Distribution	Model 5 Log Normal Distribution	Model 6 Normal Distribution
$n(r)$	$p_1 r^{-p_2} \exp(-p_3 r^{-p_4})$	$\{p_1/(\sqrt{2\pi}\, p_3 r)\} \exp[(-1/2) \{(\ln r - \ln p_2)/p_3\}^2]$	$\{p_1/(\sqrt{2\pi}\, p_3)\} \exp[(-1/2)\{(r-p_2)/p_3\}^2]$
r_m	$(p_3 p_4/p_2)^{1/p_4}$	$p_2 \exp(-p_3^2)$	p_2
$n(r_m)$	$p_1\{p_2/(p_3 p_4)\}^{p_2/p_4} \exp(-p_2/p_4)$	$\{p_1/(\sqrt{2\pi}\, p_2 p_3)\} \exp(p_3^2/2)$	$p_1/(\sqrt{2\pi}\, p_3)$
As $r \to 0$, $n(r) \approx$	0	0	$\{p_1/(\sqrt{2\pi}\, p_3)\} \exp[(-1/2)(p_2/p_3)^2] (1 + r p_2/p_3^2)$
As $r \to \infty$, $n(r) \sim$	$p_1 r^{-p_2}$	0	0
$N(r)$	$p_1\, \gamma\, (p_{42}, p_3\, r^{p_4})/(p_4 p_2^{p_{42}})$, $p_{42} = (p_2-1)/p_4$	$(p_1/2)\, \mathrm{erfc}\{(\ln r - \ln p_2)/(\sqrt{2}\, p_3)\}$	$(p_1/2)\, \mathrm{erfc}\{(r-p_2/)\sqrt{2}\, p_3)\}$
As $r \to 0$, $N(r) \approx$	$p_1\, \Gamma p_{42}/(p_4 p_3^{p_{42}})$	0	$(p_1/2)\, [1 - \sqrt{2/\pi}\, \{(r-p_2)/(p_3)\}]$
As $r \to \infty$, $N(r) \sim$	$[p_1/(p_2-1)]\, r^{-(p_2-1)}$	0	0
M_k	$(p_1/p_4) p_3^{-(p_{42}-k/p_4)} \Gamma(p_{42}-k/p_4)$	$(p_1 p_2^k) \exp(p_3^2 k^2/2)$	See Eq. (9m)

TABLE 1 (Continued)

	Model 7 Generalized Distribution Function	Model 8 Power Law—Generalized Distribution Function	Model 8B
$n(r)$	$\frac{p_1(1+p_2)^2 \exp(r/p_3)}{[p_2+\exp(r/p_3)]^2}$	$\frac{p_1 \exp(p_2/r^{p_4})}{r^{p_4+1}\{1+p_3[\exp(p_2/r^{p_4})-1]\}^2}$	$\frac{p_1 \exp(p_2/r^2)}{r^{p_4}\{1+p_3[\exp(p_2/r^2)-1]\}^2}$
r_m	$p_3 \ln p_2$	See Eq. (11b)	See Eq. (12b)
$n(r_m)$	$\frac{p_1(1+p_2)^2}{4p_2}$	See Eq. (11c)	See Eq. (12c)
As $\rightarrow 0$, $n(r) \approx$	$p_1\left[1+\left(\frac{p_2-1}{p_2+1}\right)r/p_3\right]$	0	0
$r \rightarrow \infty$, $n(r) \approx$	0	$p_1 r^{-(p_4+1)}$	$p_1 r^{-p_4}$
$N(r)$	$\frac{p_1(1+p_2)^2 p_3}{[p_2+\exp(r/p_3)]}$	$\frac{p_1[\exp(p_2/r^{p_4})-1]}{p_2 p_4\{1+p_3[\exp(p_2/r^{p_4})-1]\}}$	not applicable
As $r \rightarrow 0$, $N(r) \approx$	$p_1(1+p_2)p_3[1-r\{p_1(1+p_2)^{-1}\}]$	$p_1(p_2 p_3 p_4)^{-1}$	not applicable
As $r \rightarrow \infty$ $N(r) \approx$	0	0	not applicable
${}_{\bullet}M_k$	not applicable	not applicable	$\frac{p_1}{2p_3^2 p_2^{p_{4k}}}\Gamma p_{4k} \sum_{i=0}^{\infty}(1-\frac{1}{p_3})^i (i+1)^{-(p_{4k}-1)}$, $p_{4k} = p_4 - \frac{(k+1)}{2}$

SECTION 6

RETRIEVAL OF AEROSOL CHARACTERISTICS FROM SATELLITE BORNE SCATTERING AND EXTINCTION MEASUREMENTS

A versatile inversion code has been developed which is capable of retrieving profiles of aerosol size distribution and concentration from multi-wavelength satellite measurements of either the scattered radiance from the Earth's sunlit atmosphere in both the limb-viewing mode and downware-viewing mode, or the extinction of direct solar radiation by the earth's atmosphere. The inversion code in its present form is a composite of three sub-codes corresponding to the aforementioned three measurement modes. A description of these codes will be given. The inversion code is composed of several module algorithms (or subroutines) for treating the inverse problem in radiative transfer through a scattering and absorbing aerosol atmosphere, which is vertically inhomogeneous, spherical, and which takes into account multiple scattering and surface albedo effects. The appropriate module algorithms can be interchangeably brought into operation, as needed for any of the three different modes of measurement. The inversion code was initially developed for the problem of retrieving profiles of aerosol size distribution (S.D.) and density, ozone and NO_2 density from 8-channel measurements of scattered radiance in the limb viewing mode (Ref. 49). Work on development of various aspects of these codes, under NASA support, has been continuing since early 1970s. The inversion code has been adapted, applied, and tested using synthetic, and some real, measurements for the remote sensing techniques shown in Table 6.1 (Ref. 55).

TABLE 6.1: Remote Sensing Techniques and Observing Modes

Observation Modes	Wavelengths	Quantity Retrieved	Altitude Range
Solar extinction --limb	vis/near IR	Aerosol, O_3	10-50 km
Scattered radiance --limb	vis/near IR	Aerosol S.D.	15-40 km
		Rayleigh	10-50 km
		O_3	15-40 km
		NO_2	25-50 km
Solar aureole --limb	vis/near IR	Aerosol S.D.	Middle Atmosphere
Scattered radiance --downviewing	vis/near IR	Aerosol loading	Troposphere
SBUV--downviewing	UV	Ozone profile	25-50 km
SBUV--limb	UV	Ozone profile	35-50 km

Examples are given showing the retrieval results for the vertical profiles of aerosol size distribution, concentration, and real and imaginary parts of the refractive index (assuming spherical particles) from simulated measurements of the profiles of limb scattered radiance and atmospheric extinction (e.g., SAM II and SAGE), and for the total aerosol loading from measurements of upwelling radiance (e.g., Landsat and GOES series). In addition, we discuss the sensitivity of retrieved results to different parameters, such as, percentage random error, initial guess, surface albedo, etc.

(i) *Inversion Code*

The inversion code, originally referred to as SLIC (Sunlit Limb Inversion Code), is in its present form a composite of three codes corresponding to the different observation modes, i.e., SLIC, SEIC (Solar Extinction Inversion Code), and SURIC (Sunlit Upwelling Radiance Inversion Code), each applicable to the appropriate aforementioned problem. The physical and mathematical bases of these codes are briefly summarized.

Solutions to the remote sensing problem generally involve two elements.

An equation or modeling process is required to enable the mapping of observations onto the space of sought variables and a regularization process is required to condition the solutions so that they meet acceptable physical and mathematical criteria. SLIC and SURIC carry out the variable-observation mapping by means of a radiative transfer model named DART (Ref. 49); and SEIC carries it out by the use of Beer-Bouguer Law. It achieves regularization by application of optimal estimation theory.

Let $\underset{\sim}{M}(\underset{\sim}{x})$ represent an observation vector, and $\underset{\sim}{x}$ an observable vector of variables mapped on $\underset{\sim}{M}(\underset{\sim}{x})$ by $\underset{\sim}{M}(\underset{\sim}{x}) = H\underset{\sim}{x}$. Consider the quadratic cost functional

$$J(\underset{\sim}{x}) = (\underset{\sim}{x} - \underset{\sim}{x}_p)^T P_D^{-1} (\underset{\sim}{x} - \underset{\sim}{x}_p) + \{\underset{\sim}{M} - \underset{\sim}{M}(\underset{\sim}{x}_p)\} R^{-1} \{\underset{\sim}{M} - \underset{\sim}{M}(\underset{\sim}{x}_p)\} \quad (1)$$

where $\underset{\sim}{x}_p$ is any prior estimate of $\underset{\sim}{x}$. Minimizing J yields a minimum variance or optimal solution

$$\hat{\underset{\sim}{x}} = \underset{\sim}{x}_p + K(P_p, H_p, R) \{\underset{\sim}{M} - \underset{\sim}{M}(\underset{\sim}{x}_p)\} \quad (2)$$

where P_p and R are the state and measurement error covariances. In the inversion codes, this estimator is iterated by inserting $\underset{\sim}{x}$ for $\underset{\sim}{x}_p$ until the $\underset{\sim}{M}$ residuals are less than the observational uncertainty. Some of the important attributes of these codes are: (a) iteration to treat nonlinear problems; (b) calculation of multiple scattering in a curved atmosphere; (c) a pseudo-partial technique for speeding convergence; and, (d) a procedure for rapidly mapping aerosol physical parameters onto observation space.

(ii) *Sample Applications*

Sample application results are shown in Figs. 6.1 to 6.4 for retrieved profiles of aerosol characteristics (and ozone and NO_2 density) and retrieved

aerosol loading obtained from multispectral measurements.

Case 1: Retrieval of Profiles of Aerosol Characteristics (and ozone and NO_2 density) from Simulated Measurements of Scattered Radiance in Limb Viewing Mode.

Figure 6.1 a) shows the viewing geometry for measuring scattered radiance of the sunlit limb (i.e., in the limb viewing mode). Simulated measurements of vertical profiles of scattered radiance of the sunlit horizon in seven channels (λ = 350, 400, 490, 600, 675, 777, and 863 nm) were used to retrieve vertical profiles of the following quantities: (a) aerosol size distribution represented by Junge power law exponent ν (see Fig. 6.1 b)); (b) aerosol density, particles cm^{-3} (see Fig. 6.1 c)); (c) real part of aerosol refractive index (see Fig. 6.1 d (d) imaginary part of aerosol refractive index (see Fig. 6.1 e)); molecular density (not included here); (f) ozone density (see Fig. 6.1 f)); and (g) NO_2 density (see Fig. 6.1 g)). The retrieved results show good agreement with true values (circles). The agreement for the cases of NO_2 and aerosol refractive index at lower altitudes could be improved by increasing the upper limit of the number of iterations to, say, 20. Work is in progress on determining the sensitivity of retrievals to the initial guesses for the different parameters.

Case 2: Retrieval of Tropospheric Aerosol Content (or Optical Depth or Extinction Coefficient) from Measurements of Upwelling Radiance.

As an example, retrievals of tropospheric aerosol extinction (or aerosol content) were made from simulated upwelling radiance measurements at wavelength λ = 1.0 μm. The agreement between the retrieved value and the true value is extremely good as shown in Fig. 6.2. The viewing geometry is shown in Fig. 6.2 a).

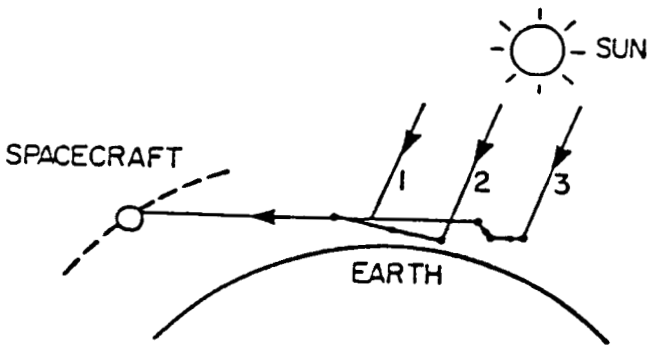

FIG. 6.1 a): Viewing Geometry for the Sunlit Limb Viewing Mode

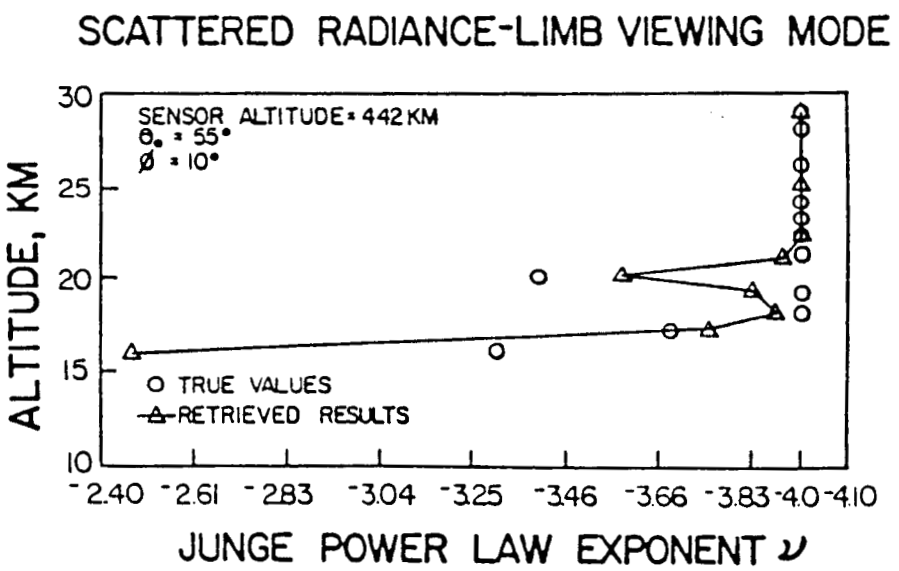

FIG. 6.1 b): Retrieved Size Distribution (Junge Power Law Exponent ν).

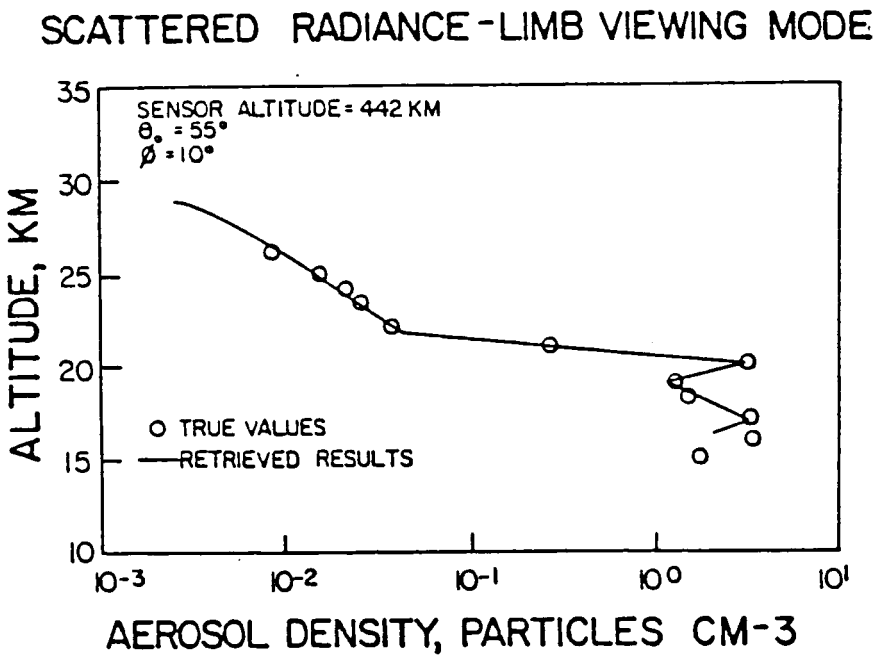

FIG. 6.1 c): Retrieved Aerosol NO Density Profile

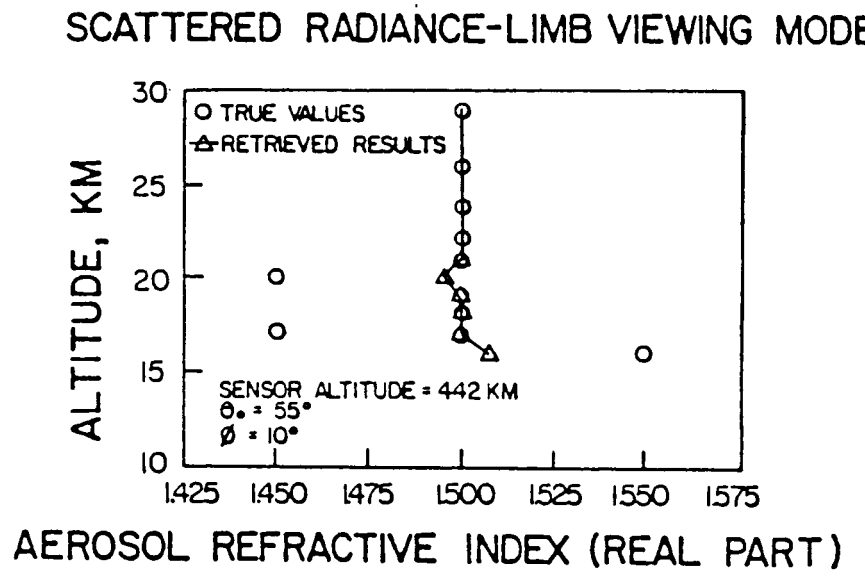

FIG. 6.1 d): Retrieved Aerosol Refractive Index (Real Part) Profile

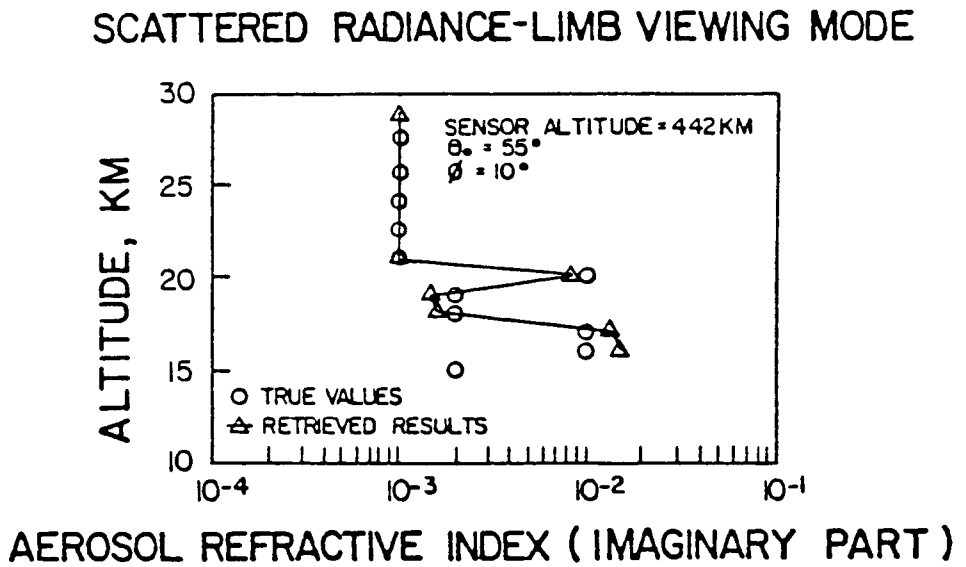

FIG. 6.1 e): Retrieved Aerosol Refractive Index (Imaginary Part) Profile

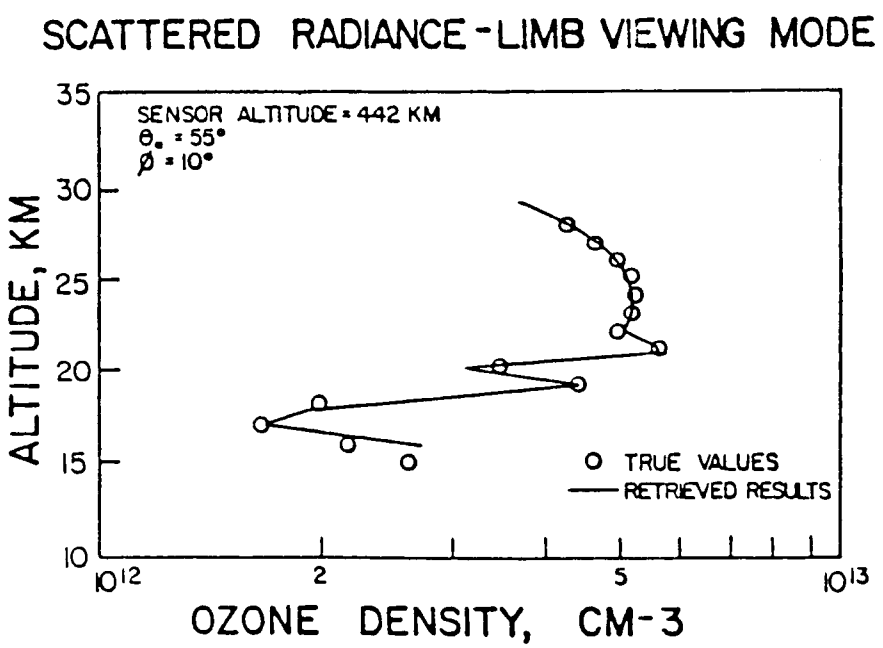

FIG. 6.1 f): Retrieved Ozone Density Profile

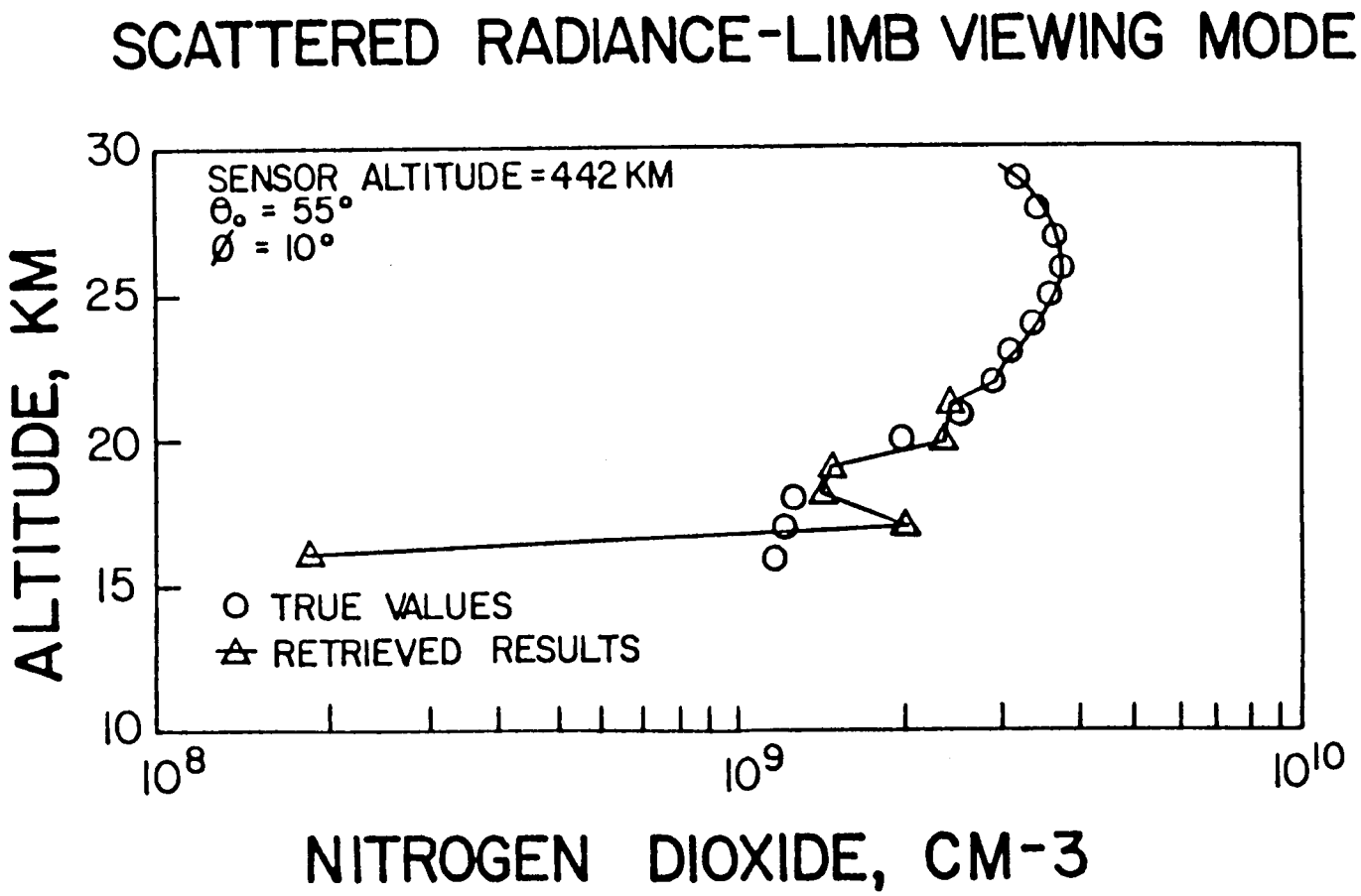

FIG. 6.1 g): Retrieved NO_2 Density Profile

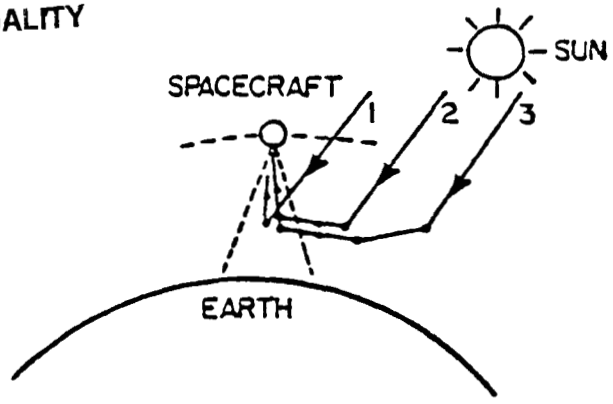

FIG. 6.2 a): Viewing Geometry for the Downviewing Observation Mode

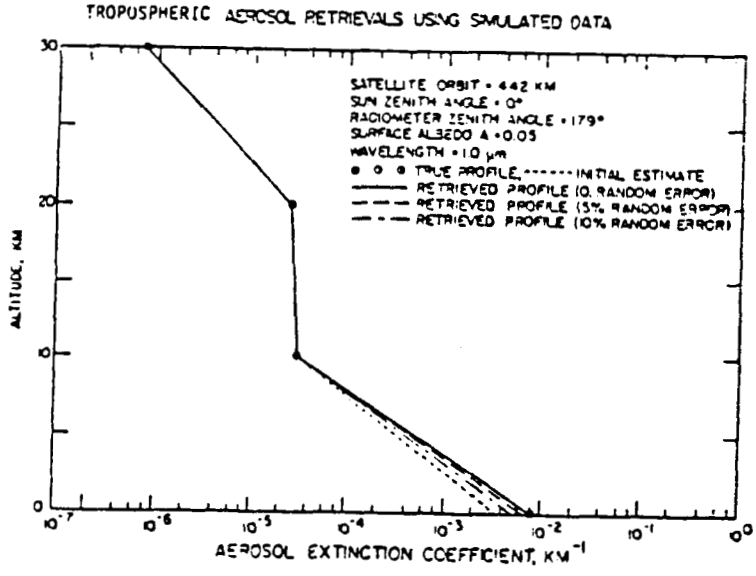

FIG. 6.2 b): Retrieval of Tropospheric Aerosol Content or Optical Depth from Simulated Upwelling Radiance Measurements at Wavelength 1.0 μm.

Case 3: The Retrieval of Aerosol and Ozone Density Profiles from Real Measurements of Direct Attenuated Solar Irradiance (Solar Extinction Mode).

The viewing geometry for the solar extinction mode during satellite sunrise/sunset is shown in Fig. 6.3. This is similar to the case of SAM I, SAM II, SAGE I, and SAGE II experiments. Figs. 6.3 b) and 6.3 c) show the retrieved results for aerosol and O_3 density profiles obtained from typical 4-channel SAGE I measurements (λ = 1.0, 0.6, 0.45, and 0.385 m). These retrievals agree with retrievals obtained by William Chu, NASA-Langley Research Center (not shown in Figs. 6.3 b) and 6.3 c)) using other inversion techniques.

Case 4: Solar Aureole-Limb Viewing

Preliminary results of retrievals from multispectral solar aureole measurements indicate that it is an accurate method for determining aerosol size distributions, and its use in future satellite aerosol sounding work is strongly recommended. A successful experimental validation of the solar aureole method using ground based observations has been performed. Forward-scattering limb radiance measurements would then be those that are made close to the sun during the satellite sunrise or sunset events. The advantages of the forward-scattering technique are that it is most sensitive to the aerosol size distribution and relatively less sensitive to refractive index and the shape.

(iii) *Validation of the Accuracy of the Inversion Codes*

In order to show that inversion codes we have developed produce accurate retrievals, we performed a retrieval of the ozone density profile from the upwelling radiance measurements in the SBUV experiment because ground truth measurements were available for this experiment. The viewing geometry of

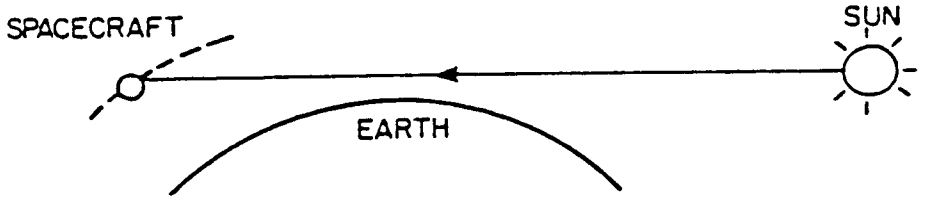

FIG. 6.3 a): Viewing Geometry for the Solar Occultation Mode

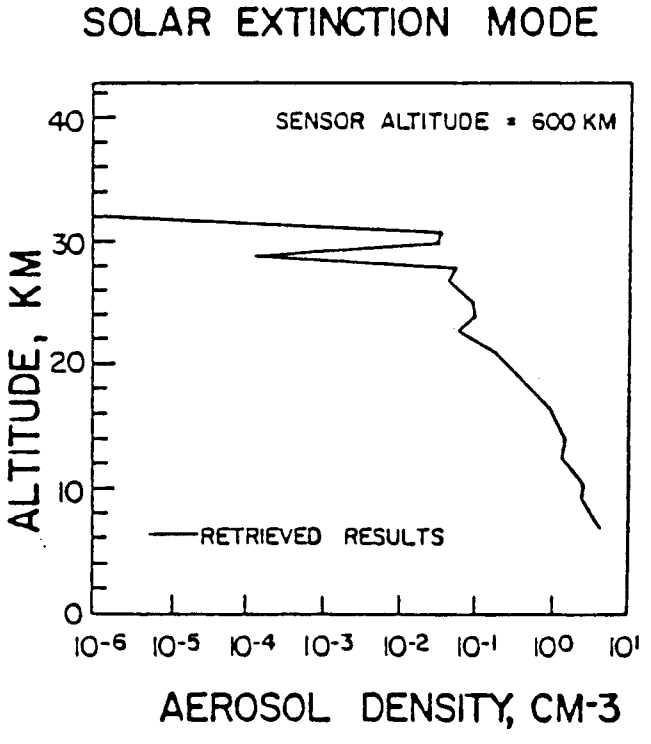

FIG. 6.3 b): Retrieved Profile of Aerosol Density from Multispectral Attenuation Measurements at λ *= 1.0, 0.6, 0.45, and 0.385* μ*m.*

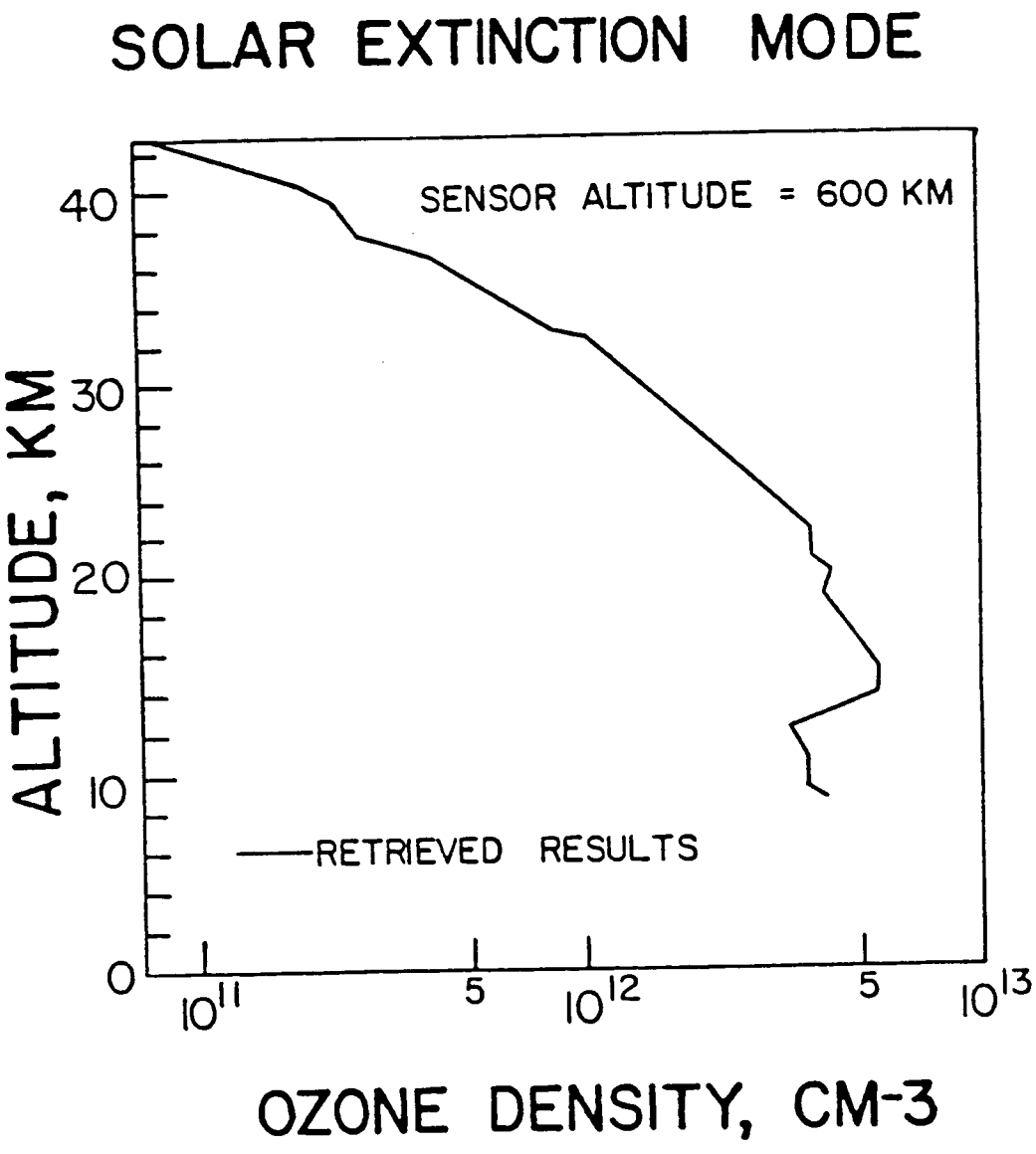

FIG. 6.3 c): Retrieval of Profile of Ozone Density from Multispectral Attenuation Measurements at λ = 1.0, 0.6, 0.45, and 0.385 μm.

radiance measurements in the downviewing mode is shown in Fig. 6.2 a). Retrievals of ozone density profile were obtained from real 7-channel SBUV measurements at Point Mugu, CA, and were compared with rocket measurements of ozone profile (shown by solid line) (Ref. 55). The agreement between the two results is excellent as shown in Fig. 6.4.

(iv) *Sensitivity Studies*

Systematic error analysis studies are currently being performed to understand how the errors in the selection of initial guess values affect the retrieved aerosol extinction β_{aer} results for various percentage rms random error values (0., 2.0, 5.0, and 10%) in the measurements at different values of the surface albedo (A = 0.05, 0.1, 0.2, and 0.3; see Table 6.2) and tangent altitude (16 and 24 km; see Table 6.3). As expected, the accuracy of the retrieved β_{aer} improves when the rms error is decreased and the initial guess is brought closer to the true value.

(v) *Advantages of Satellite-Based Scattered Radiance Technique*

The following are some of the advantages of the scattered radiance technique:

(a) No restrictions are placed on the sun's location, so that continuous or intermittent measurements can be made of the aerosol size distribution during the entire sunlit portion of the orbit, which will shed information on the temporal behavior of stratospheric aerosols and their sources and sinks. However, the most accurate information about aerosol size distributions, we believe, would be obtained from forward-scattered (aureole) limb radiance measurements when the sun's disk is close to the horizon.

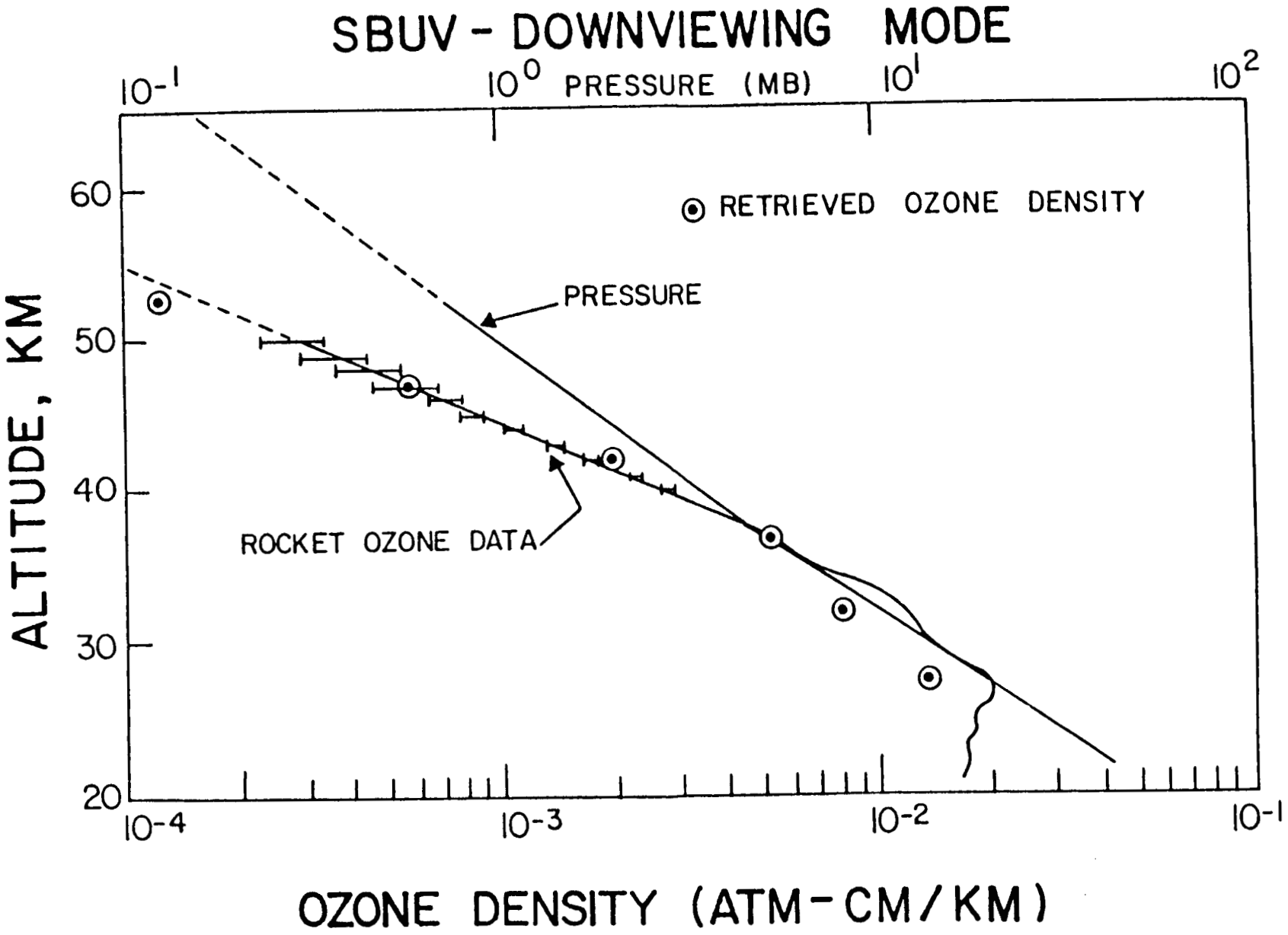

FIG. 6.4: Comparison of Rocket Ozone Data Profile and Retrieved Ozone Profile

TABLE 6.2: Retrieval Accuracy for β_{aer} at λ = 1.0 μm for Various Values of Random Error and Initial Guess. True Value of β_{aer} (at 0 km) = 7.96 x 10^{-3} km^{-1}.

Albedo	Random error (% Signal)	Initial Guess (% True Value)				
		10.0	30.0	50.0	70.0	90.0
0.05	0.	7.93(-3)	7.94(-3)	7.95(-3)	7.95(-3)	7.96(-3)
	.02	6.89(-3)	6.93(-3)	6.94(-3)	6.94(-3)	6.94(-3)
	.05	5.39(-3)	5.43(-3)	5.43(-3)	5.44(-3)	5.44(-3)
.10	0.	7.94(-3)	7.95(-3)	7.95(-3)	7.95(-3)	7.96(-3)
	.02	7.25(-3)	7.25(-3)	7.26(-3)	7.27(-3)	7.27(-3)
	.05	6.22(-3)	6.23(-3)	6.24(-3)	6.24(-3)	6.24(-3)
.20	0.	7.94(-3)	7.95(-3)	7.95(-3)	7.95(-3)	7.95(-3)
	.02	7.36(-3)	7.37(-3)	7.37(-3)	7.37(-3)	7.38(-3)
	.05	6.50(-3)	6.50(-3)	6.51(-3)	6.51(-3)	6.51(-3)
.30	0.	7.94(-3)	7.95(-3)	7.95(-3)	7.95(-3)	7.96(-3)
	.02	7.40(-3)	7.40(-3)	7.40(-3)	7.41(-3)	7.41(-3)
	.05	6.50(-3)	6.58(-3)	6.59(-3)	6.59(-3)	6.59(-3)
	.10	5.24(-3)	5.24(-3)	5.24(-3)	5.24(-3)	5.24(-3)
	.15	3.92(-3)	3.92(-3)	3.91(-3)	3.91(-3)	3.90(-3)
	.20	2.62(-3)	2.61(-3)	2.60(-3)	2.59(-3)	2.59(-3)

TABLE 6.3: Retrieval Accuracy for β_{aer} at λ = 1.0 μm for Various Values of Random Error and Initial Guess. (Detector Altitude = 600 km)

Altitude 16 km (True β_{aer} = 2.800(-4) km^{-1})

Random Error (% Signal)	Initial Guess (% True value)				
	10.	30.	50.	70.	90.
0.0	2.81(-4)	2.80(-4)	2.80(-4)	2.80(-4)	2.80(-4)
2.0	2.84(-4)	2.82(-4)	2.78(-4)	2.80(-4)	2.78(-4)
5.0	2.83(-4)	2.78(-4)	2.88(-4)	2.77(-4)	2.79(-4)
10.0	2.97(-4)	2.87(-4)	2.74(-4)	2.92(-4)	2.74(-4)

Altitude 24 km (True β_{aer} = 7.000(-5) km^{-1})

Random Error (% Signal)	Initial Guess (% True value)				
	10.	30.	50.	70.	90.
0.0	7.01(-5)	7.01(-5)	7.00(-5)	7.00(-5)	7.00(-5)
2.0	7.16(-5)	6.87(-5)	6.30(-5)	7.12(-5)	6.56(-5)
5.0	7.89(-5)	7.39(-5)	6.89(-5)	6.41(-5)	5.95(-5)
10.0	6.72(-5)	6.34(-5)	7.54(-5)	7.02(-5)	6.51(-5)

(b) Because of the measurements of angular distribution of the scattered radiance, it will be possible to make accurate retrievals of aerosol size distribution which are presently not available on a global basis.

(c) In addition, by making polarization measurements of scattered radiance it should be possible to retrieve the aerosol refractive index, which is sensitive to polarization.

(vi) *Conclusions*

These results show the sophistication and accuracy of our inversion codes. However, their capabilities can be enhanced by performing: (a) sensitivity studies such as errors in retrieved results due to bandwidth or radiometer channels and surface albedo, and (b) channel optimization studies for designing of radiometer channels to provide optimized retrievals of certain species of tropospheric aerosols that may be of special interest.

SECTION 7

SIMULATION OF LIMB SOLAR AUREOLE RADIANCE

7.1 INTRODUCTION

In Section 2, we have discussed the theory and application of solar aureole almucantar radiance. The solar aureole is the region of enhanced sky radiance close to (~ within 20^{o} of) the solar disk; and the almucantar is the observation scan for which the zenith angle equals the solar zenith angle with the axis of rotation along the local zenith. In Section 2, it was shown that columnar size distributions of atmospheric aerosols can be effectively retrieved from the almucantar radiance measurements made either from ground-based or airborne platforms. In either case, the results are regional in nature. Since the information of aerosol size distributions with a global scale coverage is highly desired for many purposes, such as for studying the potential impact of aerosols on the climate, we investigate, in this Section, extending this technique to satellite-based measurements of forward scattered solar aureole radiance at appropriate range of scattering angles for either a single wavelength or multiwavelengths. In this Section we present the results of numerical simulation of the limb solar aureole radiance and discuss if the weighting functions would permit retrieving aerosol size distributions with high vertical resolution. The results of retrievals will be discussed in a

subsequent publication.

7.2 SINGLE SCATTERING THEORY OF THE LIMB SOLAR AUREOLE RADIANCE

In this section, we consider the single scattering theory of the limb solar aureole radiance as viewed from a satellite-borne sensor. The following simplifying assumptions used in the theory are:

1. Particles are spherical so that results of the Mie theory can be applied.

2. The atmosphere is spherically symmetric, horizontally homogeneous, and vertically inhomogeneous.

3. Absorption effects are ignored by selecting to work in spectral regions for which atmospheric absorption is nil.

4. The polarization effects are small for forward-scattered light and can be ignored.

5. The multiple-scattering effects at the forward-scattering angle are small compared with the single scattering and can be ignored.

Figure 7.1 shows schematically the sensing geometry of a satellite-borne instrument measuring the limb solar aureole radiance. Point A represents the location of the satellite instrument and O is the center of the earth. The line $\overrightarrow{ABC'}$ denotes the viewing path of the detector with the portion $\overrightarrow{BC'}$

passing through the atmosphere. The sunlight is in the direction $\overrightarrow{B:B'}$. The line $\overrightarrow{CF}$ represents a typical incoming ray of the solar radiation which reaches the detector (at A) after being scattered by the volume element at point F at a scattering angle ψ. The circle given by B´E´B"E"B´ (at the outer edge of the atmosphere) defines the scanning plane of the instrument scanning across the sun disk. The line $\overrightarrow{AB´O´B"}$ corresponds to the viewing path in the case of solar occultation measurement of the attenuated solar intensity (Section 6, Fig. 6.3). From Fig. 7.1, one may notice that all the incoming rays, which are encountered by the atmosphere along the arc $\overset{\frown}{C´CC"}$, will be scattered at different locations along the viewing path BC with the same scattering angle ψ, and be able to reach the detector at A. The normal view of the scanning plane B´E´B"E"B´ is illustrated in Fig. 7.2, and that of the plane OO´F is shown in Fig. 7.3. It is important to keep in mind that, in reality, measurement of the limb solar aureole almucantar radiance can be made whenever the spacecraft sunrise or sunset occurs. This sampling opportunity is exactly the same as that of the SAM II, SAGE 1 and SAGE II instruments. Furthermore, because this scheme takes the limb viewing geometry, the measurements of scattered radiance can be carried out at different sun-tangent heights (defined by the distance h_o = OO´, Fig. 7.3). Thus, higher vertical resolution can be achieved by this technique. This is in contrast to the ground-based solar aureole almucantar radiance approach (Section 2), in which case

one obtains mainly the path integrated (or columnar) information about the aerosol size distribution.

The governing equation of the total near-forward, singly-scattered, limb solar radiance, along the viewpath BC′ at wavelength λ with a scattering angle ψ and a sun-tangent altitude h_T (=OO′ in Fig. 7.1), is given by

$$B_\lambda(\psi, h_T) - I_o(\lambda)\int_B^{C'} T_\lambda(BP)\left\{\beta_M(\lambda)P_M(\psi)\rho_M(P) + \rho_A(P)\frac{1}{2_k^2}\int_{r_2}^{r_1}(i_1+i_2)n(r)dr\right\} T_\lambda(PC)ds \tag{7.1}$$

Most of the notations in Eq. (7.1) have their conventional meanings as defined in Section 2, except that they are applied to paths with different geometry. In Eq. 7.1, we have

$$\eta(r,P)dr = \rho_A(P)n(r)dr \tag{7.2}$$

which is the number of aerosol particles with radius between r and r + dr. In introducing Eq. 7.2, we have assumed that the form of the particle size distribution n(r) does not itself change with altitude z, but only the aerosol number density varies. There are two reasons for this assumption. First, it simplifies the simulation computation. Secondly, the detailed vertical variation of $\eta(r,P)$ is still uncertain. In Eq.(7.1), P is referred as an abitrary point along the viewing path, at which an incoming ray is scattered. T(BP) is the transmission of the path from B to P, and T(PC) is the that of the path from C to P. In order to determine the values of T(BP), T(PC), and to perform

the integration along the viewing path BC′, the atmosphere is divided into appropriate concentric shells with equal thickness (= 1 km, Fig. 7.1). The input data for this simulation include a background (molecular) atmosphere of the U.S. Standard Atmosphere 1976, and an aerosol particle profile based on the lognormal size distribution (Russell, et al., 1981), with the number concentration given by McClatchey et al. (1971). The values of the parameters which specify the size distribution are r_g = 0.0725 μm, σ = 1.86 corresponding to the background aerosol model (where r_g is the mode radius, σ is the spread of the lognormal curve). Figure 7.4 illustrates this lognormal size distribution. The vertical profile of aerosol density used in the analysis is displayed in Fig. 7.5. As to the refractive index, we have used the value of 1.43 corresponding to aerosol composition of 75% H_2SO_4 and 25% H_2O.

7.3 RESULTS

Table 7.1 presents the numerical simulation data for the forward scattered radiance at 18 different scattering angles along the almucantar when the tangent height of the center of solar disk is at 10 km. The scattering angles are at 1 degree interval from 1^o to 18^o. The computed signal radiance data is given in the third column of this table. The last column gives the corresponding tangent height of the viewing path at various

scattering angles. As one may notice, the tangent height of the viewing path increases with the scattering angle ψ. This situation is illustrated in Fig. 7.3. Furthermore, Table 7.1 shows that the scattered radiance decreases monotonically with the scattering angle ψ, with the largest contribution occurring at $\psi = 1$ degree. The fourth column in Table 7.1 is the tangent altitude of the viewing path.

Equation 7.1 can be written

$$B_\lambda(\psi, h_T) = I_o(\lambda) \int_\beta^{C'} d\, W_i(\psi, P)$$

where the subscripts M and A are the volume scattering coefficients of the molecules and aerosol, respectively, and W is the weighting function with an infinitesimal field of view. This weighting function tells how much the level z, where P is located, contributes to the radiation observed along a particular viewing path with a scattering angle ψ and the sun-tangent altitude h_T (Fig. 7.1). The weighting functions corresponding to the sun-tangent height (h_T) at 10 km is displayed in Fig. 7.6. As shown in Table 7.1, there are 18 scattering angles in this case. Only the weighting functions of every other scattering angle are shown in Fig. 7.6, which exhibits many interesting features. First, the weighting function shows a peak at the tangent of the viewing path. Secondly, the envelope of the peak of all the weighting functions of this particular scan exhibits closely the

vertical profile of aerosol number concentration (Fig. 7.5). This suggests that the signal radiance (column three in Table 7.1) is mainly due to aerosol scattering contribution coming from regions near the tangent point of the corresponding viewing path. It is interesting to note that the weighting function shows a slight asymmetry in the two parts of the viewing path separated by the tangent, especially the lower several curves corresponding to small scattering angles (see for example the curve with a scattering angle of 9 degrees).

To explain this, one refers to Fig. 7.7. In this figure, P and P′ are the locations of two volume elements along the viewing path BC′. They are at equal distance from the tangent F. The weighting function contributions of these two elements are

$$T(C_2P)\{\bar{\beta}_M(P) + \bar{\beta}_A(P)\}T(PB)ds$$

and

$$T(\overline{C_1P'})\{\bar{\beta}_M(P') + \bar{\beta}_A(P)\}T(\overline{P'B})ds$$

at point P and P′, respectively. Note, since the atmosphere is assumed spherically symmetric, we have

$$\bar{\beta}_M(P) = \bar{\beta}_M(P') \quad \text{and} \quad \bar{\beta}_A(P) = \bar{\beta}_A(P')$$

However, in general

$$T(\overline{C_2P})T(PB) \neq T(\overline{C_1P'})\,T(\overline{P'B})$$

As a result, the contribution to the weighting function from the two parts of the viewing path are not the same. As one may

anticipate, this difference gradually vanishes as the tangent altitude of the viewing path increases.

Similar calculations have also been carried out for every other 1-km altitude from 12 km to 26 km. The results of the calculated signal radiance are given in Table 7.2, and also shown in Fig. 7.8. From Fig. 7.8, one can see that the aureole radiance decreases rapidly as the sun-tangent altitude increases. In order to see the sensitivity of the calculated limb solar aureole almucantar radiance with respect to mode radius (r_g) which is used in the lognormal size distribution, calculations have been made with r_g = 0.0800 μm and r_g = 0.0653 μm. These two values are chosen by increasing and decreasing the value 0.0725 μm by 10%, which is used in obtaining the results shown in Fig. 7.8. The results of these calculations for r_g = 0.800 μm and 0.0653 μm are displayed in Figs. 7.8 and 7.9, respectively. By an examination of Figs. 7.8 through 7.10, it is found that the limb solar aureole almucantar radiance is sensitive to the aerosol size distribution.

In conclusion, we have successfully simulated the near forward scattering of the limb solar radiation based on a numerical model and examined the sensitivity of the solar aureole almucantar radiance with respect to the aerosol size parameter (r_g). This is a first step toward an attempt to examine the

possibility of measuring the stratospheric aerosol size distribution with global scale coverage and with high vertical resolution by using a satellite-borne instrument. The next step is to perform numerical simulations of retrieving the aerosol size distribution from the simulated radiance. This requires a development of an appropriate inversion scheme.

It is suggested that as a first step, the limb solar aureole radiance be determined by taking limb solar aureole photographs by using the camera(s) already aboard the space shuttle, and then deriving the aureole radiance by using the well-known photographic-photometry-microdensitometer techniques. Such procedures have been successfully tested and used in determining the almucantar radiance from ground platforms, and have been described in Section 2 in detail.

Table 7.1. Limb Solar Aureole Radiance at λ = 1 μm When the Sun-Tangent Height is at 10 km. Solar Irradiance = 0.0746 (W/cm^2 - μ)

	Scattering Angle ψ (deg)	Aureole Radiance (W/cm^2-sr-μ)	View-Path Tangent-Height (km)
1	1.000	0.89426E-02	10.155
2	2.000	0.87774E-02	10.620
3	3.000	0.84725E-02	11.394
4	4.000	0.79633E-02	12.475
5	5.000	0.72371E-02	13.864
6	6.000	0.62734E-02	15.557
7	7.000	0.49738E-02	17.553
8	8.000	0.29610E-02	19.848
9	9.000	0.15995E-02	22.440
10	10.000	0.86747E-03	25.324
11	11.000	0.41891E-03	28.498
12	12.000	0.18361E-03	31.957
13	13.000	0.77006E-04	35.696
14	14.000	0.32260E-04	39.710
15	15.000	0.13934E-04	43.994
16	16.000	0.64139E-05	48.541
17	17.000	0.31276E-05	53.347
18	18.000	0.15211E-05	58.404

Table 7.2. Limb Solar Aureole Radiance at 1.0 μm Wavelength (W/cm^2-sr-u) Scaled by 10^2.
Solar Irradiance = 0.0746 (W/cm^2-μ)

Scattering Angle (deg)	Sun-Tangent Altitude (km)								
	10	12	14	16	18	20	22	24	26
1	0.894E+00	0.829E+00	0.734E+00	0.626E+00	0.480E+00	0.299E+00	0.186E+00	0.123E+00	0.796E-01
2	0.878E+00	0.805E+00	0.706E+00	0.596E+00	0.433E+00	0.266E+00	0.168E+00	0.112E+00	0.717E-01
3	0.847E+00	0.763E+00	0.661E+00	0.539E+00	0.360E+00	0.221E+00	0.143E+00	0.945E-01	0.603E-01
4	0.796E+00	0.702E+00	0.595E+00	0.442E+00	0.274E+00	0.173E+00	0.115E+00	0.742E-01	0.472E-01
5	0.724E+00	0.623E+00	0.493E+00	0.315E+00	0.197E+00	0.129E+00	0.848E-01	0.542E-01	0.343E-01
6	0.627E+00	0.508E+00	0.336E+00	0.208E+00	0.136E+00	0.903E-01	0.579E-01	0.368E-01	0.231E-01
7	0.497E+00	0.329E+00	0.205E+00	0.135E+00	0.894E-01	0.575E-01	0.367E-01	0.230E-01	0.145E-01
8	0.296E+00	0.187E+00	0.124E+00	0.823E-01	0.531E-01	0.339E-01	0.213E-01	0.135E-01	0.864E-02
9	0.160E+00	0.108E+00	0.707E-01	0.456E-01	0.291E-01	0.184E-01	0.117E-01	0.753E-02	0.492E-02
10	0.867E-01	0.564E-01	0.364E-01	0.231E-01	0.147E-01	0.944E-02	0.614E-02	0.406E-02	0.273E-02
11	0.419E-01	0.269E-01	0.171E-01	0.110E-01	0.714E-02	0.471E-02	0.315E-02	0.215E-02	0.150E-02
12	0.184E-01	0.118E-01	0.770E-02	0.509E-02	0.341E-02	0.233E-02	0.162E-02	0.114E-02	0.825E-03
13	0.770E-02	0.511E-02	0.344E-02	0.235E-02	0.164E-02	0.116E-02	0.840E-03	0.621E-03	0.465E-03
14	0.323E-02	0.222E-02	0.156E-02	0.111E-02	0.810E-03	0.600E-03	0.452E-03	0.345E-03	0.264E-03
15	0.139E-02	0.101E-02	0.740E-03	0.553E-03	0.419E-03	0.321E-03	0.246E-03	0.190E-03	0.146E-03
16	0.641E-03	0.484E-03	0.370E-03	0.285E-03	0.220E-03	0.170E-03	0.131E-03	0.998E-04	0.755E-04
17	0.313E-03	0.242E-03	0.188E-03	0.145E-03	0.112E-03	0.851E-04	0.	0.	0.
18	0.152E-03	0.117E-03	0.907E-04	0.	0.	0.	0.	0.	0.

(E-03 = 10^{-3})

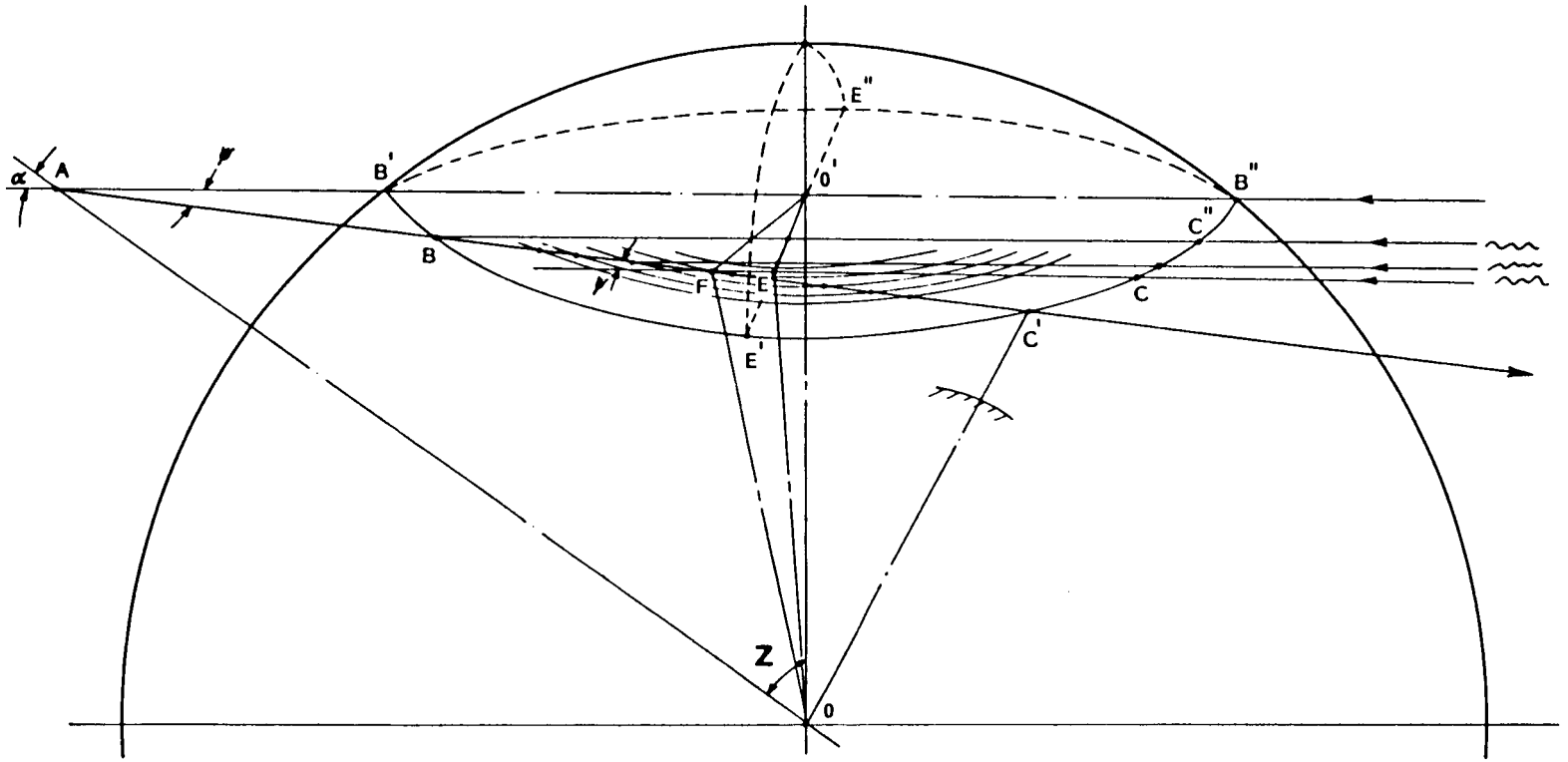

Figure 7.1. The sensing geometry of satellite-borne instrument for the measurement of near forward scattered limb radiance near the solar disc during the satellite sunrise or sunset.

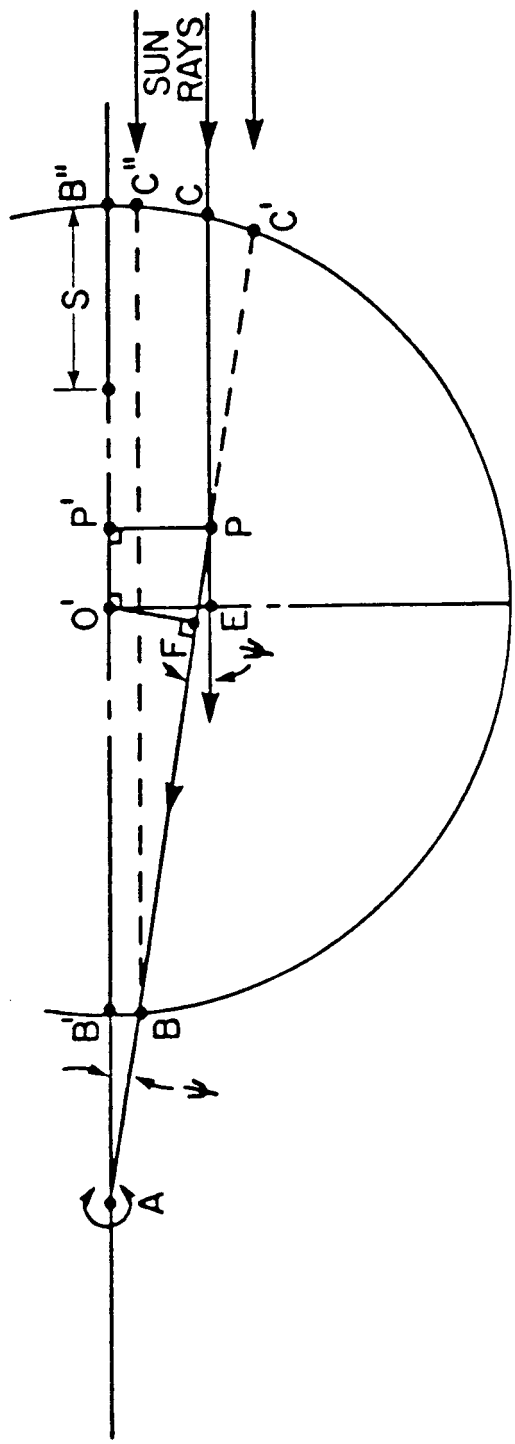

Figure 7.2. The normal view of the plane B'BC'B" shown in Fig. 7.1.

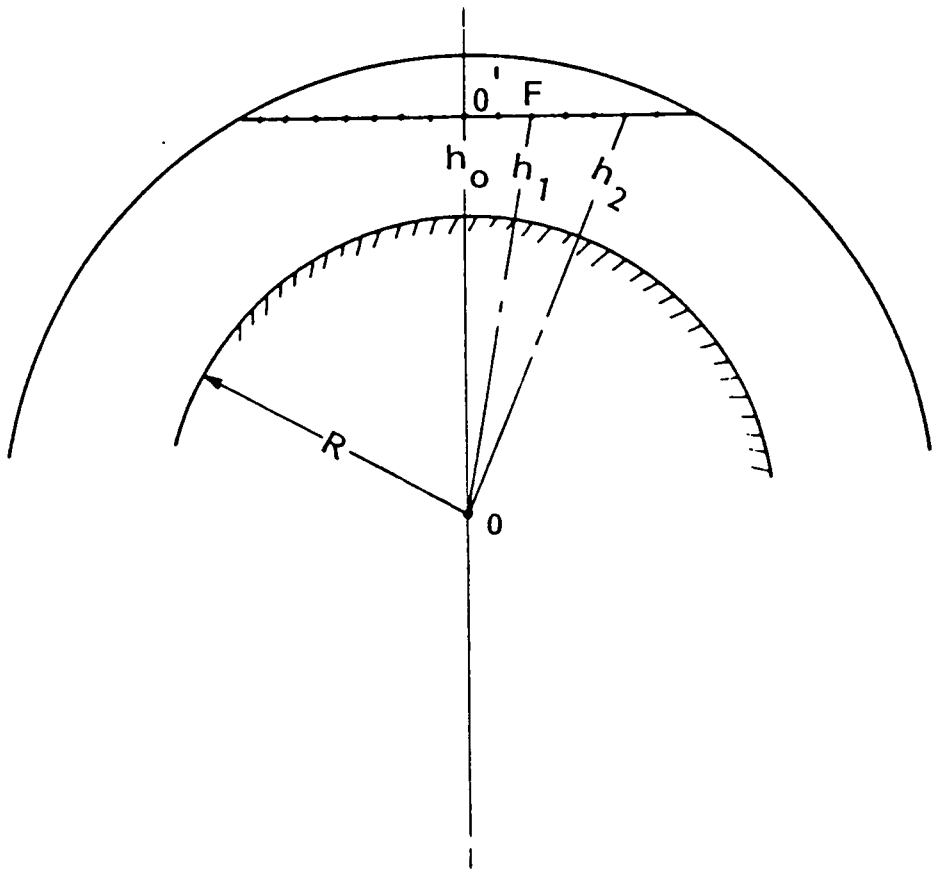

Figure 7.3. The normal view of the plane OO'F shown in Fig. 7.1.

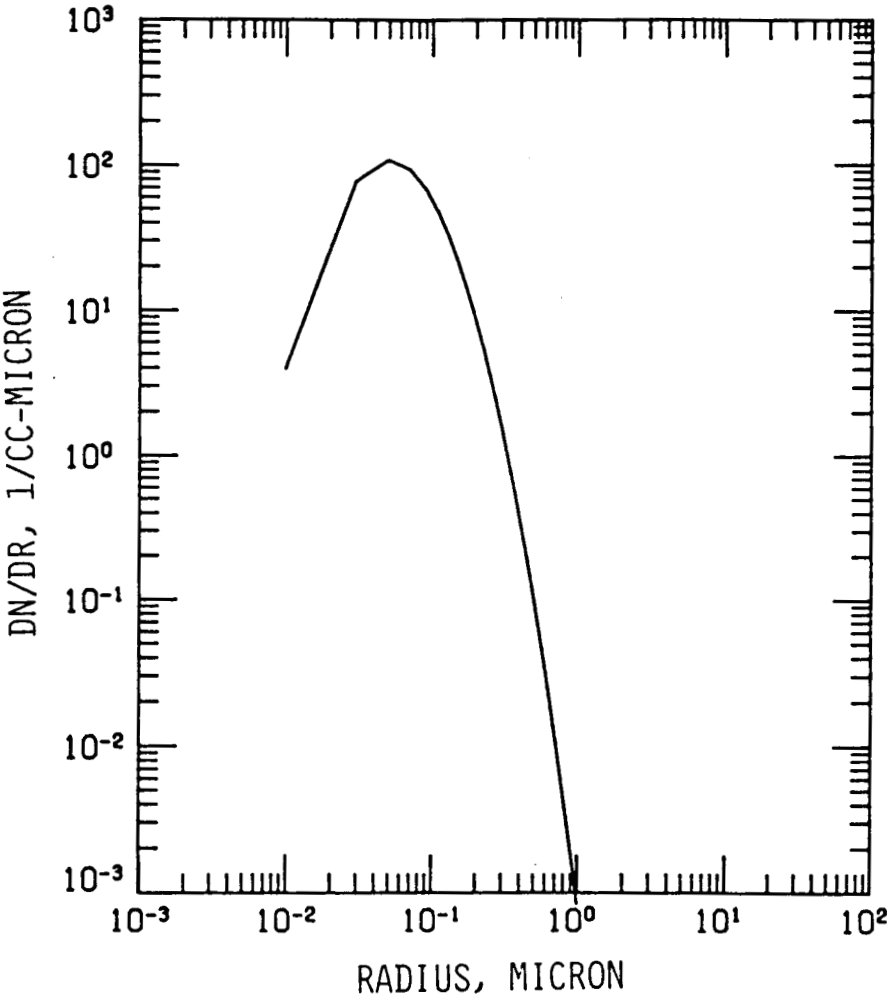

Figure 7.4. Lognormal size distribution with r_g = 0.0725 μm, σ = 1.86.

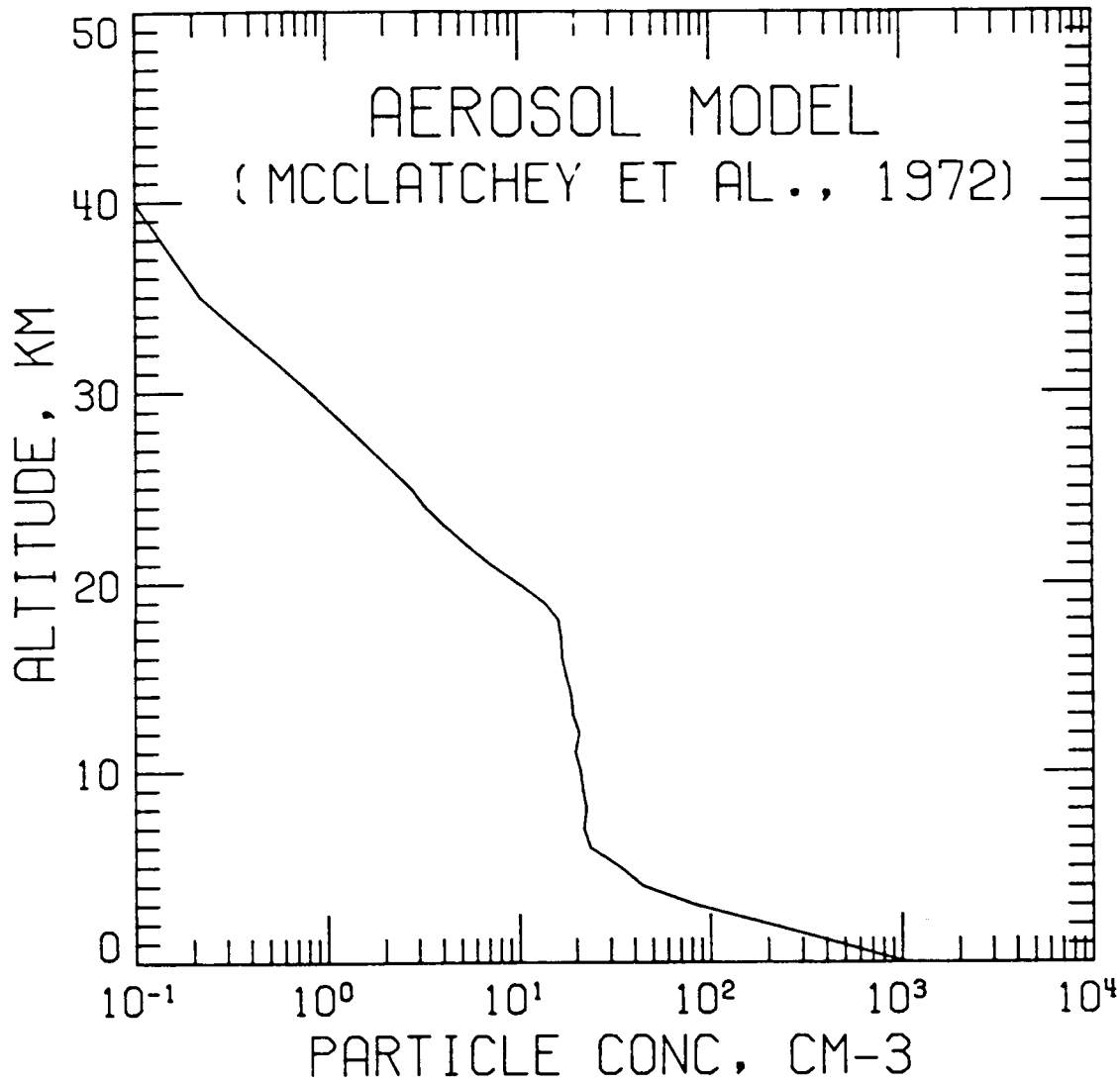

Figure 7.5. Aerosol number density profile (McClatchey et al., 1972).

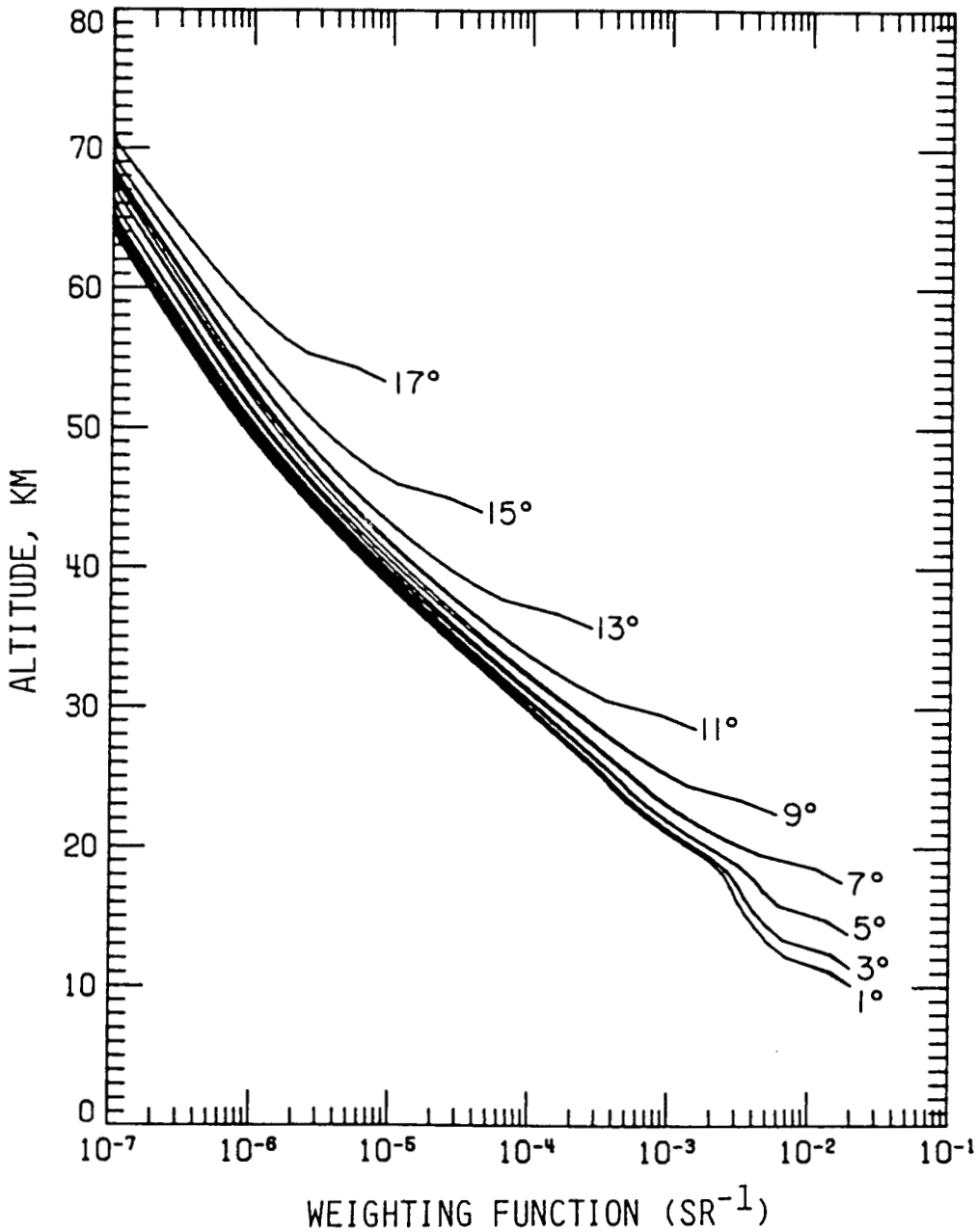

Figure 7.6. Weighting functions at a range of scattering angles from 1° to 17°. The sun-tangent is at an altitude of 10 km (corresponding to h_o-R in Fig. 7.3.)

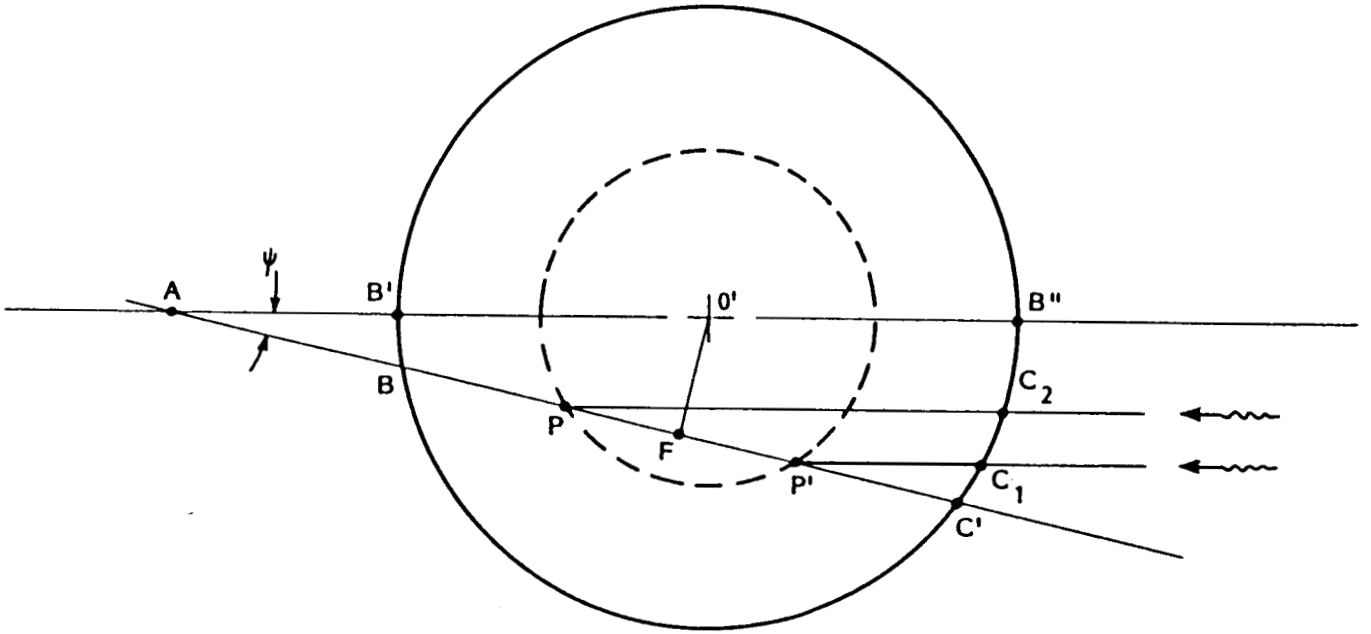

Fig. 7.7. Schematical figure used to illustrate the unsymmetric behavior of the weighting function.

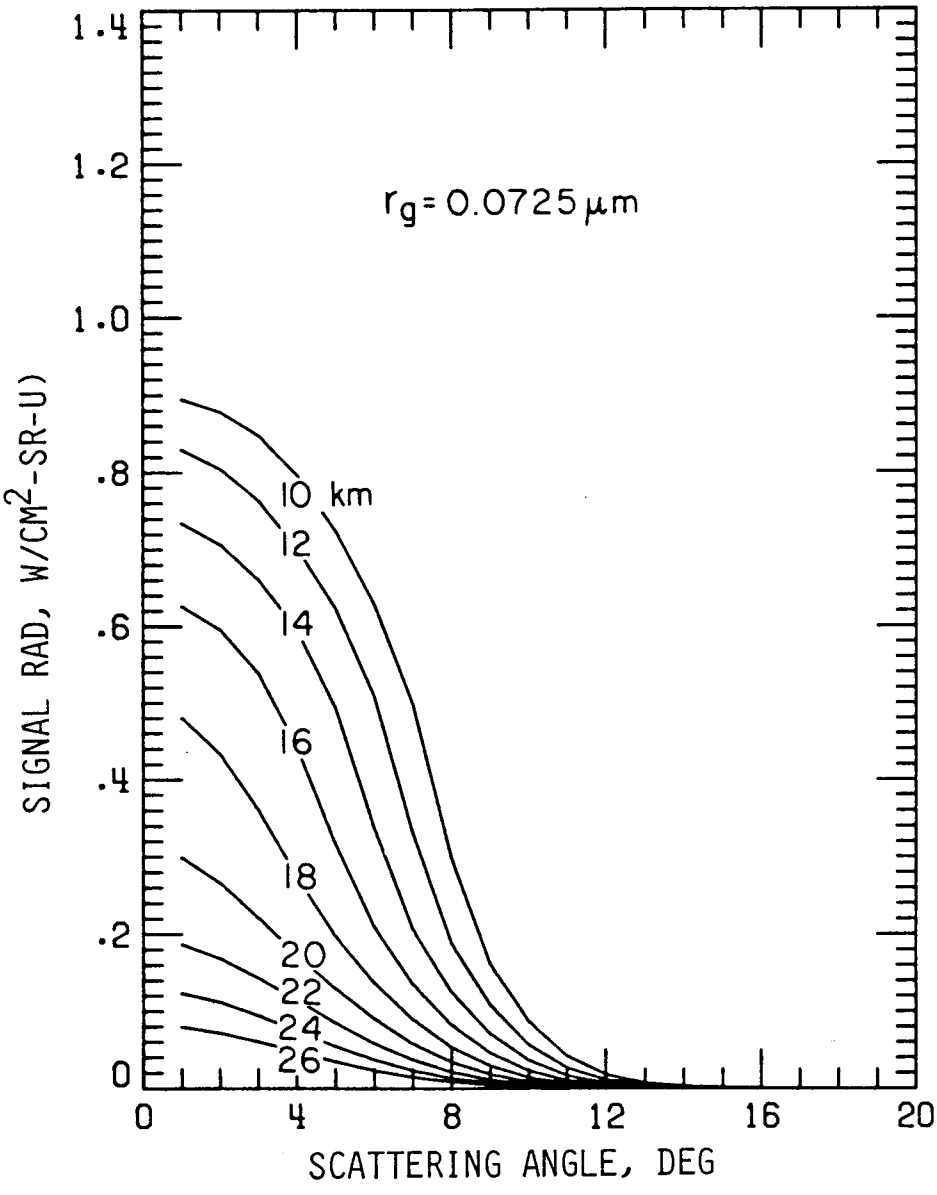

Figure 7.8. Signal radiance as a function of scattering angle ψ with fixed sun-tangent altitudes (r_g = 0.0725, σ = 1.86). Scaled by 10^2.

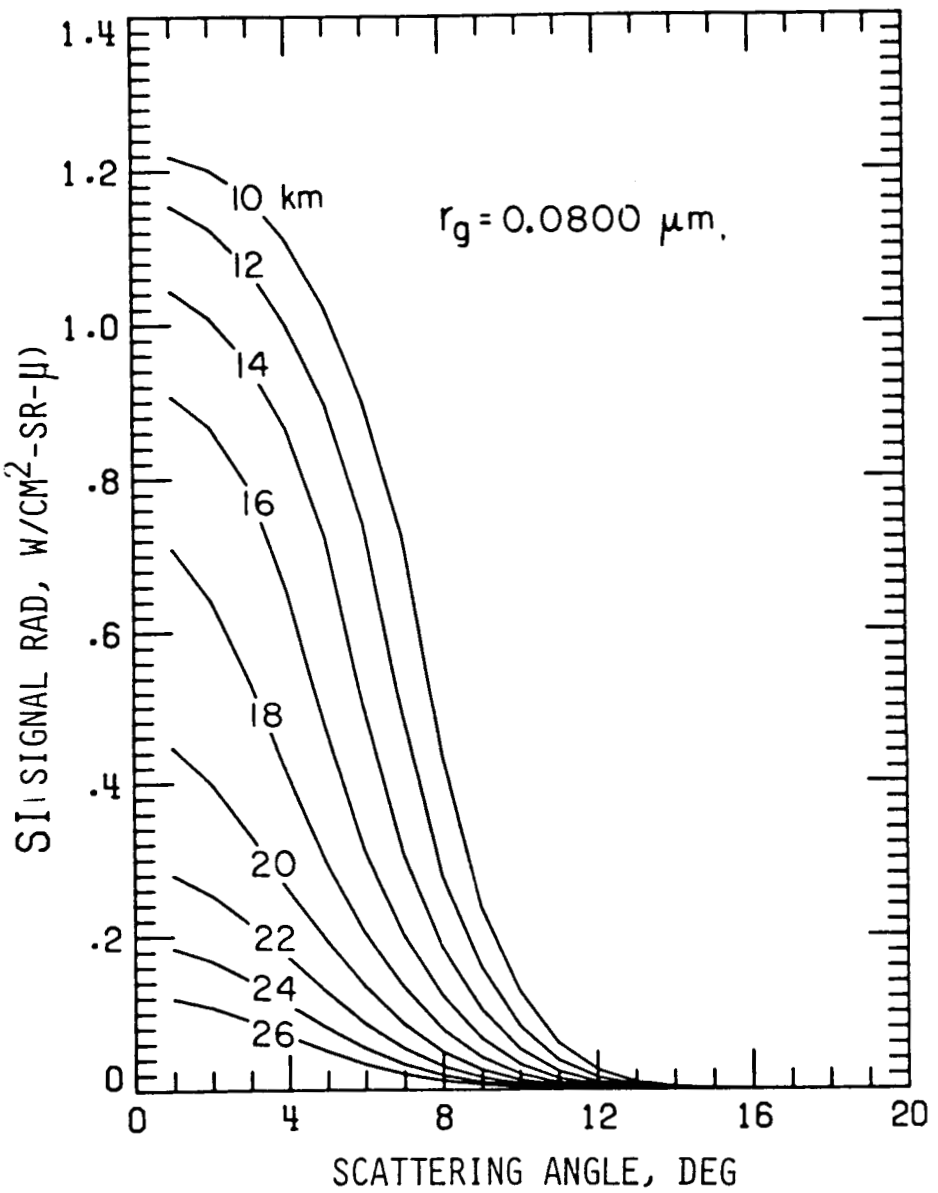

Figure 7.9. Signal radiance as a function of scattering angle ψ with fixed sun-tangent altitudes (r_g = 0.0800, σ = 1.86).

SECTION 8

VARIABILITY OF OZONE AT HIGH ALTITUDES DURING SATELLITE SUNSET/SUNRISE EVENTS

The solar occultation technique has been used for measuring the concentration of atmospheric minor constituents in the upper atmosphere. This technique determines the attenuation profile of solar intensity during sunrise and sunset encountered by the instruments mounted on the orbiting satellites. The SAGE I (McCormick et al., (Ref. 56)) is a good example of using this solar occultation technique. Due to the fact that concentrations of atmospheric species with a photochemical relaxation time scale of the order of a day or less undergo significant diurnal variations, the interpretation of the measured results using solar occultation technique require detailed knowledge of the diurnal variation of the interested species. Since ozone is one of the most important atmospheric constituents, and since it has been measured using solar occultation technique, it is significant to investigate its diurnal variation. Modeling studies on this variation have been conducted by many investigators. However, in the existing models[1] the complete diurnal integrations are carried out by assuming implicitly or explicitly that the time dependence of the overhead ozone column has a small effect on diurnal variations of photodissociation rates at the level in question. In other words, a background ozone distribution, in general, assumed to be a function of altitude but not time, is used for the complete diurnal integration. As a result, the time variation of local photodissociation rate is determined

[1] Prather (1981) has taken the sphericity and the change in local solar time along the ray path into consideration in his diurnal calculation. However, he did not describe the method of his calculation.

solely by the variation of local zenith angle. Since ozone absorbs significant amounts of solar radiation, and since its diurnal variation is important, the effect of change in local solar time along the ray path may be important in modeling of ozone diurnal variation. The purpose of this section is to describe the diurnal variation of ozone in the mesosphere (50-80 km) by using a diurnal integration with both sphericity and changes in the local solar time along the ray path taken into account. The results will be compared with that without including the change in local solar time along the path. Both, an oxygen-only atmosphere and an oxygen-hydrogen-nitrogen-carbon (O-H-N-C) atmosphere are used in this investigation. Comparison will also be made between the model results and the available measurements. It should be mentioned that most of the results in this section have been presented in the Quadrennial International Ozone Symposium, August 4-8, 1980, Boulder, Colorado, U.S.A. (Ref. 95)

8.1 PHOTOCHEMICAL MODEL

Since the calculation for the oxygen-only atmosphere is similar to that for the O-H-N-C atmosphere, we shall discuss only the latter in detail. This model includes a total of 69 reactions (Table 8.1) and 24 atmospheric species (Table 8.2). Among these 24 gases, 18 of them are expected to show diurnal variation. They are O; O(1D); O_3; H; H_2; OH; H_2O; HO_2; H_2O_2; N_2O; NO; NO_2; NO_3 CH_3; CH_2O; CHO; CH_3O; and CH_3O_2 (Table 8.2). Accordingly, the model can be described by a system of 18 simultaneous nonlinear differential equations:

$$\frac{dn_j}{dt} = P_j - L_j \quad , j = 1, 2, \ldots, 18 \qquad (1)$$

where P and L represent the production and loss terms, respectively. Since

TABLE 8.1. Reaction Rate Constants and References†. The units of rate constants are cm^3sec^{-1} and cm^6sec^{-1} for the two- and three-body reactions respectively. All reaction rates and absorption cross-section data are from NASA RP 1049 unless otherwise noted.*

Reaction	Rate	Reference
1. $O(1D) + N_2 \rightarrow O + N_2$	2.0 (-11) exp(-107/T)	
2. $O(1D) + N_2 + M \rightarrow N_2O + M$	3.5 (-37) $(T/300)^{-0.45}$	
3. $O(1D) + O_2 \rightarrow O + O_2$	2.9 (-11) exp(-67/T)	
4. $O(1D) + O_3 \rightarrow 2O_2$	1.2 (-10)	
5. $O(1D) + O_3 \rightarrow 2O + O_2$	1.2 (-10)	
6. $O(1D) + NO_2 \rightarrow NO + O_2$	1.0 (-10)	
7. $O(1D) + N_2O \rightarrow O_2 + N_2$	4.8 (-11)	
8. $O(1D) + N_2O \rightarrow 2NO$	6.2 (-11)	
9. $O(1D) + H_2 \rightarrow H + OH$	9.9 (-11)	
10. $O(1D) + H_2O \rightarrow 2OH$	2.3 (-10)	
11. $O(1D) + H_2O_2 \rightarrow OH + HO_2$	5.2 (-10)	NBS 513
12. $OH + O \rightarrow H + O_2$	4.0 (-11)	
13. $H + O_3 \rightarrow OH + O_2$	1.4 (-10) exp(-470/T)	
14. $OH + H_2 \rightarrow H + H_2O$	1.2 (-11) exp(-2200/T)	
15. $H + HO_2 \rightarrow H_2 + O_2$	4.2 (-11) exp(-350/T)	NBS 513
16. $H + HO_2 \rightarrow H_2O + O$	8.3 (-11) exp(-500/T)	NBS 513
17. $H + H_2O_2 \rightarrow HO_2 + H_2$	2.3 (-12) exp(-1400/T)	NBS 513
18. $H + H_2O_2 \rightarrow OH + H_2O$	2.9 (-12) exp(-1400/T)	NBS 513
19. $H + OH + M \rightarrow H_2O + M$	4.3 (-25) $T^{-2.6}$	NBS 513
20. $O(1D) + CH_4 \rightarrow CH_2O + H_2$	1.4 (-11)	
21. $OH + CH_4 \rightarrow CH_3 + H_2O$	2.4 (-12) exp(-1710/T)	
22. $CH_3 + O_2 + M \rightarrow CH_3O_2 + M$	c_1=2.2 (-11) EX1=2.2 c_2=2.0 (-12) EX2=1.7	
23. $OH + CH_2O \rightarrow CHO + H_2O$	1.1 (-11)	
24. $O + CH_2O \rightarrow OH + CHO$	3.2 (-11) exp(-1550/T)	
25. $H + O_2 + M \rightarrow HO_2 + M$	5.5 (-32) $(T/300)^{-1.4}$	
26. $H + HO_2 \rightarrow 2OH$	4.2 (-10) exp(-950/T)	NBS 513
27. $OH + CO \rightarrow H + CO_2$	1.35 (-13) $(1 + P_{atm})$	
28. $CHO + O_2 \rightarrow HO_2 + CO$	5.0 (-12)	
29. $O(1D) + CH_4 \rightarrow CH_3 + OH$	1.3 (-10)	
30. $O + HO_2 \rightarrow OH + O_2$	3.5 (-11)	

TABLE 8.1 (Continued)

Reaction	Rate	Reference
31. $O + H_2O_2 \rightarrow OH + HO_2$	2.8 (-12) exp(-2125/T)	
32. $OH + O_3 \rightarrow HO_2 + O_2$	1.6 (-12) exp(-940/T)	
33. $HO_2 + O_3 \rightarrow OH + 2O_2$	1.1 (-14) exp(-580/T)	
34. $OH + HO_2 \rightarrow H_2O + O_2$	4.0 (-11)	
35. $OH + OH \rightarrow H_2O + O$	1.0 (-11) exp(-500/T)	
36. $OH + H_2O_2 \rightarrow HO_2 + H_2O$	1.0 (-11) exp(-750/T)	
37. $HO_2 + HO_2 \rightarrow H_2O_2 + O_2$	2.5 (-12)	
38. $O + NO_2 + M \rightarrow NO_3 + M$	1.0 (-31)	NBS 513
39. $O + NO_3 \rightarrow NO_2 + O_2$	1.0 (-11)	
40. $NO_2 + O_3 \rightarrow NO_3 + O_2$	1.2 (-13) exp(-2450/T)	
41. $NO_3 + NO \rightarrow 2NO_2$	1.9 (-11)	NBS 513
42. $HO_2 + NO \rightarrow OH + NO_2$	4.3 (-12) exp(-200/T)	
43. $OH + OH + M \rightarrow H_2O_2$	c_1=2.5 (-31), EX1=0.8 c_2=3.0 (-11), EX2=1.0	
44. $HO_2 + CH_3O_2 \rightarrow O_2 + CH_4O_2$	6.0 (-12)	
45. $CH_3O + O_2 \rightarrow HO_2 + CH_2O$	5.0 (-13) exp(-2000/T)	
46. $OH + CH_4O_2 \rightarrow H_2O + CH_3O_2$	1.0 (-10) exp(-750/T)	
47. $O + NO + M \rightarrow NO_2 + M$	1.55 (-32) exp(584/T)	NBS 513
48. $NO_2 + O \rightarrow NO + O_2$	9.3 (-12)	
49. $NO + O_3 \rightarrow NO_2 + O_2$	2.3 (-12) exp(-1450/T)	
50. $CH_3O_2 + NO \rightarrow NO_2 + CH_3O$	7.0 (-12)	
51. $O + O_2 + M \rightarrow O_3 + M$	6.2 (-34) $(T/300)^{-2}$	
52. $O + O + M \rightarrow O_2 + M$	4.8 (-33)	NBS 513
53. $O + O_3 \rightarrow 2O_2$	1.5 (-11) exp(-2218/T)	
54. $O_2 + h\nu \rightarrow O + O(1D)$	λ < 1750 Å	Ref. 96
55. $O_2 + h\nu \rightarrow O + O$	λ < 2423 Å	Ref. 97
56. $O_3 + h\nu \rightarrow O(1D) + O_2$	λ < 3125 Å	
57. $O_3 + h\nu \rightarrow O + O_2$	λ < 11800 Å	Ref. 96
58. $H_2O + h\nu \rightarrow H + OH$	λ < 2100 Å	Ref. 98
59. $H_2O_2 + h\nu \rightarrow OH + OH$	λ < 3500 Å	Ref. 99
60. $HO_2 + h\nu \rightarrow O + OH$	λ < 4560 Å	
61. $CH_2O + h\nu \rightarrow H + CHO$	λ < 3600 Å	Ref. 98
62. $CH_2O + h\nu \rightarrow H_2 + CO$	λ < 3600 Å	

TABLE 8.1. (Continued)

Reaction	Rate	Reference
63. $CH_4O_2 + h\nu \rightarrow CH_3O + OH$	$\lambda < 3500$ A	Ref. 99
64. $CH_4 + h\nu \rightarrow CH_3 + H$	$\lambda < 2800$ A	Ref. 98
65. $NO_2 + h\nu \rightarrow O + NO$	$\lambda < 3980$ X	
66. $NO_3 + h\nu \rightarrow O + NO_2$	$\lambda < 6980$ A	
67. $NO_3 + h\nu \rightarrow O_2 + NO$	$\lambda < 6980$ A	
68. $CO_2 + h\nu \rightarrow O(1D) + CO$	$\lambda < 1660$ A	Ref. 98
69. $CO_2 + h\nu \rightarrow O + CO$	$\lambda < 2260$ A	Ref. 98

* The rate constant 1.2(-10) = 1.2×10^{-11}.

† The reference indicated by NASA RP 1049 and NBS 513 refer to Refs. 100 and 101, respectively.

TABLE 8.2. Model Atmosphere

Major Species	O_2, N_2	
Minor Species	Long Relaxation Time Scale Species	CO, CH_4O_2, CH_4, CO_2
	Short Relaxation Time Scale Species	O(1D), O, O_3, H, H_2, H_2O, OH, HO_2, H_2O_2, N_2O, NO, NO_2, NO_3, CH_3, CH_3O_2, CH_3O, CH_2O, CHO.

in the region of interest, the atmospheric dynamic processes are of secondary importance, we may replace the total derivative by the local time derivative. Because of the large variation of relaxation time scales implicit in the chemical reaction set, it is convenient to group the minor species into 3 categories:

(i) The relaxation time scale is always smaller than the order of 10^1 sec through the whole day;

(ii) The relaxation time scale can be either smaller than or greater than the order of 10^1 sec depending on the local time and altitude;

(iii) The relaxation time scale is always greater than the order of 10^1 sec through the whole day.

It should be mentioned here, that this distinction is made just for the convenience of performing the numerical integration. It was found that O(1D), H, CH_3, and CHO belong to the first category; OH, HO_2, NO_2, NO_3, and CH_3O belong to the second category, while the third category includes O, O_3, H_2, H_2O, H_2O_2, NO, N_2O, CH_3O_2, and CH_2O.

As a result, the governing equation of species under photochemical equilibrium, i.e., relaxation time scale of less than 10^1 sec, can be written

$$O = P_j - L_j , \qquad j = 1, 2, \ldots, N. \tag{2}$$

8.2. PHOTODISSOCIATION RATES

The photodissociation rates (J_j) for the jth species can be written as

$$J_j(h,t) = \int \sigma_j(\lambda') \, I^{\infty}(\lambda') \, \tau(\lambda',h,t,) \, d\lambda', \tag{3}$$

where I^{∞} is the photon flux intensity at the top of the atmosphere;

σ_j is the absorption cross section of the jth gases species;

$\tau(\lambda',h,t)$ is the atmospheric transmittance of wavelength λ' at altitude h at local time t.

The finite resolution analog of Eq. 3 is:

$$J_j(h,t) = \sum_{i=1}^{\infty} \sigma_{ji} I_i^{\infty} \tau_i (h,t) \Delta\lambda_i , \qquad (4)$$

where the subscript i indicates the ith spectral interval. If we consider the atmospheric attenuation of the solar radiation due to the absorption of atmospheric molecular oxygen and ozone only, we have

$$\tau_i(h,t) = \exp -\{[\sigma_i(O_2)\ N(O_2) + \sigma_i\ (O_3)\ N(O_3,t)]\} , \qquad (5)$$

where

$$N(O_2) = \int_S n_{O_2}(h)\ ds \ ; \quad \text{molecular oxygen column density,}$$

$$N(O_3,t) = \int_S n_{O_3}(h,t)\ ds \ ; \quad \text{ozone column density.}$$

It should be emphasized here that the dependence of photodissociation rates J_j on the time variations of ozone concentrations has been indicated explicitly in Eqs. (3), (4), and (5).

Photodissociation rates of the interested species in the mesosphere have been discussed in detail by Turco (Ref. 98). We have adopted his results with some modification. Table 8.3 indicates the wavelength interval used for photodissociation rate calculations. Simon (Ref. 102) has reviewed and discussed the current knowledge of solar irradiation between 1200 A and 4000 A. The sources of the solar irradiance in this study are given in Table 8.4. As regards the important atmospheric absorption of Schumann-Runge bands of molecular oxygen, we have used Blake's (Ref. 97) model for the photodissociation rate calculations. The description of the ozone column density $N(O_3)$ by using Eq. (5) will be discussed in detail in the next section.

TABLE 8.3 Wavelength Intervals Used for Calculation

Wavelength Range (nm)	Wavelength Interval (nm)
121.6	0.1
125.0 - 175.0	5.0
275.0 - 205.0	1.0
205.0 - 400.0	5.0
400.0 - 740.0	20.0

TABLE 8.4 Source of Solar Irradiance

Wavelength Intervals (nm)	
121.6 (Lyman - α)	Ref. 100
125.0 - 175.0	Ref. 104
175.0 - 205.0	Ref. 105
	Ref. 103
205.0 - 230.0	Ref. 106
230.0 - 320.0	Ref. 96
320.0 - 740.0	

8.3. DIURNAL INTEGRATION

A. Numerical Scheme

As implied in Section 8.1, we have to solve a set of time dependent simultaneous equations for non-equilibrium species and a set of quasi-steady state equations for the equilibrium species. To solve the system of time dependent equations, it was assumed that the densities of equilibrium species were known and an implicitly numerical scheme was used, i.e.,

$$\frac{dn_j}{dt} = \frac{\Delta n_j}{t} = \frac{n_j^f - n_j^i}{\Delta t} \quad , \text{ and } \quad n_j = \frac{n_j^f + n_j^i}{2} \quad . \tag{6}$$

Furthermore, the system was linearized by introducing the following approximations:

$$n_j n_k = 1/4 \ (1.5 \ n_j^f \ n_k^i + 1.5 \ n_j^i \ n_k^f + n_j^i \ n_k^i \ ) \tag{7}$$

where j/k = 1,2, . . . , N, and f and i indicate the final and the initial values of gas j/k, respectively. Using the approach just described, the system of time dependent equations (1) can be transferred to a set of non-homogeneous simultaneous algebraic equations for solution. In order to avoid any human error, an automated system was developed to carry out the transformation according to the above description. To obtain the solution for species under equilibrium, it was assumed that the densities of all other were known and the equations were linearized.

B. Grid and Time Stop

In order to take the change of solar local time along the ray path into account in the determination of the photodissociation rates, a special grid is designed and is presented schematically in Figure 8.1. It corresponds to

equinox condition at the equator. In the region from 50 to 80 km, the atmosphere is divided into 30 layers with 1 km of thickness. This also determines the path of solar radiation in the atmosphere along which the computation will be made (Fig. 8.1. Above 80 km, a model atmosphere is introduced in which a steady distribution of ozone as function of altitude only is assumed. Thus, ozone diurnal variation is not considered in the region above 80 km and only the variation of the local zenith angle in a spherical atmosphere is included. This additional layer of atmosphere provides us with the O_2 and O_3 column number densities which are required for the calculation of the photodissociation rates at 80 km. This may not be a good assumption. However, the error introduced as a result of the assumption will decrease as the altitude decreases and will exist only in the uppermost part of the region of interest. Note that the local time of sunrise (sunset) is allowed to begin (end) earlier (later) than 6:00 (18:00). The exact time of sunrise and sunset depends on the altitude of the air mass. In this study, solar radiation with a path tangent height above 25 km is included (Fig.8.1). The exact distance at the tangent points of two closest ray paths is set to be 1 km (Fig.8.1) in the region from 25 to 50 km. In the rest of sunlit region, the positions of ray path are determined according to the expression

$$S_i = (R + 25) \cos(\theta_i),$$

where $\theta_i = I$, and $I = 1^o, 2^o, \ldots, 180^o$, and $R = 6372$ km. A similar approach is applied to the night-time region. It is obvious that the time step associated with the grid just described is not constant. In general, small steps appear in the sunrise and sunset from about 20 seconds

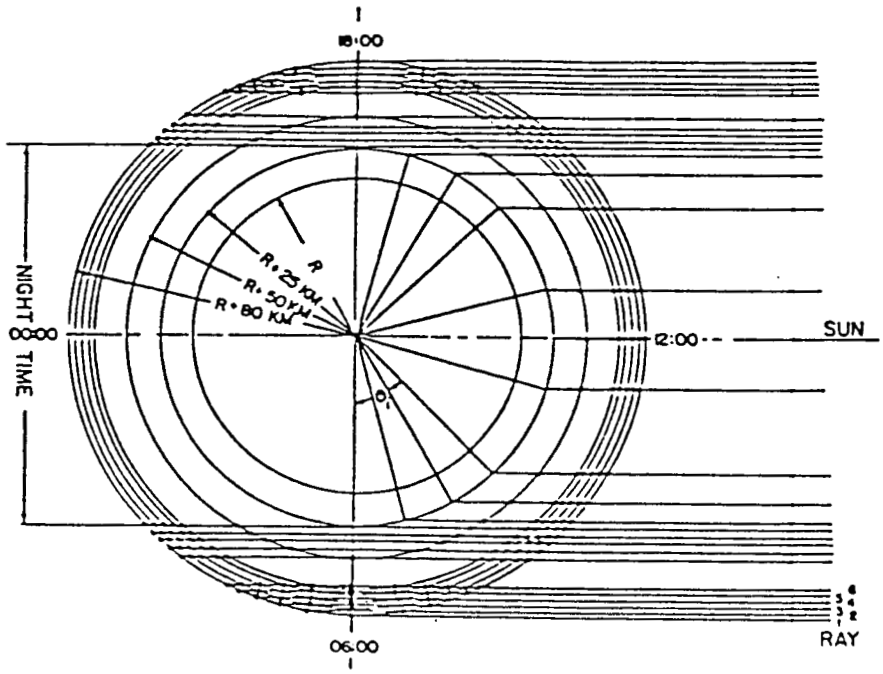

Figure 8.1. A schematic diagram shows the grid used in the model study.

to 1 minute. The longest step, which occurs at noon, is about 4 minutes.

It should be emphasized here that the method of computation used in this study enables us to carry out the time integration and to update the ozone concentration for the calculation of the local photodissociation rates at each time step.

8.4 RESULTS

The diurnal variations of ozone and atomic oxygen in the oxygen-only atmosphere are shown in Figs. 8.2 and 8.3, respectively. The solid lines denote results obtained with the consideration of the change in local solar time along the ray path and the dashed lines, without their inclusion. Both figures indicate rapid changes of ozone and atomic oxygen densities above 55 km during sunrise and sunset. The changes are more rapid when the change in local solar time along the ray path is considered in the calculation than when it is not. The results also indicate greater ozone concentrations and lower atomic oxygen concentrations in the latter case. In general, this difference in the concentration of atomic oxygen and ozone appears to be the maximum during sunrise and sunset.

The calculated diurnal variations of ozone for the O-H-N-C atmosphere are presented in Fig. 8.4. Again, the solid lines are the results with the consideration of the change of local solar time along the ray path and the dashed lines are those without. In general, it indicates the same characteristics as in Fig. 8.2. Again, differences are found in the ozone concentration between the two cases, especially during sunrise and sunset. In these cases, the neglect of temporal variation in the overhead column

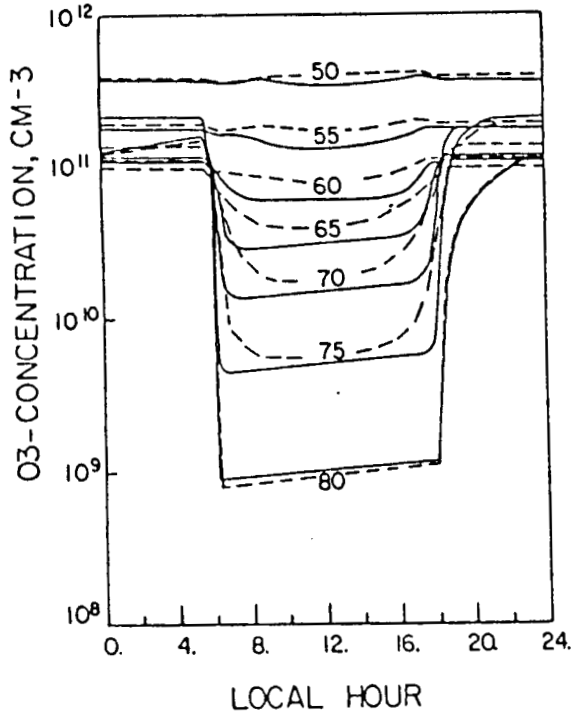

Figure 8.2. The diurnal variations of ozone in the oxygen-only atmosphere between 50 and 80 km. The solid lines denote the case with the feedback mechanism and the dashed lines are for the case without it.

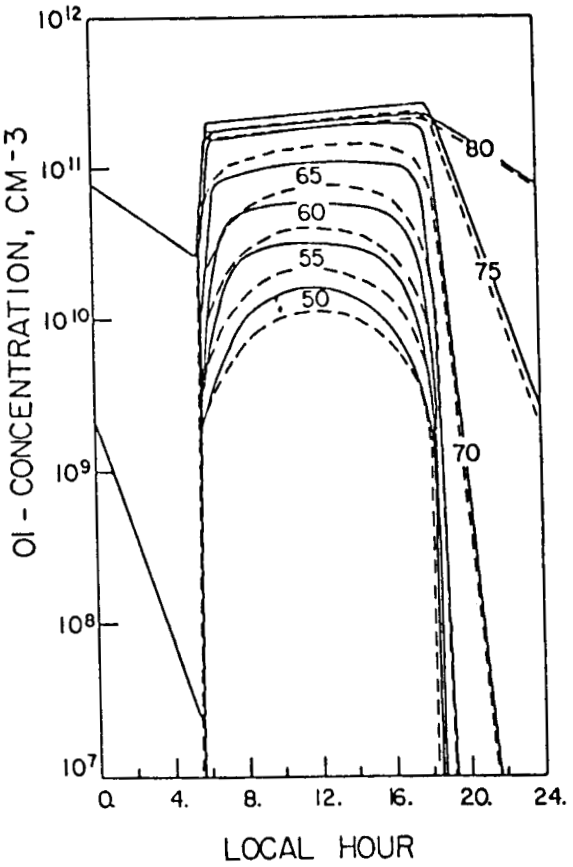

Figure 8.3. As in Fig. 8.2 but for atomic oxygen.

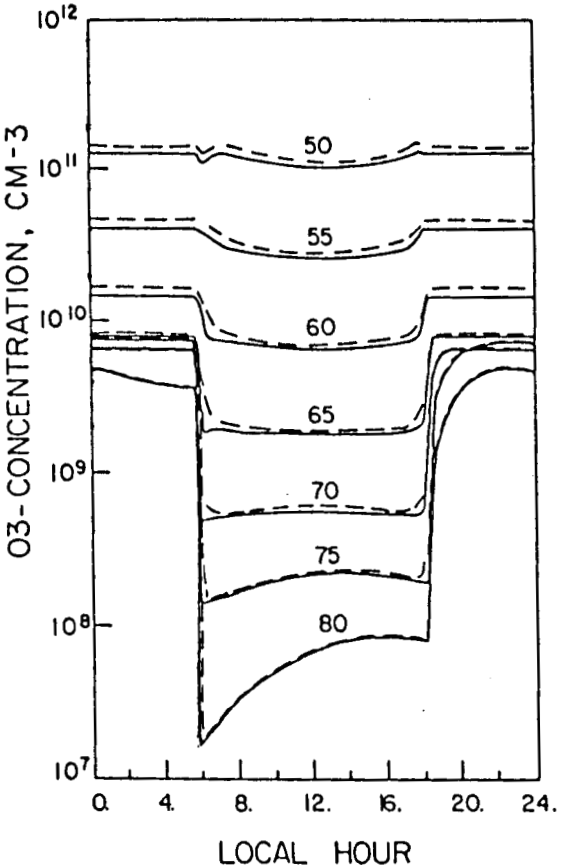

Figure 8.4. As in Fig. 8.2 but for O-H-N-C atmosphere.

amount of ozone leads to ozone concentrations which are too large. This error can be as large as a factor of 3 at 70 km. The difference in the diurnally averaged ozone concentration is found to be 15 percent at 50 km.

A comparison of the ozone distribution at noon of this model study with results of other theoretical calculations as well as the distribution of U.S. Standard Atmosphere (1976) (Ref. 107) are given in Fig. 7.5. The results of this agree very well with U.S. Standard Atmosphere (1976) and also with Logan, et al. (Ref. 92) and Prather (Ref. 94) except between 50 and 55 km, where the present re are 35-50 percent larger. Fig. 7.5 also indicates significant differences in the ozone profile between this model and earlier studies of Hesstvedt (Ref. 88), Shimazaki and Laird (Ref. 89), and Park and London (Ref. 91). These differences could be due to the fact that their studies were conducted at different latitudes, different seasons, and with different reaction rates.

Since the information of ozone nature diurnal behavior is very useful for interpretation of ozone solar occultation measurements and for testing the current knowledge of atmospheric photochemistry, effort has been increasingly toward the direct determination on the diurnal variation of mesospheric ozone (Refs. 108-112). The ozone IR satellite data also have been used to deduce the ozone diurnal variation (Anderson et al., Ref. 113). Although the difference in the detailed ozone diurnal behavior observed from different methods still exists, the measured results tend to agree generally with the nighttime enhancement of the ozone concentration in the mesosphere (Ref. 112). A comparison of the change in the daytime ozone concentration with respect to the nighttime concentration predicted by the present model and that from variou

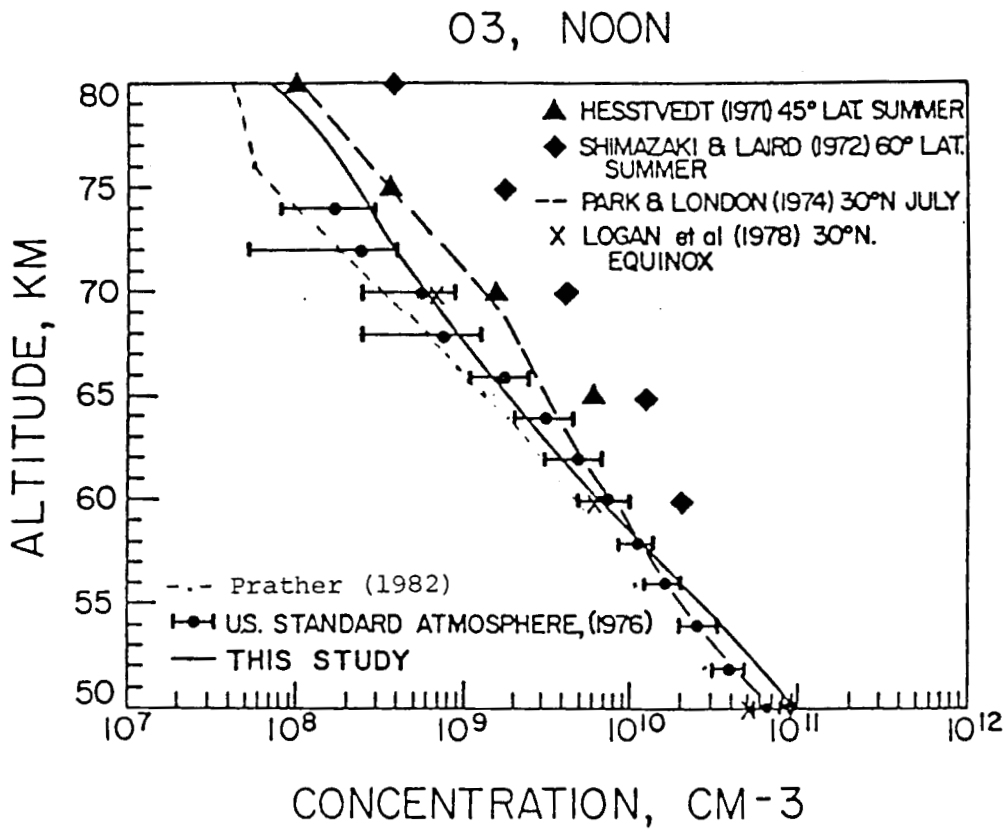

Figure 8.5. The comparison of ozone distribution at noon of this study with the U.S. Standard Atmosphere (1976), and also with earlier theoretical calculations.

measurements is given in Table 8.5 . This table provides the general trends of the diurnal changes in the mesospheric ozone rather than a detailed comparison of the measured results from different sources.

In conclusion, this section has shown that the effect of change in the local solar time along the ray path is to increase the local photodissociation rates. As a result of this effect, there is an enhancement of ozone diurnal variation, particularly during sunrise and sunset. Since the solar occultation technique measures the ozone at the local time 6:00/18:00, the results given in Fig. 8.4 suggest that, in most altitude ranges in the mesosphere, the ozone solar occultation measurements can provide good representation of day-time ozone concentration profile.

TABLE 8.5 A Comparison of the Percentage Change in Day-Time Ozone Concentration with the Night-Time Concentration of This Model Predication with That of Direct Measurements

Altitude, km	This Model predication	DIRECT MEASUREMENTS				
		Hilsenrath* (1971) (Ref. 113)	Penfield* (1976) (Ref. 108)	Wilson (1981) (Ref. 110)	Vaughan (1982) (Ref. 111)	Lean* (1982) (Ref. 112)
50	-21%	-19%			-8%	-12%
55	-33%	-22%				-15%
60	-50%	-23%	-38%			-45%
65	-71%	-51%	-40%	∿ -90%	-55%	-56%
70	-90%		-53%			-84%

SECTION 9

ACKNOWLEDGMENTS

This work was supported by NASA Contract NAS1-15198. It is a pleasure to acknowledge the valuable cooperation of and fruitful discussions with M. P. McCormick, K. Crumbly, R. R. Adams, W. P. Chu, L. R. McMaster, T. Owens, and H. Edwards of NASA-Langley Research Center (LaRC) during the course of this work. Special assistance of R. R. Adams and B. Poole, NASA-LaRC, in the photographic aspects of solar aureole technique is gratefully acknowledged. Special thanks are due the following IFAORS staff scientists, who diligently worked on and assisted in the successful completion of various portions of the work reported here: Dr. Michael A. Box for Sections 2, 3, and 4 and Dr. Gail P. Box, Sections 2, 3, and 5. The assistance of V. Bloxom, D. McQuestion, M. Phillips, M. Goodwin, M. Crotts, and C. A. Keen in the typing, copy editing, and preparation of this manuscript is gratefully acknowledged.

In addition, thanks are due to Dr. J. A. Reagan, University of Arizona, and T. Pepin, University of Wyoming, for their assistance in the fulfillment of this work.

SECTION 10

REFERENCES

1. A. E. S. Green, A. Deepak, and B. J. Lipofsky, Appl. Opt., 10, 1263 (1971).

2. A.E.S. Green, A. Deepak, T. Sawada and R.S. Sholtes, Remote Sensing of Atmospheric Aerosols, Proc. of the VIIth International Symposium on Remote Sensing of Environment, Ann Arbor, MI, Vol.III, p.1749 (1971).

3. A.E.S. Green, et al., J. Colloid Interface Sci., 39, 520 (1972).

4. R. D. McPeters and A. E. S. Green, Appl. Opt., 15, 2457 (1976).

5. A. Deepak and R. R. Adams, Equidensity and Isophote Contour Mapping of Solar Aureole for Determining Physical and Spatial Characteristics of Atmospheric Aerosols, Technical Digest, Remote Sensing of the Atmosphere, Optical Society of America Spring Meeting, Anaheim, March 17-20, 1975. (Paper No. WC-2.)

6. A. Deepak, A Photographic Solar Aureole Isophote Technique for Measurement of Atmospheric Aerosol Properties, Proc. of the International Radiation Conference, Garmisch-Partenkirchen, West Germany, (Ed.) H-J Bolle, August 18-28, 1976, Science Press, Princeton, NJ, 1977, p. 160.

7. A. Deepak, Inversion of Solar Aureole Measurements for Determining Aerosol Characteristics, in Inversion Methods in Atmospheric Remote Sounding, (Ed.) A. Deepak, Academic Press, New York (1977), pp 297-323.

8. F. E. Volz, J. of Atmos. Sci., 27, 1041 (1970).

9. G. Newkirk, J. Opt. Soc. Amer., 46, 1028 (1956).

10. K. Murai, Meteor. and Geophys., 19, 447 (1968).

11. R. Eiden, Tellus, 20, 380 (1968).

12. B. Rydgren, Tellus, 20, 55 (1968).

13. G. E. Shaw, Radiative and Physical Properties of Atmosphere Aerosols at the South Pole, Abstracts of papers presented at the Interdisciplinary Symposia, International Union of Geodesy and Geophysics, XVI General Assembly (Grenoble, France), August 25 - September 6, 1975, p. 194.

14. J. T. Twitty, J. J. Parent, J. A. Weinman, and E. L. Eloranta, Appl. Opt., 15, 980 (1976).

15. F. E. Volz, Observations and Measurements of the Solar Aureole, pp 238-240, Preprints 3rd Conference on Atmospheric Radiation, Davis, CA, June 28-30, 1978. [Available from AMS, 45 Beacon St., Boston, MA 02108]

16. A. Deepak, M. A. Box, J. T. Twitty and R. R. Adams, Appl. Opt., 17, 1977 (1978).

17. R. R. Austin, Electro-Optical Systems Design, p. 32, June 1973.

18. Eastman Kodak Publication AA-26, "Optical Formulas and Their Application," (1979), (Available from Eastman Kodak Co., Rochester, NY).

19. T. H. James, (Ed.), The Theory of Photographic Process, MacMillan Press, New York, 3d ed. (1966).

20. W. J. Smith, Modern Optical Engineering, McGraw-Hill Book Co., New York (1966).

21. H. N. Todd, Photographic Sensitometry, Wiley and Sons, New York (1976).

22. A. Deepak, Appl. Opt. 17, 1120-1124 (1978).

23. A. Deepak and R. R. Adams, Determination of the Off-Axis Illumination Distribution for a Lens-Spectral Filter Combination, Appl. Opt., 18, 131 (1979).

24. T. H. James and G. C. Higgins, Fundamentals of Photographic Theory, Morgan and Morgan, New York (1964).

25. A. Deepak, G. P. Box, M. A. Box and R. R. Adams, Determination of Aerosol Characteristics by Photographic Solar Aureole Measurement, Extended Summary, 3rd Conference on Atmospheric Radiation, Jun 28-30, 1978, Davis, CA, p 138-139.

26. M. A. Box and A. Deepak, Retrieval of Aerosol Size Distributions by Inversion of Simulated Solar Aureole Data in the Presence of Multiple Scattering, Appl. Opt., 18, 9, p. 1376, (1979).

27. M. A. Box and A. Deepak, An Approximation to Multiple Scattering in the Earth's Atmosphere: Almucantar Radiance Formulation, Complete.

28. M. A. Box and A. Deepak, Single and Multiple Scattering Contributions to Circumsolar Radiation, Appl. Opt., 17, 3794 (1978).

29. Michael A. Box and Adarsh Deepak, Multiple Scattering Corrections to the Solar Aureole, 3rd Conference on Atmospheric Radiation, June 28-30, 1978, Davis, CA, p 12-13.

30. A. Deepak, Double Scattering Corrections to the Theory of the Sun's Aureole, NASA TMX-64842 (1973).

31. A. E. S. Green and J. D. Martin, in The Middle Ultraviolet: Its Science and Technology (A. E. S. Green, Ed.), p. 140. John Wiley & Sons, Inc., New York, (1966).

32. H. C. van de Hulst, Light Scattering by Small Particles, Wiley, New York (1957).

33. J. V. Dave, Development of Programs for Computing Characteristics of U.V. Radiation, NASA Contract 5-21680 (1972).

34. J. V. Dave and P. H. Furukawa, Scattered Radiation in the Ozone Absorption Bands at Selected Levels of a Terrestrial Rayleigh Atmosphere, Meteorological Monographs, 7, no. 29, American Meteorological Society, Boston (1966).

35. K. L. Coulson, J. V. Dave and Z. Sekera, Tables Related to Radiation Emerging from a Planetary Atmosphere, University of California, Berkeley (1960).

36. B. H. Herman and S. R. Browning, A Numerican Solution to the Equation of Radiative Transfer, J. Atmos. Sci., 22, 559-566 (1965).

37. A. Deepak and G. P. Box, Analytic Modeling of Aerosol Size Distributions, NASA CR 159170 (1979).

38. D. Deirmendjian, Theory of the Solar Aureole, Part I: Scattering and Radiative Transfer, Ann de Geophys., 13, 286-306 (1957).

39. D. Deirmendjian, Theory of the Solar Aureole, Part II: Applications to Atmospheric Models, Ann de Geophys., 15, 218-249 (1959).

40. D. Deirmendjian, Electromagnetic Scattering on Spherical Polydispersions, American Elsevier, New York (1969).

41. D. Deirmendjian, Use of Scattering Techniques in Cloud Microphysics Research 1. The Aureole Method, Rand Report No. R-590-PR, Defense Document #AD-714582 (1970). (Available from Rand Corp., 1700 Main Street, Santa Monica, CA 90406.)

42. Z. Sekera, Recent Developments in the Study of the Polarization of Sky Light, Adv. in Geophys., 13, 43-104 (1956).

43. S. Chandrasekhar, Radiative Transfer, Dover, New York (1960).

44. V. V. Sobolev, Light Scattering in Planetary Atmospheres, Pergamon Press, Oxford, U.K. (1975).

45. M. A. Box and A. Deepak, The Finite Sun Effect on the Interpretation of Solar Aureole, Appl. Opt., 20, 16, 2806-2810 (1981).

46. M. D. King and D. M. Byrne, J. Atmos. Sci., 33, 2242 (1976).

47. E. Raschke (ed.), Terminology and Units of Radiation Quantities and Measurements, IAMAP Radiation Commission Report, April 1978. (Available from IAMAP, P.O. Box 3000, Boulder, CO 80307.)

48. J. T. Twitty, The Inversion of Aureole Measurements to Derive Aerosol Size Distributionsm J. Atmos. Sci., 32, 584-591 (1975).

49. H. L. Malchow and C. K. Whitney. "Inversion of Scattered Radiance Horizon Profiles for Gaseous Concentrations and Aerosol Parameters," in Inversion Methods in Atmospheric Remote Sounding, A. Deepak (ed.) Academic Press, New York, pp. 217-264 (1977).

50. A. Deepak, G. P. Box, and M. A. Box, Experimental Validation of the Solar Aureole Technique for Determining Aerosol Size Distributions, Appl. Opt., 21, 12, 2236 (1982).

51. J. A. Reagan, B. M. Herman, D. M. Byrne, and M. D. King, Third Conference on Atmospheric Radiation, June 28-30, 1978, Davis, CA, p. 241. American Meteorological Society, Boston, MA (1979).

52. J. V. Dave, Subroutines for Computing the Parameters of the Electromagnetic Radiation Scattered by a Sphere, Rep. No. 320-3237, IBM Scientific Center, Palo Alto, CA (1968).

53. A. Deepak, "Aerosol Remote Sensing," Processes in Marine Remote Sensing, Primars I, University of South Carolina Press, SC (1981).

54. G. P. Box, M. A. Box, and A. Deepak, On the Spectral Sensitivity of the Approximate Method for Retrieving Aerosol Size Distributions from Multispectral Solar Extinction Measurements, Appl. Met., 20, 8, 944-948 (1981).

55. A. Deepak, P. Wang, H. L. Malchow and C. K. Whitney, Satellite Determination of Atmospheric Aerosols and Ozone from Limb and Down Viewing Measurements, Proceedings of 1980 International Radiation Symposium, August 11-16, Fort Collins, CO.

56. M. P. McCormick, P. Hamill, T. J. Pepin, W. P. Chu, T. J. Swissler and L. R. McMaster, Satellite Studies of the Stratospheric Aerosol, Bull. Am. Meteor. Soc. 60, 9, 1038-1046 (1979).

57. M. A. Box and S. Y. Lo, Approximate Determination of Aerosol Size Distributions, J. Appl. Meteorol., 15, 1068-1076 (1976).

58. P. B. Russell, J. M. Livingston, and E. E. Uthe, Aerosol-Induced Albedo Change: Measurement and Modeling of an Incident, J. Atmos. Sci., 36, 1587-1608 (1979).

59. M. D. King, B. M. Herman and J. A. Reagan, Aerosol Size Distribution Obtained by Inversion of Spectral Optical Depth Measurements, J. Atmos. Sci., 35, 2153-2167 (1978).

60. D. L. Phillips, A Technique for the Numerical Solution of Certain Integral Equations of the First Kind, J. Assoc. Comput. Mach., 9, 84-97 (1962).

61. S. Twomey, On the Numerical Solution of Fredholm Integral Equations of the First Kind by the Inversion of the Linear System Produced by Quadrature, J. Assoc. Comput. Mach., 10, 97-101 (1963).

62. A. Deepak and M. A. Box, Forward Scattering Corrections for Optical Extinction Measurements in Aerosol Media. Part I: Monodispersions, Appl. Opt., 17, 2900-2908 (1978).

63. A. Deepak and O. H. Vaughan, Sedimentation-Extinction Inversion Technique for Measuring Size Distribution of Artificial Fogs, Appl. Opt., 17, 374-379 (1977).

64. A. Angstrom and B. Rodhe, Pyrheliometric Measurements with Special Regard to the Circumsolar Sky Radiation, Tellus, 18, 25 (1966).

65. A. K. Angstrom, On Determinations of the Atmospheric Turbidity and Their Relation to Pyrheliometric Measurements, Adv. in Geophys., 14, 269 (1970).

66. G. E. Shaw, Error Analysis of Multi-Wavelength Sun Photometry, Pageoph., 114, 1 (1976).

67. A. Deepak and M. A. Box, Forward Scattering Corrections for Optical Extinction Measurements in Aerosol Media. Part II: Polydispersions, Appl. Opt., 17, 3169 (1978).

68. L. Elterman, UV, Visible and IR Attenuation for Altitudes to 50 km, AFCRL-68-0153 (1968).

69. S. Twomey, Atmospheric Aerosols, Elsevier North-Holland, New York, NY (1977).

70. P. B. Russell, J. M. Livingston and E. E. Uthe, Aerosol-Induced Albedo Change: Measurement and Modeling of an Incident, submitted to J. Atmos. Sci.

71. C. E. Junge, Air Chemistry and Radioactivity, Academic Press, New York (1963).

72. E. J. McCartney, Optics of the Atmosphere, John Wiley and Sons, New York (1976).

73. A. Deepak (ed.), Inversion Methods in Atmospheric Remote Sounding, Academic Press, New York (1977).

74. S. Twomey, Introduction to the Mathematics of Inversion in Remote Sensing and Indirect Measurements, Elsevier, Amsterdam, The Netherlands (1977).

75. W. J. Wiscombe and P. Chylek, J. Opt. Soc. Am., 67, 572 (1977).

76. M. P. McCormick, H. B. Edwards, L. E. Mauldin III, and L. R. McMaster, Satellite Solar Occultation Measurements SAM II and SAGE, in Atmospheric Aerosols: Their Optical Properties and Effects (Paper TuB2), Williamsburg, Virginia, December 1976. (Available as NASA CP-2004.)

77. E. J. McGrath and D. C. Irving, Techniques for Efficient Monte Carlo Simulati Oak Ridge National Laboratory, ORNL-RSIC-38, Vol. I (1967). [Available from NTIS, Springfield, VA 22161.]

78. M. Kerker, The Scattering of Light and Other Electromagnetic Radiation, Academic Press, New York (1969).

79. O. M. Lidwell, A Particle-Size Distribution Function for Air-Borne Dusts, Nature, 158, 61 (1946).

80. A. E. S. Green and P. J. Wyatt, Atomic and Space Physics, Addison-Wesley, Reasing MA (1965).

81. A. E. S. Green (ed.), The Middle Ultraviolet: Its Science and Technology, pp. 118-129, Wiley, New York (1966).

82. I. S. Gradshteyn and I. W. Ryzhik, Table of Integrals, Series and Products, Academic Press, New York (1965).

83. M. R. Spiegel, Mathematical Handbook of Formulas and Tables, Schaum's Outline Series, McGraw-Hill, New York (1968).

84. M. Abramowitz and I. A. Stegun, Handbook of Mathematical Functions, Dover Publications, New York (1965).

85. S. Twomey, Atmospheric Aerosols, Elsevier, Amsterdam (1977).

86. Integraltafel (Bestimmte Integrale), Springer Verlag, New York (1966).

87. C. K. Whitney, in Standard Procedures to Compute Atmospheric Radiative Transfer in a Scattering Atmosphere (J. Lenoble, ed.), I.U.G.G., p. 80 (1975).

88. E. Hesstvedt, A Meridional Model of the Oxygen-Hydrogen Atmosphere, in Mesospheric Models and Related Experiments (G. Fiocco, ed.), pp. 52-64, Dord: Holland, Reidel (1971).

89. T. Shimazaki and A. R. Laird, Seasonal Effects on Distribution of Minor Neutral Constituents in the Mesosphere and Lower Thermosphere, Radio Science, 7, 23-43.

90. I. S. A. Isaksen, Diurnal Variations of Atmospheric Constituents in an Oxyge: Hydrogen-Carbon Atmospheric Model and the Role of Minor Neutral Constituents in the Chemistry of the Lower Ionosphere, Geofys. Publ., 30, 1-63.

91. J. H. Park and J. London, Ozone Photochemistry and Radiative Heating of the Middle Atmosphere, J. Atmos. Sci., 31, 1898-1916.

92. J. A. Logan, M. J. Prather, S. C. Wofsy, and M. B. McElroy, Atmospheric Chemistry: Response to Human Influence, Phil. Trans. Roy. Soc. London, Ser. A., 290, 1367, 187-234.

93. J. R. Herman, The Response of Stratospheric Constituents to a Solar Eclipse, Sunrise and Sunset, J. Geophys. Res., 84, 3701-3710 (1979).

94. M. J. Prather, Ozone in the Upper Stratosphere and Mesosphere, J. Geophys. Res., 86, 5325-5338 (1981).

95. P. H. Wang, G. K. Yue, A. Deepak and R. J. Kurzeja, A Model Study of the Diurnal Variation of Mesospheric O_3, in Proceedings of the Quadrennial International Ozone Symposium (J. London, ed.), pp. 876-883, IAMAP (1980).

96. M. Ackerman, Ultraviolet Solar Radiation Related to Mesospheric Processes, in Mesospheric Models and Related Experiments (G. Fiocco, ed.), pp. 149-159, Dordrecht, Reidel (1971).

97. A. J. Blake, An Atmospheric Absorption Model for the Schumann-Runge Bands of Oxygen, J. Geophys. Res., 84, 3272-3282 (1979).

98. R. P. Turco, Photodissociation Rates in the Atmosphere Below 100 km, Geophys, Surveys, 2, 153-192 (1975).

99. M. J. Molina and G. Arguello, Ultraviolet Absorption Spectrum of Methylhydroperoxide Vapor, Geophys. Res. Lett., 6, 953-955 (1979).

100. R. D. Hudson and I. Reed, The Stratosphere Present and Future, NASA Reference Publication 1049 (1979). [Available from NTIS, Springfield, Virginia 22161.]

101. R. F. Hampson and D. Garvin, Reaction Rate and Photochemical Data for Atmospheric Chemistry-1977, US Department of Commerce, NBS Special Publication 513 (1977).

102. P. C. Simon, Irradiation Solar Flux Measurements Between 120 and 400 nm: Current Position and Future Needs, Planet. Space Sci., 26, 355-365 (1978).

103. P. C. Simon, Balloon Measurements of Solar Fluxes Between 1960 and 2300 Å in Proceedings of the Third Conference on the Climatic Impact Assessment Program (Broderick and Hard, eds.), p. 137, DOT-TSC-OST-74-15 CN-140,104 (1974).

104. L. Heroux and R. A. Swirbalux, Full-Disk Solar Fluxes Between 1230 and 1940 Å, J. Geophys. Res., 81, 436-440 (1976).

105. G. E. Brueckner, J. D. F. Bartoe, O. Kjeldseth Moe, and M. E. Van Hoosier, Absolute Solar UV Intensities and Their Variation with Solar Activity Part I: The Wavelength Region 1750-2100 Å, Astrophys. J., 209, 935-944 (1976).

106. A. L. Broadfoot, The Solar Spectrum 2100-3200 Å, Astrophys. J., 173, 681-689 (1972).

107. U.S. Standard Atmosphere Supplement, U.S. Government Printing Office, Washington, DC (1966); U.S. Standard Atmosphere, U.S. Government Printing Office, Washington, DC (1976).

108. H. Penfield, M. M. Litvak, C. A. Gottlieb and A. E. Lilley, Mesospheric Ozone Measured from Ground-Based Millimeter Wave Observations, J. Geophys. Res., 81, 6115-6120 (1976).

109. F. I. Shimabukuro, P. L. Smith and W. J. Wilson, Estimation of the Daytime and Nighttime Distribution of Atmospheric Ozone from Ground-Based Millimeter Wavelength Measurements, J. Appl. Meteorol., 16, 929-934 (1977).

110. W. J. Wilson and P. R. Schwartz, Diurnal Variations of Mesospheric Ozone Using Millimeter Wave Measurements, J. Geophys. Res., 86, 7385-7388 (1981).

111. G. Vaughan, Diurnal Variation of Mesospheric Ozone, Nature, 296, 133-135 (1982).

112. J. L. Lean, Observation of the Diurnal Variation of Atmospheric Ozone, J. Geophys. Res., 87, 4973-4980 (1982).

113. G. P. Anderson, J. C. Gille, P. L. Bailey, and S. Solomon, LRIR Observations of Diurnal Ozone Variation in the Mesosphere, Paper presented at Quadrennial International Ozone Symposium, Int. Ozone Comm. and IAMAP, Boulder, CO August 1980.

114. E. Hilsenrath, Ozone Measurements in the Mesosphere and the Stratosphere During Two Significant Geophysical Events, J. Atmos. Sci., 28, 295-297 (1971).

APPENDIX 1

DENSITOMETRY OF SOLAR AUREOLE PHOTOGRAPHS BY SPOT AND SCANNING DENSITOMETERS: AN INTERCOMPARISON OF RESULTS

This paper describes methods of making optical density measurements along the film projection of the almucantar, which is a conic, by means of scanning and spot densitometers and intercompares their results.[1]

INTRODUCTION

The photographic measurements of the solar aureole almucantar radiance require that densitometry be performed on the photograph to determine the optical density along the film projection of the almucantar, which is a conic in the film plane (Ref. 1). The equations for the almucantar conic are given in Refs. 1 and 2, dealing with photogrammetry of the solar aureole. As explained in Refs. 3-6, these almucantar radiance measurements are used for the retrieval of aerosol size distribution. There are several types of densitometers in existence, and in order to explore ways in which the data reduction of aureole photographs could be reduced in the cost of the equipment, we decided to perform densitometry with a relatively inexpensive model of a typical transmissometer-type of spot densitometer (in which measurements along the conic must be performed by a manual positioning of the photograph--a task somewhat cumbersome and prone to error--and compare these results against those obtained

[1]*Assistance of R. R. Adams of NASA-Langley Research Center is gratefully acknowledged.*

for the same photograph by an automatic scanning microdensitometer (Joyce-Loebl). The latter can measure and digitize on an output tape the optical density of the photographic frame at a prescribed number of picture elements called pixels. In the latter case, one can simply read off the tape the densities for only those pixels whose x- and y-coordinates are prescribed by the conic equation, a procedure which seems less prone to error. This paper describes simple techniques for making accurate optical density measurements along such conics with the help of a spot densitometer.

Optical Density

In the field of photographic densitometry, the concept of optical density, as a measure of the attenuation of radiant flux, is of fundamental importance. When the attenuation relates to the flux transmitted (reflected) by the developed image, the term transmission (reflection) density is used. For an excellent discussion of what follows in this section, see Ref. 7. Only the transmission density will be dealt with in this paper.

The transmission density is defined, in general, as the logarithm of the opacity (Q) or reciprocal transmittance (T) of the developed image, which is just the ratio of the radiant flux P_o incident on the developed image to the radiant flux P_t transmitted by the image.

$$D = \log_{10}(Q) - \log_{10}\left(\frac{1}{T}\right) = \log \frac{P_o}{P_t} \qquad (1)$$

The design of the photometer used in the measurement of density strongly influences the values of density obtained. All attenuators

scatter some energy and thereby degrade the image quality. Whenever optical energy measurements relating to T are made by collecting light over a large solid angle (normally 180^{o}), the measurements are termed diffuse. Conversely, specular measurements are those taken on axis or over a small cone angle only. Values for diffuse measurements are normally the sum of the specular value plus the amount of scattered energy. The conditions of illumination and light collection used in measurement of specular and totally diffuse density are shown in Figs.1(a) and 1(b) which are adapted from Ref. 7. The ratio of specular to diffuse density, known as the Callier coefficient or Callier Q factor, increases with emulsion grain size. In both cases illumination angle α is small, but the view cone angle θ varies from 0^{o} to 90^{o}. The Q factor is not constant for all values of density but increases rapidly at the lower values of density, reaches a maximum and then gradually decreases. Also, the development of film to different values of gamma, the H-D coefficient, have profound effect on the Q factor, Q increases for higher γ. Photoelectric transmission densitometers are classified into two types: deflection and null densitometers. In the former type of densitometer, the sample is placed in the path of a narrow collimated beam traversing to the photoelectric cell, and density is read from the relative meter readings; in the latter type, the cell current produced by light from the test-sample beam is balanced by an equivalent current which may be derived from another cell and light beam through a controlled calibrated stepwedge. The Joyce-Loebl microdensitometer is a null-type of instrument which measures specular density.

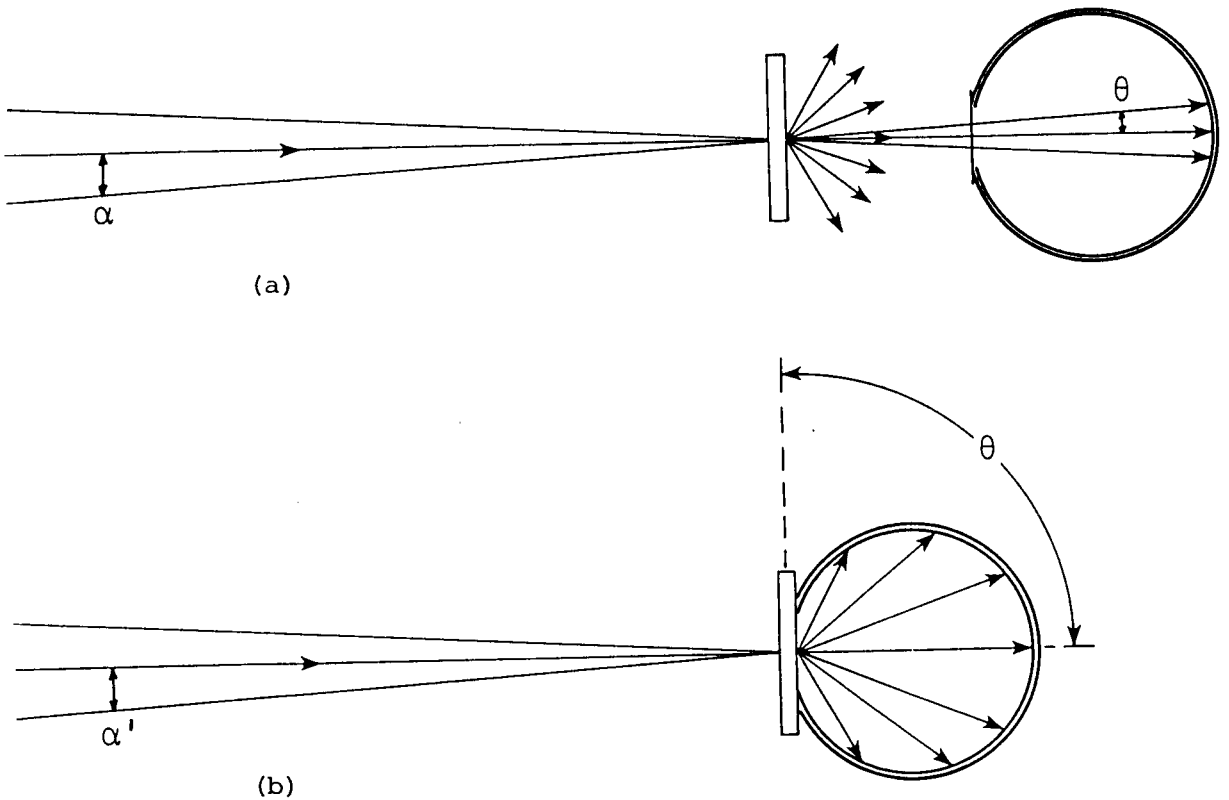

Figure 1(a). Geometrical conditions for measurement of specular density
1(b). Geometrical conditions for measurement of totally difuse density.

Measurement of Density with
a Spot Densitometer

An available transmission-type spot densitometer (McBeth TD-102) was used to make the density measurements along the conic projection of the almucantar. The coordinates (X_p, Y_p) of the points that lie on the conic can be obtained by either substitution in Eq. (10) Ref. 2, or by multiplying the x-y values from Table 1 in Ref. 2 for the approximate almucantar conic by the lens focal length f, namely, 55 mm. Another way of positioning the photograph to read the densities are at various x-y positions along the conic is by using the graphs of conics, such as shown in Fig. 2. in Ref. 2. (X_p, Y_p) values for f = 1 mm are given in Table 1, in Ref. 2, so that (X_p, Y_p) values for another lens focal length f can be obtained by multiplication by f.

Procedures for making the optical density measurements with the spot densitometer are described as follows.

The use of this method assumes that the aureole photograph was taken with the lens axis coincident with the sun line (sun centered in frame) with one edge of the frame horizontal and that the lens focal length (f) and the solar elevation angle (ϕ_s) at the time of photography are known.

The example presented in this paper serves to demonstrate the technique for the case of an 80 mm focal length lens on a 70 mm Hasselblad camera. An available McBeth TD-102 spot densitometer was used for density readings.

Figure 2 is a full-size reproduction of the spot densitometer alignment guide. The distance between circles marked (a) and (b) was chosen

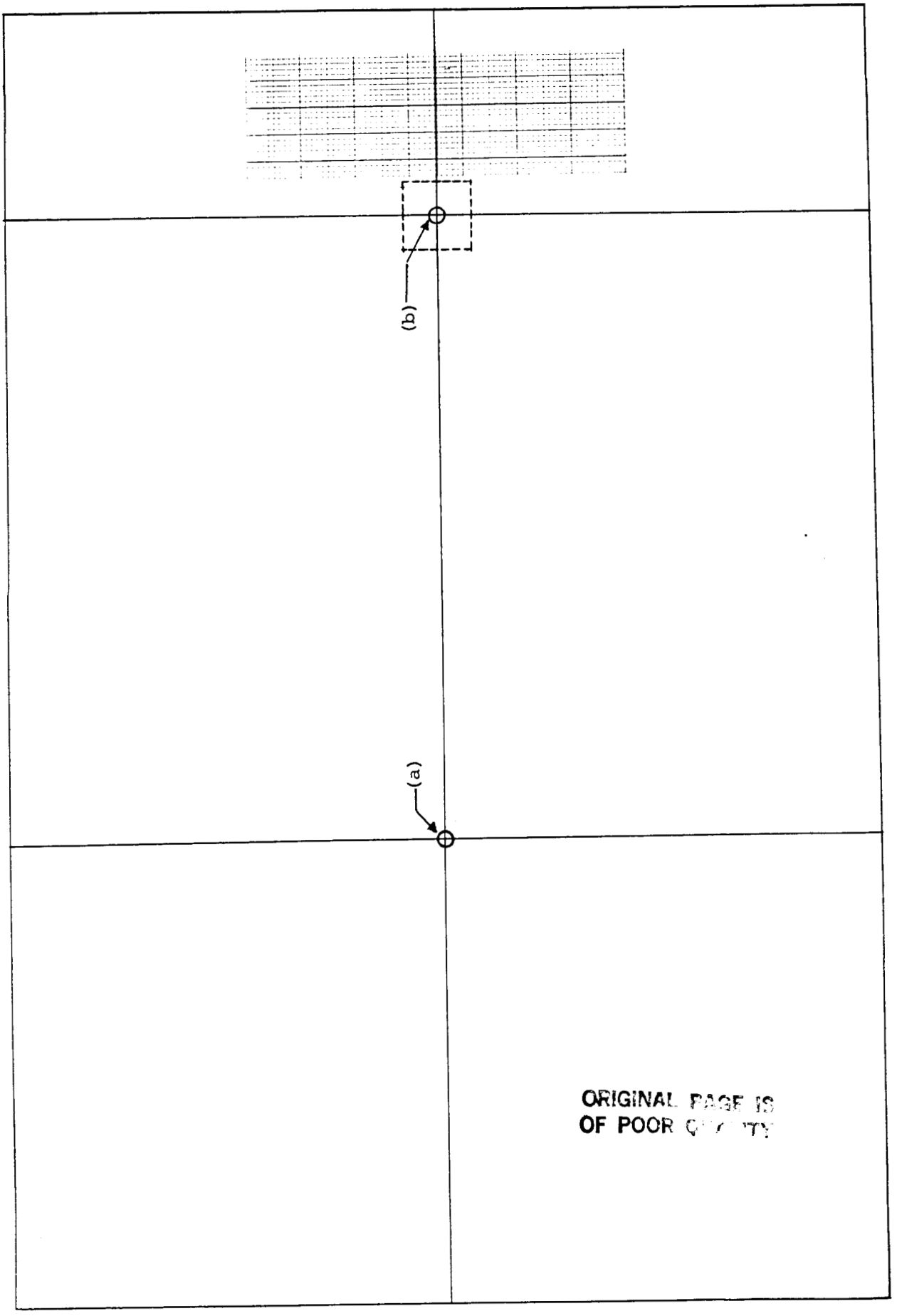

such that (a) was clearly visible and on the Densitometer table when (b) was centered in the light beam.

Figure 3 is a 1:1 reproduction of the transparency upon which the negative to be analyzed is precisely positioned and taped. The curves shown within the x-y mm grid were computed from Eq.(10) in Ref. 2 for an 80 mm focal length lens for values of ϕ_s from 10^o to 70^o. The sun line (x = 0 mm) is extended outside the grid area for proper negative alignment. The dotted or dashed rectangles are cut from the transparency for 35 mm or 70 mm negatives, respectively. The area outside the dot-dash line is removed from the transparency.

Following is a step-by-step procedure for taking density readings:

(1) Remove Figures 2 and 3 from body of paper.

(2) Make a 1:1 transparency of Figure 3. A contact-type viewgraph may be used.

(3) Remove the dashed rectangle from the transparency, using a straight edge and sharp blade. Cut also along dot-dash line.

(4) Place Figure 2 face up on a flat surface with circle (a) to the left.

(5) Align Figure 3 transparency over Figure 2 such that the x-y grid is to the left and the sun line (x = 0 mm) is coincident with the line connecting circles (a) and (b). Then, slide the sun line of Figure 3 along the line (a)(b) of Figure 2 until the proper ϕ_s curve of the negative to be read is exactly centered above circle (a) and temporarily tape Figure 3 to Figure 2.

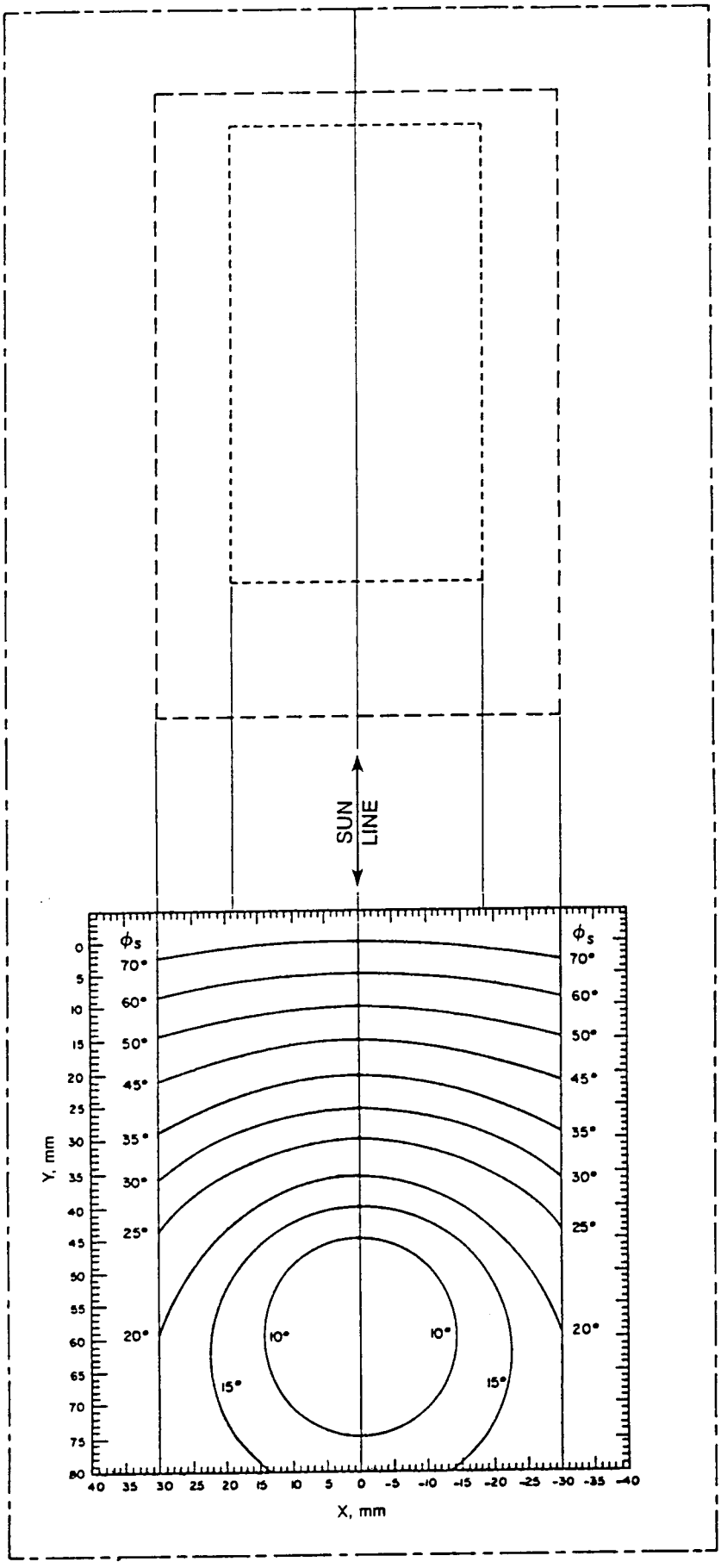

Figure 3. One-to-one ratio reproduction of transparency.

(6) Place the photograph negative, emulsion side down, within the cut portion of Figure 3 such that the central sun image is exactly centered above circle (b) and rotate it until the bottom exposed portion of the negative (nearest horizon in scene) is parallel to y, mm = 0, using the grid to the right of (b) as a guide. Carefully tape in place on Figure 3 outside of the exposure area.

(7) Remove Figure 3 from Figure 2 and place Figure 2 on Densitometer table such that circle (a) is clearly visible and on the table while circle (b) is directly centered in the measurement beam. Mark this location of Figure 2 on the table so that it can be replaced without reference to circle (b), remove Figure 3 and cut out dashed rectangle enclosing circle (b). Reposition on Densitometer table and fasten down securely with tape.

Readout technique. For periodic values of x, we proceed to carefully position Figure (and, thus, the negative) over the alignment guide in such a manner that the desired ϕ_s curve remains centered over circle (a) and that line (a)(b) and the sun-line always remain parallel as evidenced by equal values of x at both ends of the x-y grid located directly over line (a)(b). Note that as this happens, the line perpendicular to (a)(b) through circle (a) reads corresponding values of y, mm. Thus, tabular values of y, mm vs. x, mm as computed from Eq.(10), in Ref. 2, may be used to properly position the negative instead of the curve drawn for ϕ_s within the grid.

A density reading is recorded each time the negative is properly positioned within the measurement beam at the desired increments of x.

REFERENCES FOR APPENDIX 1

1. Deepak, A., Photogrammetry of the Solar Aureole, Appl. Opt., 17, 1120-1124 (1978).

2. Deepak, A. and P.-H. Wang, Photogrammetric Interpretation of Solar Almucantar Scan, Appendix 2 of this report (IFAORS TR 215).

3. Green, A. E. S., A. Deepak, and B. J. Lipofsky, Interpretation of the Sun's Aureole Based on Atmospheric Aerosol Models, Appl. Opt. 10, 1263-1279 (1971).

4. Green, S. E. S., et al., Light Scattering and the Size-Altitude Distribution of Atmospheric Aerosols, J. Colloid Interface Sci. 39, 520-535 (1972).

5. Green, A. E. S., A. Deepak, T. Sawanda, and R. S. Sholtes, Remote Sensing of Atmospheric Aerosols, Proc. of the VIIth International Symposium on Remote Sensing of Environment, Vol. III, 1749-1763 (1971).

6. Deepak, A., M. A. Box, and R. R. Adams, Measurement of Atmospheric Aerosol Characteristics by Photographic Solar Aureole Isophote (PSAI) Method, Ninth International Conference on Atmospheric Aerosols, Condensation and Ice Nuclei, September 21-27, 1977, Pergamon Press, N. Y. (1977).

7. James, T. H. (Ed.), The Theory of Photographic Process, MacMillan Press, New York, 3rd ed. (1966).

APPENDIX 2

PHOTOGRAMMETRIC INTERPRETATION OF SOLAR ALMUCANTAR SCAN

The almucantar, which is a conical scan of solar zenith angle with local zenith axis as the axis of rotation, projects on the film plane as a conic.

In order to photographically measure almucantar radiance, optical density measurements must be made along the conic. If a spot densitometer is used for this purpose, the problem of positioning the densitometer spot at any point along the almucantar conic requires the knowledge of its rectangular coordinates (x,y). A standard table for computing the x-y coordinates for almucantar conics corresponding to the solar zenith angles $10^{o}(2^{o})$ 44^{o}, 45^{o}, $46^{o}(2^{o})$ 70^{o} and for any lens focal length is given. The table is based on formulae for the almucantar conic which are derived in this section.[1]

INTRODUCTION

An earlier paper (Ref. 1) presented the photogrammetry of the solar aureole, giving derivation of the important relations involved. In order to photographically measure radiance along the almucantar, which projects on the film plane as a conic, for any solar zenith angle, the optical density at points along the conic needs to be measured. Almucantar is defined as the

[1] *Assistance of Dr. M. A. Box, Staff Scientist, IFAORS (1977-1979) and presently at the University of New South Wales, is gratefully acknowledged.*

conical scan of solar zenith angle, with the local zenith as the axis of rotation. If a scanning microdensitometer, with a digital tape output is used, the task of making the optical density measurements along the conic is simple, since one can select the data for the points falling along the conic by the use of the appropriate equations. However, in the case of a manual spot densitometer, the problem of positioning the spot at positions (x,y) along the conic is tedious; it requires a set of (x,y) values for the almucantar conic corresponding to the particular solar zenith angle. In order to simplify the task of computing the x-y values along the conic, we have constructed a standard table of (x,y) values for several solar zenith angles (namely, $10^{o}(2^{o})44^{o}$, 45^{o}, $46^{o}(2^{o})70^{o}$), and camera lens focal length f = 1 mm.

In order to obtain the (x_p, y_p) coordinates of image points defined by locii of various types of measurement scans made in the sky, a brief deviation of the equations which differs from that given in Ref. 1, is presented as follows.

PHOTOGRAMMETRIC RELATIONS FOR ALMUCANTAR SCAN

Let (X,Y,Z) and (x,y,z) be the coordinate systems with their respective origins at the optical center O of the camera lens and the center C of the film frame (Fig. 1). In addition, Z and z represent the local zenith and the optical axis, respectively. X is horizontal and perpendicular to the page; f is the lens focal length. These two coordinate systems are related by the equations,

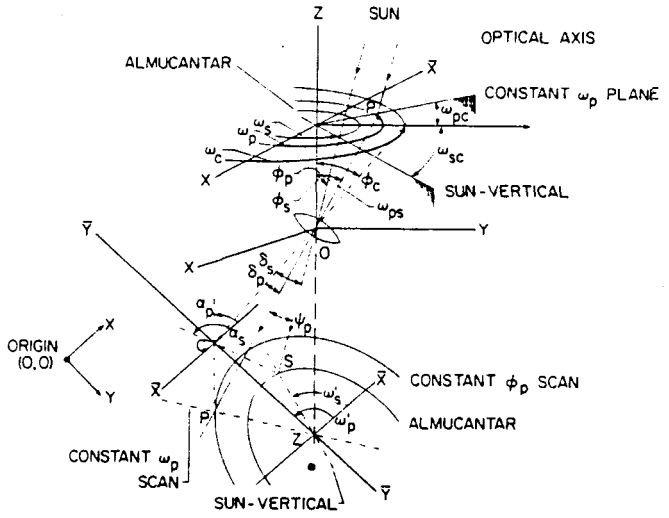

FIG. 1: Schematic illustrations of the film projection of the scans of constant zenith angle ϕ_p, the almucantar, constant azimuth angle ω_{ps}, and the sun-vertical.

$$\left.\begin{aligned} X &= x,\ Y = y\cos\phi_c - (z - f)\sin\phi_c, \\ Z &= y\sin\phi_c + (z - f)\cos\phi_c \end{aligned}\right\} \qquad (1)$$

The equation of the film plane is $z = 0$.

The purpose of photogrammetry is to reconstruct the positions in the object space corresponding to the points in the image space. Let (ϕ_p, ω_p) be the angular coordinates of a point P in the (X, Y, Z) system. The zero azimuth position is defined by setting ω_c, the optical axis azimuth, equal to zero. Then the equation of a ray of light having angular coordinates (ϕ_p, ω_p) and passing through the optical center O, is given in terms of (XY) coordinates by

$$\left.\begin{aligned} X_p &= Z\tan\phi_p\sin\omega_p \\ Y_p &= -Z\tan\phi_p\cos\omega_p \end{aligned}\right\} \qquad (2)$$

or, in terms of x,y coordinates by

$$\left.\begin{aligned} x_p &= \tan\phi_p \sin\omega_p (y_p \sin\phi_c - f\cos\phi_c) \\ y_p\cos\phi_c + f\sin\phi_c &= \tan\phi_p \cos\omega_p (f\cos\phi_c - y_p\sin\phi_c) \end{aligned}\right\} \quad (3)$$

i.e.,

$$y_p = f\,\frac{\tan\phi_p \cos\omega_p \cos\phi_c - \sin\phi_c}{\tan\phi_p \cos\omega_p \sin\phi_c + \cos\phi_c}$$

However, in photographic interpretation work, one usually needs to know the angular coordinates (ϕ_p, ω_p) of the line-of-sight in the object space corresponding to a given location (x_p, y_p) in the photographic frame. Then from Eq. (3), one obtains

$$\begin{aligned} \tan\phi_p \cos\omega_p (f\cos\phi_c - y_p\sin\phi_c) &= y_p\cos\phi_c + f\sin\phi_c \\ \tan\phi_p \sin\omega_p (f\cos\phi_c - y_p\sin\phi_c) &= -x_p \end{aligned} \quad (4)$$

so that,

$$\tan\omega_p = -x_p/(y_p\cos\phi_c + f\sin\phi_c) \quad (5)$$

Thus, using Eq. (3), one can determine ϕ_p from x_p and ω_p.

The projection of the constant zenith angle scan in (X,Y) and (x,y) planes is obtained by eliminating ω_p from Eqs. (2) and (3), which yields

$$x_p^2 + y_p^2 = Z^2 \tan^2\phi_p \quad (6)$$

or

$$\begin{aligned} x_p^2 + y_p^2(1 - \sin^2\phi_c \sec^2\phi_p) + y_p f \sin 2\phi_c \sec^2\phi_p \\ + f^2(1 - \cos^2\phi_c \sec^2\phi_p) = 0 \end{aligned} \quad (7)$$

Then the film projection of the almucantar scan is obtained from Eq. (7) by setting $\phi_p = \phi_c$, so that

$$x_p^2 + y_p^2 (1 - \tan^2\phi_c) + 2y_p \, f \tan \phi_c = 0 \qquad (8)$$

If $\phi_c = 45^\circ$, Eq. (8) reduces to the following relation

$$x_p^2 + 2 \, f \, y_p = 0 \qquad (9)$$

From Eq. (8), one obtains

$$\frac{y_p}{f} = \frac{-2 \tan \phi_c + \sqrt{2 \tan^2\phi_c - 4(x_p/f)^2(1 - \tan^2\phi_c)}}{2(1 - \tan^2\phi_c)} \qquad (10)$$

DESCRIPTION AND USE OF STANDARD TABLE

One can obtain a standard tabulation (Table 1) of (x_p, y_p) values of the almucantar projection for any solar zenith angle $\phi_s = 10^\circ(2^\circ)44^\circ, 45^\circ, 46^\circ(2^\circ)70^\circ$, and for f = 1 mm. It is assumed here that $\phi_c = \phi_s$. The (x_p, y_p) values of conic sections can be obtained for a lens of any other focal length f (mm) by multiplying the values of x_p, y_p in Table 1 by the factor f. Figure 2 illustrates the conic sections for four focal lengths, namely, 35, 50, 55, and 80 mm for almucantar corresponding to a few solar zenith angles in the range 10° - 70°.

In passing, it may be mentioned that in case the projection of the sun vertical scan ($\phi_p = 0$) is required, it can be obtained by eliminating ω_p from Eqs. (2) and (3). For further details, see Ref. 1.

TABLE 1: Tabulation† of Some x(mm) and y(mm) Values for Film Projections of Almucantar Scans for Various Solar Zenith Angles ϕ_s for a Lens of Focal Length 1 mm††

x (mm)	y, mm														
	$\phi_s = 10^\circ$	12°	14°	16°	18°	20°	22°	24°	26°	28°	30°	32°	34°	36°	38°	40°
.03	.0026	.0021	.0018	.0016	.0014	.0012	.0011	.0010	.0009	.0009	.0008	.0007	.0007	.0006	.0006	.0005
.06	.0105	.0086	.0073	.0063	.0056	.0050	.0045	.0041	.0037	.0034	.0031	.0029	.0027	.0025	.0023	.0022
.09	.0246	.0200	.0168	.0145	.0127	.0113	.0101	.0092	.0084	.0077	.0070	.0065	.0060	.0056	.0052	.0048
.12	.0469	.0369	.0306	.0262	.0229	.0203	.0182	.0164	.0149	.0137	.0126	.0116	.0107	.0099	.0092	.0086
.15	.0825	.0614	.0498	.0421	.0365	.0321	.0287	.0259	.0235	.0215	.0197	.0182	.0168	.0156	.0145	.0134
.18		.0976	.0758	.0628	.0539	.0472	.0419	.0377	.0341	.0311	.0285	.0263	.0243	.0225	.0208	.0194
.21		.1646	.1121	.0898	.0758	.0657	.0581	.0520	.0469	.0427	.0391	.0359	.0331	.0307	.0284	.0264
.24			.1696	.1257	.1033	.0885	.0775	.0690	.0621	.0563	.0514	.0472	.0435	.0402	.0372	.0345
.27				.1776	.1386	.1163	.1007	.0890	.0797	.0721	.0656	.0601	.0553	.0510	.0472	.0438
.30					.1862	.1507	.1285	.1125	.1001	.0901	.0818	.0747	.0686	.0632	.0585	.0542
.33					.2622	.1948	.1619	.1399	.1236	.1107	.1001	.0912	.0836	.0769	.0710	.0657
.36						.2564	.2031	.1723	.1506	.1340	.1206	.1096	.1001	.0919	.0847	.0783
.39						.3932	.2562	.2108	.1817	.1604	.1436	.1299	.1184	.1085	.0998	.0921
.42							.3334	.2581	.2180	.1903	.1693	.1525	.1385	.1266	.1163	.1071
.45								.3191	.2607	.2244	.1980	.1774	.1605	.1463	.1341	.1234
.48								.4104	.3125	.2635	.2301	.2048	.1846	.1677	.1533	.1408
.51									.3787	.3090	.2662	.2351	.2108	.1908	.1740	.1595
.54									.4758	.3632	.3069	.2685	.2393	.2158	.1962	.1794
.57										.4306	.3535	.3055	.2704	.2427	.2200	.2007
.60										.5231	.4078	.3467	.3043	.2717	.2454	.2233
.63											.4728	.3929	.3413	.3030	.2725	.2473
.66											.5552	.4452	.3818	.3366	.3014	.2727
.69											.6767	.5057	.4264	.3728	.3322	.2995
.72												.5774	.4757	.4119	.3650	.3279
.75												.6672	.5308	.4541	.3999	.3578
a =	.182	.223	.266	.312	.363	.420	.483	.555	.640	.741	.866	1.025	1.238	1.539	2.005	2.836
b =	.179	.218	.257	.299	.344	.391	.442	.497	.559	.628	.707	.800	.914	1.057	1.252	1.543
c =	.176	.213	.249	.287	.325	.364	.404	.445	.488	.532	.577	.625	.675	.727	.781	.839

TABLE 1: Continued

x (mm)	y, mm															
	$\phi_s = 42^\circ$	44°	45°	46°	48°	50°	52°	54°	56°	58°	60°	62°	64°	66°	68°	70°
.03	.0005	.0005	.0005	.0004	.0004	.0004	.0004	.0003	.0003	.0003	.0003	.0002	.0002	.0002	.0002	.0002
.06	.0020	.0019	.0018	.0017	.0016	.0015	.0014	.0013	.0012	.0011	.0010	.0010	.0009	.0008	.0007	.0007
.09	.0045	.0042	.0041	.0039	.0037	.0034	.0032	.0029	.0027	.0025	.0023	.0022	.0020	.0018	.0016	.0015
.12	.0080	.0075	.0072	.0070	.0065	.0060	.0056	.0052	.0049	.0045	.0042	.0038	.0035	.0032	.0029	.0026
.15	.0125	.0117	.0113	.0109	.0101	.0094	.0088	.0082	.0076	.0070	.0065	.0060	.0055	.0050	.0045	.0041
.18	.0180	.0168	.0162	.0156	.0146	.0136	.0126	.0117	.0109	.0101	.0093	.0086	.0079	.0072	.0065	.0059
.21	.0246	.0229	.0221	.0213	.0198	.0184	.0172	.0159	.0148	.0137	.0126	.0116	.0107	.0097	.0088	.0080
.24	.0321	.0299	.0288	.0278	.0259	.0241	.0224	.0208	.0193	.0178	.0165	.0152	.0139	.0127	.0115	.0104
.27	.0407	.0378	.0365	.0352	.0327	.0304	.0283	.0263	.0244	.0225	.0208	.0191	.0175	.0160	.0145	.0131
.30	.0502	.0467	.0450	.0434	.0404	.0375	.0349	.0324	.0300	.0277	.0256	.0236	.0216	.0197	.0179	.0161
.33	.0609	.0565	.0545	.0525	.0488	.0453	.0421	.0391	.0362	.0335	.0309	.0284	.0260	.0237	.0215	.0194
.36	.0725	.0673	.0648	.0624	.0580	.0539	.0500	.0464	.0430	.0397	.0366	.0337	.0309	.0281	.0255	.0230
.39	.0852	.0790	.0761	.0733	.0680	.0631	.0586	.0543	.0503	.0465	.0429	.0394	.0361	.0329	.0298	.0268
.42	.0990	.0916	.0882	.0849	.0788	.0731	.0678	.0628	.0581	.0537	.0495	.0455	.0417	.0380	.0344	.0310
.45	.1138	.1052	.1013	.0974	.0903	.0837	.0776	.0719	.0665	.0614	.0566	.0520	.0476	.0434	.0393	.0354
.48	.1297	.1198	.1152	.1108	.1026	.0951	.0881	.0815	.0754	.0696	.0641	.0589	.0539	.0491	.0445	.0400
.51	.1467	.1353	.1301	.1250	.1157	.1071	.0992	.0918	.0848	.0783	.0721	.0662	.0606	.0552	.0500	.0449
.54	.1648	.1518	.1458	.1401	.1295	.1198	.1109	.1025	.0947	.0874	.0804	.0739	.0676	.0615	.0557	.0501
.57	.1840	.1692	.1625	.1560	.1441	.1332	.1231	.1138	.1051	.0969	.0892	.0819	.0749	.0682	.0617	.0555
.60	.2043	.1876	.1800	.1728	.1594	.1472	.1360	.1257	.1160	.1069	.0983	.0902	.0825	.0751	.0679	.0611
.63	.2258	.2070	.1985	.1904	.1755	.1619	.1495	.1380	.1273	.1173	.1079	.0989	.0904	.0823	.0744	.0669
.66	.2484	.2273	.2178	.2088	.1922	.1772	.1635	.1509	.1391	.1281	.1177	.1080	.0986	.0897	.0812	.0729
.69	.2722	.2487	.2381	.2281	.2097	.1932	.1781	.1642	.1513	.1393	.1280	.1173	.1071	.0974	.0881	.0792
.72	.2972	.2710	.2592	.2482	.2279	.2097	.1932	.1780	.1640	.1509	.1386	.1270	.1159	.1054	.0953	.0856
.75	.3234	.2943	.2813	.2691	.2468	.2269	.2089	.1923	.1770	.1628	.1495	.1369	.1250	.1136	.1027	.0922
a =	4.757	14.318		14.318	4.757	2.836	2.005	1.539	1.238	1.025	.866	.741	.640	.555	.483	.420
b =	2.070	3.718		3.851	2.299	1.838	1.602	1.455	1.355	1.281	1.225	1.181	1.145	1.117	1.093	1.074
e =	.900	.966	1.000	1.036	1.111	1.192	1.280	1.376	1.483	1.600	1.732	1.881	2.050	2.246	2.475	2.747

† Sun's image is at the geometrical center C of the frame, the origin being at C.

†† Similar tables for lenses of other focal lengths f mm, may be obtained by simply multiplying the x, y, a and b values by a factor f.

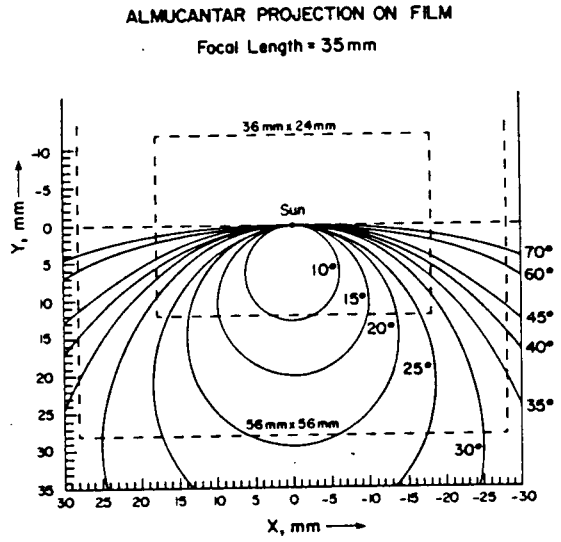

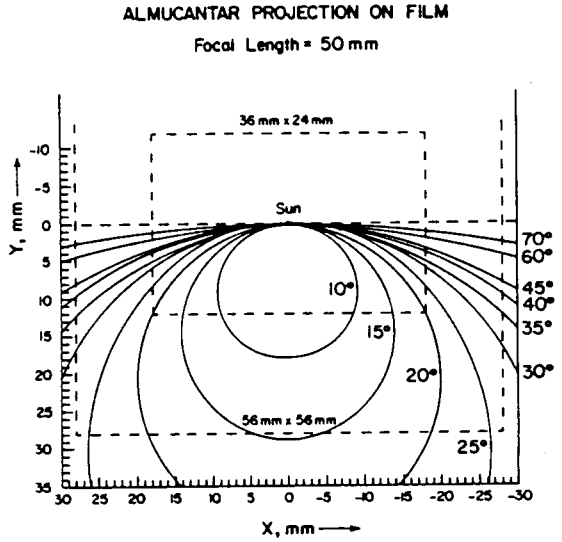

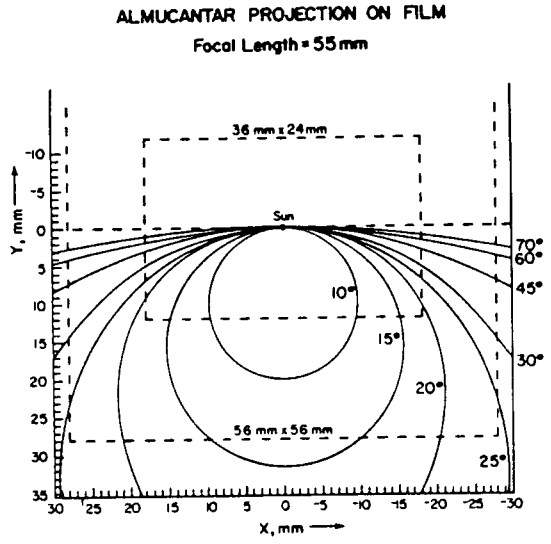

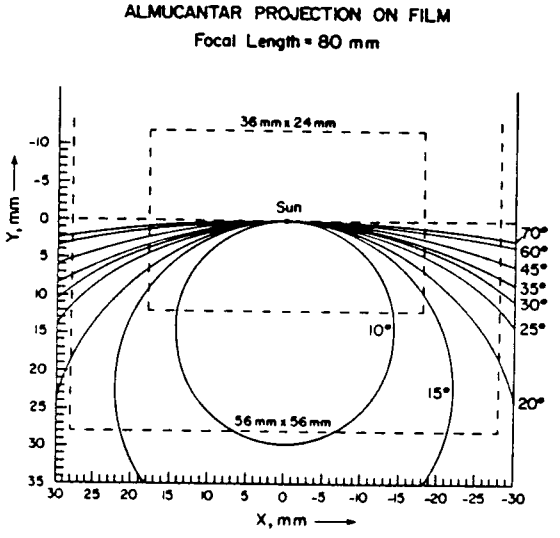

FIG. 2: Conic sections for four focal lengths, namely, 35, 50, 55, and 80 mm for almucantar corresponding to a few solar zenith angles in the range 10° to 70°.

REFERENCES FOR APPENDIX 2

1. Deepak, A., Photogrammetry of the Solar Aureole, Appl. Opt., 17, 1120-1124 (1978).

APPENDIX 3

LIST OF RESEARCH PUBLICATIONS PREPARED UNDER CONTRACT NAS1-15198

1. Deepak, A., M. A. Box, and R. R. Adams, Measurement of Atmospheric Aerosol Characteristics by Photographic Solar Aureole Isophote (PSAI) Method, *Ninth International Conference on Atmospheric Aerosols, Condensation and Ice Nuclei, September 21-27, 1977,* Pergamon Press, NY (1977).
2. Deepak, A., Photogrammetry of the Solar Aureole, *Appl. Opt., 17,* 1120-1124 (1978).
3. Deepak, A., and A. H. Fluellen, A Comparative Study of Conroy and Monte Carlo Methods Applied to Multiple Quadratures and Multiple Scattering, NASA CR-3059 (1978).
4. Deepak, A., and M. A. Box, Forward Scattering Corrections for Optical Extinction Measurements In Aerosol Media. Part 1. Monodispersions, *Appl. Opt., 17,* 2900-2908 (1978).
5. Deepak, A., and M. A. Box, Forward Scattering Corrections for Optical Extinction Measurements In Aerosol Media. Part 2. Polydispersions, *Appl. Opt., 17,* 3169-3176 (1978).
6. Deepak, A., M. A. Box, J. T. Twitty, and R. R. Adams, A Comparison Between Photographic and Photoelectric Measurements of the Solar Aureole Almucantar Radiance, *Appl. Opt., 17,* 1977-1978 (1978).
7. Deepak, A., and R. R. Adams, Determination of the Off-Axis Illumination Distribution for A Lens-Spectral Filter Combination, *Appl. Opt., 18,* 131 (1979).
8. Box, M. A., and A. Deepak, Single and Multiple Scattering Contributions to Circumsolar Radiation, *Appl. Opt., 17,* 3794 (1978).
9. Deepak, A., G. P. Box, M. A. Box, and R. R. Adams, Determination of Aerosol Characteristics by Photographic Solar Aureole Measurement, Preprint Volume: Third Conference on Atmospheric Radiation, June 28-30, 1978, Davis, CA, pp. 138 and 139.
10. Box, M. A., and A. Deepak, Multiple Scattering Corrections to the Solar Aureole, Preprint Volume: Third Conference on Atmospheric Radiation, June 28-30, 1978, Davis, CA, pp. 12-13.
11. Deepak, A., Solar Aureole as a Measure of Atmospheric Aerosol Properties, Technical Digest, OSA Topical Meeting on Meteorological Optics, August 28-29, 1978, Keystone, CO, p. MB4-1.
12. Box, M. A., and A. Deepak, Atmospheric Scattering Corrections to Solar Radiometry, *Appl. Opt., 18,* 1941 (1979).
13. Deepak, A., and R. R. Adams, Photographic Photometry of the Solar Aureole, *Appl. Opt.,* 1983 (in press).
14. Box, M. A., and A. Deepak, Retrieval of Aerosol Size Distributions by Inversion of Simulated Aureole Data in the Presence of Multiple Scattering, *Appl. Opt., 18,* 1376 (1979).
15. Box, M. A., G. P. Box, and A. Deepak, Special Techniques for Remote Sensing of Physical Characteristics of Submicron Atmospheric Aerosols, *J. Aerosol Science, 10,* 210-211 (1979).
16. Deepak, A., and G. P. Box, Analytic Modeling of Aerosol Size Distributions, NASA CR-159170 (1979).
17. Box, M. A., and A. Deepak, An Approximation to Multiple Scattering in the Earth's Atmosphere: Almucantar Radiance Formulation, *J. Atmos. Sci., 38,* 5, 1037-1048 (May 1981).
18. Deepak, A., M. A. Box, and G. P. Box, Determination of Tropospheric Aerosol Size Distribution from Multispectral Solar Aureole and Extinction Measurement Techniques, J. J. Singh and A. Deepak (eds.), *Environmental and Climatic Impact of Coal Utilization,* Academic Press, NY (1980), pp. 135-146.
19. Box, M. A., and A. Deepak, Scattering Effects of Aerosols on Optical Extinction and Visibility Measurements, J. J. Singh and A. Deepak (eds.), *Environmental and Climatic Impact of Coal Utilization,* Academic Press, NY (1980), pp. 237-245.
20. Box, M. A., and A. Deepak, Small Angle Approximation to the Transfer of Narrow Laser Beams in Anisotropic Scattering Media, NASA Contractor Report 3407 (1981).
21. Wang, P.-H., A. Deepak, and S. S. Hong, General Formulation of Optical Paths for Large Zenith Angles in the Earth's Curved Atmosphere, *J. Atmos. Sci., 38,* 3, 650-658 (March 1981).

22. Deepak, A., M. A. Box, and G. P. Box, Retrieval of Aerosol Size Distributions from Scattering and Extinction Measurements in the Presence of Multiple Scattering, A. Deepak (ed.) *Remote Sensing of Atmospheres and Oceans,* Academic Press, NY (1980), pp. 95-113.
23. Deepak, A., and G. P. Box, Representation of Aerosol Size Distribution Data by Analytic Models, A. Deepak (ed.), *Atmospheric Aerosols: Their Formation, Optical Properties, and Effects,* Spectrum Press, Hampton, VA (1982).
24. Deepak, A., P.-H. Wang, H. Malchow, and C. Whitney, Satellite Determination of Atmospheric Aerosols and Ozone from Limb and Down Viewing Measurements, Volume of Extended Abstracts, 1980 International Radiation Symposium, August 11-16, Fort Collins, CO, pp. 523-525.
25. Wang, P. H., G. K. Yue, A. Deepak, and R. J. Kurzeja, A Model Study of the Diurnal Variation of Mesospheric O_3, J. London (ed.) *Proceedings of the Quadrennial International Ozone Symposium*, IAMAP (1980), pp. 876-883 (1980).
26. Wang, P.-H., S. Hong, M.-F. Wu, and A. Deepak, A time Fourier analysis of zonal averaged ozone heating rates, *AMS Preprint for the Fourth Conference on Atmospheric Radiation,* June 16-18, 1981, Toronto, Ontario, Canada, pp. 149-152.
27. Wang, P.-H., S.-s. Hong, M.-F. Wu, and A. Deepak, A Model Study of the Temporal and Spatial Variations of the Zonally-Averaged Ozone Heating Rate , *J. Atmos. Sci., 39,* 6, 1398-1409 (1982).
28. Box, G. P., M. A. Box, and A. Deepak, On the Spectral Sensitivity of the Approximate Method for Retrieving Aerosol Size Distributions from Multispectral Solar Extinction Measurements, *J. Appl. Meteor., 20,* 8, 944-948 (1981).
29. Deepak, A., Aerosol Remote Sensing, J. F. Vernberg (ed.), *Processes in Marine Remote Sensing, Primars I,* University of South Carolina Press, SC (1981).
30. Box, M. A., and A. Deepak, The Finite Sun Effect on the Interpretation of Solar Aureole, *Appl. Opt., 20,* 16, 2806-2810 (1981).
31. Deepak, A., G. P. Box, and M. A. Box, Experimental Validation of the Solar Aureole Technique for Determining Aerosol Size Distributions, *Appl. Opt., 21,* 2236 (1982).

1. Report No.	2. Government Accession No.	3. Recipient's Catalog No.
NASA CR-172599		

4. Title and Subtitle	5. Report Date
THE INVESTIGATION OF ADVANCED REMOTE SENSING, RADIATIVE TRANSFER AND INVERSION TECHNIQUES FOR THE MEASUREMENT OF ATMOSPHERIC CONSTITUENTS	March 1985
	6. Performing Organization Code
7. Author(s)	8. Performing Organization Report No.
Adarsh Deepak and Pi-Huan Wang	IFAORS TR 215
	10. Work Unit No.
9. Performing Organization Name and Address Institute For Atmospheric Optics and Remote Sensing 101 Research Drive Hampton, Virginia 23666	11. Contract or Grant No. NAS1-15198
	13. Type of Report and Period Covered Contractor Report
12. Sponsoring Agency Name and Address National Aeronautics and Space Administration Washington, DC 20546	14. Sponsoring Agency Code

15. Supplementary Notes
Langley Technical Monitor: L. R. McMaster
Final Report

16. Abstract

This report documents the research program for developing space and ground-based remote sensing techniques performed during the period from December 15, 1977 to March 15, 1985. The program involved the application of sophisticated radiative transfer codes and inversion methods to various advanced remote sensing concepts for determining atmospheric constituents, particularly aerosols. It covers detailed discussions of the solar aureole technique for monitoring columnar aerosol size distribution, and the multispectral limb scattered radiance and limb attenuated radiance (solar occultation) techniques, as well as the upwelling scattered solar radiance method for determining the aerosol and gaseous characteristics. In addition, analytical models of aerosol size distribution and simulation studies of the limb solar aureole radiance technique and the variability of ozone at high altitudes during satellite sunrise/sunset evens are also described in detail.

17. Key Words (Suggested by Author(s))	18. Distribution Statement
Atmospheric Remote Sensing	Unlimited

19. Security Classif. (of this report)	20. Security Classif. (of this page)	21. No. of Pages	22. Price
Unclassified	Unclassified	326	

For sale by the National Technical Information Service, Springfield, Virginia 22161